Modelling Corona Noise on High Voltage Transmission Lines

Rodney Urban

Supervisors:

Prof. H.C. Reader
Dr. J.P. Holtzhausen

Thesis presented in partial fulfilment for the requirements of the degree of Master of Engineering at the University of Stellenbosch

October 2001

Stellenbosch University http://scholar.sun.ac.za/

Declaration

I, the undersigned, hereby declare that the work contained in this thesis is my own work and has not previously in its entirety or in part been submitted at any university for a degree.

Signature:

Date:

Stellenbosch University http://scholar.sun.ac.za/

Abstract

The corona performance of a compact transmission line design must be accurately determined. In particular, the conducted radio interference (RI) noise level will significantly affect the power line carrier communication used for teleprotection on the line. This conducted RI noise can be calculated with a numerical transmission line code. This thesis investigates the extraction of corona and RI noise elements for inclusion into such a code. The required RI noise measurements are made in a small laboratory corona cage in the bandwidth 5 kHz to 1 GHz. The measurement system is modelled for frequencies below 30 MHz and corona and RI noise elements are extracted in this low-frequency regime. RI noise measurements are made with a time domain oscilloscope and with a frequency domain EMI receiver and spectrum analyser. A strong correlation is observed between the narrowband peak EMI receiver measurements and the swept narrowband spectrum analyser measurements. Accurate quasi-peak measurements cannot be made in the small corona cage due to a low number of RI sources on the short corona cage centre conductor. The work presented in this thesis will be used in future research to develop a small-scale corona cage, a generation transform for small corona cages and a conversion between peak and quasi-peak or RMS measurements made in the small corona cage.

Stellenbosch University http://scholar.sun.ac.za/

Opsomming

Die korona-werkverrigting van 'n kompakte transmissielyn ontwerp moet akkuraat bepaal word. Die vlak van radio interferensie (RI) ruis het 'n groot invloed op die kraglyn-dragolf kommunikasie wat tele-beveiliging aan die lyn verskaf. 'n Numeriese transmissielyn programkode kan gebruik word vir die bepaling van hierdie RI-vlak. Hierdie tesis ondersoek die onttrekking van korona en RI-ruis elemente vir insluiting in so 'n programkode. Die RI-ruis word in 'n klein korona-kou gemeet in die frekwensiegebied vanaf 5 kHz tot 1 GHz. Die meetstelsel is gemodelleer vir frekwensies laer as 30 MHz. Die korona en RI-ruis elemente is vir hierdie frekwensiegebied onttrek. Die metings is met 'n tydgebied-ossilloskoop asook 'n frekwensiegebied EMI-ontvanger en spektrumanaliseerder gemaak. 'n Sterk korrellasie is tussen die nouband EMI-ontvanger metings en die geveegde nouband spektrumanaliseerder metings gevind. Die klein korona-kou kan nie gebruik word om akkurate kwasi-piek metings te neem nie. Dit is waarskynlik omdat daar te min RI-bronne bestaan op die kort middelste geleier van die klein korona-kou. Die werk in hierdie tesis gaan gebruik word in toekomstige navorsing om 'n korona-kou op kleinskaal te ontwikkel asook vir omskakelings tussen piek en kwasi-piek of WGK metings, gemeet in 'n klein korona-kou.

Stellenbosch University http://scholar.sun.ac.za/

Acknowledgements

Special thanks must be given to:

God, my family and my friends for your love, help and support;

Prof. Howard Reader and Dr. Koos Holtzhausen for your help, guidance and attention to detail which has helped me develop as both a person and an engineer;

Mr. Tony Britten and Mr. Roy Hubbard for your ongoing interest and support of this corona research.

Jan Greyling, Petrus Pieterse, Ulrich Buttner and Wilhelm Schwardt for your help during the past year.

Who's _ got the brain of jfk _...
what's it mean to us now _ ... ?
ed vedder

Stellenbosch University http://scholar.sun.ac.za/

Contents

1 Introduction 1

1.1 Transmission Line Design and Corona Considerations 1
1.2 The Need for a Corona Model 1
1.3 Research Objectives 2
1.4 Outline of Thesis 2

2 Corona Physics 3

2.1 Introduction 3
2.2 Ionization 3
2.2.1 Excitation and Ionization 3
2.2.2 Recombination and Electron Attachment 4
2.2.3 Electron Emission from Conductors 4
2.2.4 Non-Self-Sustained Electron Avalanche 5
2.2.5 Self-Sustained Discharge 5
2.3 Corona Discharge 6
2.3.1 Negative (Cathode) Corona Discharge 7
2.3.2 Positive (Anode) Corona Discharge 8
2.4 Induced Currents 9
2.5 DC Corona Modes 9
2.5.1 Trichel Pulses 10
2.5.2 Pulseless Glow 11
2.5.3 Negative Streamers 11
2.5.4 Onset Pulses 12
2.5.5 Hermstein's Glow 13
2.5.6 Positive Streamers 13
2.6 AC Corona 14
2.7 Environmental Conditions 14
2.8 Conclusions 16
2.9 References 17

3 Experimental Setup 19

3.1 Introduction 19
3.2 Literature Survey 19
3.2.1 Field Measurements 19
3.2.1.1 Long-Line Measurements 20
3.2.1.2 Short-Line Measurements 21
3.2.1.3 Large Corona Cage Measurements 23
3.2.2 Laboratory Measurements 25
3.2.2.1 Small Corona Cage Measurements 26
3.2.2.2 Other Experimental Setups 26
3.3 Corona Cage Design 27
3.3.1 Electric Field Distribution 27
3.3.2 Natural Transmission Line Parameters 31

Stellenbosch University http://scholar.sun.ac.za/

3.3.3 Bandwidth Considerations 32
3.3.4 Measurement Devices 35
3.3.5 Physical Construction 38
3.4 The High Voltage Laboratory 41
3.4.1 Current Modes 42
3.4.2 Grounding and the Transfer Impedance Concept 42
3.4.3 Existing Grounding Structures and Ground Loops 44
3.4.4 Spurious Noise 46
3.5 Shielding Techniques 46
3.5.1 Coaxial Cables 46
3.5.2 Cable Trays 47
3.5.3 The EMC Cabinet 48
3.5.4 Filters 49
3.6 Conclusions 51
3.7 References 52

4 Transmission Line Modelling with Corona Effects 54

4.1 Introduction 54
4.2 Literature Survey 56
4.2.1 Transmission Line Modelling with Corona Effects 57
4.2.1.1 Linear-Element Time Domain Modelling 57
4.2.1.2 Non-Linear-Element Time Domain Modelling 59
4.2.1.3 Frequency Domain Modelling 60
4.2.1.4 RI Current Injection 61
4.2.2 Model Parameter Extraction 62
4.2.2.1 Frequency-Dependent Parameter Extraction 62
4.2.2.2 Overview of Corona Branch Extraction 62
4.2.2.3 Corona Branch Extraction From Measured Q-V Curves 64
4.2.2.4 Corona Branch Extraction From Predicted Q-V Curves - Mathematical Models 64
4.2.2.5 Corona Branch Extraction From Predicted Q-V Curves - Physics Models 66
4.3 Proposed Low-Frequency Models 69
4.3.1 Comparison of Linear-Element and Non-Linear-Element Models 69
4.3.2 Comparison of Non-Linear Element Models 70
4.3.3 Proposed Low-Frequency Corona Cage Model 70
4.3.4 Proposed Low-Frequency Transmission Line Model 72
4.4 Model Parameter Extraction 72
4.4.1 Q-V Curve Measurement 72
4.4.2 Extraction of the Corona Branch Elements 76
4.5 Conclusions 77
4.6 References 78

5 RI Current Measurement 80

5.1 Introduction 80
5.2 Literature Survey 80
5.2.1 Time Domain Measurements 80

Stellenbosch University http://scholar.sun.ac.za/

5.2.2 Frequency Domain Measurements 81
5.2.2.1 Radio Noise Meters 81
5.2.2.2 The Spectrum Analyser 82
5.2.2.3 The EMI Receiver 82
5.2.3 Extraction of Statistical Properties 82
5.3 Source Voltage Harmonics 83
5.4 Time Domain Oscilloscope Measurements 84
5.4.1 Oscilloscope Basics 85
5.4.2 Triggering on Random Corona Pulses 86
5.4.3 Measurement Results 88
5.5 Frequency Domain EMI Receiver Measurements 94
5.5.1 The Narrowband Radio Noise Meter 94
5.5.2 Making Wideband Measurements with the EMI Receiver 96
5.5.3 Triggering on Random Corona Pulses 97
5.5.4 Measurement Results 99
5.6 Frequency Domain Spectrum Analyser Measurements 102
5.6.1 Spectrum Analyser Basics 103
5.6.2 Wideband Measurement of Random Corona Pulses 104
5.6.3 Swept Narrowband Measurement of Random Corona Pulses 105
5.6.4 Measurement Results 106
5.7 Extraction of Statistical Properties 109
5.7.1 Sampling Rate and Measurement Bandwidth 110
5.8 Conclusions 111
5.9 References 113

6 Conclusions 114

7 Recommendations 117

A Appendix A: Theory 118
A1 Generation Function Theory 119
A2 Time Domain Non-Linear-Element Siluciu Model Formulation 123

B Appendix B: Simulations 125
B1 The Coulomb Static/Quasi-Static Field Solver 126
B2 A Repetitive Laplace Electric Field Solver 129
B3 A Physics-Based Q-V Model 132

C Appendix C: Metrology 136
C1 Extraction of Natural Transmission Line Parameters 137
C2 Extraction of Low-Frequency Dielectric Properties 140
C3 Transfer Impedance Measurement 143
C4 An Alternative Q-V Curve Measurement Method 146

D Appendix D: Hardware 148
D1 Coaxial Shunt Design 149
D2 High Voltage Coupling/Decoupling Capacitor Design 151
D3 External-Trigger Hardware Design 153

Stellenbosch University http://scholar.sun.ac.za/

E Appendix E: GPIB Instrument Control 155
E1 ESPC EMI Receiver Control 156
E2 HP8562A Spectrum Analyser Control 158

Stellenbosch University http://scholar.sun.ac.za/

List of Abbreviations

PLC	Power Line Carrier
STP	Standard Temperature and Pressure
RMS	Root Mean Square
RI	Radio Interference
RIV	Radio Influence Voltage
TVI	Television Interference
CM	Common Mode
DM	Differential Mode
QP	Quasi-Peak
EMI	Electro-Magnetic Interference
DUT	Device Under Test
FDTD	Finite-Difference Time-Domain

Stellenbosch University http://scholar.sun.ac.za/

List of Figures

Figure 2.1: Schematic diagram illustrating the progress of a self-sustained discharge. 5
Figure 2.2: Schematic cross-section of a coaxial geometry with a negative source voltage showing the space charge distribution and the resultant electric field. 7
Figure 2.3: Schematic cross-section of a coaxial geometry with a positive source voltage showing the space charge distribution and the resultant electric field 8
Figure 2.4: Typical (a) visual and (b) electrical characteristics of a Trichel pulse discharge. 10
Figure 2.5: Typical visual characteristics of a pulseless glow discharge. 11
Figure 2.6: Typical visual characteristics of a negative streamer discharge. 11
Figure 2.7: Typical (a) visual and (b) electrical characteristics of an onset streamer discharge. 12
Figure 2.8: Typical visual characteristics of Hermstein's glow discharge. 13
Figure 2.9: Possible corona modes under 50 Hz AC conditions. 14
Figure 3.1: Photographs of a typical long-line field measurement showing (a) placement of the test site along the long transmission line and (b) the experimental setup at one of the test sites. 20
Figure 3.2: A photograph of a short test line terminated at one end for coupling transient voltage pulses onto the line and for RIV measurements. 22
Figure 3.3: Photographs of a large corona cage (a) with a rectangular cross-section and (b) with a circular cross-section. 23
Figure 3.4: A photograph of a typical small laboratory corona cage. 26
Figure 3.5: The coaxial electrode geometry of the corona cage and its associated non-uniform electric field distribution in the absence of space charge. 27
Figure 3.6: (a) The simulated coaxial geometry with finite length and (b) the calculated electric field distribution on the conductor surface extracted from the Coulomb simulation. 29
Figure 3.7: The Coulomb simulation model showing the geometry of the proposed corona cage design (all dimensions are in millimetres). 30
Figure 3.8: Schematic cross-section of the corona cage illustrating two possible RI current pulse paths to the measurement point. 33
Figure 3.9: (a) Schematic cross-section of the modified measurement setup and (b) a circuit diagram of the measurement resistor and measurement device. 34
Figure 3.10: A narrowband, electro-quasi-static circuit diagram of the corona cage for the 50Hz sinusoidal excitation. 35
Figure 3.11: A large RI current pulse measured in the positive half-cycle at a voltage just below the flash-over voltage: (a) time domain plot and (b) energy spectral density plot. 36
Figure 3.12: (a) The coaxial shunt proposed in [22] and (b) a photograph of various resistive devices. 37
Figure 3.13: Impedance of the various non-ideal resistors in figure 3.12: (a) magnitude and (b) phase plots. 37
Figure 3.14: Photographs of the corona cage constructed at the University of Stellenbosch. 38
Figure 3.15: A photograph of the support cradle used to tension the centre conductor and keep the cage and guard rings in position. 39
Figure 3.16: (a) A Corocam photograph of the corona discharges occurring on the

Stellenbosch University http://scholar.sun.ac.za/

tensioning nut and thread of the centre conductor and (b) a cross-sectional cut-away view of the corona ring used to remove this spurious corona. 39
Figure 3.17: (a) A Corocam photograph of the surface discharges occurring in the vicinity of the slot in the tensioning support and (b) a photograph of the cross-section of a piece of pressed board showing the selection of samples. 40
Figure 3.18: (a) A schematic cross-sectional view of the corona rings used to reduce the electric field near the slot in the tensioning supports and (b) the Coulomb simulation results confirming the reduction in electric field strength near the slot. 41
Figure 3.19: Schematic diagram of (a) a differential mode (DM) coupling and (b) a common mode (CM) coupling in a typical experimental setup. 42
Figure 3.20: (a) Schematic diagram of a large ground loop that will result in CM current flow and (b) a grounding structure that can be used to reduce such interference. 43
Figure 3.21: Schematic diagram illustrating the definition of transfer impedance per unit length given in equation 3.15. 43
Figure 3.22: (a) Photograph of the experimental setup in the laboratory and (b) connection of permanent grounding structures to the laboratory ground. 44
Figure 3.23: Schematic diagram of the experimental setup showing connections to the laboratory grounding structures and potential ground loops that are formed. 45
Figure 3.24: The measured transfer impedance of the two significant ground loops defined in figure 3.23: (a) ground loop B and (b) ground loop C. 45
Figure 3.25: A comparison of the transfer impedance of the measurement loop with and without a foil layer surrounding the RG-58 coaxial cable. 46
Figure 3.26: Cross-sectional view of a typical metal cable tray showing the B-field distribution and field strength [nH/m] (h = 45 mm and w = 90 mm). 47
Figure 3.27: (a) A cross-sectional schematic view of the measurement setup showing the position of the cable tray and (b) the transfer impedance of this measurement system with and without the RG-58 coaxial cable placed in the cable tray. 48
Figure 3.28: Schematic view of (a) a fully enclosed EMC cabinet and (b) the rear panel of an EMC cabinet. 48
Figure 3.29: The transfer impedance of the measurement system with and without an EMC cabinet used to shield the sensitive measurement equipment. 49
Figure 3.30: (a) A circuit diagram of the LC filter used in the source loop and (b) the frequency response of this filter assuming ideal components. 50
Figure 3.31: A comparison between the measured transfer impedance of the source loop with and without the LC filter presented in figure 3.30 (a). 50
Figure 4.1: Schematic diagram of the distributed models for a corona cage and a single conductor transmission line showing lumped-parameter differential sections for each model. 54
Figure 4.2: Schematic diagram of a proposed differential segment of the distributed-parameter model for a transmission line with corona and frequency-dependent effects. 55
Figure 4.3: An overview of transmission line modelling with corona and frequency-dependent effects 57
Figure 4.4: The linear-element circuit model used to simulate transient pulse propagation along transmission lines with corona effects. 58
Figure 4.5: An ideal non-linear circuit model of the corona branch. 59

Stellenbosch University http://scholar.sun.ac.za/

Figure 4.6: An analog equivalent circuit of the shunt conductance used in the Siluciu model corona branch. 60
Figure 4.7: (a) A Q-V curve with its piecewise-linear approximation, (b) the division of the source waveform into voltage levels corresponding to the piecewise-linear Q-V curve in (a). 61
Figure 4.8: An example of a typical Q-V curve showing hysteresis. 62
Figure 4.9: Overview of the methods used for the extracting the corona branch elements. ...63
Figure 4.10: A typical corona cage Q-V curve measurement setup. 64
Figure 4.11: Schematic cross-section of the corona cage illustrating the basis for the formulation of the mathematic corona branch model. 65
Figure 4.12: Comparison of simulated Q-V curves for a 50 Hz source voltage, extracted from a linear-element circuit model [3] and a non-linear-element model [14], with a measured Q-V curve (R = 300 mm, a = 8 mm and V(peak) = 120 kV). ..70
Figure 4.13: Schematic diagram of the proposed low-frequency corona cage model. 70
Figure 4.14: The measured frequency response of the measurement system confirming the validity of the low-frequency corona cage model in the frequency range: 150kHz to 30MHz. 71
Figure 4.15: Proposed low-frequency distributed-parameter transmission line model. 72
Figure 4.16: The phase of an ideal integrator and that of the non-ideal integrator used in the charge measurement (R = 1k Ω and C = 690nF). 73
Figure 4.17: Schematic diagram of the experimental setup for an alternative Q-V curve measurement method and (b) the frequency response of this measurement system. 74
Figure 4.18: The input impedance of the TDS3032 oscilloscope (10 MΩ setting) used in the Q-V measurement system in figure 4.17 (a). 74
Figure 4.19: Comparison of a simulated Q-V curve for the AC source voltage with an equivalent measured Q-V curve (R = 300 mm, a = 8 mm and V(peak) = 120 kV). The simulated Q-V curve is extracted from the physics-based model in [14]. 75
Figure 4.20: A set of Q-V curves measured in the corona cage design in chapter 3 made with 5 kV steps from 95 kV to 120 kV (R = 300 mm, a = 8 mm). 75
Figure 4.21: The dynamic capacitance between the corona sheath and the corona cage for one period of the AC source voltage waveform, extracted from the measured and simulated Q-V curves (R = 300 mm, a = 8 mm and V(peak) = 120 kV). 76
Figure 4.22: The (a) average power loss and (b) series loss resistance in the corona cage extracted from the measured and simulated Q-V curves for a peak applied voltage of between 100 kV and 120 kV. (R = 300 mm, a = 8 mm). 77
Figure 5.1: The (a) measured time domain and (b) calculated frequency domain plot of the applied source voltage used in the experimental setup described in chapter 3. 83
Figure 5.2: The relationship between the fundamental amplitude and the amplitude of the 3rd, 5th and 7th harmonic components. 84
Figure 5.3: Block diagram of a typical digitizing oscilloscope. 85
Figure 5.4: (a) Schematic diagram of the input section and (b) the theoretical and measured input impedance of the TDS3032 digital oscilloscope. 85
Figure 5.5: The measured RI noise waveform with the source harmonic components remove showing the position and shape of various corona pulses that make up the AC corona modes. 87

Stellenbosch University http://scholar.sun.ac.za/

Figure 5.6: The (a) measured time domain and (b) calculated frequency domain plot of a RI pulse observed at 90 kV (peak) using level triggering. 89
Figure 5.7: Time domain RI waveforms measured at (a) 100 kV and (b) 110 kV using level triggering indicating the repetitive pulse sequences at these applied voltages. 90
Figure 5.8: The (a) measured time domain and (b) calculated frequency domain plot of a RI pulse observed at 110 kV (peak) using level triggering. 91
Figure 5.9: A time domain RI waveform measured at 120 kV using level triggering. 91
Figure 5.10: Phase triggering applied to a 120 kV source voltage waveform at a phase angle of (a) + 90 and (b) - 90 showing both the applied voltage and RI current waveforms. 92
Figure 5.11: The (a) measured time domain and (b) calculated frequency domain plot of a RI pulse observed at 120 kV (peak) using phase triggering and a phase angle of -95. 93
Figure 5.12: Comparison of the frequency spectrum of the Trichel pulse in figure 5.11 (a) and a positive streamer that was also captured at an applied voltage of 120 kV. 93
Figure 5.13: A block diagram of a typical radio noise meter. 94
Figure 5.14: Circuit diagrams of (1) an average, (2) a peak and (3) a quasi-peak detector weighting circuit. 95
Figure 5.15: The output level of the three weighting circuits for a pulsed RF waveform. 95
Figure 5.16: A block diagram of a typical EMI receiver. 96
Figure 5.17: Time domain measurements of the source voltage and RI waveforms observed in (a) the positive half-cycle and (b) the negative half-cycle illustrating the phase triggering method of the EMI receiver. 98
Figure 5.18: The variation in the measured RI frequency spectrum for (a) the peak and (b) the quasi-peak detectors with various measure times applied. 99
Figure 5.19: The variation in the measured RI frequency spectrum for the peak detector with various averaging factors applied to the measurement. 100
Figure 5.20: (a) A nest of measured peak detector curves for the source voltage range 30 kV to 125 kV in 5 kV steps and (b) the measured curves at four indicated source voltages. 100
Figure 5.21: Positive half-cycle corona modes observed with the EMI receiver using a measure time of 1 ms and phase triggering at (a) + 35° and (b) + 65° with a source voltage of 120 kV. 101
Figure 5.22: The negative half-cycle Trichel pulse frequency spectrum observed with the EMI receiver using a measure time of 2 ms and phase triggering at - 80 with a source voltage of 120 kV. 102
Figure 5.23: A block diagram of a typical spectrum analyser. 103
Figure 5.24: A comparison between the source voltage waveform and a spectrum analyser sweep waveform that is (a) periodically related and (b) not periodically related to the source voltage. 104
Figure 5.25: Schematic diagram of various signals in the spectrum analyser measurement path described in figure 5.23, illustrating the signal processing for the swept narrowband method. 105
Figure 5.26: Wideband spectrum analyser measurements with various sweep times. 106
Figure 5.27: (a)Wideband measurement results made at various applied voltages with a sweep time of 500 ms and more than 100 sweeps, (b) a time domain positive streamer RI pulse. 107

Stellenbosch University http://scholar.sun.ac.za/

Figure 5.28: The dependence of the swept narrowband spectrum analyser frequency spectrum on (a) the resolution bandwidth and (b) the sweep time. 108
Figure 5.29: The displayed spectrum analyser trace for an applied voltage of 120 kV at a centre frequency of (a) 5 MHz and (b) 15 MHz. 108
Figure 5.30: The peak frequency spectrum measured at various source voltages using the swept narrowband spectrum analyser method. 109
Figure 5.31: The time domain plot of a typical RI pulse (Vs = 120 kV and f_s = 2.5Gs/s) ...110
Figure 5.32: A comparison of the measured frequency spectra of (a) positive streamers and (b) Trichel pulses observed with various oscilloscope and EMI receiver measurement methods. 111
Figure 5.33: A comparison of the measured frequency spectra of positive streamers observed with the random triggering ESPC, wideband and swept narrowband SA measurement methods. 112

Stellenbosch University http://scholar.sun.ac.za/

List of Tables

Table 3.1: Natural transmission line parameters for the corona cage design in figure 3.7. 31
Table 5.1: A qualitative summary of the voltage dependence of the RI pulse characteristics extracted from level triggered oscilloscope measurements. 92
Table 5.2: The division of the measured RF frequency spectrum into four frequency bands and their associated IF bandwidth according to the CISPR 16 standard. 94
Table 5.3: Input RF power limits of the R&S ESPC and the measured maximum RI power values extracted in section 3.3.4. 97
Table 5.4: The bandwidth of the measured RI noise in discrete voltage ranges. 101

Stellenbosch University http://scholar.sun.ac.za/

Chapter 1

Introduction

1.1 Transmission Line Design and Corona Considerations

High voltages are used on transmission line conductors to facilitate the transfer of large amounts of energy between various locations on a national energy grid. Each transmission line is designed to transfer a maximum amount of energy. Increasing energy demands eventually surpass these maximum ratings. To accommodate the increased energy needs, either more transmission lines must be built or a more compact transmission line design is required. The latter method is more economically viable and is therefore preferred. Electrically, the compact line design causes an increase in the electric field magnitude at the surface of the conductors. This may cause excessive corona activity if the transmission line is not correctly designed. Other factors such as mechanical strength, construction cost and installation considerations will also influence the design process. It is therefore necessary to define limits for corona performance and extract the anticipated performance from a transmission line design. This will enable the transmission line designer to make the compromises necessary to accommodate all the requirements and produce a good compact transmission line design.

Various corona effects need to be considered since they will all impact on the overall performance of the transmission line. Acoustically, corona activity can create noise levels which exceed human annoyance limits. Electrically, the corona discharges cause radio frequency current pulses to flow on the conductors, increased power loss to the system and radiated noise in the vicinity of the transmission line. An important aspect of a transmission line design is the system protection used to protect the transmission line during fault conditions. A widely used protection method is teleprotection which utilises the transmission line conductors for power line carrier (PLC) communication. This entails the use of high-frequency signals that are coupled onto one end of the transmission line and decoupled at the receiver end. In South Africa, PLC communication has been allocated the frequency band 5 kHz to 500 kHz. Conductor corona causes a high level of background noise in this frequency range. The exact level of this background noise must therefore be known when designing a transmission line. Space charge generated in the air gap adjacent to the conductors alters the electric field near the surface of the conductors. This causes an increase in the attenuation of high-frequency signals propagating along the transmission line. The calculation of the corona noise level at the line terminations is therefore complex and requires considerable effort.

1.2 The Need for a Corona Model

Research conducted on existing transmission lines has enabled the derivation of empirical formulas which can be used to predict the corona performance of transmission line designs of similar geometry. These empirical formulas do not however accurately predict the corona performance of compact transmission line designs which have a different geometry. An analytical or numerical method of predicting the corona performance is therefore required for these designs.

Stellenbosch University http://scholar.sun.ac.za/

The availability of numerical transmission line codes and the increasing computational ability of digital computers makes a numerical prediction method possible. The numerical transmission line codes do not however include corona elements. A corona model must therefore be derived from accurate measurements and included into an existing numerical model. Model elements must also be included to model the changes in surface electric field due to space charges adjacent to the surface of the conductors. The corona phenomena that must be included in such a model and the measurements required to extract them must now be defined since these form the subject of the research presented in this thesis.

1.3 Research Objectives

The primary objective of the research in this thesis is the inclusion of a wideband corona element into a numerical transmission line code. This corona element must accurately model the high-frequency current pulses induced on the conductors by corona discharges adjacent to their surface. This will enable the calculation of the background noise at the transmission line terminations. An experimental setup that can be used to extract this model element from measurements must be defined and characterised. The setup must be accommodated in the facilities available to the research in this thesis. While only the macroscopic corona phenomena need to be modelled, the microscopic corona processes must be considered to ensure that the corona measurements made in the experimental setup are equivalent to measurements made on the actual transmission line design. The experimental setup must therefore be accurately modelled and the model elements must be compatible with existing transmission line models.

The research in this thesis will exclusively consider 50 Hz AC conditions. The relationship between the corona current frequency spectrum and the source voltage waveform must be extracted and included in the model. Attention must also be given to the influence of environmental conditions on the corona current. Fair weather conditions at standard temperature and pressure will be used throughout this thesis. While the PLC frequency band is of primary interest in this thesis, extraction of a wideband model of the corona phenomena ensures that the model is not restricted to only this application. The proposed frequency band considered in this thesis is therefore chosen as 5 kHz to 1 GHz.

1.4 Outline of Thesis

In order to better understand the approach required and interpret the measurements made, a discussion on the basic physical corona process is needed. This is presented in chapter 2. Emphasis is placed on the various forms of corona and its dependence on the source voltage and environmental conditions, in particular power frequency AC corona in a shielded laboratory environment. The choice and characterization of the experimental setup used to observe the required corona phenomena is discussed in chapter 3. The selected experimental setup must then be modelled so that the results extracted from it can be included in the transmission line model used to calculate the corona noise at the transmission line terminations. The modelling of the experimental setup and the transmission line with corona effects is presented in chapter 4. Having chosen and modelled the experimental setup used in the thesis, the measurements required to extract the macroscopic corona phenomena must be defined and made. Various measurement methods are proposed in chapter 5 and the measurement results obtained from these methods are compared so that the most accurate and appropriate methods can be identified. Finally conclusions are drawn up in chapter 6 and recommendations for future research are made in chapter 7.

Stellenbosch University http://scholar.sun.ac.za/

Chapter 2

Corona Physics

2.1 Introduction

The need to understand the physical corona processes on a qualitative level was discussed in section 1.3. In this chapter terms related to corona discharge will be defined and the physical processes necessary for a clear understanding of the various macroscopic corona phenomena will be described. Emphasis is placed on how the system geometry and the applied source voltage affect the macroscopic electrical properties of corona discharges. The visual properties of corona will also be discussed. This should enable visual identification and confirmation of the presence of various forms of corona.

Most of the literature on corona physics referred to in this chapter is derived from experiments that utilise a point-to-plane geometry (e.g. [1], [2] and [3]). The experiments in [1] and [4] also involve a cylinder-to-plane geometry and a coaxial geometry respectively. Most of the corona on a transmission line originates from the cylindrical conductors (i.e. a cylinder-to-plane geometry). There will however be isolated perturbations on the conductors and on the transmission line fittings from which corona can occur (i.e. a point-to-plane geometry). The differences between the corona from these two geometries will be highlighted throughout this chapter. This comparison will again be made qualitatively so that the discussion is not confined to a specific geometry.

In section 2.2 the physical ionization process, as it applies to transmission line corona, is discussed. This leads to a description of the basic corona discharge process in section 2.3. In section 2.4 the mechanism by which corona discharges induce currents in the electrodes is discussed. The effect of space charge in the ionization region is initially excluded since it complicates the discussion. These effects will be later included in section 2.5. Finally the effect of AC voltage conditions and various environmental conditions on corona is briefly summarized in sections 2.6 and 2.7 respectively. The most important conclusions are presented in section 2.8.

2.2 Ionization

Ionization is defined in [5] as "The process by which neutral molecules or atoms dissociate to form positively and negatively charged particles". These charged particles can cause current flow between the excited conductors, thus reducing the electrical insulation of the system. Insulation between conductors is achieved on a transmission line by means of a dielectric medium, air. Air is made up primarily of neutral gas molecules and water vapour.

2.2.1 Excitation and Ionization

If an electron is attached to an atom (i.e. it is in a fixed orbital around the nucleus of the atom) it has a finite and discrete kinetic energy. Electrons in the atom's outermost orbital have the most

Stellenbosch University http://scholar.sun.ac.za/

energy. These electrons can only remain in their high energy state if the lower energy orbitals (i.e. those closer to the nucleus) have been completely filled by other electrons. If this is not the case, the electron will release the excess energy in the form of a light photon and enter the lower energy orbital. To move an electron to a higher energy orbital, a finite and discrete amount of energy must be imparted on the atom. The atom is then said to be excited. The excited electron can only remain in the higher energy orbital for a short time period (in the order of 10^{-8} seconds [6]). After this time the electron will return to a lower energy orbital, releasing a light photon. If enough energy is imparted on the atom, the excited electron may move far enough away from the nucleus so that it will not return to a lower energy orbital. The electron is then lost to the atom, forming a positively charged ion and a free electron. The atom is therefore ionized.

Any free electrons in the air gap between the electrodes will be accelerated by the electric field applied between the conductors. These accelerated electrons collide with neutral air molecules. If the accelerated electrons (e^-) have sufficient kinetic energy they will ionize the molecules (A) upon impact. This is called ionization by electron impact and can be summarized as [6]:

$$A + e^- \rightarrow A^+ + 2e^- \tag{2.1}$$

A second form of ionization that is of importance in this thesis is photo-ionization. In this mechanism a light photon, emitted when an excited electron returns to a lower energy orbital, imparts the energy required to ionize the molecule.

It is evident that ionization can only be initialised if free electrons are present in the electric field. There are two important mechanisms for generating these free electrons. In the first, the natural radio-activity of the earth generates gamma radiation capable of ionizing neutral air molecules. The second mechanism is cosmic radiation and will also ionize the air. Together these mechanisms produce on average about 1000 ionized molecules of each polarity per cubic centimetre at sea level and ambient temperature [6].

2.2.2 Recombination and Electron Attachment

Groups of positively and negatively charged particles that co-exist in a gas will combine forming neutral molecules. This process is called recombination. A light photon is emitted during recombination if the negative particle is an electron. An electronegative gas consists of neutral molecules that lack an electron in their outer orbital. They therefore have an affinity for electrons and capture free electrons in a process called electron attachment. This process is responsible for the formation of negative space charge during corona discharge. Oxygen is an electronegative gas and free electrons will attach themselves to oxygen (O_2) or ozone (O_3) molecules forming heavy negative ions.

2.2.3 Electron Emission from Conductors

Free electrons in the air adjacent to the outermost atomic layer of the metallic electrode are able to move freely into the metal surface. However, to move from the metal surface to the adjacent air they require a discrete amount of energy called the work function. Only cathodes (i.e. negative electrodes) can release free electrons directly into the air gap due to their polarity. When a heavy positive ion is accelerated into the cathode surface it can potentially impart a discrete amount of energy on electrons in the metal upon collision. If this energy is greater than the work function,

Stellenbosch University http://scholar.sun.ac.za/

the ion will impart enough energy on an electron in the metal to release it into the air gap. This process is called emission by positive ion impact. A second process that can release an electron directly into the air gap is photo-electric emission. In this process a photon, incident on the cathode surface, provides the energy required to release the electron from the electrode.

2.2.4 Non-Self-Sustained Electron Avalanche

When an electron attains sufficient energy to ionize a neutral air molecule at least one electron is emitted from the ionized molecule. Two free electrons are then present in the electric field. These two electrons are accelerated in the electric field and collide with neutral molecules. If both electrons cause ionization upon impact, then at least four free electrons will exist in the field. The process continues in this fashion causing the number of free electrons in the electric field to grow exponentially. In this way a single free electron can produce an electron avalanche. The electron avalanche consists of a fast moving electron head that is attracted towards the anode and a trail of slow moving positive ions that result from the ionization. The separation of these positive and negative charges produces a strong electric field. As the avalanche progresses the charge separation increases together with its associated electric field. This field reduces the applied electric field in the vicinity of the electron head. The kinetic energy of the electrons in the discharge head is therefore reduced until eventually the electrons can no longer ionize air molecules. The electron avalanche therefore extinguishes itself. The result is that an electron avalanche is physically restricted to a small critical length. These discharges are termed non-self-sustaining since free electrons are constantly required to initiate them. Such discharges only produce small localized fields and cannot be measured with conventional measurement equipment.

2.2.5 Self-Sustained Discharge

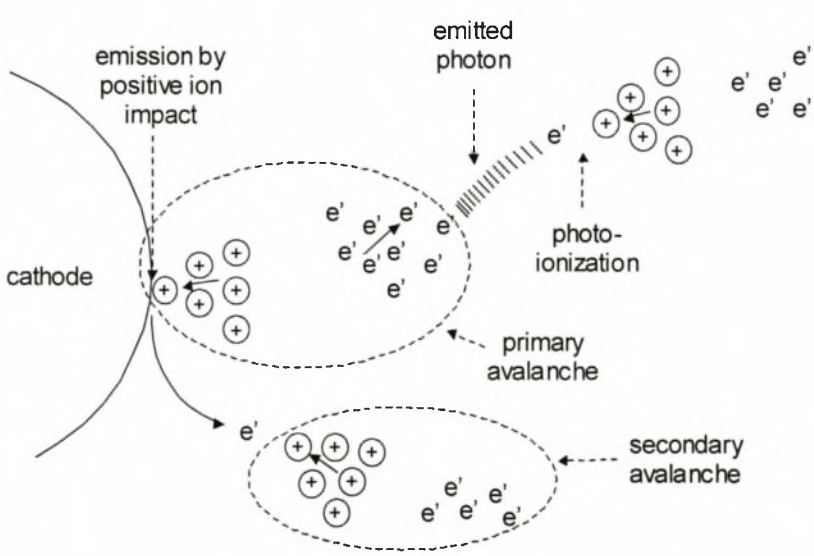

Figure 2.1: Schematic diagram illustrating the progress of a self-sustained discharge.

If a secondary ionization process exists then one electron avalanche can initiate another avalanche. In this way a series of avalanches can be produced. Two secondary ionization processes are illustrated in figure 2.1. Such discharges will progress much further towards the

Stellenbosch University http://scholar.sun.ac.za/

anode and are self-sustaining since they only require one free electron to initiate the first avalanche. Secondary ionization will then initiate the subsequent avalanches.

Only the two secondary ionization mechanisms illustrated in figure 2.1 exist at standard temperature and pressure (STP). The first mechanism is emission by positive ion impact at the cathode surface (i.e. secondary emission). This mechanism was discussed in section 2.2.3. The positive ions involved in the collisions require enough energy to emit two electrons from the electrode surface. One electron is needed to neutralize the positive ion and the other electron is needed to initiate a new avalanche in the air gap. Since the series of avalanches propagate much further into the air gap than a single avalanche, the discharge has measurable macroscopic properties. Certain metals have high work functions and emission by positive ion impact is less effective. Higher voltages are required in this case to generate self-sustained discharges. This mechanism is the main secondary emission mechanism for negative corona discharge.

The second mechanism is photo-ionization. If highly energized electrons in the electron head recombine with positive ions or become attached to electronegative molecules they will emit a light photon. This emitted photon can then cause ionization and a new electron avalanche. This mechanism is the only significant secondary emission mechanism for positive corona discharge. Self-sustained discharges produced by photo-ionization progress faster than those produced by secondary emission since the photons propagate much faster than the heavy positive ions.

2.3 Corona Discharge

Corona is defined in [5] as "Self-sustained electrical discharges in which the field-intensified ionization is localized over only a portion of the distance between the electrodes". The first part of the definition requires that the discharge is self-sustaining. Any applied voltage will accelerate free electrons and can therefore cause ionization of the air. These are the non-self-sustained discharges discussed in section 2.2.4. To generate a self-sustained discharge, the applied voltage must be above an inception level. Only self-sustained discharges produce significant macroscopic events. The second part of the definition requires that the discharge is localized over a portion of the gap between the electrodes (i.e. a partial discharge). This requires a non-uniform electric field such as the field between electrodes in a coaxial geometry. Such a field only exceeds the corona inception level in a specific region between the electrodes. The location and size of this region is determined by the applied voltage magnitude and the geometry of the electrodes.

Stellenbosch University http://scholar.sun.ac.za/

2.3.1 Negative (Cathode) Corona Discharge

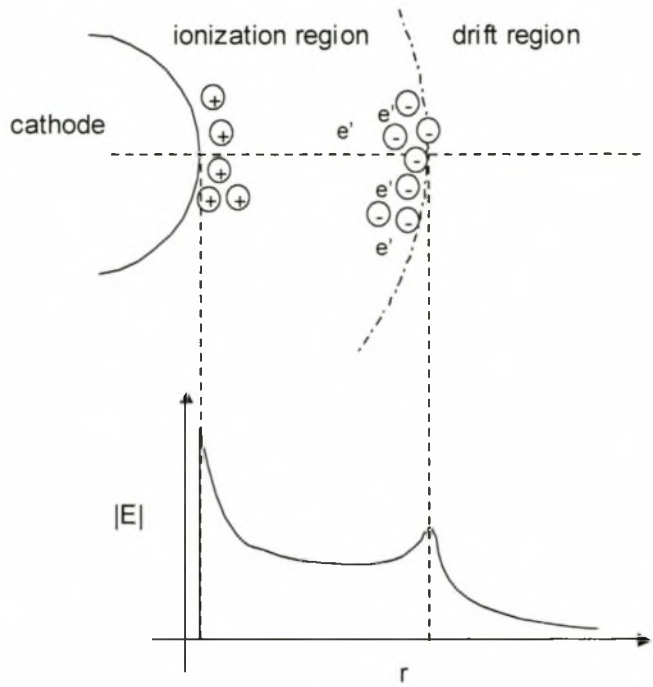

Figure 2.2: Schematic cross-section of a coaxial geometry with a negative source voltage showing the space charge distribution and the resultant electric field (after [3])

Free electrons near the cathode surface are repelled into the air gap. Since the electric field decreases rapidly the further they move from the cathode, their kinetic energy will also decrease rapidly as they propagate into the gap. The chance of an electron initiating an electron avalanche in the air gap will therefore also decrease rapidly the further it moves away from the cathode surface. Not all free electrons are thus assured of initiating an electron avalanche. If an avalanche is initiated, the positive ions formed are attracted towards the cathode. The efficient secondary ionization processes discussed in section 2.2.5 then create a series of avalanches. The self-sustaining discharge propagates far into the air gap. The local field near the cathode surface is reduced by the positive space charge. The kinetic energy of the electrons in the discharge head will therefore also be reduced. The electrons can no longer ionize the air molecules and the discharge ceases. In the gap, the electrons at the discharge head become attached to electronegative gas molecules. Since electrons have a high mobility, this negative space charge layer is formed far from the conductor surface. Before another discharge can occur in the same region, the space charge formed by the previous discharge must first be cleared. Electrons emitted at the cathode due to positive ion impact neutralize the positive space charge at the cathode surface. Also, since the negative space charge is formed far away from cathode, this charge species will have no significant effect on the applied electric field at the cathode surface. Negative corona therefore has a very effective clearing mechanism and the time between successive cathode corona discharges will be small. The negative space charge that accumulates on the edge of the ionization region decreases the electric field in the ionization region and increases the electric field at its perimeter. The conductor has therefore been effectively extended radially outwards into the gap [7].

Stellenbosch University http://scholar.sun.ac.za/

2.3.2 Positive (Anode) Corona Discharge

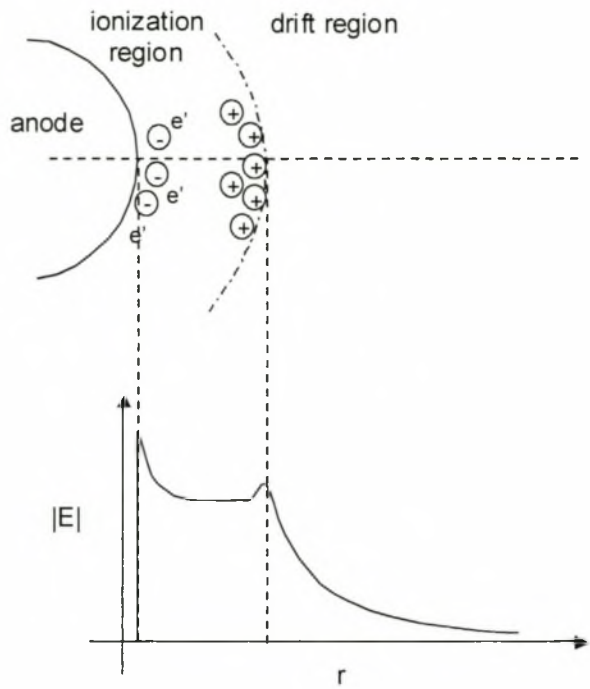

Figure 2.3: Schematic cross-section of a coaxial geometry with a positive source voltage showing the space charge distribution and the resultant electric field (after [3])

The anode accelerates free electrons in the air gap towards itself. Since the electric field increases significantly near the anode surface, the kinetic energy of the electron will also increase significantly as it gets closer to the anode. Within a certain distance from the anode the kinetic energy is sufficient to initiate a self-sustained discharge. This region is known as the ionization region. Since free electrons gain kinetic energy in an increasing field they are almost assured of initiating corona discharges. This is in contrast to cathode corona where an electron loses kinetic energy as it propagates into the gap and is not assured of initiating a corona discharge. Anode corona is said to have more favourable corona inception conditions. The corona inception level of positive corona is therefore slightly lower than that of negative corona. The secondary ionization mechanism required to sustain the corona discharge is photo-ionization. Photo-ionization is a faster secondary process than ionization by positive ion impact. Anode discharges therefore have faster rise times [8]. Once a corona discharge is initiated, the heavy positive ions formed move many orders slower than electrons. The space charge field is therefore formed closer to the conductor surface than the negative space charge layer that formed in the cathode discharge. The result is that anode corona has a less effective clearing mechanism since it must first move the positive ions further away from the anode surface before a second discharge can occur in the same region. Electron attachment near the surface of the anode generates slow moving negative ions. This negative space charge will impede the forward path of the discharge head as it progresses towards the anode.

Stellenbosch University http://scholar.sun.ac.za/

2.4 Induced Currents

Charged particles moving in the gap between two electrodes will induce current in both electrodes. The total current flow is determined by applying the superposition principle to the current contributions of each individual moving charge in the inter-electrode gap. In this way, the Shockley-Ramo theorem (see [6]) defines the current induced in any electrode of a multi-electrode configuration, due to the arbitrary motion of a charged particle in the inter-electrode gap. The current (i_c) induced on the outer conductor, of radius R, of a coaxial configuration with centre conductor radius r_c, by a particle with charge e, position r_p and velocity v_p is derived in [6] as:

$$i_c = -\frac{e.v_p}{r_p \ln(R/r_c)} \tag{2.2}$$

It is evident in equation 2.2 that the induced corona current is proportional to the velocity of the charged particles. Since the electrons move many orders faster than the heavy space charge, the current induced by moving space charge is insignificant in comparison to the current induced by electron movement. It is therefore only necessary to calculate the corona current flow due to electron motion. It is also evident in equation 2.2 that the induced current is proportional to the density and inversely proportional to the position of the electron head in a corona discharge. Since induced corona current is the measured macroscopic quantity in this thesis, the electron density, displacement and velocity in the corona discharge will be the focus of the remainder of this chapter.

2.5 DC Corona Modes

The corona process discussed thus far has been greatly simplified by ignoring the effect of slow moving charged ions (i.e. space charges) that are formed during the ionization process. While the space charge contribution to the induced current is negligible it will significantly affect the steady state electric field distribution in the inter-electrode gap and therefore has a significant effect on the macroscopic properties of corona discharges. Space charge effects are therefore discussed in this section. Corona discharges affected by space charge can be classified into a discrete number of corona modes. Each corona mode has unique macroscopic properties (e.g. amplitude, rise and decay time and repetition rate). The applied voltage and electrode geometry (i.e. the applied electric field) determines how well defined these modes are as well as the transition between the modes. As discussed in section 2.1, various electrode geometries are of interest. The discussion in this section is therefore not restricted to any one specific geometry.

UNIVERSITEIT STELLENBOSCH
BIBLIOTEEK

Stellenbosch University http://scholar.sun.ac.za/

The various corona modes are better defined and more observable under DC voltage conditions since the inception conditions remain constant and the space charge is moved in a constant direction away from the ionization region. Under AC conditions the inception conditions vary sinusoidally and remnant space charge, of both polarities, from previous half-cycles exists in the ionization region. The corona modes will therefore first be defined and classified for DC voltages (see [1]) in this section. The effect of AC voltage on these well defined modes will then be discussed in the next section.

2.5.1 Trichel Pulses

This corona discharge mode is the first measurable discharge in the negative half-cycle. The electron avalanches are accelerated away from the cathode for tens of nanoseconds until they can no longer sustain themselves. This is due to the reduced electric field in the presence of the positive space charge. The space charge formed by the discharge must first be cleared before another discharge can occur in the same region. The effective clearing mechanism of cathode corona was discussed in section 2.3.1. The time between successive discharges originating from the same region is therefore short (i.e. the repetition rate of this corona mode is high). As the voltage at the cathode becomes more negative, the number of electrons at the conductor surface increases. The positive ions at the surface can then be neutralised faster thus improving the space charge clearing mechanism. The remaining free electrons near the cathode surface will be subjected to a greater force due to the increased voltage. This will result in more effective ionizing collisions and a subsequent increase in repetition rate. The increased discharge activity will also increase the density of the negative space charge layer. The electric field in the ionization region will then be further reduced and the discharges will not propagate as far into the gap. The amplitude of Trichel pulses will therefore decrease as the voltage becomes more negative.

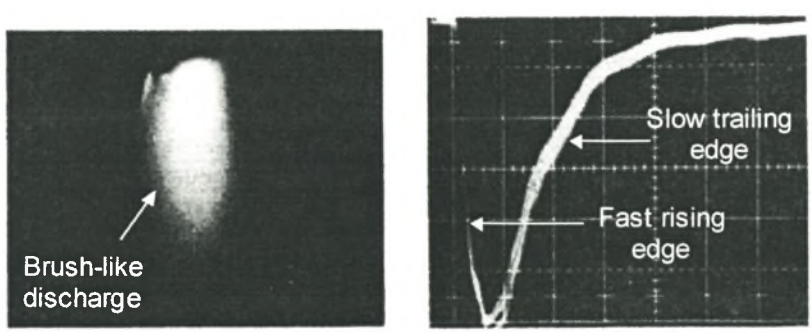

(a) (b)

Figure 2.4: Typical (a) visual and (b) electrical characteristics of a Trichel pulse discharge [6].

Trichel pulse discharges propagate into a decreasing electric field. They therefore move out radially along the steepest gradient and do not branch. The positive space charge at the cathode surface is cleared faster than the slow moving negative space charge in the air gap. The next discharge will therefore originate from the same point near the cathode but will terminate in a region away from the termination point of the previous discharge. At high repetition rates the discharges merge optically producing a brush-like discharge with a single base point (see figure 2.4 (a)). It can however be seen in figure 2.4 (b) that the Trichel pulses do not merge electrically. At a certain voltage the repetition rate reaches a maximum (i.e. a critical frequency). This critical

Stellenbosch University http://scholar.sun.ac.za/

frequency is dependent on the surface condition and the geometry of the electrode. In a point-to-plane geometry, the critical frequency is as much as three orders greater than that of large electrode geometries.

2.5.2 Pulseless Glow

Figure 2.5: Typical visual characteristics of a pulseless glow discharge [6].

If the voltage is increased above the voltage associated with the critical frequency of Trichel pulses, a transition to pulseless glow corona occurs. This cathode corona mode is stable and the individual pulses merge electrically producing a DC current with a small high-frequency ripple. If the corona source is a metallic perturbation on the conductor, a large localized current will flow from the small surface area. The resultant power flow can melt the metal at the source point. For this reason, the corona current flow in conductors decreases with age as the metal surface perturbations are reduced in size resulting in a reduction in the local field at these points.

2.5.3 Negative Streamers

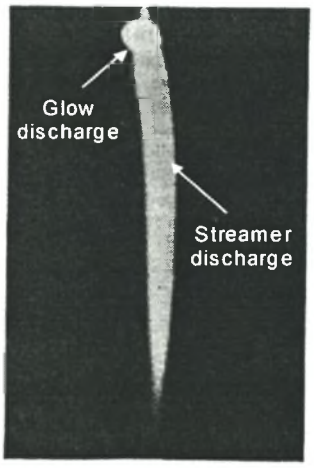

Figure 2.6: Typical visual characteristics of a negative streamer discharge [6].

This is the final cathode corona mode. When the voltage is increased above the level at which pulseless glow corona occurs, the electric field at the perimeter of the dense negative space charge layer is sufficient to cause ionization. The corona discharge initiated at the edge of the ionization region then propagates further into the gap. Since the negative space charge layer forms far from the electrode surface, a large voltage is required to generate negative streamers. Electrically the negative streamer will have a DC component (i.e. the pulseless glow corona component) and a large pulse component (i.e. the streamer discharge component). Negative streamers have a long rise time that is about two orders greater than that of Trichel pulses.

Stellenbosch University http://scholar.sun.ac.za/

2.5.4 Onset Pulses

The first anode corona mode is the onset pulse mode. There are two types of onset pulses, namely burst pulses and onset streamers. These two discharge types are classified as one mode since they are closely related. Burst pulses are in fact described in [9] as "frustrated" onset streamers. The electron avalanches of the discharge propagate radially inwards towards the anode through the ionization region. In this region there remains slow moving negative ions from previous discharges that impede the radial path of the discharge and lower the electric field in the ionization region. Since the electrons in the avalanche head are accelerated towards the anode, the negative ions will not terminate the discharge but rather only reroute its path to the anode. Anode corona therefore branches laterally. The favourable discharge conditions of anode corona mean that free electrons far away from the anode can cause corona discharge. The result is that onset streamers produce currents that have amplitudes about an order greater than Trichel pulses. Since the electron head must move around remnant negative ions on its way to the anode and does not follow a direct radial path as in the case of cathode corona, the rise time of onset streamers will be longer than that of Trichel pulses.

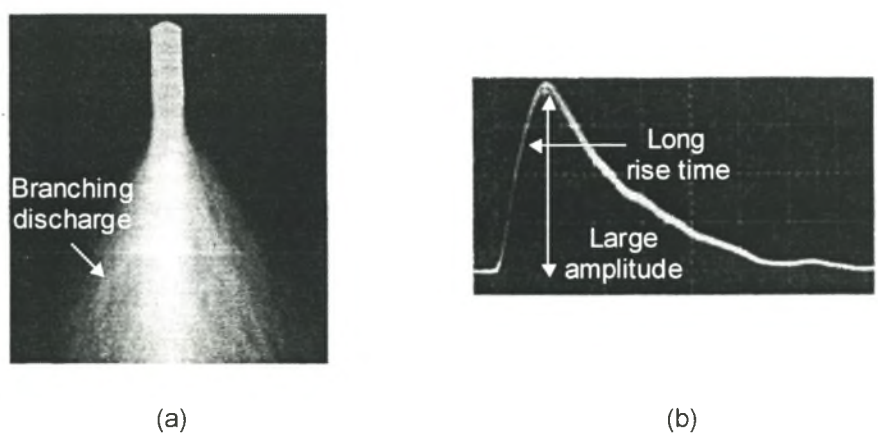

Figure 2.7: Typical (a) visual and (b) electrical characteristics of an onset streamer discharge [6].

The clearing mechanism for anode corona is less effective due to the slow negative ions that remain close to the anode surface. These must first be removed since they reduce the local electric field. The repetition rate of onset streamers is therefore about an order lower than Trichel pulses. This repetition rate also increases to a maximum critical frequency when the voltage is increased. The amplitude of the onset streamers remains fairly constant as the voltage is increased. Optically the large lateral branches of the discharge emit a bluish light. If the negative ion concentration near the conductor surface is dense then some streamers are forced to travel laterally for a long time and eventually cease. There are therefore only a few paths that terminate on the anode. The result is a brush-like appearance for this corona mode (see figure 2.7 (a)). As the negative space charge becomes sufficiently dense near the maximum repetition rate, the field in the ionization region becomes so low that only electrons very close to the surface generate discharges. These discharges are then forced to propagate laterally near the conductor surface before they can terminate on the conductor. These discharges are called burst pulses.

Stellenbosch University http://scholar.sun.ac.za/

2.5.5 Hermstein's Glow

Figure 2.8: Typical visual characteristics of Hermstein's glow discharge [6].

This anode corona mode forms when the voltage is increased after the critical frequency for onset pulses is reached. At this voltage the negative space charge at the anode surface becomes dense enough to suppress all onset pulses. Hermstein's glow is an ionized sheath that surrounds the anode surface. Electrically this results in a DC current flow in the anode. In large anode geometries the transition between onset pulses and Hermstein's glow is gradual. The DC current of the Hermstein's glow discharge will increase as the voltage is increased and has a small ripple that has a frequency in the order of a few Megahertz.

2.5.6 Positive Streamers

The ionized sheath of Hermstein's glow corona is never stable and localized regions of high space charge density form momentarily in random positions near the anode surface. At these points the electric field on the edge of the space charge layer is high enough to cause ionization further into the gap. The amplitude of these pulses at onset of the mode is of the same order as the onset pulses. This amplitude then increases rapidly as the voltage is increased above their inception level. Their repetition rate also increases with increasing voltage. Discharges from anodes of smaller geometry such as point-to-plane geometries have a more uniform repetition rate and amplitude than do those from larger geometry anodes. Electrically this corona mode has a rise time of the same order as the Trichel pulses. Their magnitude is about an order greater than that of onset streamers.

Continuous corona is defined in [5] as "Corona pulses which recur at regular intervals for periods of several minutes or more". In this chapter, thus far, the corona inception voltage has implied that voltage at which measurable corona pulses are initiated. This implied definition is not consistent with the definition adopted by most researchers interested in the engineering consequences of corona. The definition adopted in their research is given in [5] as "The minimum voltage which must be applied to the system to initiate continuous corona". While the definition adopted thus far in this chapter is physically more correct, the engineering definition in [5] will be adopted in the remainder of this thesis unless otherwise stated. Positive streamers are the first continuous anode corona mode. The minimum voltage at which positive streamers occur is therefore referred to as the positive corona inception level. For negative corona, Trichel pulses become continuous with increasing voltage. The voltage at which they become continuous is the negative inception level and is typically lower than the positive inception level.

Stellenbosch University http://scholar.sun.ac.za/

2.6 AC Corona

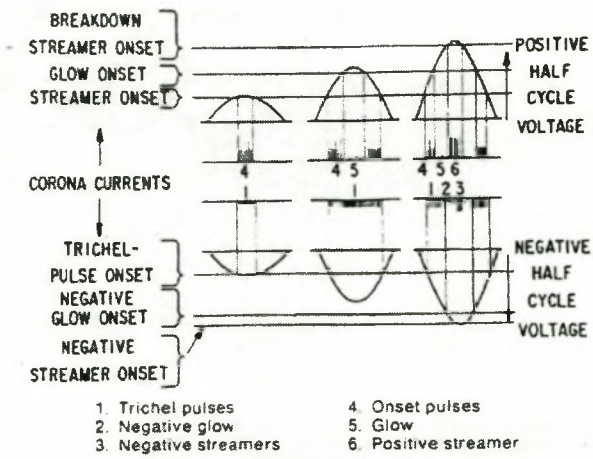

Figure 2.9: Possible corona modes under 50 Hz AC conditions [8].

Under alternating voltage conditions, the alternating electric field moves the space charge of previous corona discharges in and out of the ionization region periodically. Nett charge is therefore never lost to the system. Space charge can only be removed by neutralization. Only two neutralization mechanisms are present under normal environmental conditions. These are recombination and collision with the electrodes and both have been dealt with in previous sections. To understand the properties of AC corona, the effect of remnant space charge on the corona modes, defined in section 2.5, must be investigated. Possible corona modes that may appear on the 50 Hz AC source voltage waveform are suggested in figure 2.9. The most important effects of remnant space charge for each half-cycle can be summarized as follows:

1. Positive half-cycle: The remnant negative space charge in the ionization region suppresses onset pulse formation thus aiding the formation of Hermstein's glow. On small electrodes the onset pulses can be completely absent while on large electrodes they will be present but small in magnitude.

2. Negative half-cycle: The remnant positive space charge limits the area of Trichel pulse activity on the cathode. The initial Trichel pulses will however have a larger amplitude. It was noted in section 2.5 that the negative voltage required to initiate negative streamers is larger than the positive voltage required to initiate positive streamers. With an alternating voltage, breakdown will therefore occur in the positive half-cycle before a negative streamer is initiated. For this reason it is unlikely that a negative streamer will be observed on an AC electrode [6].

2.7 Environmental Conditions

Finally environmental conditions must be considered since these will affect the macroscopic properties of the corona discharges. Temperature and pressure affect the energy and density of air molecules per unit volume respectively. They therefore affect the number of collisions that occur between neutral molecules and free electrons as well as the movement of space charge. The nett result is a change in corona inception levels and a change in the voltages at which specific

Stellenbosch University http://scholar.sun.ac.za/

corona modes occur. Measurements will be made at sea level and ambient temperature throughout the course of this thesis. Results presented in this thesis are therefore only valid under these conditions. Wind will significantly affect the movement of remnant space charge in the air gap and will therefore affect the corona process under AC conditions.

Particles other than the gas molecules normally found in air can significantly affect corona properties. There are two important classifications for such particles. The first classification is for particles that occur in the air gap adjacent to the energized electrode. The second classification is for particles that attach themselves, either temporarily or permanently, to the energised electrode surface. The effect of these particles on corona properties can be summarized according to this classification as follows:

1. Particles in the air gap: These include particles such as water vapour, water droplets, dust particles, fire particles and insects. In the experiments performed in [2], an increase in water vapour in the gap increased the inception voltage and decreased the distance travelled by space charge in the gap. The nett amount of space charge is also decreased. This is primarily because water vapour has a high affinity for electrons and reduces the number of free ionization electrons by electron attachment. In the experiments in [10], water droplets (i.e. precipitation) were present in the gap. Water droplets have a high dielectric constant ($\varepsilon_r = 80$). When they enter the high field region, they will therefore be deformed by electro-static forces that tend to flatten them and form sharp points. The electric field in the vicinity of the water drop is then significantly increased. Breakdown between the raindrops and the conductor can also occur if the rain drops are large enough. Precipitation in the gap will therefore significantly increase corona activity and decrease the inception level. It was also found that precipitation reduced the amplitude of corona pulses in the negative half-cycle.

2. Particles on the electrode: Water drops that collect on the conductor surface will be deformed by both gravity and the applied electric field. As a result the water drops assume a conical shape. The electric field is therefore greatly increased in the vicinity of the water drops and corona discharges can be initiated at much lower voltages. The electrode geometry near the deformed water drop is of the point-to-plane geometry and not the cylinder-to-plane geometry that exists in the absence of the water drop. The difference between the corona discharges in these two geometries was highlighted in section 2.5. Precipitation on the electrode will therefore change the properties of the corona current. Water is not a good secondary emitter [10]. This means that the secondary emission mechanism necessary for a high repetition rate will be absent when water drops attach themselves to the conductor. Corona activity and space charge formation will therefore be suppressed.

From the preceding discussion it can be seen that there is a need to classify the environmental conditions, with respect to foreign particles, when making corona measurements. The classifications and definitions of relevant weather conditions are given in an IEEE standard [11] and the most important conditions can be summarized as follows:

1. Fair weather conditions: Weather conditions characterized by zero precipitation intensity and a dry conductor surface. Precipitation intensity is defined as the rate of precipitation measured in millimetres per hour. It can also be measured as an instantaneous quantity or as an average value taken over a period of time, preferably less than an hour.

Stellenbosch University http://scholar.sun.ac.za/

2. Foul weather conditions: Weather conditions characterized by non-zero precipitation intensity or those conditions that cause the conductor surface to be wet. Two prominent forms of precipitation that cause such conditions are rain and fog. Rain is defined as liquid water drops with diameters greater than 0.5 mm unless they are widely scattered, in which case the diameters can be smaller.

A detailed investigation into the effects of particles associated with both foul weather and fair weather conditions is given in [12] and [13]. Such an investigation is beyond the scope of this thesis, as defined in section 1.3. While the results of the investigation in [12] and [13] will therefore not be required, it is important to note that foreign particles and other environmental conditions have a significant effect on corona. Corona measurements should therefore include a detailed description of the environmental conditions in the experimental setup in accordance with the definitions and classifications in [11]. All measurements made in the course of this thesis are made under fair weather conditions with no foreign particles present

2.8 Conclusions

- For the purposes of this thesis, corona discharge will be defined as those partial discharges that produce significant corona currents which can be measured on the available equipment. Such discharges require a non-uniform electric field distribution such as the field in a corona cage and an effective secondary ionization mechanism (i.e. secondary emission by positive ion impact or photo-ionization).

- The macroscopic properties of corona discharges are significantly influenced by the electrode geometry. This is particularly true when comparing corona discharges occurring in point-to-plane geometries and large coaxial geometries. Since conductor corona will be studied in this thesis, point-to-plane corona sources must be removed from the experimental setup.

- The properties of the measured corona current pulse are dependent on the density, velocity and position of the electrons in the discharge. The position and velocity of the discharge's electron cloud are in turn significantly influenced by the concentration and position of the space charge in the inter-electrode gap. The effect of space charge on the measured corona current properties can be classified into a discrete number of corona modes. These modes are best defined under DC conditions. Under AC conditions, the periodic movement of space charge in the inter-electrode gap changes the appearance of certain corona modes as well as the transition between the various corona modes.

- The first negative corona mode is the Trichel pulse discharge mode. These discharges have a high repetition rate due to an effective clearing mechanism. The current pulse amplitude decreases and the pulse repetition rate increases as the magnitude of the negative voltage is increased. The repetition rate will increase to a maximum critical frequency. This critical frequency is much higher in point-to-plane electrode geometries than that of large electrode geometries. The presence of remnant positive space charge in the inter-electrode gap under AC conditions results in an increase in the amplitudes of Trichel pulses but reduces the total number of Trichel pulses.

Stellenbosch University http://scholar.sun.ac.za/

- When the magnitude of the negative voltage is increased beyond the voltage associated with the critical frequency of the Trichel pulse mode, pulseless glow corona forms. This corona mode is stable and results in a DC current flow on the electrodes with a small high-frequency ripple.

- The final negative corona mode is the negative streamer mode. This mode only appears at a very large negative voltage. Under AC conditions, flash-over will first occur in the positive half-cycle before negative streamers will appear. This corona mode will therefore not be observed under AC conditions.

- The first positive corona mode is the onset pulse mode. In comparison to Trichel pulses, onset pulses are larger in magnitude with a lower repetition rate and a longer rise time. As the voltage is increased, the amplitude of the pulses decreases. Under AC conditions, remnant negative space charge suppresses the formation of burst pulses. Only small onset pulses will therefore be observed. Transition to the next corona mode (i.e. Hermstein's glow) therefore occurs almost immediately. This corona mode results in DC current flow with a small high-frequency ripple component on the electrodes.

- The final positive corona mode is the positive streamer mode. The pulse amplitude of this corona mode increases rapidly with increasing voltage and is greater than the onset pulse amplitude. The pulse rise time is of the same order as that of the Trichel pulse mode.

- Environmental conditions will significantly affect the properties of the various corona modes as well as the inception levels of these modes. The environmental conditions of an experimental setup must therefore be accurately documented.

2.9 References

[1] T.N. Giao and J.B. Jordan, "Modes of Corona Discharges in Air", IEEE Transactions on Power Apparatus and Systems, Vol. PAS-87, No. 5, May 1968, pp. 1207-1212.

[2] N.L. Allen, D. Dring and S. Burger, "The Influence of Humidity on Positive Impulse Corona in a Rod/Plane Gap", Sixth International Conference on Gas Discharges and their Applications - Part 1, IEE Conference Publication number 189, 8 - 11 September 1980, pp. 122 - 124.

[3] E. Nasser, *Fundamentals of Gaseous Ionization & Plasma Electronics*, Wiley-Interscience, 1971, pp. 305 - 395.

[4] J.D. Cobine, *Gaseous Conductors*, Dover Publications, 1958, pp. 252 - 289.

[5] AIEE Working Group on Definitions, "Definition of Terms Related to Corona", IEEE Transactions on Power Apparatus and Systems, Vol. 82, December 1963, pp. 1044-1047.

[6] P. Sarma Maruvada, *Corona Performance of High-Voltage Transmission Lines*, Research Studies Press Ltd., 2000, pp. 55 - 87.

[7] E.W. Boehne, Discussion to paper, "Attenuation and Successive Reflections of Travelling Waves", J.C. Dowell, Transactions of the American Institute of Electrical Engineers, Vol. 50, June 1931.

[8] M.G. Comber, D.W. Deno and L.E. Zaffanella, "Corona Phenomena on AC Transmission Lines", Transmission Line Reference Book- 345kV and above, Chapter 4, EPRI, Second Edition, Revised 1987, pp. 169-184.

Stellenbosch University http://scholar.sun.ac.za/

[9] L.B. Loeb, *Electrical Coronas*, Berkeley and Los Angeles: University of California Press, 1965.

[10] L. Boulet and B.J. Jakubczyk, "A-C Corona in Foul Weather I - Above Freezing Point", IEEE Transactions on Power Apparatus and Systems, Vol. 83, May 1964, pp. 508-512.

[11] IEEE Standard No. 539 - 1990, IEEE Standard Definitions of Terms Related to Corona and Field Effects of Overhead Power Lines.

[12] H.H. Newell, T. Liao and F.W. Warburton, "Corona and RI Caused by Particles On or Near EHV Conductors: I - Fair Weather", IEEE Transactions on Power Apparatus and Systems, Vol. PAS-86, No. 11, November 1967, pp. 1375-1381.

[13] H.H. Newell, T. Liao and F.W. Warburton, "Corona and RI Caused by Particles On or Near EHV Conductors: II - Foul Weather", IEEE Transactions on Power Apparatus and Systems, Vol. PAS-87, No. 4, April 1968, pp. 911-921.

Stellenbosch University http://scholar.sun.ac.za/

Chapter 3

Experimental Setup

3.1 Introduction

Corona discharges produce various macroscopic phenomena that are of interest to engineers. Each phenomenon is studied in a specific experimental setup using specialised measurement equipment. To determine the experimental setup required in this thesis, the phenomena that need to be investigated must be defined. This was discussed in section 1.3, where it was concluded that the conducted corona noise at the transmission line terminations must be calculated, the charge-voltage (Q-V) relationship must be extracted to determine changes in surface electric field and wideband radio interference (RI) current pulses must be measured. Since the measured radio interference currents are potentially small in magnitude and the measurements made are to be wideband, special effort must be made to remove non-corona interference currents from the measurements.

A literature survey of the various measurement setups used to make such measurements is presented in section 3.2. The design of a small corona cage is discussed in section 3.3. In section 3.4, the available facilities are described and characterized. Finally shielding techniques used to remove interference currents from the measurements are described in section 3.5. Conclusions drawn from this chapter are summarized in section 3.6.

3.2 Literature Survey

Radio interference (RI) is defined in [1] as a radiated corona disturbance-field measurement made on a vertical antenna at a designated lateral distance from the outer phase of a transmission line using a radio noise meter. In [2] these radiated disturbances are further divided into two classifications according to the centre frequency of the narrowband radio noise meter. For frequencies below 75 MHz the disturbances are called radio interference (RI) and for frequencies above 75 MHz they are called television interference (TVI). In this thesis we will adopt the more general definition of [1] and refer to all radiated corona emissions as RI. The unit of measure of RI is volts per metre. Radio influence voltage (RIV) is defined in [1] as a conducted corona disturbance-voltage measurement made using a meter, coupled capacitively to the device under test (DUT), with negligible attenuation of the disturbance between the DUT and the meter. The unit of measure of RIV is volts. The experimental setup required in this thesis must allow careful wideband measurement of transmission line RI currents that will flow on specified conductor configurations so that the total RI current flow on a proposed transmission line design can be calculated.

3.2.1 Field Measurements

The simplest RI measurement technique involves measurement of the electromagnetic fields radiated from the RI currents that propagate along the multi-conductor transmission line. These

Stellenbosch University http://scholar.sun.ac.za/

measurements are made with antennas at a defined test location near the long transmission line under investigation. The meters used are mostly narrowband radio noise meters equipped with quasi-peak detectors. These measurements are referred to as long-line measurements.

3.2.1.1 Long-Line Measurements

RI generation on a long transmission line is assumed to occur from a uniform distribution of uncorrelated sources [3]. The total RI current flow (I_{total}) from n individual RI currents sources (I_{pulse}) on the transmission line conductors is therefore [3]:

$$I_{total} = \sqrt{\sum_{i=1}^{n} (I_{pulse})_i^2} = \sqrt{n}.I_{pulse} \tag{3.1}$$

High-frequency components of the RI current will be greatly attenuated while propagating along the multi-conductor transmission line. Two sources of RI can therefore be measured using antennas: (a) a narrowband antenna with a low resonant frequency will indicate a selected low-frequency component of the distributed RI current (i.e. I_{total} in equation 3.1), (b) a narrowband antenna with a high resonant frequency will indicate a selected high-frequency component of the localised RI current (i.e. I_{pulse} in equation 3.1) present at the measurement location.

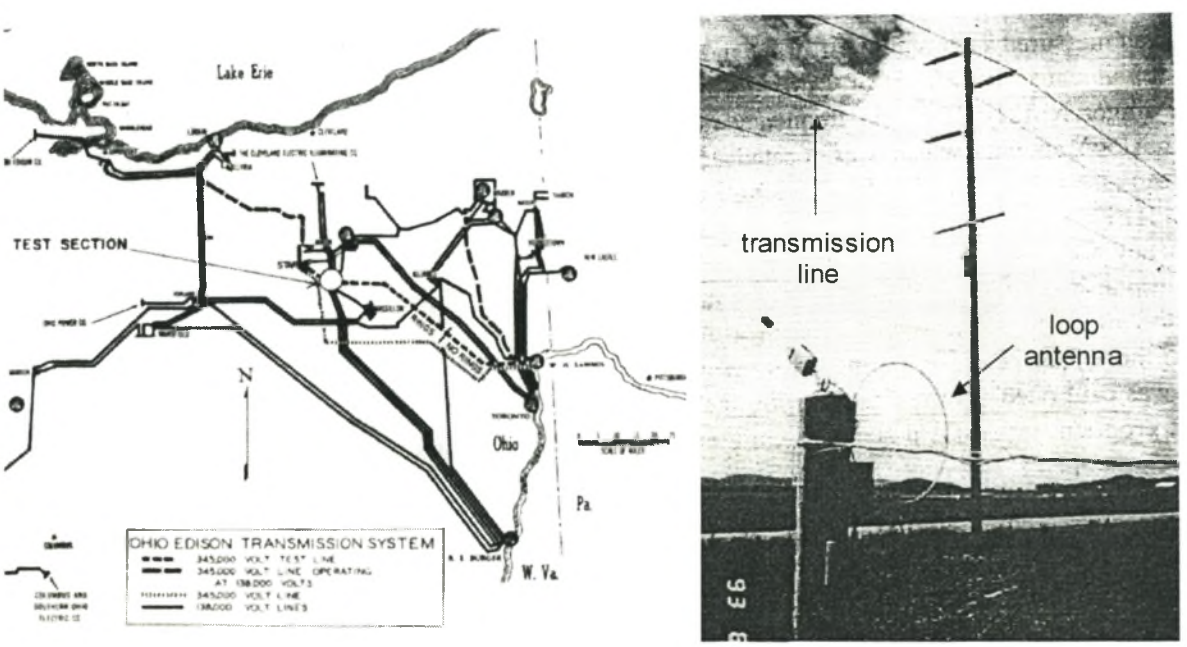

(a) (b)

Figure 3.1: Photographs of a typical long-line field measurement showing (a) placement of the test site along the long transmission line [4] and (b) the experimental setup at one of the test sites [5].

It is suggested in [1] that distributed RI current measurements be made using a monopole antenna placed at a designated lateral distance from the outermost phase. The resonant frequency of the narrowband monopole antenna is usually chosen as 1 MHz. In [5] a loop antenna with a centre frequency of 1 MHz is used to make distributed RI current measurements (see figure 3.1(b)). The IEEE standard for long-line measurements requires that the centre frequency of the quasi-peak

Stellenbosch University http://scholar.sun.ac.za/

detector used to make the measurements is 500 kHz. Localised RI current measurements are made in [6] using a dipole antenna with a centre frequency at 75 MHz and a radio noise meter with a peak detector. The bandwidth of the detector was 220 kHz and the antenna was positioned 60 metres from the transmission line. Directional antennas are also useful when measuring localised RI current and allow engineers to identify line equipment with high levels of point-source corona discharge. An important consideration when making long-line measurements is the position of the test location along the transmission line. Line terminations, line traps, abrupt transpositions and other discontinuities along the line cause reflections and standing waves at certain frequencies. Care must be taken not to make measurements at these frequencies if the test site is situated near such a discontinuity.

An important problem with long-line measurements is that there is no control over environmental conditions These ambient environmental conditions are also not often uniform along the entire length of the long transmission line. It is therefore necessary to record long-term RI current measurements together with a complete description of the ambient environmental conditions. Average RI current values for a given weather condition (e.g. heavy rain) can then be determined over a specified time period. The IEEE standard for long-term RI measurements requires that the measurement antennas are placed 15 metres laterally from the outermost phase. Continuous, long-term, long-line measurements are described in [7]. In this investigation, the test site was chosen far from any discontinuities on the line and ambient environmental conditions were recorded along the entire length of the transmission line. Three radio-noise meters were used to make the measurements. One was placed directly under the east phase conductor bundle, the second was placed 30 metres from the first noise meter in a lateral direction. The third noise meter was placed 45 metres from the first noise meter also in a lateral direction. Measurements from the third noise meter were not used due to metrology difficulties with the measurements at that distance from the line. The noise meters were calibrated every day and average measurements were recorded at the same time on every fair weather day.

The most significant disadvantage of long-line measurements is that the transmission line must first be built before its RI performance can be measured. It is not economically feasible to make significant changes to a transmission line after it has been built in order to improve its RI performance. Long-line measurements are therefore only useful for determining the RI performance of existing lines and cannot be used to predict the RI performance of a proposed line design. An alternative which will overcome this problem is the construction of a short test line that is identical to the long transmission line but is only a few kilometres long. In this case it will be economically feasible to test the RI performance of a proposed line design and make necessary changes based on the measurement results.

3.2.1.2 Short-Line Measurements

Transmission line dimensions such as conductor size, span length and height above the ground are exactly replicated on short test lines [2]. The same test equipment, described in the previous section, is used to make measurements on short test lines. The only important difference between long-line and short-line measurements is the position of the test site along the line. In the case of a short test line, this position must correspond to the electrical centre of the line. The line's electrical centre is dependent on the terminating impedances of the short test line. For radiated RI current measurements, the short test line is open circuited at both ends. This results in standing waves at frequencies that have half-wavelengths that correspond to integer multiples of the test line's length. The electrical centre in this case is at the geometrical centre of the short

Stellenbosch University http://scholar.sun.ac.za/

test line. Conducted RIV measurements are often also made on short test lines. For these measurements, capacitors in series with terminating impedances are used to decouple the current from the line to the measurement device at one end of the line. The other end is most often left unterminated. The termination impedance greatly affects the radiation properties and therefore also the electrical centre of the test line. This is particularly true when it has a significant reactive component. The effect of a non-ideal termination impedance on the radiated RI measurements is investigated in [8].

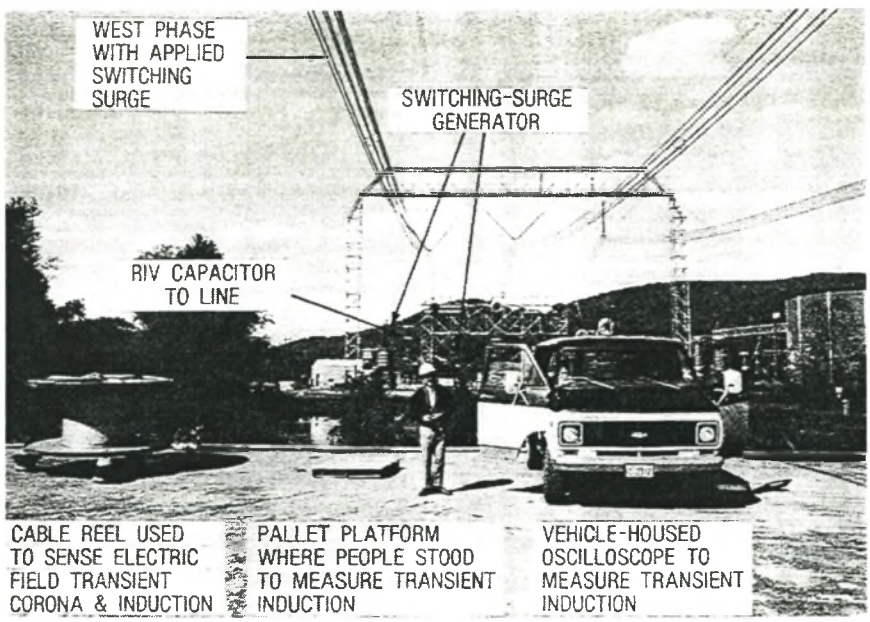

Figure 3.2: A photograph of a short test line terminated at one end for coupling transient voltage pulses onto the line and for RIV measurements [2].

A long transmission line may traverse various terrains and sections along the line may vary significantly in altitude. If this is the case, short-line measurements may not accurately predict the RI performance of a long-line even though the line geometry was exactly replicated. The positioning of the short test line is therefore essential. An example of bad positioning is described in [5] where the short test line was positioned too close to a noisy 500 kV transmission line. As a result, effective short-line measurements could not be made on the test line.

In an attempt to replicate exactly the long-line environmental conditions on a short test line, so that the effect of open-ended line terminations can be isolated and investigated, wave traps were used on a long-line in [4]. A 112 kilometre transmission line section was used for the long-line measurements. For the short test line, a 1370 metre section of the long-line was isolated using radio frequency choke-coils. Bypass switches on the choke-coils were used so that long-line and short-line measurements could be made on the same line under the same electrical and environmental conditions. Measurements were made at frequencies blocked by the wave traps. The short test line therefore had infinite termination impedances at both ends at these frequencies. The measurement antennas were positioned at the electrical centre of the line. This position corresponded with the geometrical centre of the line due to the ideal open-circuit line terminations. The results were used to derive a short-line calibration technique. A similar calibration technique is described in [2]. The geometric mean of the measured short-line frequency spectrum was found to correlate in both cases with the measured long-line frequency spectrum. A more accurate long-line to short-line conversion technique is described in [9]. In this

Stellenbosch University http://scholar.sun.ac.za/

paper the effect of non-ideal short-line terminations is included in the calibration by deriving analytical equations. These analytical equations account for the various modes of propagation on a multi-conductor, multi-phase transmission line. It was found in this paper that the geometric mean transform is only valid for ideal open-circuit terminations.

RI and RIV measurements were also made on a short test line in [4]. The short test line was however not positioned at the site of the proposed transmission line due to economic and practical reasons. The results show that short-line measurements are dependent on humidity, relative air density and wind velocity. It was concluded in chapter 2 that any corona noise investigation would need to include an investigation of the effects of these environmental conditions on the corona noise characteristics. A disadvantage of both long-line and short-line measurements, cited in [2], [10], [11] and [12], is the inability to control the environmental conditions of the experimental setup. Environmental conditions such as precipitation can occur on one section of the test line and not on the other sections. This makes short-line measurements difficult to interpret. Furthermore, since the geometry of the short-line is the same as that of the long-line, large transformers and expensive high voltage equipment is required for the experimental setup. It also takes considerable time to change the conductors when testing a new transmission line design. A smaller, less expensive experimental setup is therefore required. This would ensure uniform environmental conditions along the entire length of the test line, reduce the time required to change conductor configurations and would be less expensive to construct and maintain. One such experimental setup is the corona cage.

3.2.1.3 Large Corona Cage Measurements

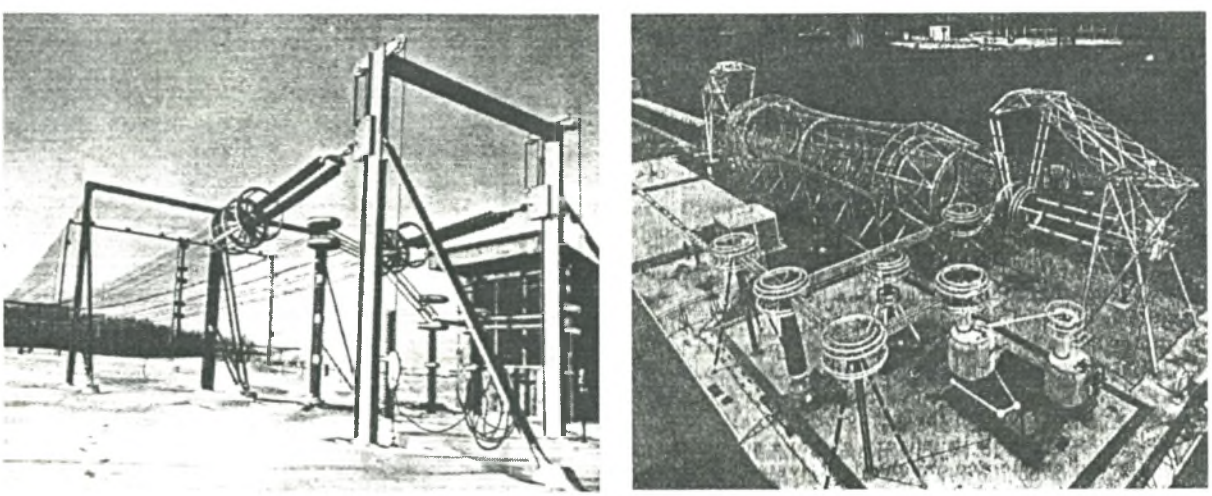

(a) (b)

Figure 3.3: Photographs of a large corona cage (a) with a rectangular cross-section [3] and (b) with a circular cross-section [13].

A typical corona cage, such as the one shown in figure 3.3 (a), is described in [2] as a rectangular grounded-mesh structure with a centred, single phase, conductor bundle of between 15 and 60 metres in length. Corona cage lengths are generally much shorter than short test lines. The applied voltage is of such a magnitude as to create a surface gradient on the centred conductor that is equivalent to the surface gradient on transmission line conductors. The corona cage is however not restricted to the study of single conductor corona. Multi-conductor bundles can also be used in the corona cage. A method of moments simulation technique, used to determine the surface gradient on individual sub-conductors of the conductor bundle in the corona cage

Stellenbosch University http://scholar.sun.ac.za/

geometry, is described in [14]. Such calculations are needed when multi-conductor bundles are placed in the corona cage. A method of recreating the electric field on the surface of the multi-conductor bundles by offsetting the conductors inside the corona cage is proposed in [3]. The applied voltage in the corona cage is lower than the transmission line voltage due to the grounded-mesh cage that is in close proximity to the conductors. Furthermore, the small size of the corona cage means that only a single span length is required. This makes the experimental setup more affordable and makes it significantly easier and quicker to change the conductor bundle configuration. Various transmission line designs can therefore be tested in a short period of time under the same ambient environmental conditions. It is also possible to apply and control uniform rain conditions of a specified intensity along the entire length of the conductor. This is achieved by mounting rain apparatus on the cage structure [13]. The conductors are matched to the surge impedance of the coaxial geometry in [3] using expensive decoupling capacitors and resistors. If the corona cage is electrically small at the measurement frequencies, the conductors are not terminated in the surge impedance but are left open circuited.

Macroscopic corona effects such as RI currents occur unpredictably with respect to time. They are therefore considered as random events and are characterized using statistical methods [15]. Since the required quantity is the RI current flow on actual transmission line conductors, it is essential that the transmission line conditions be accurately recreated. This includes the statistical distribution of corona sources along the conductors. It is noted in [3] that short conductor lengths produce few RI current sources under fair weather conditions. RI measurements made in corona cages with conductors that are too short to produce the statistical distribution of RI sources that are found on transmission lines are therefore potentially invalid. It is suggested in [3] that the corona cage must be longer than 30 metres to ensure valid RI current measurements. This length is disputed in [16] where a length of at least 1 kilometre is suggested for fair weather RI measurements. The required length has however not been determined experimentally in the literature. In this thesis, corona cages that have the correct statistical distribution of RI sources will be referred to as large corona cages and those that do not will be referred to as small corona cages.

On short, capacitively-terminated or open-circuited corona cage conductors, the electric field is not uniform along the length of the conductor due to charge accumulation at the conductor ends. The electric field distribution is therefore not a valid replication of the field on the transmission line conductors. This non-uniformity is negated in [3] by making the cage length much longer than the gap between the cage and the conductor bundle (i.e. the inter-electrode gap length). The length of the region of increased electric field intensity at the conductor ends is therefore insignificant in comparison to the length of the region of uniform electric field distribution. If the cage length is not much longer than the inter-electrode gap length then a calibration technique, proposed in [3], accounts for the small increase in total RI current due to the end effects. A preferred alternative is the use of guard rings. In this method, the corona cage is divided into three electrically isolated sections. The central section surrounds the region of the conductor with a uniform electric field along the length of the conductor. The guard rings on either side of the central section surround the regions affected by the end effects. RI current measurements made from the central section are therefore valid since they exclude the end effects. Sag is greatly reduced in the corona cage due to the short length of the cage and by tensioning the conductor between anchored structures that are isolated from the conductors (see figure 3.3). The sag and variation in terrain that occurs on actual transmission lines and short test lines is therefore absent in the corona cage. This will lead to differences between the corona cage measurements and either short-line or long-line measurements. The average conductor height of the transmission

Stellenbosch University http://scholar.sun.ac.za/

line is therefore used when comparing transmission line and corona cage RI values.

If the surface gradient on the conductors of a transmission line is exactly recreated in a corona cage as well as the statistical distribution of RI current sources, then the physical corona generation process on the transmission line will be duplicated in the corona cage. The RI current induced on a transmission line will however not be duplicated due to differences in electrical and environmental conditions between the transmission line and the corona cage. In order to determine the RI current that will flow on an actual transmission line from corona cage measurements, an analytical transform must be derived. This transform must be a function of geometry and significant environmental factors so that the differences in these properties between the transmission line and corona cage can be accounted for. Such a transform is called a generation function (also known as an excitation function) and was first proposed by G.E. Adams [11]. A computational method is then used to propagate these induced currents along the transmission line. Questions are raised in [10] as to how accurately the corona cage measurements reflect the actual operating conditions, in particular factors such as conductor temperature, wind and space charge movement. These questions are addressed in [10] by comparing the various existing generation functions and identifying factors that lead to more accurate results. The generation functions considered were the Electricite de France Method (EdF), project HVTRC methods (HVTRC and WETCON), the Hydro-Quebec method (IREQ), the BPA Corona and Field Effects method (CFE) and the International Conference on Large High Voltage Electrical Systems method (CIGRE). A discussion of the Gary approach [12] to the generation function is presented in appendix A1.

3.2.2 Laboratory Measurements

Making corona measurements in an enclosed laboratory has many advantages. The most important advantage is the ability to subject the experimental setup to controlled, defined environmental conditions. For example, experiments can be performed to investigate the effect of rain on RI performance since rain of a specified precipitation rate can be uniformly applied along the entire length of the conductor. This was done in [17] and [18]. The electrical environment of a laboratory can also be controlled more easily than is the case with field tests. The measurements in [19] were unusable due to high levels of electromagnetic noise at the test location. This can be avoided in a laboratory. A disadvantage of the laboratory is the cost of construction. The size of the laboratory is therefore usually small. Typically only small corona cages (see definition in section 3.2.1.3) can be used in most laboratories.

Stellenbosch University http://scholar.sun.ac.za/

3.2.2.1 Small Corona Cage Measurements

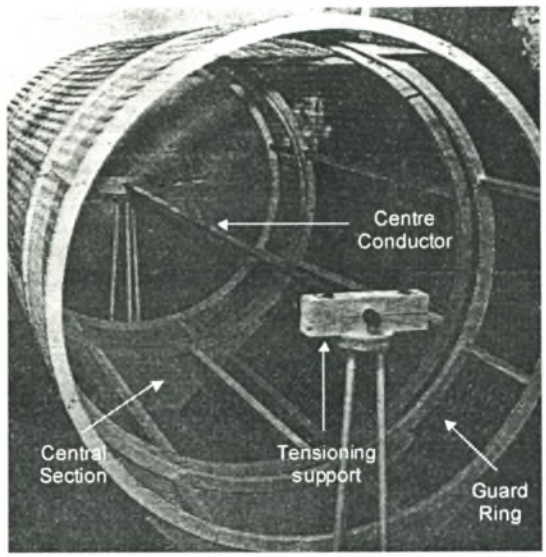

Figure 3.4: A photograph of a typical small laboratory corona cage [20]

As already mentioned in section 3.2.1.3, small corona cages cannot be used to make quantitative measurements of RI current under fair weather conditions. This is because there are too few RI current sources on the short conductor. RI measurements can however be used under heavy rain conditions. These measurements are made in [17] using a narrowband measurement system with a centre frequency of 1 MHz. The small corona cage was open circuited at one end and terminated in its surge impedance at the other end using a 1600 pF capacitor in series with a resistor. Small corona cages are also used to obtain qualitative measurements of RI under various controlled environmental conditions. This helps researchers to understand the physical discharge processes under these conditions and is done in the experiments in [18] where RI current from single water drops on the conductor surface is measured. The experiments in [18] required wideband RI measurements. The corona cage was electrically large at the highest measured frequency. Fast current pulses induced on the corona cage therefore reflected off the open circuited termination of the cage as well as the measurement point where the current pulses were channelled to ground through a measurement impedance. These reflections were reduced by galvanically connecting the grounded guard rings to the corona cage using impedances matched to the surge impedance of the cage. The measurement impedance was also matched to the cage's surge impedance.

3.2.2.2 Other Experimental Setups

A cylinder-to-plane geometry is suggested in [19]. This geometry was used so that the inter-electrode gap length could be easily varied. In coaxial corona cages, only the centre conductor geometry is easily varied. The tangential variation in surface electric field is also a more realistic representation of the field on actual transmission line conductors. This is however unnecessary since neither this geometry nor the corona cage geometry is exactly the same as an actual transmission line. Both setups therefore require a generation function to transform the measurements to equivalent transmission line conditions. The axial symmetry of the electric field on the surface of the centre conductor of the corona cage will increase the number of RI source and will therefore improve the measurement. A corona cage is also easier to shield electrically.

Stellenbosch University http://scholar.sun.ac.za/

3.3 Corona Cage Design

The facility available at the University of Stellenbosch is a small laboratory equipped with a 150kVA AC transformer. From the literature survey in section 3.2 it is evident that the best experimental setup for studying the macroscopic corona phenomena defined in section 1.3 in this facility would be a small corona cage. The use of a small corona cage will allow close control of electrical and weather conditions. Interpretation of small corona cage measurements, however, requires a transform to transmission line conditions (i.e. a generation function). At present, small corona cage generation functions have only been used under heavy rain conditions in the literature. It will therefore be necessary, since a small corona cage is to be used, to determine a valid generation function or possibly an alternative transform technique for all appropriate environmental conditions. The design and characterization of the small corona cage that will be used throughout this thesis is presented in this section.

3.3.1 Electric Field Distribution

It was noted in section 2.3 that the occurrence of corona discharge requires that the electric field is above an inception value over a partial section of the inter-electrode gap. A non-uniform electric field is therefore required.

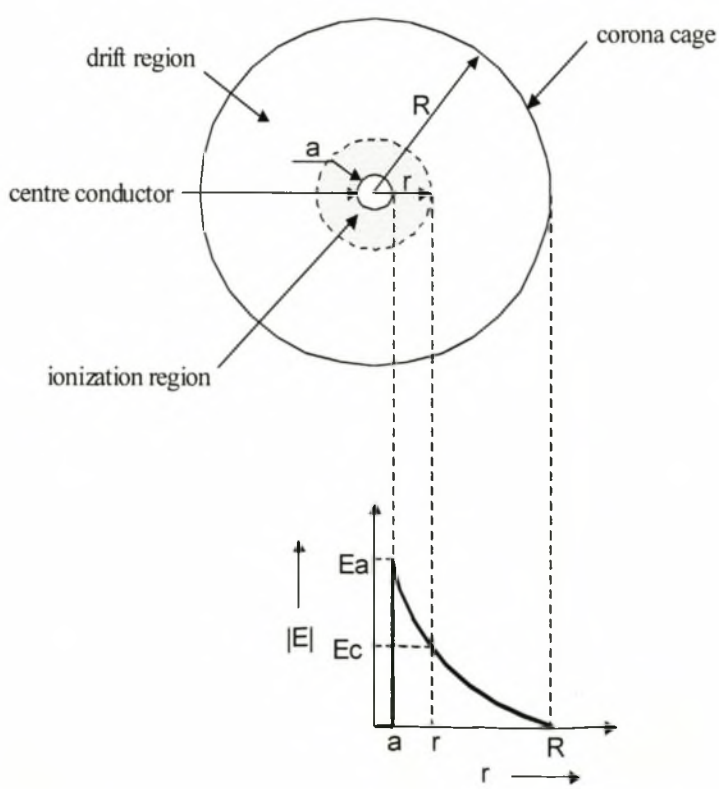

Figure 3.5: The coaxial electrode geometry of the corona cage and its associated non-uniform electric field distribution in the absence of space charge.

Stellenbosch University http://scholar.sun.ac.za/

The coaxial geometry of the corona cage will create the required non-uniform electric field distribution as illustrated in figure 3.5. The electric field (E_r) at radius r in the inter-electrode gap is [21]:

$$E_r = E_a\left(\frac{a}{r}\right) \qquad \text{[V/m]} \tag{3.2}$$

where E_a is the electric field on the surface of the centre conductor of radius a (see figure 3.5). For a grounded outer conductor with radius R and a voltage V applied to the inner electrode, the electric field strength on the inner conductor surface is [21]:

$$E_a = \frac{V}{a\ln\left(\frac{R}{a}\right)} \qquad \text{[V/m]} \tag{3.3}$$

An advantage of the small laboratory corona cage is that a smaller, less expensive high voltage transformer can be used to generate the required electric field on the conductor surface. The required source voltage in equation 3.3 can be reduced by decreasing either the cage radius or the conductor radius. There is however a minimum distance for the gap between the centre conductor and the corona cage. This critical distance is equal to the maximum distance travelled by a space charge under the influence of the alternating electric field of frequency f. It ensures that space charge does not collide and recombine with the corona cage conductor. If this were to happen, charge would be lost to the system and the physical corona process would be affected. The corona process in such a corona cage would therefore not be an accurate replication of the actual transmission line corona process. The critical gap length (d_c) is given empirically for a coaxial geometry with inner conductor radius (a) in [22]:

$$(d_c + a)^2 - a^2 = \frac{akE_c}{f} \tag{3.4}$$

In equation 3.4, k is the space charge mobility and E_c is the inception field level. For positive ions $k^+ = 1.5$ cm^2/V.s [23] and for negative ions $k^- = 1.8$ cm^2/V.s [23]. The drift and ionization regions, indicated in figure 3.5, were discussed in chapter 2. The boundary between these two regions is defined in figure 3.5 by the corona inception level, E_c which was defined qualitatively in section 2.5. It was noted in this section that the inception level marks the transition of corona discharges to electrically significant corona modes. Less significant corona discharge modes will appear if the electric field on the conductor surface is lower than the corona inception level (i.e. the ionization region defined in figure 3.5 has zero area). Quantitatively the corona inception level for the geometry in figure 3.5, with a the radius of the inner electrode in centimetres, is defined empirically as [21]:

$$E_c = 31m\delta\left(1 + \frac{0.308}{\sqrt{\delta a}}\right) \qquad \text{[kV/cm]} \tag{3.5}$$

Stellenbosch University http://scholar.sun.ac.za/

In equation 3.5, m is an indication, on a scale of 0 to 1, as to the irregularity of the inner electrode surface, with the value one corresponding to an ideal, smooth surface. The measurements made in this thesis are made at standard temperature and pressure (STP). The relative air density factor, δ, is therefore equal to one. The corona inception level in equation 3.5 is dependent on the radius of the inner conductor. The minimum radius of the inner conductor corresponds to a corona inception level that equals the electric field magnitude at which flash-over occurs. It was found in section 2.6 that the various corona modes can be best observed under AC conditions if a smooth cylindrical conductor with a large radius is used. An important objective of this thesis, defined in section 1.3, is to identify and measure the electrical properties of the various corona modes as well as the transition between the modes (i.e. the relationship between the applied waveform and the RI source frequency spectrum). A smooth copper pipe is therefore used in the proposed corona cage design. Copper has a relatively low work function. This will ensure that the secondary emission process discussed in section 2.2.3 is not inhibited. The formation of the various corona modes is therefore also not inhibited. Surface perturbations that could potentially initiate point-to-plane corona discharges are removed using fine sandpaper.

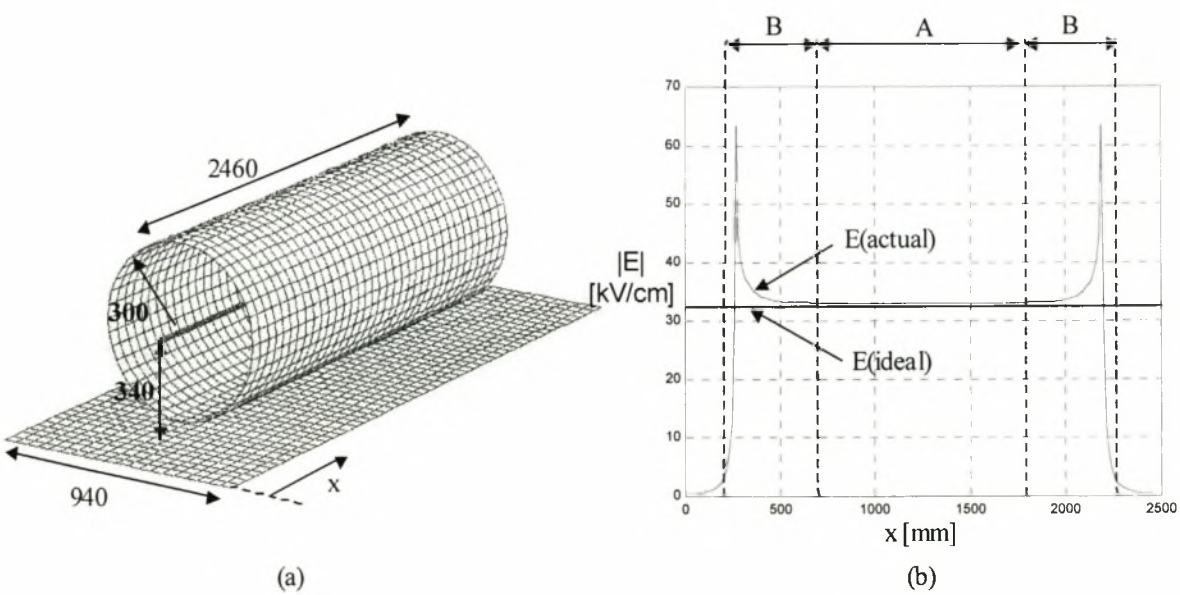

Figure 3.6: (a) The simulated coaxial geometry with finite length and (b) the calculated electric field distribution on the conductor surface extracted from the Coulomb simulation.

Thus far, only electric field distributions in coaxial geometries with infinite length in the axial direction have been considered. In reality this length is finite and will in fact be short due to the limited size of the laboratory. The Coulomb electric field solver that will be used in this thesis to solve electric field distributions is discussed in appendix B1. The simulation results in figure 3.6 (b) indicate that the finite length of the corona cage and inner conductor result in an electric field that is non-uniform along the length of the centre conductor. Corona activity will therefore be significantly higher near the ends of the excited centre conductor. An accurate correlation between the level of RI current and the electric field strength on the centre conductor surface can therefore not be made. The uniform electric field distribution for an infinite conductor length is

Stellenbosch University http://scholar.sun.ac.za/

also plotted in figure 3.6 (b). The RMS deviation of the actual electric field distribution and the ideal electric field distribution along the surface of the centre conductor of length l is:

$$D_{RMS} = \sqrt{\frac{1}{l}\int_0^l \left(E_{actual} - E_{ideal}\right)^2 dl} \tag{3.6}$$

The RMS deviation in region A in figure 3.6 (b) is less than 0.1% of the ideal electric field strength. This will lead to a negligible increase in RI current. If the RI current flow on this section of the corona cage could be isolated, the RI current measurements would not be affected by the finite conductor and cage lengths. This can be achieved by dividing the corona cage into three electrically isolated sections as was proposed in the literature survey. The two outer sections are called guard rings and are grounded and galvanically isolated from the central section. In order to determine the optimum guard ring length for a specified maximum RMS deviation, a finite difference (Repetitive Laplace) numerical code was written This code is discussed in appendix B2. The accuracy of the Repetitive Laplace simulation is confirmed by comparison with an equivalent Coulomb simulation. The Repetitive Laplace simulation has a shorter simulation time and it is easier to vary the cage dimensions, in particular the ratio of the cage length to the guard ring length. The Simulation starts with an initial minimum guard ring length, calculates a converged field distribution and then finally calculates the RMS deviation of the calculated electric field. If this value is not acceptable, the guard ring length is increased and the next iteration begins. This procedure is repeated until the RMS deviation is less than the specified maximum value.

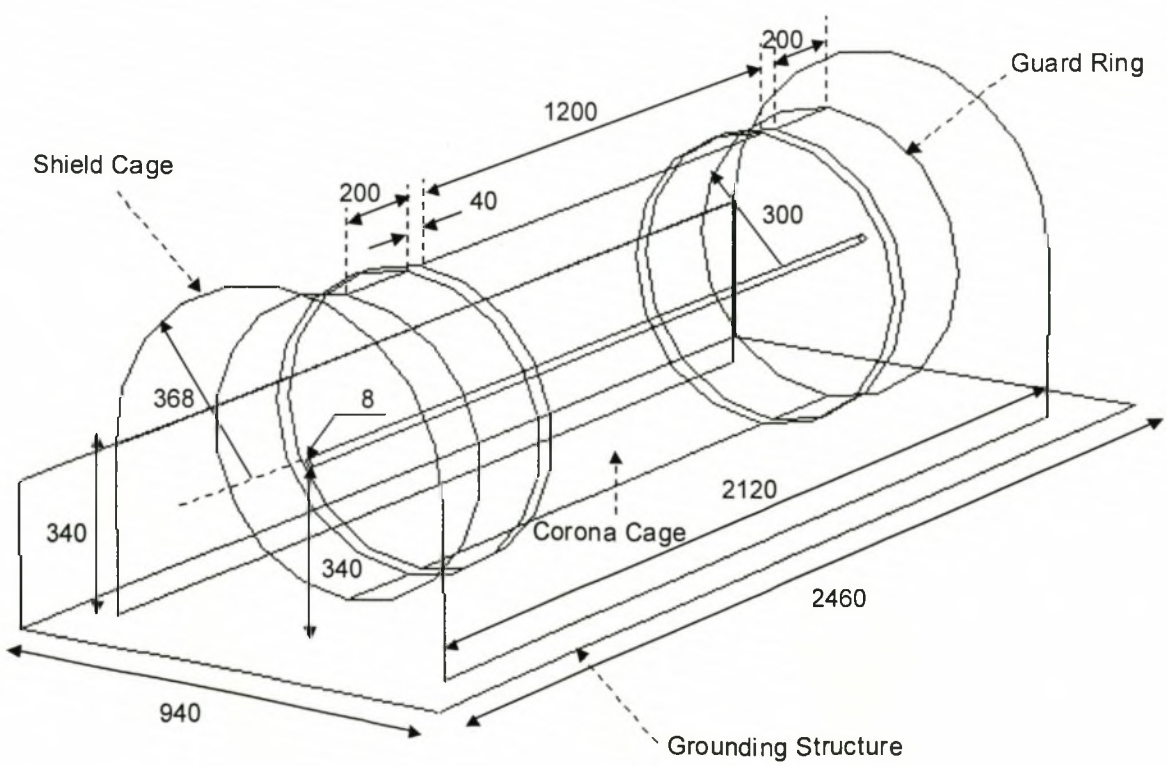

Figure 3.7: The Coulomb simulation model showing the geometry of the proposed corona cage design (all dimensions are in millimetres).

Stellenbosch University http://scholar.sun.ac.za/

Copper piping with a radius of 8 mm was available. This was the same radius as a standard transmission line conductor used in a larger corona cage at the University of Stellenbosch. The corona inception level for this conductor was experimentally determined to be 34.5 kV/cm (peak). The measurement of the corona inception level will be discussed in chapter 4. Substituting the conductor radius and the inception level into equation 3.5 gives an irregularity factor of 0.83 for the smooth copper conductor. The electric field magnitude at which flash-over occurs was measured at 44 kV/cm (peak) which is significantly larger than the inception level. The 8 mm inner conductor is therefore acceptable. Substituting the centre conductor radius into equation 3.4 gives a minimum cage radius of 0.307 m. This minimum value is used in the design so that the validity of the empirical formulae in equation 3.4 can be tested. The available high voltage transformer is capable of providing the peak voltage if required. Finally the length of the cage is chosen as 1.2 m. This length should produce numerous RI sources on the centre conductor and fits conveniently into the laboratory. The length of the guard rings needed to create a deviation in the electric field of less than 1 %, is calculated with the Repetitive Laplace code as 0.2 m.

3.3.2 Natural Transmission Line Parameters

In order to fully characterize the unexcited corona cage, the natural transmission line parameters must be defined and extracted. When the corona cage is excited by an AC voltage that is large enough to generate significant corona activity, the space charge formed by the corona will distort the electric field and therefore alter the natural transmission line parameters. This will be discussed in chapter 4 and will not be dealt with in this section.

The most important low-frequency, lumped LC parameters of the corona cage will be determined using theoretical formulas, Coulomb simulations and measurements.

Parameter	Theoretical	Coulomb	Measured
Centre conductor - to - ground capacitance [pF] (C_s)	12.5	12.4	15
Centre conductor - to - corona cage capacitance [pF] (C_1)	18.4	18.9	22
Corona cage - to - ground capacitance [pF] (C_2)	326.8	366.3	400
Centre conductor - to - ground inductance [nH]	626.9	-	800
Corona cage - to - ground inductance [nH]	49.0	-	100

Table 3.1: Natural transmission line parameters for the corona cage design in figure 3.7.

Stellenbosch University http://scholar.sun.ac.za/

The theoretical formulas for the free space capacitance and inductance calculated in table 3.1 for an infinitely long, uniform coaxial geometry, with inner radius a and outer radius R, are [2]:

$$C = \frac{2\pi\varepsilon_0}{\ln(R/a)} \qquad [\text{F/m}] \tag{3.7}$$

$$L = \frac{\mu_0}{2\pi}\ln\left(\frac{R}{a}\right) \qquad [\text{H/m}] \tag{3.8}$$

The measurement techniques used to measure the low-frequency, lumped LC parameters presented in table 3.1 are discussed in appendix C1. The theoretical formulas in equations 3.7 and 3.8 assume a uniform coaxial geometry with infinite length along the axis of symmetry. They also assume that the dielectric medium in the inter-electrode gaps is free space. The actual corona cage design in figure 3.7 does not have a perfectly coaxial cross-section (see figure 3.7 where the sides of the shield cage terminate perpendicular to the ground structure). It also has finite length and some of the space between the shield cage and corona cage is filled with pressed-board dielectric material. The values calculated from the empirical formulas therefore differ significantly from the simulated and measured values. The Coulomb simulation model includes the effect of finite length and the pressed board dielectric material. The model also assumes that the corona cage and guard rings are right-circular cylinders and that the grounding structure is perfectly flat. The large corona cage, shield cage and grounding structure are made out of thin metal plates that are bent into shape. As a result, the cage cylinders constructed for this thesis are not perfectly circular in cross-section and the grounding structure is also not perfectly flat as assumed in the Coulomb simulation model. The simulation results should therefore be more accurate than the empirical formulas but not as accurate as the measurements made on the actual corona cage. The measured lumped LC parameters will be used in the remainder of this thesis.

The surge impedance of a lumped parameter transmission line with energy propagation in one direction is [24]:

$$Z_{line} = \left|\frac{V}{I}\right| = \sqrt{\frac{R + j\omega L}{G + j\omega C}} \qquad [\Omega] \tag{3.9}$$

For a lossless transmission line the series resistance and shunt conductance are negligible (i.e. $R = G = 0$), equation 3.9 simplifies to [24]:

$$Z_{line} = \sqrt{\frac{L}{C}} \qquad [\Omega] \tag{3.10}$$

The surge impedance of the various transmission lines defined by the corona cage conductors can therefore be calculated by substituting the measured parameters in table 3.1 into equation 3.10.

3.3.3 Bandwidth Considerations

It was discussed in section 3.2 that short corona cages do not have a correct statistical RI source distribution under most environmental conditions. A new excitation function or transform technique must therefore be derived for the small corona cage irrespective of the conductor

Stellenbosch University http://scholar.sun.ac.za/

length. The most convenient length can therefore be chosen arbitrarily. It should be noted however that the longer the conductor is, the higher the level of RI current produced. In this thesis, a distributed transmission line model of the corona cage which includes a corona excitation element is a required output. This model needs to be tested. The conductor and corona cage must therefore be electrically large and should include numerous wavelengths at the test frequencies. The corona cage must also fit conveniently into the laboratory. A conductor length of 2 metres was therefore chosen. With the tensioning supports and measurement components, the maximum corona cage length is 1.2 metres with 0.2 metre guard rings. The measurement bandwidth that was proposed in section 1.3 was 150 kHz to 1 GHz. Both the conductor and the corona cage will therefore be electrically large at 1 GHz.

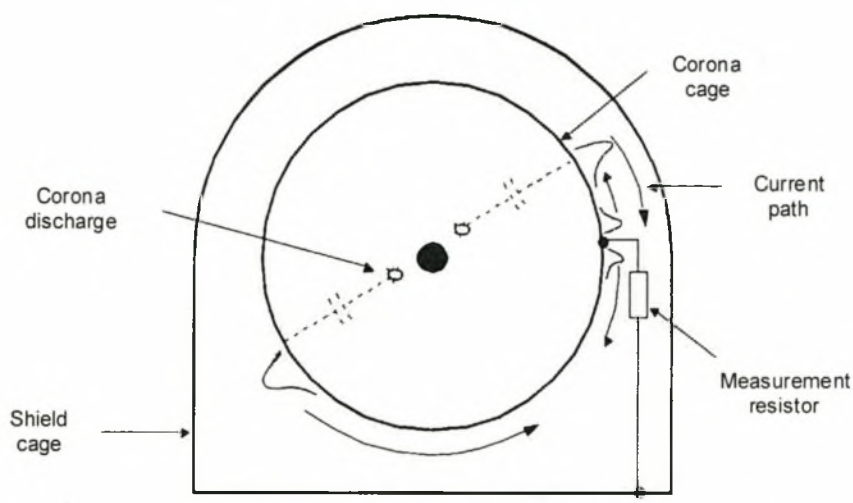

Figure 3.8: Schematic cross-section of the corona cage illustrating two possible RI current pulse paths to the measurement point.

In reality, the transmission line will not be lossless. There will be finite series impedance and shunt conductance losses. These losses will be frequency dependent. The determination of these losses will be dealt with in chapter 4 where a high-frequency corona cage model is investigated. The effects of a lossy transmission line will therefore only be discussed qualitatively in this section. RI current flow along the lossy transmission line defined by the corona cage and shield cage conductors will result in attenuation of the propagating RI pulses. The shape of the RI current pulses is therefore dependent on the path length. Since the transmission line has a uniform coaxial geometry, the RI current pulses induced on the corona cage will flow along the geometrically shortest path to the measurement point. This point is galvanically connected to the shield cage through a finite measurement resistance. Figure 3.8 illustrates two such RI current paths of different lengths. If the wavelength of the highest measured frequency component is much shorter than the path length, the attenuation at this frequency may be significant. This attenuation must be accounted for in the measurements or the path length must be shortened. Reference [18] suggests a method of reducing the path length by connecting the grounded guard rings to the corona cage edges using resistors matched to the surge impedance of the corona cage-shield cage transmission line. Not all RI current paths will then terminate at the measurement point and the length of the longest RI current path that terminates at the measurement point will be significantly reduced. This idea can be extended to matching non-edge points of the corona cage so that the longest current path can be further reduced. Also indicated in figure 3.8 is the

Stellenbosch University http://scholar.sun.ac.za/

reflection of the RI current pulses at the measurement point. This is prevented by matching the measurement resistance to the surge impedance of the cage-shield transmission line. Reflections will however also occur if the cage-shield transmission line is not uniform. This is the case in figure 3.7 where the most convenient shield construction was used.

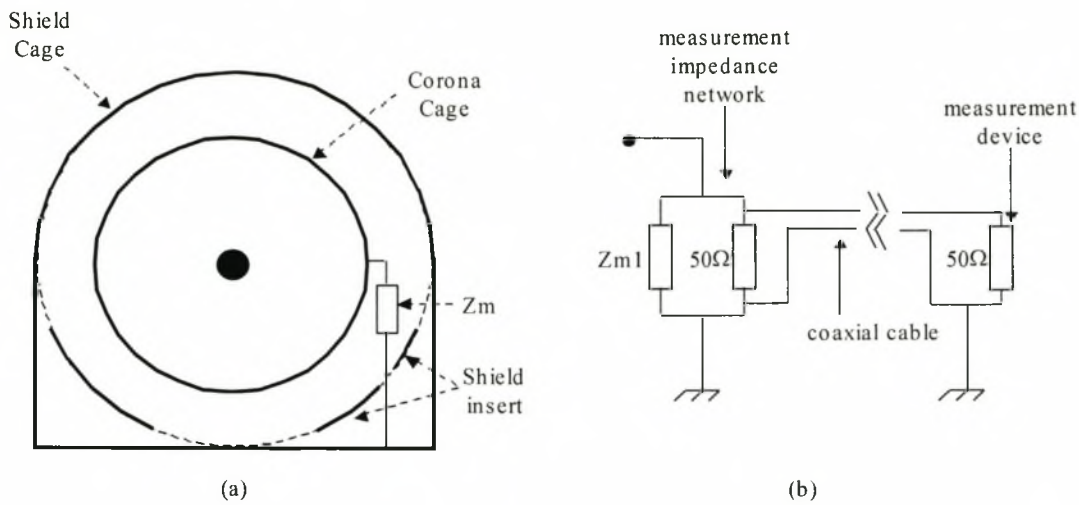

Figure 3.9: (a) Schematic cross-section of the modified measurement setup and (b) a circuit diagram of the measurement resistor and measurement device.

Cage inserts, such as those proposed in figure 3.9 (a), can be used to make the existing cage-shield transmission line into a more uniform coaxial geometry. The surge impedance (Z_0) of the existing corona cage with no cage inserts is calculated by substituting the appropriate parameters into equation 3.9. The lowest reflection coefficient will be achieved with a measurement resistance (Z_m) matched to the surge impedance.

The measurement resistance is connected to the measurement device (e.g. an oscilloscope) with a 50 Ω coaxial cable. The corona cage is separated from the measurement device by a significant distance for safety reasons. The coaxial cable used will therefore be long. Attenuation of the measured pulses will occur on the lossy coaxial cable and must be calibrated out in the measurements. Reflections will also occur at either end of the coaxial cable if the termination impedance at these ends is not matched to the 50 Ω characteristic impedance of the coaxial cable. The shunt impedance network illustrated in figure 3.9 (b) is therefore used to make RI current pulse measurements off the corona cage. The 50 Ω coaxial cable is connected across the shunt 50 Ω resistor thus preventing reflections at this connection. The other end of the coaxial cable is terminated in a 50 Ω load (i.e. the input impedance of the measurement device), preventing reflections at this end. Finally, in order to prevent reflections at the measurement point of the corona cage, the value of Z_{m1} in figure 3.9 (b) is chosen as:

$$Z_{m1} \| 25 = Z_0 \Rightarrow Z_{m1} = \frac{25.Z_0}{25 - Z_0} \qquad [\Omega] \tag{3.11}$$

While measurements will be made over the entire proposed frequency band, only a low-frequency model will be extracted from the corona cage design in figure 3.7. This is because the corona cage is electrically large across the proposed frequency band and considerable attention

Stellenbosch University http://scholar.sun.ac.za/

must be given to extracting a high-frequency model. The measurements can therefore only be accurately interpreted in the modelled low-frequency bandwidth. A more detailed and complete interpretation of the measurement results can then be made later when a high-frequency model has been extracted. In the low-frequency bandwidth, the transmission line can be assumed lossless and the surge impedance is calculated by substituting the low-frequency lumped LC parameters in table 3.1 into equation 3.10. The surge impedance of the corona cage-shield cage transmission line is 15.8 Ω . The value of Z_{m1} is then calculated from equation 3.11 as 43 Ω . Attenuation of low-frequency RI current pulse components propagating along various paths on the corona cage is negligible and can be ignored.

3.3.4 Measurement Devices

The measurement system required to make measurements from the corona cage in the bandwidth 150 kHz to 1 GHz was illustrated in figure 3.9. This system needs to be implemented with non-ideal resistors. The impedance and power specifications for these resistors are defined in this section and practical resistors are obtained to meet the specifications.

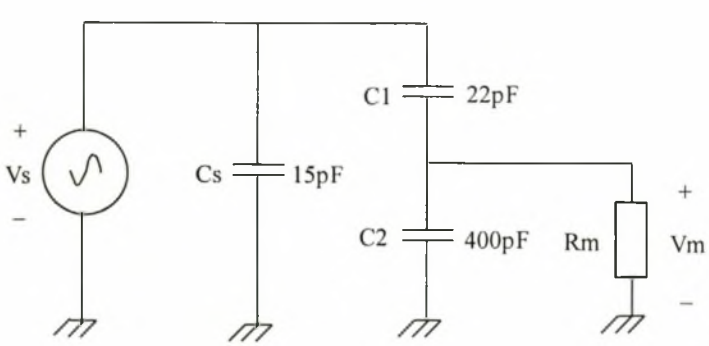

$$v_s = V_s \cos(\omega t)$$

$$v_m = V_m \cos(\omega t)$$

$$v_m = v_s \left(\frac{C_1}{C_1 + C_2} \right) \left(\frac{j\omega}{j\omega + 1/(C_1 + C_2) R_m} \right)$$

$$P_{AVG} = \frac{V_{RMS}^2}{R_m} = \frac{V_m^2}{2R_m}$$

Figure 3.10: A narrowband, electro-quasi-static circuit diagram of the corona cage for the 50Hz sinusoidal excitation (symbols as defined in table 3.1).

The power in the 50 Hz source component that appears across the 15.8 Ω measurement resistor can be determined from the narrowband, electro-quasi-static model in figure 3.10 using circuit theory. At the flash-over voltage of 128 kV (peak), the average power dissipation in the measurement resistor is only 0.003 mW and is therefore insignificant.

Stellenbosch University http://scholar.sun.ac.za/

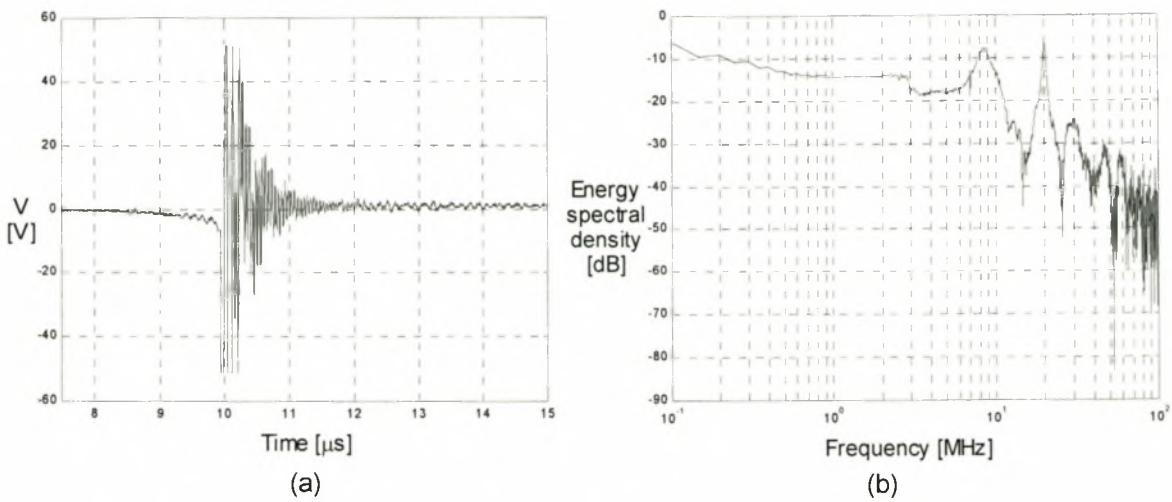

Figure 3.11: A large RI current pulse measured in the positive half-cycle at a voltage just below the flash-over voltage: (a) time domain plot and (b) energy spectral density plot.

The RI current pulse power and energy spectral content is determined from the largest RI current pulse measured in the positive half-cycle at an applied voltage just below the flash-over voltage. This pulse is plotted in figure 3.11 (a) and its energy spectral density curve is plotted in figure 3.11 (b). The total energy contained in the single time domain pulse $x(t)$ in figure 3.11 (a) is [25]:

$$E = \lim_{T \to \infty} \int_{-T}^{T} |x(t)|^2 \, dt = \int_{-\infty}^{\infty} |X(f)|^2 \, df \tag{3.12}$$

In equation 3.12, $|X(f)|^2$ is the energy spectral density of the pulse and is plotted in figure 3.11 (b). The total energy can therefore be calculated by integrating this energy spectral density curve. Since the curve is a sampled approximation, it is integrated by adding the samples. The total energy is therefore:

$$E \approx \sum_{n=-f_{\max}+1}^{n=f_{\max}} |X_n(f)|^2 \qquad [W.s] \tag{3.13}$$

It was found in chapter 2 that both the amplitude and the repetition rate of the significant RI current pulses increase with increased applied voltage. A periodic pulse train will have a finite, non-zero average power. This average power will increase with increasing pulse amplitude and repetition rate. The maximum pulse amplitude was measured and plotted in figure 3.11 (a). To find the maximum average RI power, the maximum repetition rate must be measured. The measurement of the repetition rate will be discussed in chapter 5. For the purposes of this section it will be noted that the maximum repetition rate is 20 kHz without a discussion on how this was measured.

Stellenbosch University http://scholar.sun.ac.za/

The average power of the RI pulse in figure 3.11 (a), with period T_0, is [25]:

$$P_{AVG} = \frac{1}{T_0}\int_{T_0} |x(t)|^2 dt = \sum_{n=-\infty}^{\infty} |X_n|^2 \qquad [\mathrm{W}] \tag{3.14}$$

The average power of the RI pulse train is therefore the sum of the powers in the individual phasor components of its Fourier series. The total energy in the pulse in figure 3.11 (a) is 0.21mW.s and the average power of the periodic series of these pulses, with a repetition rate of 20 kHz, is 0.78 W. The measurement resistor must therefore have an impedance of 15.8 Ω in the frequency range 150 kHz to 1 GHz and a power rating of 0.78 W and must be able to handle a pulse with 0.21mW.s of total energy.

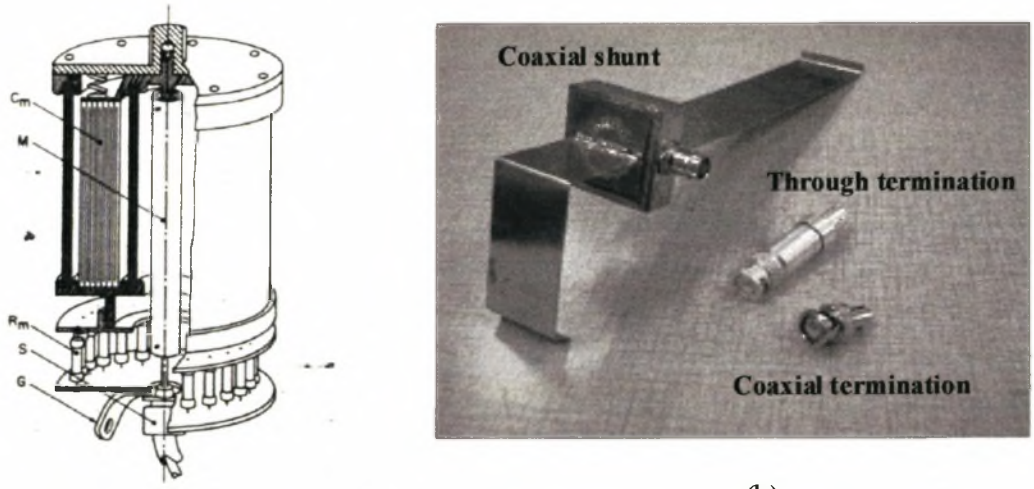

(a) (b)

Figure 3.12: (a) The coaxial shunt proposed in [22] and (b) a photograph of various resistive devices.

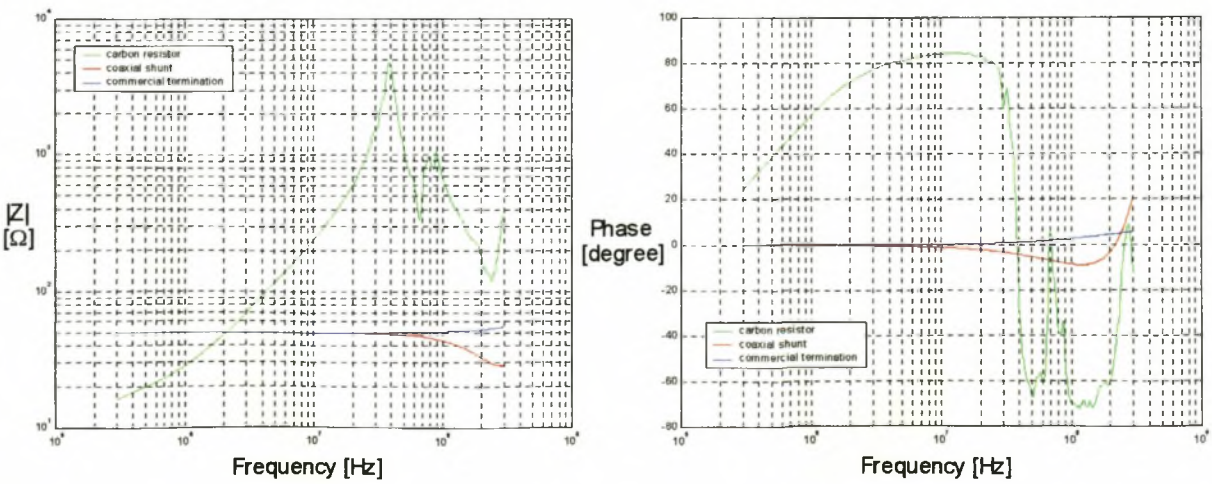

(a) (b)

Figure 3.13: Impedance of the various non-ideal resistors in figure 3.12: (a) magnitude and (b) phase plots.

Stellenbosch University http://scholar.sun.ac.za/

Ideally the measurement resistor must have a negligibly small reactive component. Magnitude and phase plots of various non-ideal high-power resistors are given in figure 3.13. Single carbon resistors with the required power rating have a large inductance at high frequencies. A low-inductance, high-power carbon resistive device, the coaxial shunt, is proposed in [22] and is shown in figure 3.12 (a). The coaxial shunt is made up of a shunt connection of low-power, low-inductance carbon resistors, uniformly arranged in a concentric circle around a central resistor. The current flow is evenly distributed amongst the resistors, increasing the power rating while maintaining a low inductance. The measurement is then made off the central resistor. A description of the design of the coaxial shunt used in this thesis is presented in appendix D1. While the commercial coaxial terminations offer the lowest reactance, they are only available in 75 Ω and 50 Ω resistance values. The 50 Ω resistor in figure 3.9 (b) will be implemented with a commercial through-termination and the 43 Ω resistor in figure 3.9 (b) will be implemented with a coaxial shunt. The non-zero reactive component of the coaxial shunt can then be calibrated out when a high-frequency model is extracted from the corona cage design.

3.3.5 Physical Construction

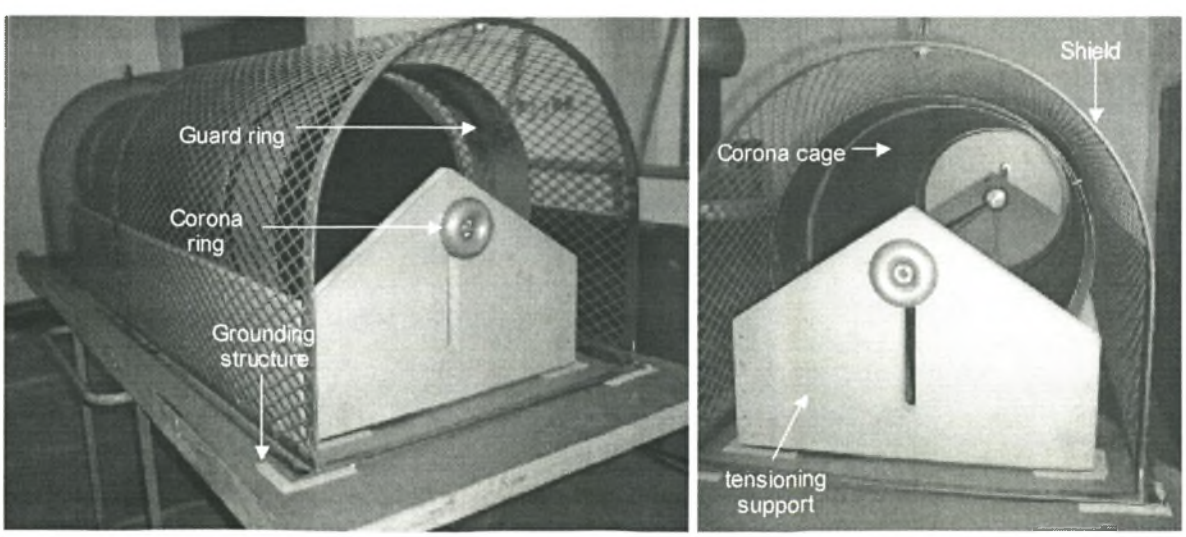

Figure 3.14: Photographs of the corona cage constructed at the University of Stellenbosch.

The proposed corona cage design in figure 3.7 was constructed at the University of Stellenbosch. The central corona cage section and the outer guard rings were made out of solid metal plates that were bent into right-circular cylinders. The shield cage was constructed out of metal meshing. Photographs of the corona cage are presented in figure 3.14.

Stellenbosch University http://scholar.sun.ac.za/

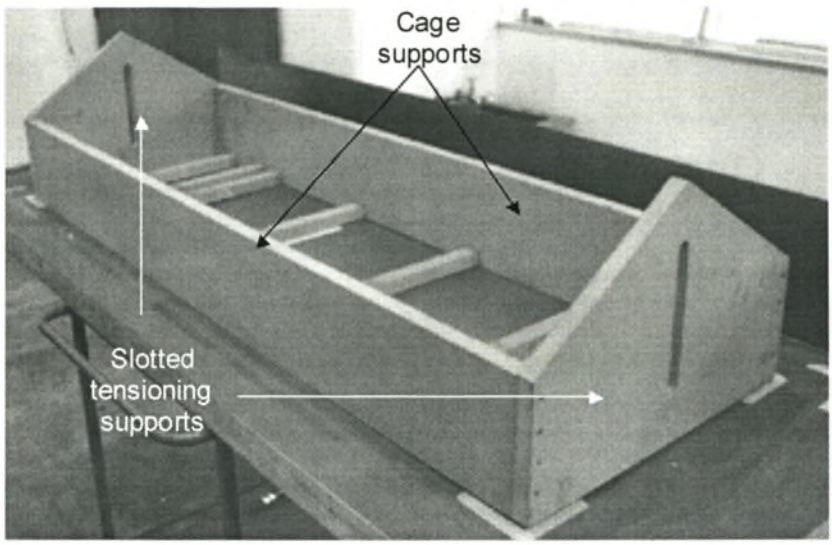

Figure 3.15: A photograph of the support cradle used to tension the centre conductor and keep the cage and guard rings in position.

Since the corona cage is a right-circular cylinder, the centre conductor must have no sag. This ensures a uniform electric field distribution on the surface of the centre conductor along its entire length. Sag is avoided by using a hollow copper pipe rather than a solid copper rod and by tensioning this centre conductor. To tension the centre conductor and keep the cage and guard rings in position, a support structure (i.e. a support cradle) had to be built. The cradle, shown in figure 3.15 was made out of pressed board since this would provide the required rigidity and strength. It is apparent in figure 3.15 that the tensioning supports are slotted. This allows the centre conductor to be moved vertically so that various cage sizes can be tested if required.

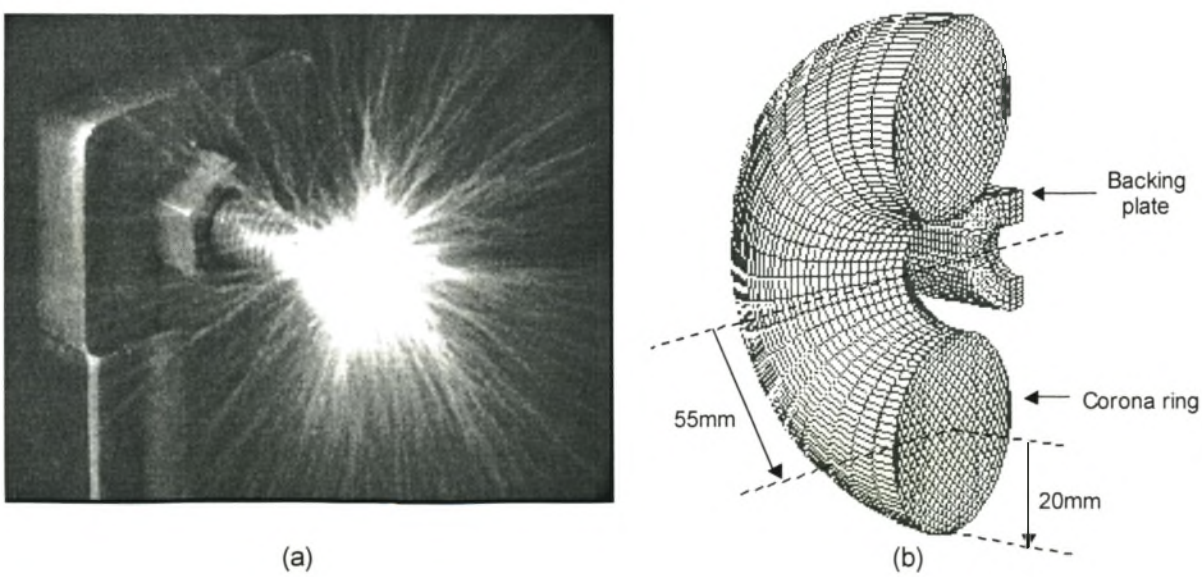

Figure 3.16: (a) A Corocam photograph of the corona discharges occurring on the tensioning nut and thread of the centre conductor and (b) a cross-sectional cut-away view of the corona ring used to remove this spurious corona.

Stellenbosch University http://scholar.sun.ac.za/

Corona discharges will occur at the sharp edges of the screw thread and tensioning nut (see figure 3.16 (a)). These corona discharges induce currents on the centre conductor which then couple into the corona cage measurements and must therefore be removed. This is done by reducing the electric field in the vicinity of the sharp edges using a corona ring such as the one illustrated in figure 3.16 (b). The effect of the corona ring on the applied electric field at the centre conductor surface will be discussed later in this section when the tensioning mechanism used to hold the centre conductor in the desired position is discussed.

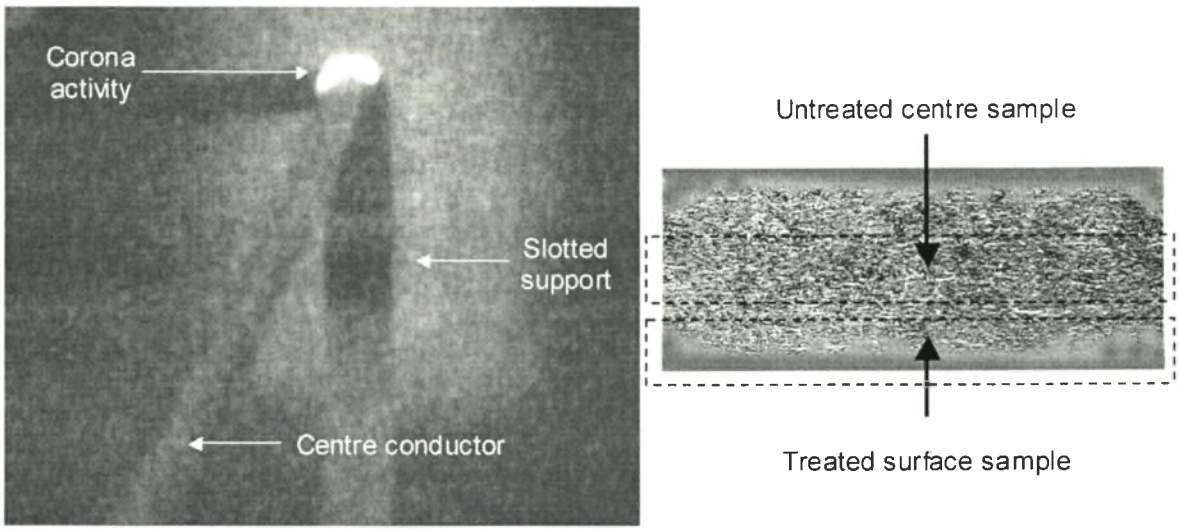

Figure 3.17: (a) A Corocam photograph of the surface discharges occurring in the vicinity of the slot in the tensioning support and (b) a photograph of the cross-section of a piece of pressed board showing the selection of samples.

The extraction of the dielectric properties of the pressed board used for the support cradle is discussed in appendix C2. Two samples of the pressed board, both 5 mm thick, were used to determine its dielectric properties. The samples were taken from the edge and centre of the board respectively. This was because the unmachined board had a surface treatment that penetrated into the board near the surface. This can be seen in the photograph of a cross-sectional cut through a piece of pressed board presented in figure 3.17 (b). The extracted permittivity and surface conductivity indicate that the surface treatment increases the permittivity and decreases the surface conductivity. Furthermore, the surface conductivity of the sample with no surface treatment varies with air humidity. This suggests that the surface treatment seals off the wood fibres that make up the pressed board, preventing them from absorbing moisture in the surrounding air. When the slot was made in the tensioning support, the seal was removed and the wood fibres were able to absorb moisture. The surface conductivity between the energized centre conductor and the grounding structure is therefore increased, causing the surface discharges seen in figure 3.17 (a). These surface discharges induce currents on the centre conductor which couple into the corona cage measurements and must therefore be removed. This can be accomplished by treating the machined surface with a non-conductive seal or by reducing the electric field in the vicinity of the machined surface. The latter method is used in this thesis to remove the spurious corona activity.

Stellenbosch University http://scholar.sun.ac.za/

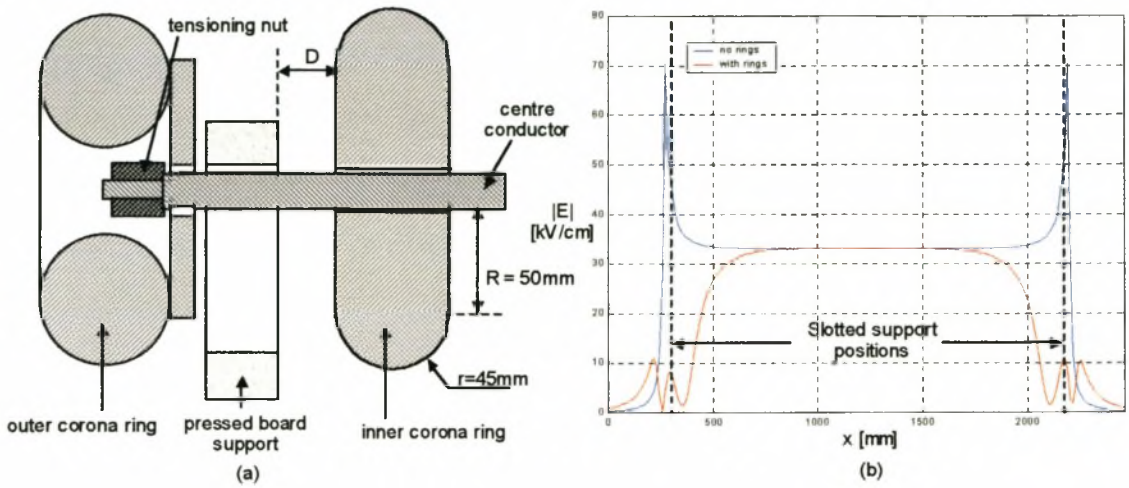

Figure 3.18: (a) A schematic cross-sectional view of the corona rings used to reduce the electric field near the slot in the tensioning supports and (b) the Coulomb simulation results confirming the reduction in electric field strength near the slot.

Corona rings are used as illustrated in figure 3.18 (a) to reduce the electric field near the slot in the tensioning supports. This approach successfully removed the surface discharges in this region. It can be seen in figure 3.18 (b) that the corona rings significantly change the electric field distribution along the length of the centre conductor. The dimension D in figure 3.18 (a) is therefore critical if the electric field between the corona cage and the centre conductor is to be uniform along the conductor length. The Repetitive Laplace code used to determine the optimal guard ring length can again be used to find the optimum value of D.

3.4 The High Voltage Laboratory

As already mentioned in previous sections, the weather and electrical environment of a laboratory can be fully characterized and controlled. This is the most important advantage of laboratory measurements. In this section, the electrical environment of the high voltage laboratory at the University of Stellenbosch will be characterized. Methods of controlling this environment will then be discussed in section 3.5.

Stellenbosch University http://scholar.sun.ac.za/

3.4.1 Current Modes

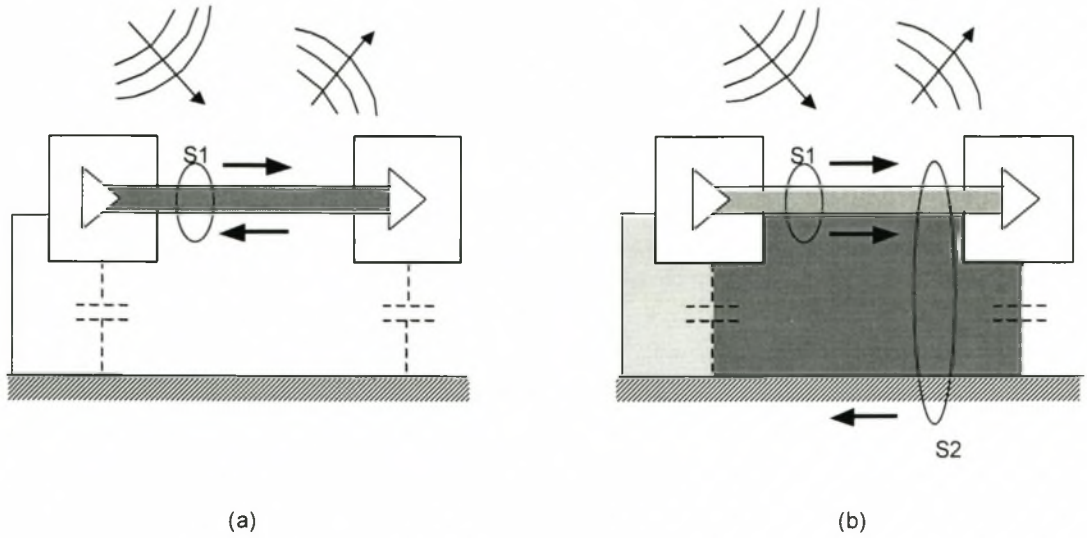

Figure 3.19: Schematic diagram of (a) a differential mode (DM) coupling and (b) a common mode (CM) coupling in a typical experimental setup (after [26]).

Two possible interference coupling methods in a typical experimental setup are illustrated in figure 3.19. Integration of the current flowing along the two wire transmission line and passing through surface S1 in figure 3.19 (a) will equal zero if the current flow is purely differential mode (DM). The shaded surface in the figure is bounded by a continuous low-impedance loop (i.e. assuming the input and output impedance of the two circuits, modelled as amplifiers, is low). A radiated interference magnetic field passing through this shaded surface will then induce a small DM interference current in the low-impedance current path which encloses only a small surface area. In figure 3.19 (b), the integral of the currents flowing through surface S1 is not zero. This is the result of common mode (CM) current flow on the transmission line. Magnetic flux passing through the shaded surfaces, which are larger than the shaded surface in figure 3.19 (a), will induce common mode current flow on the transmission line. It should be noted that current will only flow in a closed, low-impedance loop. The ground-return current path in figure 3.19 (b) completes the required closed current-loop which is therefore referred to as a ground loop. An integral of the current flow through surface S2 will therefore equal zero. Significant DM and CM interference currents must be removed since they will corrupt the RI current measurements. In order to quantify the susceptibility of the experimental setup to these interference currents and objectively compare various shielding methods aimed at improving this susceptibility, the transfer impedance concept must be introduced.

3.4.2 Grounding and the Transfer Impedance Concept

It is recognised in [27] that the design of "correct grounding" is a fundamental aspect of EMC considerations when dealing with electrical systems. This is particularly true when the system is as large as the corona cage. "Grounding" is defined in [27] as " ... the design and construction of the low voltage sides of all current loops.". We therefore need to firstly identify all low impedance current loops (i.e. ground loops) that will potentially affect measurements in the experimental setup.

Stellenbosch University http://scholar.sun.ac.za/

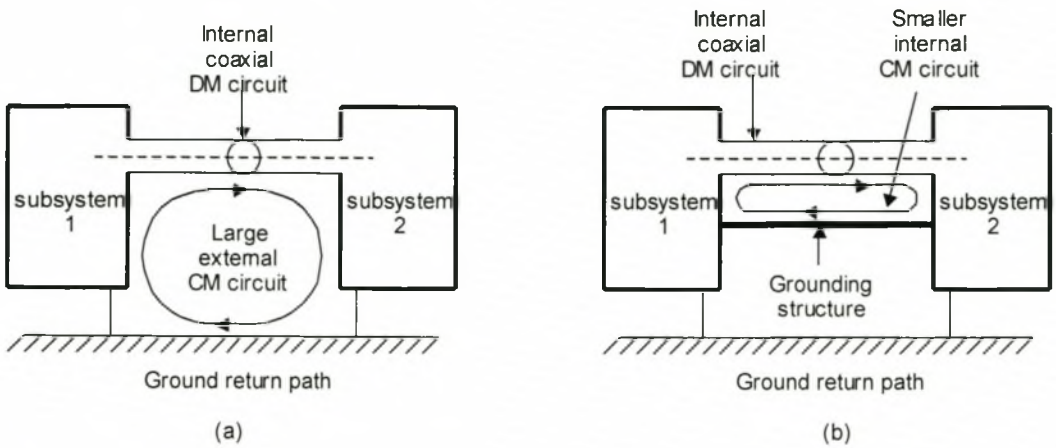

Figure 3.20: (a) Schematic diagram of a large ground loop that will result in CM current flow and (b) a grounding structure that can be used to reduce such interference (after [27]).

Well designed grounding structures can be used to reduce current loops near sensitive measurement equipment and in this way improve the local electrical environment as is illustrated in figure 3.20. In order to quantify the efficacy of such grounding structures, a figure of merit needs to be defined. One such quantity, used in [27], [28] and [29], is the transfer impedance of the grounding structure. Transfer impedance is defined in [28] as "... the ratio of the differential mode voltage and the disturbance current causing it; ...". This is similar to the definition given in [27] for the transfer impedance per unit length:

$$Z_T^{'}(\omega) = \frac{V_{DM}(\omega)}{I_{CM}(\omega) l} \qquad [\Omega / m] \tag{3.15}$$

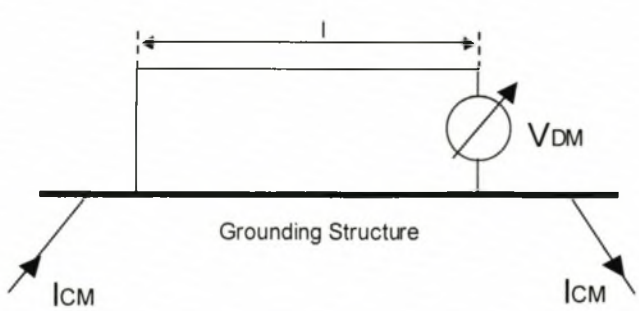

Figure 3.21: Schematic diagram illustrating the definition of transfer impedance per unit length given in equation 3.15 (after [27]).

It should be noted that equation 3.15 is only valid for an electrically small system (i.e. $l << \lambda /4$). For an electrically large system, the transfer impedance is described in terms of z-parameters in [29] as:

$$Z_T = \frac{Z_{21}}{1 + (Z_{22} / Z_0)} \qquad [\Omega] \tag{3.16}$$

Stellenbosch University http://scholar.sun.ac.za/

The transfer impedance of a structure can therefore be measured by injecting a disturbance CM current onto the structure and measuring the resulting DM voltage as illustrated in figure 3.21. The measurement technique used to measure transfer impedances in this thesis is discussed in appendix C3.

3.4.3 Existing Grounding Structures and Ground Loops

For safety reasons, the control panel and the measurement equipment must be securely connected to the laboratory ground. It is not adequate to rely on the outer conductor of the coaxial cable to provide this ground connection. If the outer conductor or the measurement resistor fails, a dangerous floating voltage will result on the chassis of the measurement equipment.

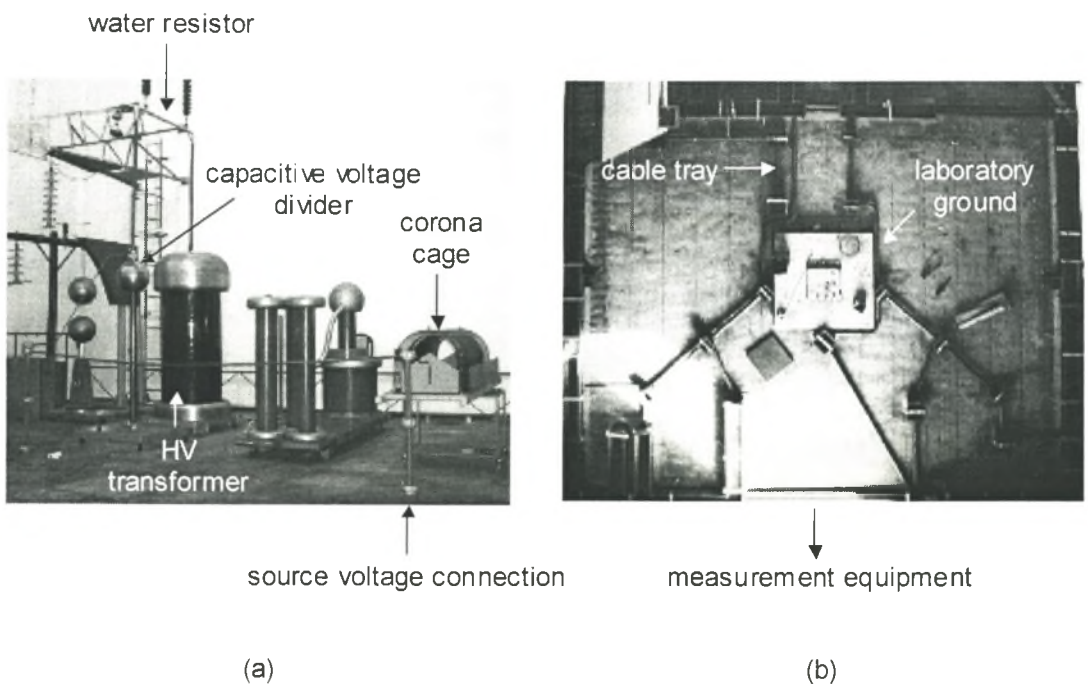

Figure 3.22: (a) Photograph of the experimental setup in the laboratory and (b) connection of permanent grounding structures to the laboratory ground.

The experimental setup in the high voltage lab is shown in figure 3.22 (a). The high voltage transformer, capacitive voltage divider and source voltage connections are all designed to prevent corona at their maximum rated voltages. The only corona generated in the experimental setup will therefore be in the corona cage. To ensure this, the water resistor was redesigned by Mr. P. Pieterse to prevent corona near the grounded support structures. The laboratory ground consists of a metal cylinder submerged 5 metres into the ground and filled with water from the underground water table. Inaccessible metal strips connect accessible connection points and cable trays to this laboratory ground. This is shown in figure 3.22 (b). The low voltage side of the laboratory equipment is then connected to the accessible connection points. Potential ground loops are therefore formed.

Stellenbosch University http://scholar.sun.ac.za/

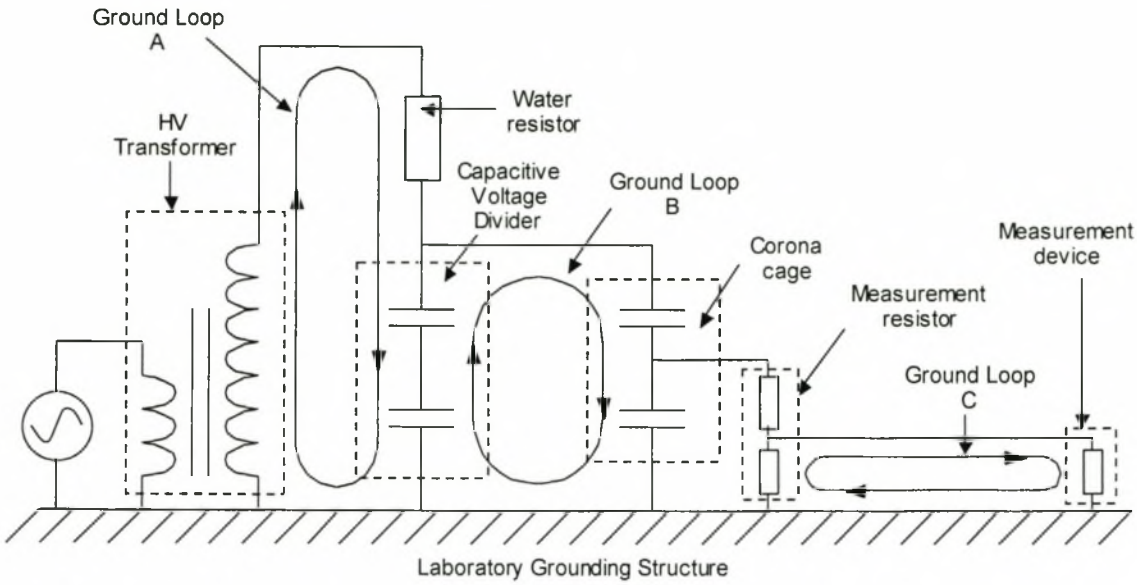

Figure 3.23: Schematic diagram of the experimental setup showing connections to the laboratory grounding structures and potential ground loops that are formed. .

The ground loops formed in the experimental setup are shown in figure 3.23. CM current flow in these ground loops will enter the corona cage RI measurements and corrupt them. The degree to which CM current flow in the ground loops couples into the DM RI measurements must therefore be determined. This is done by measuring the transfer impedance of the ground loops.

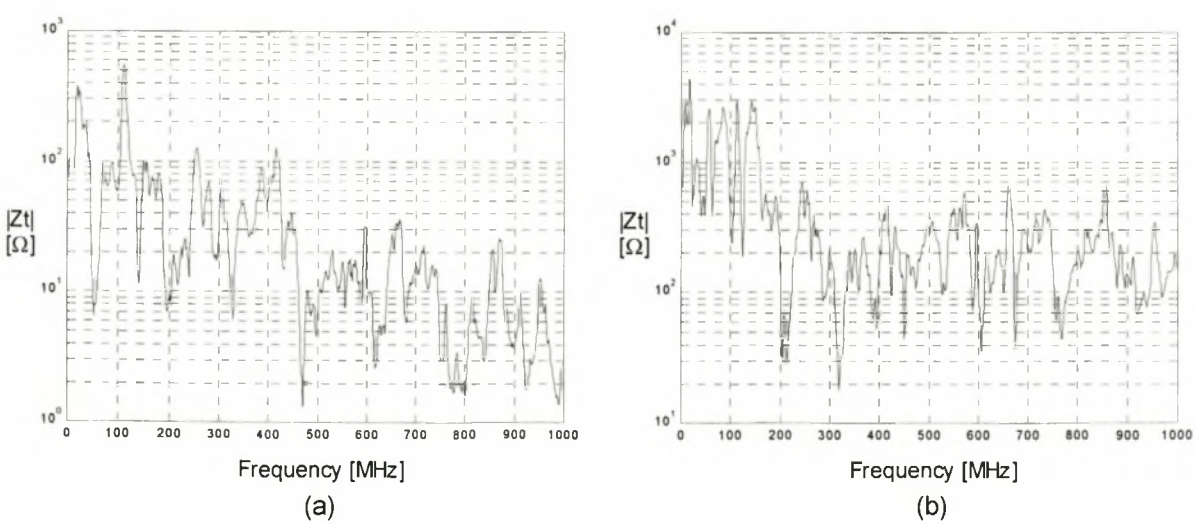

Figure 3.24: The measured transfer impedance of the two significant ground loops defined in figure 3.23: (a) ground loop B and (b) ground loop C.

The measurement technique used to measure the transfer impedances presented in this section is described in appendix C3. Only the transfer impedance of ground loop B, the source ground loop, and ground loop C, the measurement ground loop, are significant. The transfer impedance of these two ground loops in the frequency range 150 kHz to 1 GHz is plotted in figure 3.24. Special attention must be given to reducing the transfer impedance of these ground loops.

Stellenbosch University http://scholar.sun.ac.za/

3.4.4 Spurious Noise

The dynamic range of the corona cage RI measurements is determined by the level of ambient noise in the laboratory. It has already been described how radiated noise can induce CM current in the ground loops identified in the previous section. It is therefore important to reduce both the level of ambient noise in the laboratory and the susceptibility of the measurement setup to this radiated noise. Of particular concern are the fields radiated from corona discharges that occur outside the corona cage. This is caused by large floating voltages that are induced on laboratory equipment that has not been correctly connected to the laboratory grounding structure.

3.5 Shielding Techniques

In this section, the electric environment of the laboratory, characterized in section 3.4, is modified using various shielding techniques. This is done to increase the dynamic range of the corona cage DM voltage measurements. In particular, the large separation between the corona cage and the measurement device necessitates the need for effective shielding techniques. The efficacy of the various shielding techniques is quantified using the transfer impedance concept defined in section 3.4. The selected shielding techniques must reduce the flow of induced CM interference current in the experimental setup.

3.5.1 Coaxial Cables

The manually operated measurement equipment and the energized corona cage are separated by a significant distance for safety reasons. The DM voltage measurement must therefore be guided over this distance to the measurement equipment. This is best done using coaxial cables since the inter-electrode gap is shielded from interference fields. For non-ideal coaxial cables with braided outer conductors, CM current induced on the outer surface can enter the inner surface through discontinuities in the braid, aperture radiation and porpoising. The result is a finite transfer impedance that is dependent on the quality of the braiding. This can be improved by carefully wrapping a uniform, uninterrupted layer of conductive foil around the conductor.

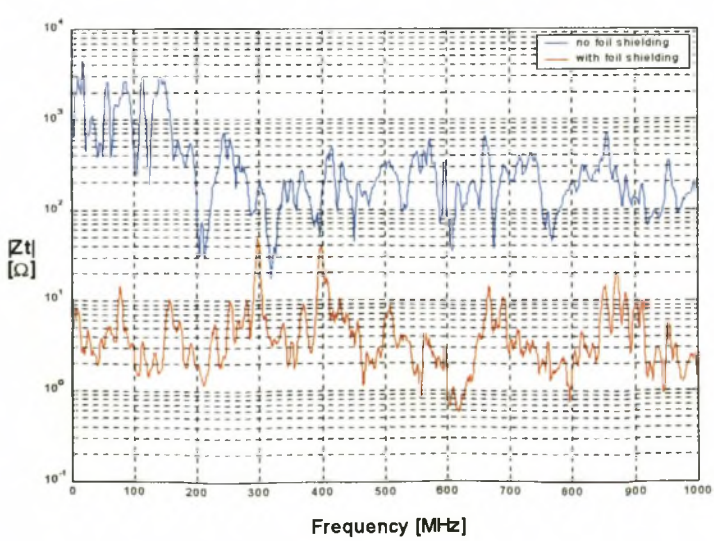

Figure 3.25: A comparison of the transfer impedance of the measurement loop with and without a foil layer surrounding the RG-58 coaxial cable.

Stellenbosch University http://scholar.sun.ac.za/

The foil layer surrounding the coaxial cable is securely connected to the laboratory grounding structure as the cable enters the measurement area of the laboratory. CM current flowing on the foil layer will therefore be diverted away from the measurement equipment to the grounding structure of the laboratory along a low-impedance path. The measured transfer impedance with and without this grounded foil layer is plotted in figure 3.25. The result confirms that the shielding method is very effective in reducing the susceptibility of the measurement loop to interference fields in the laboratory.

3.5.2 Cable Trays

It was found in the previous section that coaxial cables have a non-zero transfer impedance. A layer of tin foil will improve the transfer impedance of the cable. Damage to this foil layer or a poor connection between the foil layer and the laboratory grounding structure can actually increase the transfer impedance. This will happen if the surface resistance of the foil is lower than that of the cable braid, resulting in lower attenuation. A cable tray is a grounding structure with a low transfer impedance that will reduce the CM current induced on the foil or braid surface of the coaxial cable and therefore reduce the transfer impedance of the measurement system.

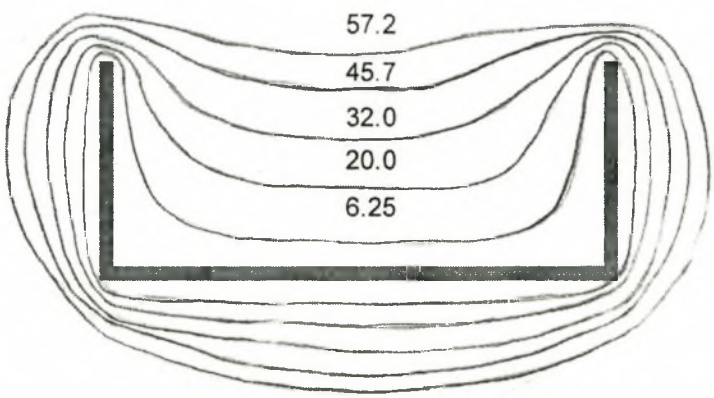

Figure 3.26: Cross-sectional view of a typical metal cable tray showing the B-field distribution and field strength [nH/m] (h = 45 mm and w = 90 mm) (after [28]).

Since the cable tray is conductive, the penetration of the interference fields into the structure is reduced to a few multiples of its skin depth. The interference B-field is therefore forced to go around the cable tray. This is illustrated in figure 3.26 for a typical cable tray. Only a negligibly small B-field will then pass between the cable conductor and the grounding structure, reducing the induced CM current on the coaxial cable.

A conductive pipe is an ideal cable tray since interference fields would be completely excluded from the interior region provided the walls are thick enough. Such a cable tray is however not always practical since it is difficult to access the cables inside it. It is also not necessary for our measurements since the cable tray in figure 3.26 significantly should exclude most interference magnetic flux from the region surrounding the cable. The reduction in transfer impedance obtained with a circular cable tray will in fact not be significantly more than that obtained with a rectangular cable tray without a lid.

Stellenbosch University http://scholar.sun.ac.za/

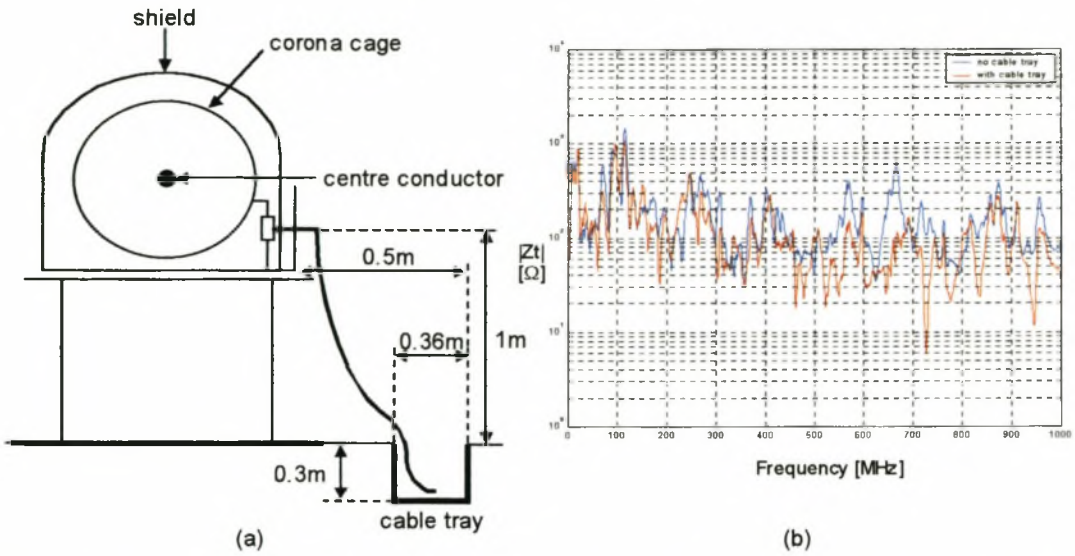

Figure 3.27: (a) A cross-sectional schematic view of the measurement setup showing the position of the cable tray and (b) the transfer impedance of this measurement system with and without the RG-58 coaxial cable placed in the cable tray.

The position and dimensions of the cable tray used in the experimental setup are presented in figure 3.27 (a). The corona cage is placed high above the grounding structure of the laboratory to ensure that no corona activity is generated on the source voltage connections outside the corona cage. A large ground loop is therefore formed and is indicated in figure 3.27 (a). Significant CM current will therefore be induced on the measurement cable before it enters the cable tray. A large improvement in the transfer impedance due to the cable tray is therefore not expected. This is confirmed in the comparison plotted in figure 3.27 (b).

3.5.3 The EMC Cabinet

The metallic casing of a measurement device has many discontinuities and openings for practical reasons such as access to the control panel. Both radiated disturbances and disturbances conducted along the measurement cables connected to its inputs will therefore create interference. An EMC cabinet can be used to reduce this interference.

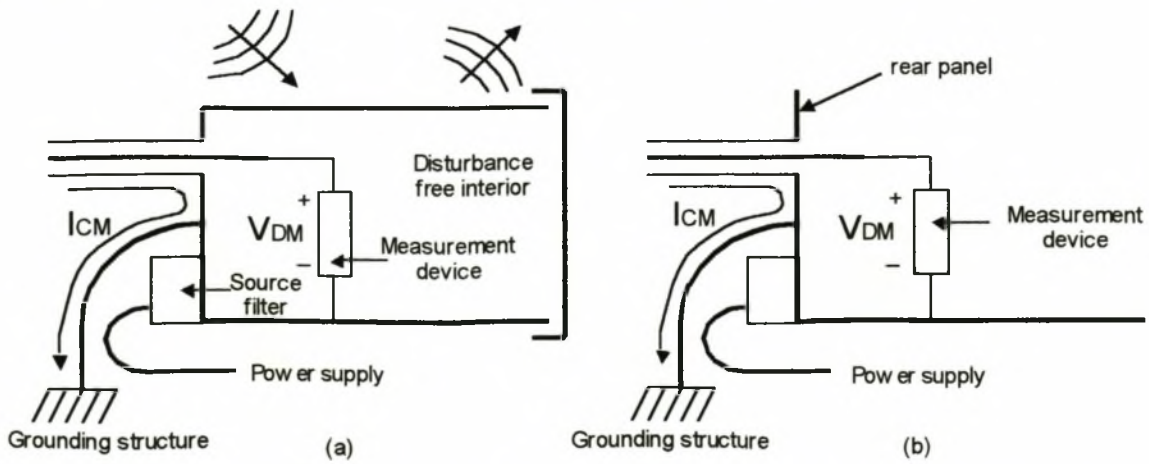

Figure 3.28: Schematic view of (a) a fully enclosed EMC cabinet and (b) the rear panel of an EMC cabinet (after [27]).

Stellenbosch University http://scholar.sun.ac.za/

An example of a fully enclosed EMC cabinet is illustrated in figure 3.28 (a). The level of radiated noise in the measurement section of the laboratory is not significant. The fully enclosed EMC cabinet is therefore not necessary and a rear panel will suffice. This grounding structure is shown in figure 3.28 (b). CM current flowing on the outer surface of the coaxial conductor will be diverted away from the measurement device by the grounded rear panel of the EMC cabinet. It is therefore essential that good contact is made between the rear panel and the braid of the coaxial conductor as well as the foil surrounding the coaxial conductor. Conducted noise can also enter the measurement device through the power supply. The EMC cabinet is therefore equipped with a supply filter.

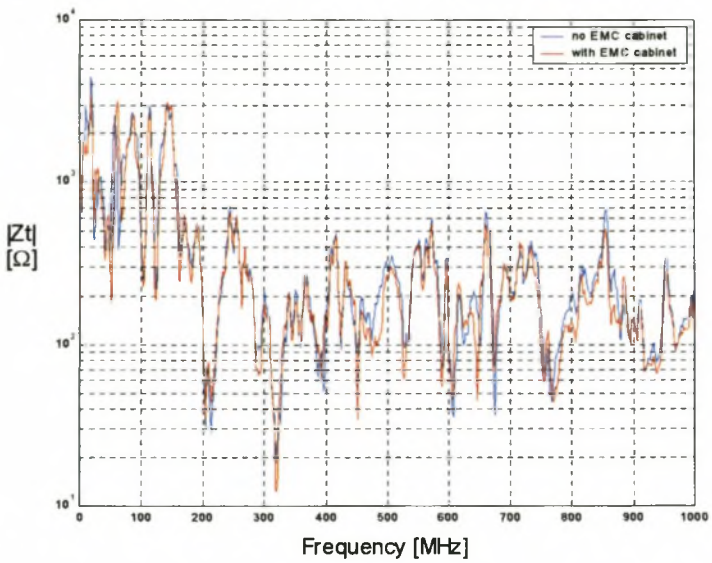

Figure 3.29: The transfer impedance of the measurement system with and without an EMC cabinet used to shield the sensitive measurement equipment.

A comparison of the transfer impedance measurements for an unshielded coaxial measurement cable connected directly to the measurement device and then connected to the measurement device placed in an EMC cabinet, such as the one in figure 3.28 (b), is plotted in figure 3.29. The plot suggests that the use of the EMC cabinet has no significant effect on the transfer impedance. This suggests that the CM interference current flowing on the coaxial cable has already coupled into the DM measurement circuit due to the long length of the cable and the coupling mechanisms already mentioned. The most effective shielding method for the measurement loop is therefore the continuous foil layer applied to the coaxial measurement cable.

3.5.4 Filters

All the shielding techniques used thus far have focussed on reducing the transfer impedance of ground loop C in figure 3.23. It is however more difficult to reduce the transfer impedance of ground loop B in figure 3.23 (i.e. the source loop). This is because the high voltage side of this ground loop is excited by the high energy 50 Hz source. Grounding structures can therefore not be placed near these conductors without causing flash-over. Filters offer the only effective shielding in such a ground loop. Ideally these filters increase the impedance of the ground loop at high frequencies while offering zero impedance at the 50Hz source frequency. Non-ideal filters are however frequency dependent and are therefore only effective in a narrow bandwidth. The filter components will be attached to the highly energised source conductors and must therefore be capable of handling the high power levels.

Stellenbosch University http://scholar.sun.ac.za/

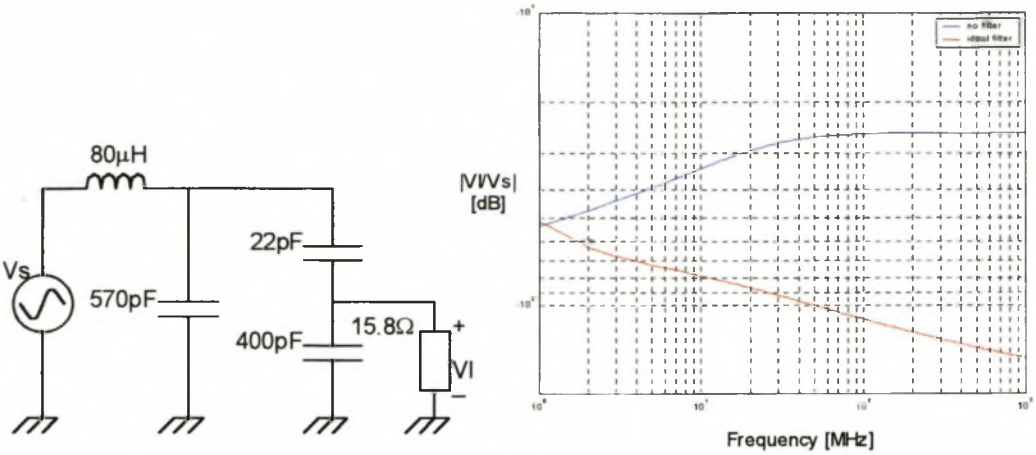

(a) (b)

Figure 3.30: (a) A circuit diagram of the LC filter used in the source loop and (b) the frequency response of this filter assuming ideal components.

A circuit diagram of the LC filter used in the source loop is plotted in figure 3.30 (a). The components are assumed ideal. The capacitor is placed next to the guard ring so that high-frequency signals can be coupled onto the coaxial transmission line defined by the centre conductor and the corona cage and guard ring cylinders. This is needed in later research for the extraction and verification of a high-frequency model. The positioning of the capacitor is therefore essential since reflections will occur at the start of the coaxial transmission line if the capacitor is placed elsewhere. This capacitor will also offer a low-impedance path to ground for high-frequency signals preventing them from entering the corona cage and therefore the measurement circuit. In addition, an inductor is placed in series in the source loop. This will increase the impedance of the source loop at high frequencies. The frequency response of this ideal circuit is plotted in figure 3.30 (b). It was however found that the capacitor becomes inductive above 20 MHz and the stray capacitance between the windings of the inductor also become significant above this frequency. The filter will therefore only be effective below 20MHz.

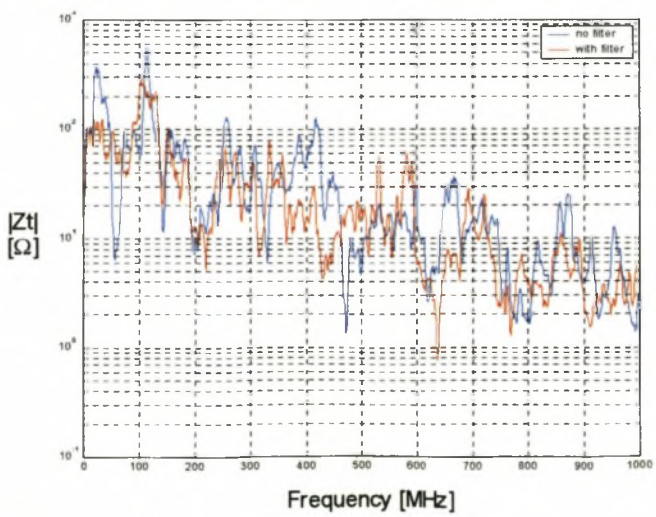

Figure 3.31: A comparison between the measured transfer impedance of the source loop with and without the LC filter presented in figure 3.30 (a).

The transfer impedance of the source loop with and without the filter is presented in figure 3.31. The result suggests that the filter is only effective at frequencies below 20 MHz as expected. The design of the high voltage capacitor is presented in appendix D2.

Stellenbosch University http://scholar.sun.ac.za/

3.6 Conclusions

- RI noise measurements made on long or short transmission lines are easier to interpret than those made in corona cages since only environmental conditions need to be accounted for when relating them to the corona performance of an actual transmission line. Long or short transmission line experiments require expensive installations and are susceptible to interference. Their dependence on environmental conditions is difficult to isolate since environmental conditions cannot be controlled. Long-term RI noise measurements are therefore required.

- Corona cages can be used to make RI noise measurements. They are cheaper to install and the electrical and environmental conditions can be controlled. RI noise measurements made in a corona cage must first be transformed to equivalent transmission line conditions using a generation function transform before they can be interpreted.

- Small corona cages do not have a correct statistical distribution of RI noise sources along the length of the centre conductor under most environmental conditions. A new generation function or an alternative transform technique must therefore be derived for the small corona cage. Due to the limited available space in the laboratory at the University of Stellenbosch, a small corona cage will be used for the RI noise measurements in this thesis.

- A uniform electric field is required along the length of the corona cage centre conductor so that accurate RI noise measurements can be made in the corona cage. This is obtained by dividing the corona cage into three electrically isolated sections. The optimum length of the two outer sections (i.e. the guard rings) can be determined using the Repetitive Laplace field calculation technique. RI noise measurements are made off the central section of the corona cage.

- The minimum distance between the centre conductor and the corona cage is determined by the maximum distance travelled by a charged ion in the inter-electrode gap under the influence of the 50 Hz AC field. This ensures that no charge is lost to the system so that the corona process is an exact replica of the process occurring on a transmission line.

- In order to extract a wideband model for the RI noise, the corona cage must be fully characterised by extracting its natural transmission line parameters. The attenuation and reflection of RI pulses propagating along the electrically large corona cage can then be determined and accounted for. In this thesis only a low-frequency model will be extracted. Only quasi-static lumped circuit parameters are therefore extracted. RI measurements will be made in the full frequency band proposed in section 1.3. Conclusions will however be based only on the results in the frequency band of the extracted low-frequency corona cage model. A high-frequency corona cage model will then be investigated in future research so that the conclusions can be extended to the full measurement bandwidth.

- The pulsed power specifications of the measurement resistors are significant and must be considered. The RMS continuous wave (CW) power specification is however negligibly small and can be ignored. The measurement resistors must have a very small reactive component. These specifications are best met using coaxial shunts and commercial through-terminations.

Stellenbosch University http://scholar.sun.ac.za/

- Spurious corona discharges must be removed from the measurement system. The spurious noise from the tensioning nut is removed with corona rings. Pressed-board used for the tensioning supports has a high surface conductivity when machined. This will result in spurious surface discharges. These discharges are removed using a second set of corona rings. The tensioning supports should be made out of a material with a lower surface conductivity (such as an insulator).

- Significant ground loops exist in the experimental setup. Common mode current flow in these low-impedance current paths will couple into the differential mode RI noise measurements thus corrupting them. The susceptibility of the differential mode measurements to interference fields is quantified by measuring the transfer impedance of the measurement system. The transfer impedance of the measurement loop is reduced (i.e. improved) with cable trays, EMC cabinets and cable shielding. The most significant improvement is obtained by shielding the coaxial cable with a continuous foil layer. The transfer impedance of the source loop can only be reduced by reducing the size of the loop or by using a LC filter on the high voltage side of the current loop. The improvement obtained with the filter is however restricted to frequencies below 20 MHz.

3.7 References

[1] IEEE Committee Report, "Transmission System Radio Influence", IEEE Transactions on Power Apparatus and Systems, Vol. 84, August 1965, pp. 714 - 724.

[2] M.G. Comber, D.W. Deno and L.E. Zaffanella, "Corona Phenomena on AC Transmission Lines", Transmission Line Reference Book - 345kV and above, Chapter 4, EPRI, Second Edition, Revised 1987, pp. 187 - 204.

[3] M.G. Comber and L.E. Zaffanella, "The Use of Single-Phase Test Lines and Test Cages to Evaluate the Corona Effects of EHV and UHV Transmission Lines", IEEE Transactions on Power Apparatus and Systems, Vol. PAS-93, 1974, pp. 81 - 89.

[4] C.R. Bond, W.E. Pakala, R.E. Graham and J.E. O'Neil, "Experimental Comparisons of Radio Influence Fields From Short and Long Transmission Lines", IEEE Transactions on Power Apparatus and Systems, Vol. 82, April 1963, pp.175 - 184.

[5] V.L. Chartier, D.E. Blair, M.D. Easley and R.T. Raczkowski, "Corona Performance of a Compact 130-kV Line", IEEE Transactions on Power Delivery, Vol. 10, No. 1, January 1995.

[6] C.F. Clark and M.O. Loftness, "Some Observations of Foul Weather EHV Television Interference", IEEE Transactions on Power Apparatus and Systems, Vol. PAS-89, No. 6, July/August 1970, pp. 1157-1165.

[7] J.J. LaForest, "Seasonal Variation of Fair-Weather Radio Noise", IEEE Transactions on Power Apparatus and Systems, Vol. PAS-87, No. 4, April 1968, pp. 928 - 931.

[8] R.D. Dallaire and P. Sarma Maruvada, "Analysis of Radio Interference from Short Multiconductor Lines", IEEE Transactions on Power Apparatus and Systems, Vol. PAS-100, No. 4, April 1981, pp. 2109 - 2116.

[9] J.J. LaForest, C.B. Lindh, D.D. MacCarthy, F. Olsen and M.W. Schultz, Jr, "Radio Noise and Corona Loss Results from Project EHV", IEEE transactions on Power Apparatus and Systems, Vol. 82, October 1963, pp. 735 - 748.

[10] R.G. Olsen and S.D. Schennum, "A Method for Calculating Wide Band Electromagnetic Interference From Power Line Corona", IEEE Transactions on Power Delivery, Vol.10, No.3, July 1995, pp. 1535 - 1540.

Stellenbosch University http://scholar.sun.ac.za/

[11] G.E. Adams, "The Calculation of the Radio Interference Level of Transmission Lines Caused by Corona Discharges", AIEE Transactions Power Apparatus and Systems, Vol. 75, pt. III, 1956, pp. 411 - 418.

[12] C.H. Gary, "The Theory of the Excitation Function: A Demonstration of its Physical Meaning", IEEE Transactions on Power Apparatus and Systems, Vol. PAS-91, January 1972, pp. 305 - 310.

[13] R. Cortina, P. Nicolini and G. Frate, "A UHV Cage for the Study of Corona Phenomena", 2nd International Conference on Progress in Cables and Overhead Lines for 220kV and Above", IEE Conference Publication No. 176, 4 - 6 September 1979, pp. 67 - 70.

[14] P. Sarma Maruvada, "Application of Moment Methods to the Computation of Electrostatic Fields. Part I - Parallel Cylindrical Conductor Systems", IEEE Conference Paper No. C72 574-2, IEEE PES Summer Meeting, San Francisco, Calif. July 9-14, 1972.

[15] P. Sarma Maruvada, *Corona Performance of High-Voltage Transmission Lines*, Research Studies Press Ltd., 2000, pp. 19 - 22.

[16] C.H. Gary and M.R. Moreau, Discussion on "The Use of Single-Phase Test Lines and Test Cages to Evaluate the Corona Effects of EHV and UHV Transmission Lines", IEEE Transactions on Power Apparatus and Systems, Vol. PAS-93, 1974, page 89.

[17] N. Giao Trinh and P. Sarma Maruvada, "A Method of Predicting the Corona Performance of Conductor Bundles Based on Cage Test Results", IEEE Transactions on Power Apparatus and Systems, Vol. PAS-96, No. 1, January/February 1977, pp. 312 - 320.

[18] M. Akazaki, "Corona Phenomena from Water Drops on Smooth Conductors under High Direct Voltage", IEEE Trans. Power Apparatus and Systems, Vol. 84, Jan. 1965, pp. 1-8.

[19] Q. Vuhuu and R.P. Comsa, "Influence of Gap Length on Wire-Plane Corona", IEEE Trans. Power Apparatus and Systems, Vol. PAS 88, No. 10, October 1969, pp. 1463-1471.

[20] J.L. Phan-Cong, P. Pirotte, R. Brunelle and N.G. Trinh, "A Study of Corona Discharges At Water Drops Over the Freezing Temperature Range", IEEE Transactions on Power Apparatus and Systems, Vol. PAS-93, 1974, pp. 727 - 734.

[21] JD Cobine, *Gaseous Conductors*, Dover Publications, 1958.

[22] P. Sarma Maruvada, H. Menemenlis, R. Malewski, "Corona Characteristics of Conductor Bundles Under Impulse Voltages", IEEE Transactions on Power Apparatus and Systems, Vol. PAS-96, No. 1, January/February 1977, pp. 102 - 115.

[23] J.J. Clade, C.H. Gary and C.A. LeFevre, "Calculation of Corona Losses Beyond the Critical Gradient in Alternating Voltage", IEEE Transactions on Power Apparatus and Systems, Vol. PAS-88, No. 5, May 1969.

[24] J.D. Kraus, *Electromagnetics*, 5th edition, McGraw-Hill, 1999, pp. 552 -556.

[25] R.E. Ziemer and W.H. Tranter, *Principles of Communications: Systems, Modulation, and Noise* , 4th Edition, John Wiley & Sons, Inc., 1995.

[26] T.Williams, *EMC for Product Designers* , Second edition, Reed Educational and Professional Publishing Ltd, 1996.

[27] M.A. van Houten, Ph.D. Thesis, "Electromagnetic Compatibility in High-Voltage Engineering" , October 1990.

[28] M.J. van Helvoort, "Grounding Structures for EMC - Protection of Cabling and Wiring" , Ph.D. Thesis, Technishe Universiteit Eindhoven, November 1995.

[29] P.C.L. Yip, *High-frequency Circuit Design and Measurement* , Chapman & Hall, 1990.

Stellenbosch University http://scholar.sun.ac.za/

Chapter 4

Transmission Line Modelling with Corona Effects

4.1 Introduction

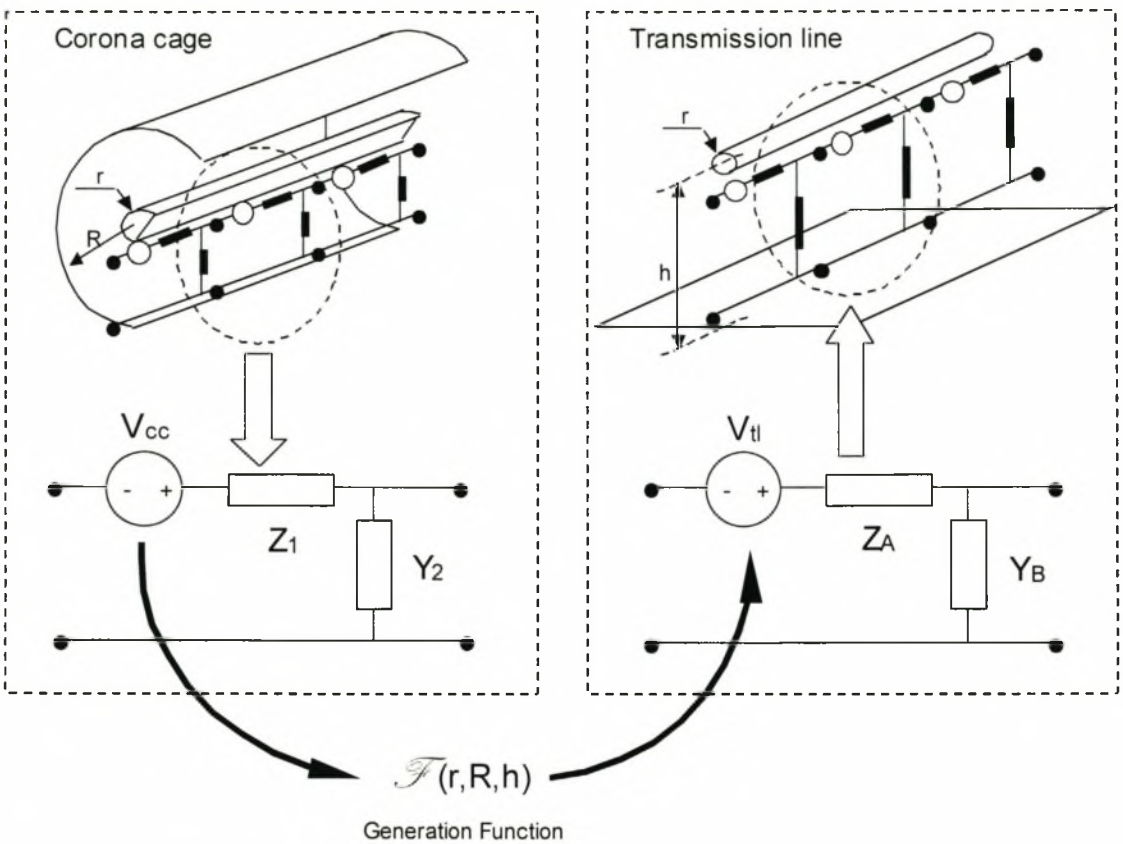

Figure 4.1: Schematic diagram of the distributed models for a corona cage and a single conductor transmission line showing lumped-parameter differential sections for each model.

Having decided on the experimental setup needed to observe RI current flow on conductors in corona in chapter 3, RI noise measurements can now be made in a controlled environment. However, before these measurements can be presented, a method of interpreting the measurements and deriving the required electrical parameters from these measurements must be investigated. These required electrical parameters are derived from the RI current flow on the conductors of the proposed transmission line design. The geometry of the corona cage and the geometry of the proposed transmission line will be significantly different. As a result, the corona cage RI current will not be equivalent to the transmission line RI current even though the surface electric field on the conductors is equivalent. A transform method is therefore required to transform corona cage RI noise measurements to equivalent RI current flow on the conductors of the proposed transmission line design. The transform most often used in the literature is the generation function method. The principle of this method is illustrated in figure 4.1.

Stellenbosch University http://scholar.sun.ac.za/

Distributed-parameter models of a corona cage and a single conductor transmission line are illustrated in the figure. The geometry-dependent parameters of the two structures are represented by the series impedances Z_1 and Z_A and the shunt admittances Y_2 and Y_B. The remaining geometry-independent parameter in each model is then the RI excitation element and is included in figure 4.1 as a series voltage source. This series voltage source is only dependent on the surface electric field and environmental factors such as precipitation rate and the concentration of airborne particles adjacent to the conductor surface. Under fair weather conditions, with the surface electric field equivalent on both the corona cage and transmission line conductors, the two series voltage sources are related by the generation function. A discussion on the derivation and extraction of the generation function is presented in appendix A1. The RI current flow on the transmission line conductors can therefore be calculated by extracting the RI excitation source from the corona cage measurements, applying the generation function transform to this extracted element and then inserting the transformed element into the transmission line model. To do this, accurate models of both the corona cage and transmission line must be derived . This is the subject of this chapter.

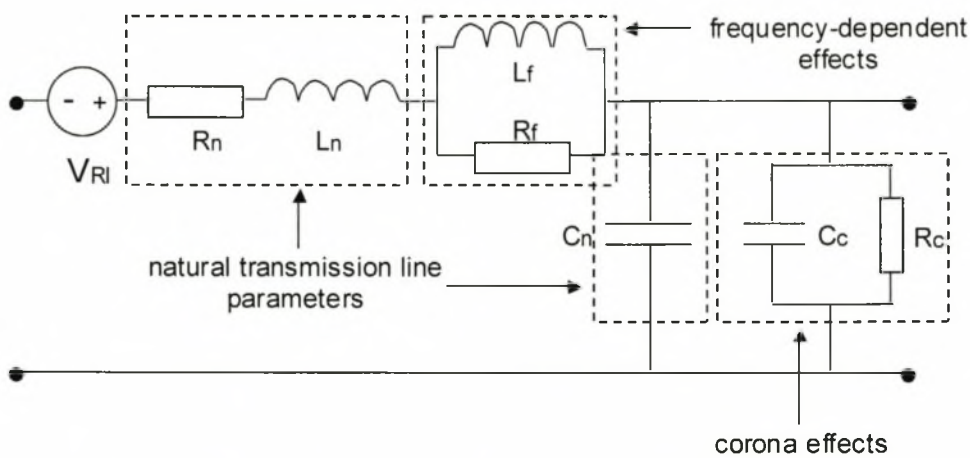

Figure 4.2: Schematic diagram of a proposed differential segment of the distributed-parameter model for a transmission line with corona and frequency-dependent effects.

A proposed differential segment for the corona cage and transmission line distributed-parameter models is illustrated in figure 4.2. The use of distributed models in figure 4.1 is based on the assumption that the systems are electrically large at the measured frequencies. This is a valid assumption for the transmission line model due to the length of the transmission line, even at power line carrier (PLC) frequencies (i.e. 5 kHz to 500 kHz). The small laboratory corona cage is however many orders shorter than a typical transmission line and may indeed be electrically small in a specified frequency band within the measured frequency band proposed in section 1.3 (i.e. 5 kHz to 1 GHz). A distinction can therefore be made between lumped-parameter and distributed-parameter models based on the size of the experimental setup and the measurement frequency bandwidth. This distinction is the basis for the definition of low-frequency and high-frequency models in [1] but will not be adopted in this thesis. Certain frequency-dependent effects have a significant effect on the impedance of the transmission line at high frequencies. At lower frequencies these effects can be omitted from the model since they have no significant effect on the transmission line impedance. This observation will be the basis for the distinction between low-frequency and high-frequency models in this thesis.

Stellenbosch University http://scholar.sun.ac.za/

A literature survey of the models proposed for transmission lines with corona and frequency-dependent effects is presented in section 4.2. Methods of extracting the model parameters are also investigated in this section. The low-frequency models used in this thesis are presented in section 4.3. Finally the extraction of the low-frequency model parameters is discussed in section 4.4 and the most important conclusions of the chapter are summarised in section 4.5.

4.2 Literature Survey

Corona loss, attenuation of high voltage transient pulses propagating along transmission lines and RI current flow on transmission line conductors are corona related topics that have been studied since the first high-voltage transmission systems were constructed at the beginning of the last century. While these studies are inter-related, they are often studied in isolation. For example, the change in capacitance effect that causes the attenuation of high voltage transients propagating along a transmission line will also increase the attenuation of RI current pulses and can be used to predict the amount of corona loss in the system. Models presented in this section will not always be specific to the thesis topic defined in section 1.3 but can be adapted for the specific needs of this thesis in later sections.

An important corona effect is that on the system capacitance. This effect was first observed and investigated by researchers studying the attenuation of the steep rising edge of high voltage transients propagating along transmission lines. The phenomenon was qualitatively modelled as an effective increase in the conductor radius into the inter-electrode gap. This is based on the experimental observation that the electric field in the region of effective conductor radius extension, denoted the corona sheath region, is constant. This is because of the electric field generated by the space charge that accumulates in the corona sheath and deforms the applied electric field in this region. It was also observed that the corona sheath only forms when the electric field on the surface of the conductor exceeds the critical level defined in chapter 2. This corona sheath description was first proposed in [2]. The change in capacitance effect is included in the transmission line model as a transverse element referred to as the corona branch (see figure 4.2). The most important frequency-dependent effects are the increased impedance due to the skin effect and the imperfect ground return paths for current flow. These effects are included in the transmission line model as longitudinal elements (see figure 4.2). The properties of these elements and their inclusion into existing numerical transmission line models, as well as their extraction from measurements and models will be discussed in this section

Stellenbosch University http://scholar.sun.ac.za/

4.2.1 Transmission Line Modelling with Corona Effects

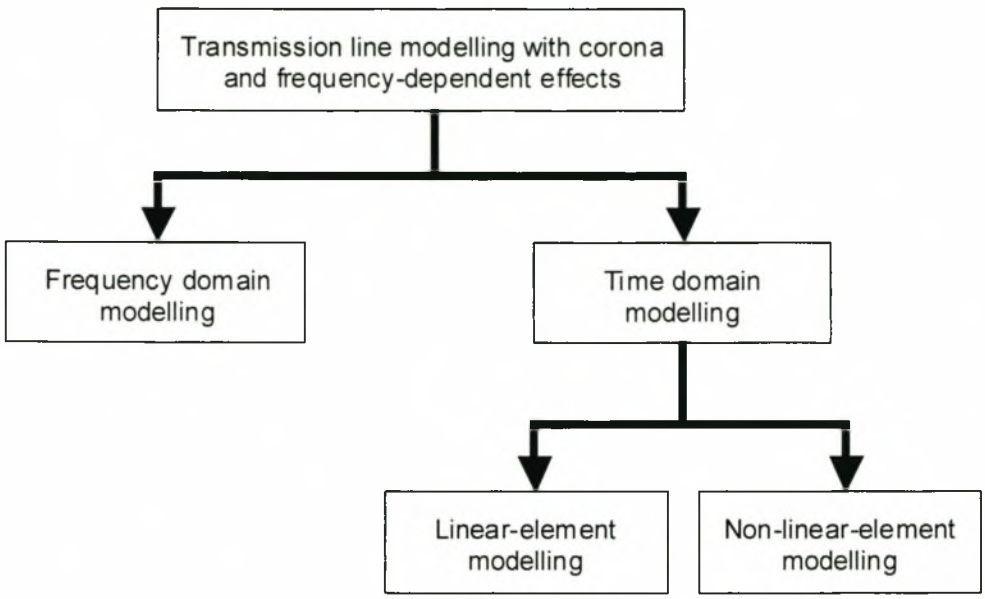

Figure 4.3: An overview of transmission line modelling with corona and frequency-dependent effects

An outline of the various modelling techniques used to model transmission lines with corona and frequency-dependent effects is presented in figure 4.3. In order to determine the conducted RI current at specified points along the conductor, a simulation code is required. This code must predict the propagation of the RI current along the conductors of a multi-conductor transmission line. The extracted corona model will be added to this transmission line code and must therefore be compatible with it. The choice of model used is therefore determined by the accuracy of the model in predicting the required macroscopic corona quantities and the compatibility of the model to existing transmission line codes that are available. Both frequency domain and time domain models will be investigated in this section. The time domain models are further classified into linear-element models and non-linear-element models.

4.2.1.1 Linear-Element Time Domain Modelling

Linear, constant-valued RLC elements are used to model the various transmission line parameters in the models discussed in this section. The non-linear nature of the corona effect is accounted for in these models by including ideal diodes biassed by DC voltage sources. A set of linear equations is then derived for each possible circuit state, defined by the ideal diodes, using circuit theory. The state of the model at any point in time is determined by the state of the ideal diodes (i.e. by the past and present voltage values in the circuit). The extracted system of equations is then solved using a finite difference method. Various available finite difference simulation programs, such as PSpice, can be used to extract the required electrical parameters from the model. The propagation of steady state or transient waveforms along a long transmission line with corona effects using these models is simulated by cascading these linear-element circuits. The cascaded circuits are used to derive two first-order, coupled, differential equations at each node point (i.e. the connection point between consecutive circuits). The equations are coupled at each node point by the Q-V relationship calculated in the two circuit models that form the node point.

Stellenbosch University http://scholar.sun.ac.za/

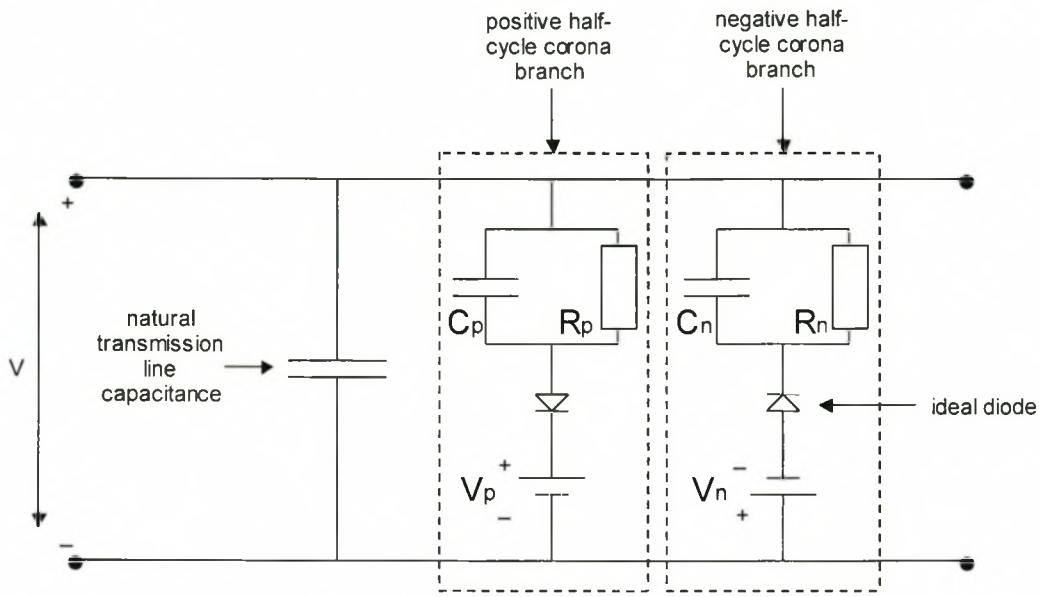

Figure 4.4: The linear-element circuit model used to simulate transient pulse propagation along transmission lines with corona effects (after [3]).

An example of a linear-element circuit model (also known as an analogue model) is presented in [3]. The circuit used in this model is presented in figure 4.4. The model assumes ideal conductors and therefore does not include series resistance or frequency-dependent effects. It is therefore a low-frequency model and is only valid in a specific frequency band of the measurement bandwidth. The corona branches are indicated in figure 4.4. The elements of these corona branches model the change in capacitance and power loss effects that occur on transmission lines due to the presence and displacement of space charge in the inter-electrode gap. The model is greatly simplified by including only the two most important time constants for space charge decay, one for each polarity. This simplification does however reduce the accuracy of the simulation. The DC voltage sources that bias the diodes represent the critical inception voltage in the appropriate half-cycle. Both the formation of space charge and the recombination of space charge are represented by the single RC time constant of the appropriate corona branch in the circuit.

In [4], a linear-element model which includes frequency dependence is sought for inclusion into an existing frequency-dependent, multi-phase transmission line modelling code so that it can include both corona and frequency-dependent effects (i.e. a high-frequency model). It was found in [4] that the shunt resistors that are used in [3] to model space charge decay have no significant influence on the simulation and can be excluded. It was also found in this paper that the "switching on" of corona branches by the non-linear action of the ideal diodes results in numerical instabilities that are evident in the simulations as high-frequency oscillations. A special numerical technique, proposed in [5], is required to successfully remove the numerical instabilities in the simulation.

Stellenbosch University http://scholar.sun.ac.za/

4.2.1.2 Non-linear-Element Time Domain Modelling

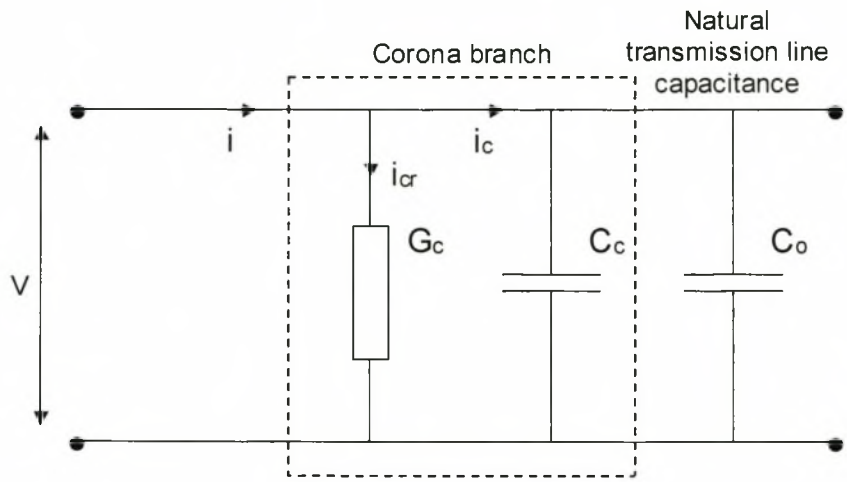

Figure 4.5: An ideal non-linear circuit model of the corona branch (after [6]).

In this modelling technique, the non-linear model elements are included directly into the linear partial differential equations that describe the propagation of transients along the transmission line in such a way that these equations can be solved by non-iterative methods such as a finite-difference time-domain formulation. This approach is adopted in [6], [7], [8] and [9]. In the case of a two-wire transmission line, wave propagation is fully described by two first-order partial differential equations (i.e. the telegrapher's equations). These two equations can be combined to form a second-order partial differential equation (i.e. the wave equation). The non-linear corona branch elements make an analytical solution to the wave equation too difficult. The models presented in this section will therefore attempt to solve the telegrapher's equations numerically.

A finite difference time domain formulation for the model in figure 4.5 is attempted in [8]. This formulation uses a hybrid scheme consisting of both forward and backward differences which result in a tri-diagonal difference equation with a stable and efficient regressive solution. The model is also extended in [8] to multi-conductor transmission lines. The discretised telegrapher's equations with corona and frequency-dependent effects for a two wire transmission line are [8]:

$$\frac{V(i+1,j)-V(i,j)}{\Delta x} = L(x,t,v,i)\frac{I(i,j)-I(i,j-1)}{\Delta t} + R(x,t,v,i)I(i,j)$$

$$\frac{I(i,j)-I(i-1,j)}{\Delta x} = C(x,t,v,i)\frac{V(i,j)-I(i,j-1)}{\Delta t} + G(x,t,v,i)V(i,j) \qquad (4.1)$$

where i and j are spatial and time discretisation units respectively.

It is noted in [6] that while the equivalent, non-linear-element, corona-branch circuit in figure 4.5 will produce the most accurate results, it is difficult to implement numerically in many existing programs (e.g. the widely used EMTP program). A simpler model that is easier to implement is therefore required. Such a simplified non-linear-element model is presented in [7]. The formulation of this model is discussed in appendix A2. In this model, the corona effect is included as a shunt conductance that is described by the time dependent charge-voltage (Q-V)

Stellenbosch University http://scholar.sun.ac.za/

relationship of the transmission line in corona. This is a simpler model than the shunt RC corona branch model in [8] (i.e. the model illustrated by the circuit in figure 4.5) and is easier to implement numerically. In the model, G is required to be a smooth, piecewise-continuous function of q and v and is extracted from the appropriate Q-V curve.

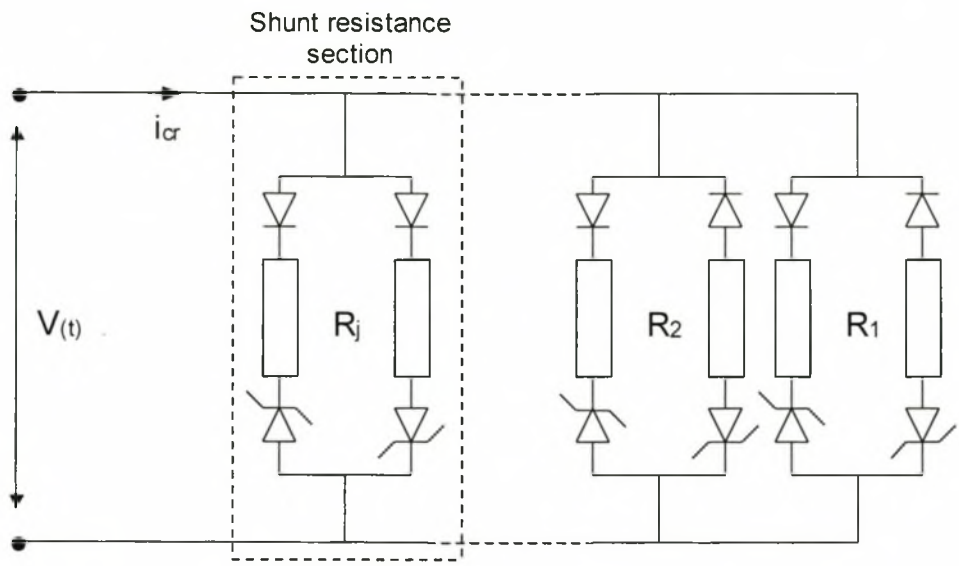

Figure 4.6: An analog equivalent circuit of the shunt conductance used in the Siluciu model corona branch (after [6]).

The model in [7] is referred to in the literature as the Siluciu model. The Siluciu model is adapted in [6] for the study of corona attenuation under dynamic over-voltage conditions. The equivalent circuit diagram of this numerical model is given in figure 4.6 and consists of resistors, diodes and zener diodes. This figure illustrates the simplified shunt conductance representation of the corona effect of the Siluciu model. The shunt conductance is made up of many shunt resistance sections. The accuracy of the model is increased by adding more shunt resistance sections.

4.2.1.3 Frequency Domain Modelling

The distributed non-ideal transmission line model with frequency-dependent and corona effects was illustrated in figure 4.2. This model will be implemented in frequency domain numerical formulations in this section. It is suggested in [10] that the corona loss resistance be included as a series element in the transmission line model since no space charge is lost to the system. This element was however included as a shunt conductance in figure 4.2. Either method can be used since both methods will produce the same result.

The basis for frequency domain modelling is the linear time-harmonic wave equation with loss terms [10]:

$$\begin{aligned} v(z,t) &= V_{\max} e^{-\alpha z} \cos(\omega t - \beta z) \\ &= \mathrm{Re}\left\{ V_{\max} e^{j\omega t} e^{-(\alpha + j\beta)z} \right\} \end{aligned} \tag{4.2}$$

Two methods of solving this time-harmonic equation for a transient pulse are the Bewley method [11] and the Magnusson method [12]. The Bewley method involves decomposing the transient

Stellenbosch University http://scholar.sun.ac.za/

pulse into a finite superposition of step functions using Duhamel's integral method. The step response of the transmission line is then calculated for each step input and the solutions are recombined using superposition to find the solution to the transient pulse. The Magnusson method solves equation 4.2 for a transient pulse by decomposing the pulse into its Fourier series and then solves for each sinusoidal component. The frequency-dependent effects vary with frequency and are easily included into the frequency domain model. However, since the corona branch elements vary with time and not frequency, a method must be devised to include the corona effects into the frequency domain model. Such a method is discussed in [10]. It requires that the transmission line be divided into small differential sections.

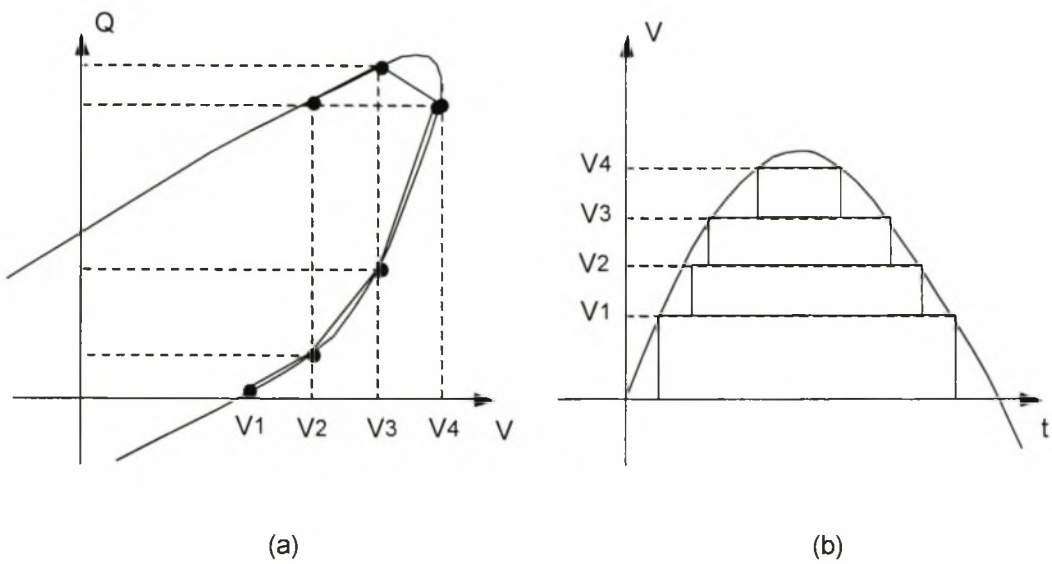

Figure 4.7: (a) A Q-V curve with its piecewise-linear approximation, (b) the division of the source waveform into voltage levels corresponding to the piecewise-linear Q-V curve in (a).

The corona capacitance is approximated by a piecewise-linear curve as illustrated in figure 4.7 (a). This can be done by sampling the time dependent Q-V curve in such a way that the change in capacitance between two consecutive samples is not large enough to significantly affect the accuracy of the simulation. The capacitance along the transmission line is now constant for a certain voltage range of the source waveform as illustrated in figure 4.7 (b). These voltage levels of constant capacitance are then decomposed into their Fourier series. The propagation of these sinusoids can be calculated from the time-harmonic wave equation (i.e. equation 4.2) for the corona capacitance appropriate to that voltage level. At the end of each line segment, the voltage levels are reconstructed from the Fourier series components and added together to produce the source transient. The attenuated and deformed source transient is then again broken up into voltage levels and the same procedure is repeated for the next line section.

4.2.1.4 RI Current Injection

In the general transmission line modelling discussion in [1], it is noted that disturbances such as the RI current produced by corona discharge can be included as a lumped or distributed source. In figure 4.1, it was illustrated how a distributed RI current source can be extracted from the corona cage and then included into the distributed-parameter transmission line model. The induced disturbance can also be included as either a series voltage source or as a shunt current

Stellenbosch University http://scholar.sun.ac.za/

source. In figure 4.2 the disturbance was introduced into the model as a distributed series voltage source.

4.2.2 Model Parameter Extraction

Having defined the model parameters that can be included into transmission line models with corona and frequency-dependent effects, the extraction of these parameters should next be investigated. The natural transmission line parameters for the corona cage have already been extracted in chapter 3 (see table 3.1). It should be noted that while it is convenient to measure the corona cage model parameters in the laboratory corona cage, it is not possible to measure the transmission line parameters since the proposed transmission line would have to be first constructed. The parameters will therefore have to be extracted from models or empirical formulas.

4.2.2.1 Frequency-Dependent Parameter Extraction

Frequency-dependent effects are included as longitudinal RL branches in the transmission line models. The frequency-dependent effects included in the model in [10] are the skin effect (i.e. the transition from bulk current flow to surface current flow at high frequencies) and ground current flow in non-ideal ground conductors (i.e. current flow in a medium with non-ideal and possibly variable resistivity and permeability such as earth). Analytical solutions are available for both the skin effect and the earth current effect (e.g. [10] and [13]).

4.2.2.2 Overview of Corona Branch Extraction

The linear-element models in [3] and [4] require both positive and negative corona inception levels to bias the ideal diodes that determine the state of the circuit. The non-linear-element models also require both positive and negative inception levels to derive the time dependent elements of the corona branch. These inception levels are assumed to be the same in [3] and [14]. For single conductors this single inception level is calculated for these models from Peek's formula (i.e. equation 3.5 in chapter 3).

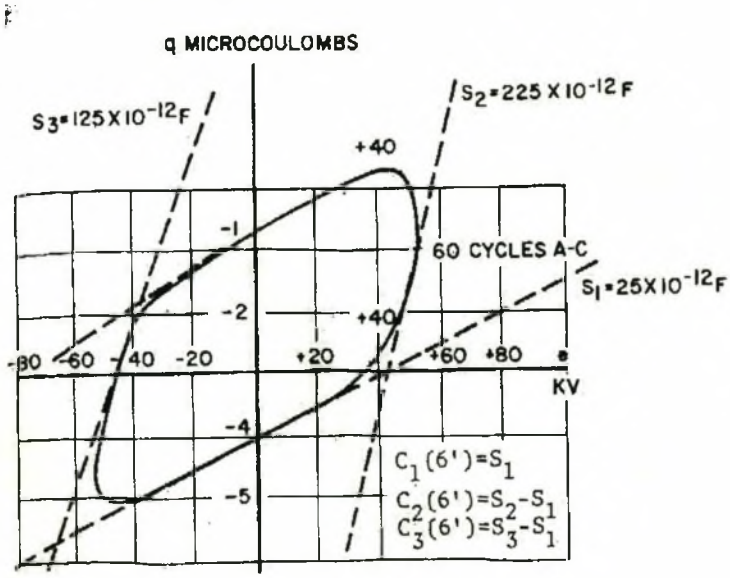

Figure 4.8: An example of a typical Q-V curve showing hysteresis [3].

Stellenbosch University http://scholar.sun.ac.za/

When the electric field at the surface of a conductor exceeds the corona inception level, space charge in the inter-electrode gap deforms the applied electric field at the conductor surface. This effect can be clearly seen if the charge (Q) on the conductor is plotted against the applied voltage (V) (i.e. a Q-V curve plot). The plotted curve displays hysteresis. Such a Q-V curve is presented in figure 4.8. The charge-voltage relationship in a dielectric such as the air dielectric in the inter-electrode gap is [14]:

$$Q = CV \tag{4.3}$$

The instantaneous capacitance between the corona sheath and the low-voltage electrode is therefore the gradient of the Q-V curve. Since the gradient of a hysteresis curve varies, so will the capacitance. This phenomenon is referred to as the change in capacitance effect of transmission lines in corona. The power loss during a single 50 Hz cycle can be calculated by determining the area of the Q-V curve [14]. The shunt resistance can then be calculated from the power loss value.

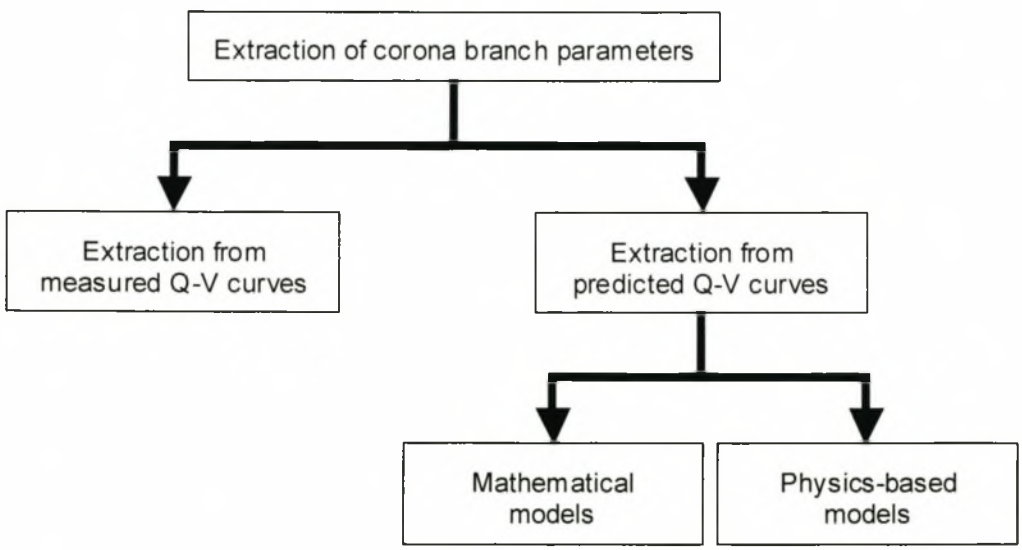

Figure 4.9: Overview of the methods used for the extracting the corona branch elements.

In figure 4.9, an overview of methods used to extract the corona branch elements is presented. The easiest method is to extract the parameters from measured Q-V curves. This is however only possible on an existing transmission line. As already mentioned, a model is needed for extracting the model elements of a proposed transmission line design. Such a model will predict the Q-V relationship of a transmission line conductor with only the geometry and the applied voltage as input parameters. Two main categories of corona branch models are found in the literature. One involves deriving non-linear equations that describe the simplified macroscopic corona processes. These equations are then solved iteratively. The other method avoids non-linear equations by implementing a physics-based approach. The resulting equations can then be solved directly. Both models are implemented with a finite difference formulation.

Stellenbosch University http://scholar.sun.ac.za/

4.2.2.3 Corona Branch Extraction From Measured Q-V Curves

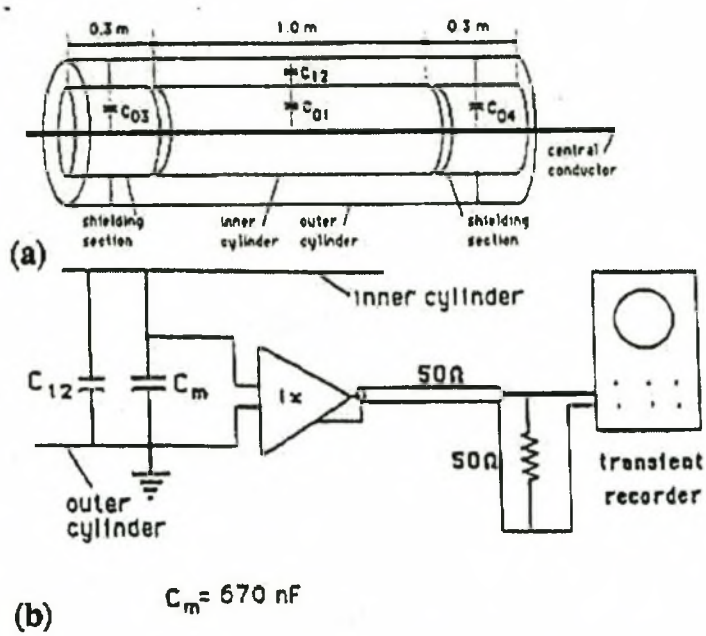

Figure 4.10: A typical corona cage Q-V curve measurement setup [15].

The dynamic capacitance between the corona sheath and the corona cage is calculated by measuring the charge on the corona cage and plotting this against the instantaneous voltage applied to the centre conductor. In [15] the charge was measured by placing a 670 nF capacitor between the corona cage and the grounding structure (see figure 4.10). A high capacitance value was chosen so that the voltage induced on the corona cage would be small. The charge is then calculated using equation 4.3, with C in this equation equal to the capacitance between the corona cage and the grounding structure (i.e. C_{12} in figure 4.10). In the linear-element models in [3] and [4], only one time constant is modelled for each polarity. These capacitor values equal the dominant gradient of the Q-V curve in the appropriate half-cycle. The shunt resistors in these models are determined by measuring the DC leakage current when the conductor is in corona [3]. Finally the shunt loss resistance for the remaining models can be found by integrating the Q-V curve to find the average power loss and then substituting this value into:

$$R_{loss} = \frac{P_{AVG}}{(I_{RMS})^2} \tag{4.4}$$

The RMS current flow between the corona cage and the grounding structure can be calculated from the charge measurement by noting that the instantaneous charge is the derivative of the charge induced on the corona cage.

4.2.2.4 Corona Branch Extraction From Predicted Q-V Curves - Mathematical Models

Modelling of the actual system in order to extract the system's Q-V relationship, with only the applied voltage and system geometry known, will result in partial differential equations that have variable limit conditions. Such equations cannot be integrated. An alternative method of modelling the Q-V characteristics of a proposed transmission line design is to derive a simplified model of the macroscopic corona processes and extract from this model mathematical equations

Stellenbosch University http://scholar.sun.ac.za/

that relate the charge of the system to the applied voltage. These equations will be non-linear but can be solved using an iterative method. This approach is adopted in [10], [15], [16] and [17].

The model in [15] is derived for a coaxial corona cage geometry. The applied electric field therefore has symmetry about the centre conductor and is uniform along its length. This simplifies the extracted equation to a single spatial dimension (i.e. the radial distance from the centre conductor). In order to extract the mathematical model of the complex corona processes two assumptions are made. The corona sheath is assumed to form only when the applied electric field exceeds the inception level and, secondly, the field in this corona sheath is assumed to be constant with respect to the radial dimension and equal to the critical level. The models in [15], [16] and [17] note a difference between the critical field level and the inception field level. The electric field in the corona sheath decreases to the lower critical level after corona inception. This observation is not made in the other corona branch models presented in this literature survey. Time taken for the corona-sheath electric field to settle to the critical value was chosen in [15] as 0.5 μs. The difference was specifically included in [16] and [17] to account for the change in inception level caused by a decrease in the rise time of the transient source pulses. It was considered essential in [16] since the propagation of lightning pulses was studied. A difference between the positive and negative inception levels was also included and is also related to the fast rise time of transient source pulses.

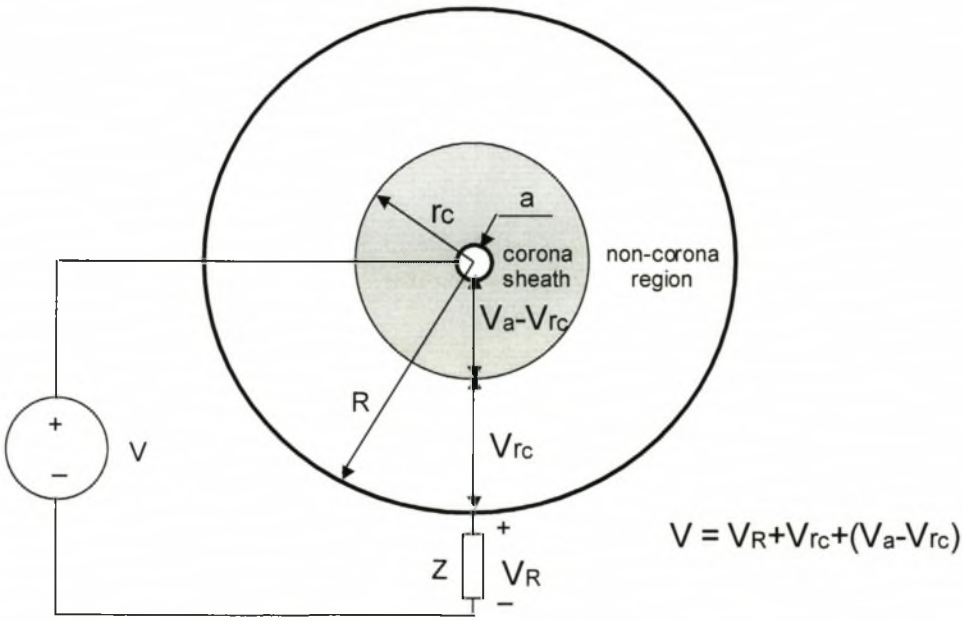

Figure 4.11: Schematic cross-section of the corona cage illustrating the basis for the formulation of the mathematic corona branch model.

The basic principle used to formulate the required non-linear mathematical equation is the requirement that the potential difference across the corona sheath and the non-corona region (see figure 4.11) must equal the voltage applied between the two electrodes. This equation is then solved iteratively. The electric field in the corona sheath is assumed constant and equal to the critical field level (E_c). The potential difference across the corona sheath region with radius r_c is therefore [10]:

$$V_a - V_{r_c} = E_c(r_c - a) \tag{4.5}$$

Stellenbosch University http://scholar.sun.ac.za/

In equation 4.5, a is the radius of the centre conductor. The electric field in the non-corona region is unaffected by the space charge field and is described by the normal field distribution for a coaxial geometry with outer radius R [10]:

$$V_{r_c} = E_c r_c \ln\left(\frac{R}{r_c}\right) \tag{4.6}$$

The sum of equation 4.5 and 4.6 must then equal the applied voltage. This leads to a non-linear equation that relates the radius of the corona sheath to the system geometry and the electric field in the corona sheath. With the electric field in the corona sheath and the system geometry known, the radius of the corona sheath can be calculated by solving the equation iteratively. The model is implemented using a finite difference method. At each time step, the corona sheath radius is calculated. The charge is then calculated from [10]:

$$Q = 2\pi\varepsilon_0 E_c r_c \tag{4.7}$$

The model in [10] is unable to account for recombinations that will occur under AC conditions. The model is therefore only useful for unipolar pulses or DC conditions.

The instantaneous capacitance is extracted from the gradient of the Q-V relationship between the n'th and (n-1)'th time step [10]:

$$C = \frac{dQ}{dV} = \frac{Q_n - Q_{n-1}}{V_n - V_{n-1}} \tag{4.8}$$

The mathematical models presented in this section do not include a satisfactory recombination law. They are therefore only intended for fast transient unipolar source voltages and cannot be directly applied to the AC source voltage conditions required for the research in this thesis. A physics-based Q-V model, which would include a comprehensive recombination law, is therefore required.

4.2.2.5 Corona Branch Extraction From Predicted Q-V Curves - Physics-Based Models

The aim of the research in [14] is to predict the corona loss on high voltage transmission lines. It is found in [14] that power loss on the transmission lines becomes significant due to corona only when the electric field gradient on the surface of the conductors exceeded the inception level. This is because enough space charge has formed in the inter-electrode gap to constitute a uniform corona sheath. This space charge is displaced in alternating directions in this gap by the AC electric field. Since the space charges have no significant mass, the energy is not stored as potential energy but rather expended as kinetic energy. This results in power loss. The power loss is dependent on the amount of space charge produced (i.e. the ionic emission of the conductor) and the displacement of this space charge in the inter-electrode gap. It can therefore be described by the relationship between the charge on the conductor and the applied voltage (i.e. the Q-V relationship can be extracted). It is found in both [14] and [18] that the Q-V relationship can be best modelled by implementing simplified physical laws based on macroscopic corona events since such a model will result in linear equations that can be solved directly. The physics-based model in [18] is slightly more sophisticated than the model in [14]. The increased complexity of the model in [18] allows it to predict frequency-dependent properties of the corona branch (i.e.

Stellenbosch University http://scholar.sun.ac.za/

a dynamic corona branch model). It therefore permits the extraction of the Q-V relationship for a fast transient source which the static corona branch model in [14] cannot do. The source voltage studied in this thesis is a 50 Hz AC voltage. The simpler static model will therefore be satisfactory. It is also noted that the model in [18] requires numerical parameters to be derived from measured Q-V curves for a specific geometry. It is therefore not appropriate for the purposes of the research in this thesis, where the model must predict the Q-V curve with only the geometry and applied voltage known. Only the model in [14] will therefore be discussed in this section.

Firstly an emission law is required to determine the amount of space charge in the inter-electrode gap. Corona discharge produces equal numbers of both positive and negative space charge. The conductor repels only one charge species into the inter-electrode gap. It is the movement of this charge species that will cause power loss. Only the space charge in the inter-electrode gap will therefore be considered in the model. Since this space charge is of the same polarity as the conductor, the process is described as the ionic emission of the conductor (i.e. an emission law). The electric field of the space charge sheath near the conductor surface distorts the applied electric field in this region. The actual surface electric field is the superposition of applied (superficial) field and the space charge field. In this way the emission law is self-regulated. When the applied electric field exceeds the inception level on the conductor surface, space charge is formed in a corona sheath which reduces the applied field. An increase in applied field increases the amount of space charge in the corona sheath, compensating for the increase in the applied field and thus maintaining a constant field in the corona sheath. The observation that the field is constant in the corona sheath is consistent with the observation made in the mathematical models of the previous section. The amount of space charge emitted can therefore be calculated by determining the amount of space charge needed to maintain a constant electric field. Since the total voltage on the conductor surface remains constant (v_0), the conductor charge will also remain constant (Q_0). This constant conductor charge is the superposition of the applied charge (Q_a) and the charge (Q_i) induced on the centre conductor by the space charge (Q_e) in the corona sheath. In a coaxial geometry such as the corona cage, the induced charge is [14]:

$$Q_i = -(1 - C.\ln(r/a)/2\pi\varepsilon_0)Q_e \tag{4.9}$$

The space charge emitted can then be calculated by determining the amount of induced charge required to maintain a constant conductor charge [14]:

$$Q_i = -C(v - v_0) \tag{4.10}$$

A simplified emission law is therefore obtained by substituting equation 4.10 into equation 4.9 to find the relationship between the space charge and the applied voltage.

Next a displacement law is required to monitor the movement of the emitted space charge in the inter-electrode gap due to the applied electric field. It can be proven experimentally that thermal agitation and diffusion have no significant nett effect on the displacement of the space charge at standard temperature and pressure (STP) and quasi-static field conditions. The simplified displacement law is therefore fully described by the viscous friction law [14]:

$$\overline{V} = \mu \cdot \overline{E} \tag{4.11}$$

Stellenbosch University http://scholar.sun.ac.za/

In equation 4.11, $\mu^+ = 1.5 \times 10^{-4}\ m^2/V.s$ [14] is the mobility of the positive space charge and $\mu^- = 1.8 \times 10^{-4}\ m^2/V.s$ [14] is the mobility of the negative space charge. It should be noted that there is a region in the corona sheath were avalanches are able to propagate due to a highly divergent field. This region is defined by an electric field strength greater than about 20 kV/cm [14] and smaller than the critical level. A modified displacement law must therefore be derived for space charge displacement in this region. The electric field at each space charge shell is calculated using Gauss' theorem. The implementation of the displacement law in the dynamic model in [18] requires an additional drift law to accurately predict the Q-V curves for slowly varying sources such as a 50 Hz AC source.

Since the applied voltage is alternating, the movement of space charge will also alternate. A recombination law is therefore also required for when ions of opposite polarity collide. The simplified recombination law for ionic concentrations n^+ and n^- is [14]:

$$\frac{dn^+}{dt} = \frac{dn^-}{dt} = -\alpha \cdot n^+ \cdot n^- \tag{4.12}$$

where α is the ionic recombination factor and equals 1.5 $e^{-12}\ m^2/s$ for air at STP [14].

A requirement of the physics-based models is that the quantity and displacement of the space charge in the inter-electrode gap must be known at all times. The model is therefore implemented in both [14] and [18] using a finite difference method with the position and quantity of space charge calculated at each iteration. This is best done by describing the charge emitted at each iteration as a three dimensional charge shell. The charge on this charge shell is determined from the emission and recombination laws and its position is calculated from the displacement law. These two state variables are stored and updated at each iteration. If the charge on a charge shell is completely removed by recombination or by collision with an electrode, the variables describing that charge shell can also be removed. In the case of collision with the centre conductor, the charge is returned to the conductor. The recombination law described above must be simplified for the charge shell formulation since charge concentrations are not calculated. The simplified recombination law is [14]:

$$\frac{dq^+}{dt} = \frac{dq^-}{dt} = \frac{|q^+ - q^-|}{|v^+ - v^-|} \tag{4.13}$$

where q is the charge of the charge shell and v is the velocity of the charge shell. The law therefore states that the change in charge of the two colliding charge shells during an iteration is proportional to their relative charge and inversely proportional to their relative crossing velocity. In a corona cage, which has a electric field that is symmetrical around the centre conductor and uniform along its length, the model can be further simplified to one dimensional charge shells. These charge shells occupy only a position along a single radial path between the centre conductor and the corona cage. They are therefore effectively point charges, described fully by their charge and position along the radial line. This approximation results in a simplified displacement law [14]:

$$dr = \mu \cdot E(r,t) \cdot dt \tag{4.14}$$

Stellenbosch University http://scholar.sun.ac.za/

The modified displacement law for the highly divergent region near the corona sheath is [14]:

$$dr = a\sqrt{1 + 2dt \cdot \mu \cdot E / a} \tag{4.15}$$

The formulation and implementation of the physics-based Q-V curve model in [14] in a Matlab simulation code is presented in appendix B3.

4.3 Proposed Low-Frequency Models

Having investigated the various transmission line models that include corona and frequency-dependent effects in the literature, the most appropriate model for the research in this thesis must now be selected. The two considerations when deciding on a specific model are the accuracy of the solution and the compatibility of the model to existing transmission line codes. Two codes that have been used at the University of Stellenbosch for the study of modal propagation along transmission lines are: the Wedepohl code [19] which is a frequency domain code and a finite-difference time-domain code written by Dr. Jaco van der Merwe [20].

It was suggested in section 3.3.3 that the corona cage will be electrically small only in a certain low-frequency bandwidth. Indeed, the natural transmission line parameters extracted in section 3.3.2 from the corona cage were found to be only valid for frequencies below 30 MHz (see appendix C1). It was also suggested in section 4.1 of this chapter that a distinction will be made, when modelling transmission lines, between low-frequency and high-frequency models. Low-frequency models were defined in this section as those models that excluded all frequency-dependent effects. The frequency bandwidth of such models is restricted to frequencies at which frequency-dependent effects are negligible (i.e. frequencies below 30 MHz for the corona cage used in this thesis). Only low-frequency models will be presented and used in this thesis. Extraction of a high-frequency model from the corona cage will be investigated in future research. Low-frequency models for both the corona cage and a transmission line will be proposed in this section.

4.3.1 Comparison of Linear-Element and Non-Linear-Element Models

It is noted in [3] that the non-linear-element model derived requires the calculation of the corona branch elements at each differential segment of the distributed transmission line if the voltage source is a wideband pulse. This is time consuming and computationally inefficient. The linear-element model has constant value elements. Their values are extracted from the two main time constants of the Q-V relationship. This argument is not valid for a sinusoidal 50 Hz waveform and is acknowledged as such in [3]. The corona branch elements are identical along the entire length of the line at any given time since the transmission line is electrically small at 50 Hz. It is also noted in [4] that the length of the cascaded linear-element circuit sections is about an order shorter than the non-linear-element differential sections if the source voltage has high-frequency components. Fewer nodes and therefore fewer iterations are required in the simulation of fast high voltage transients using a linear-element model.

Stellenbosch University http://scholar.sun.ac.za/

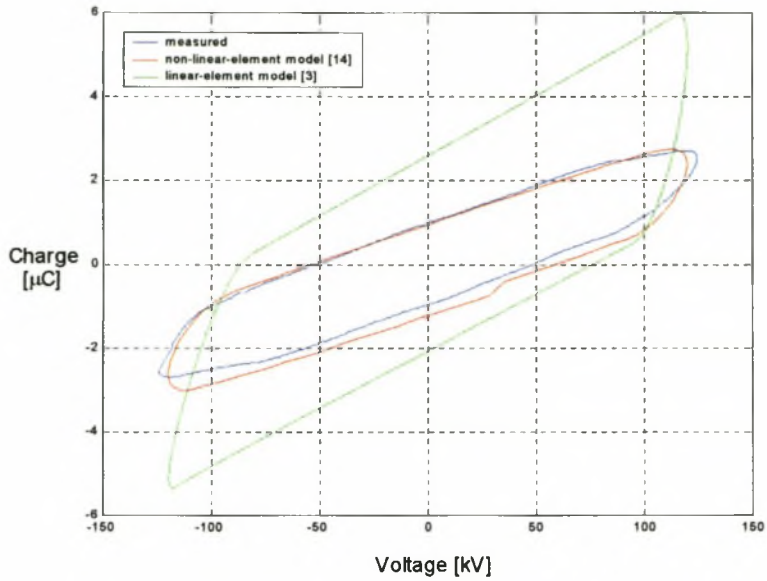

Figure 4.12: Comparison of simulated Q-V curves for a 50 Hz source voltage, extracted from a linear-element circuit model [3] and a non-linear-element model [14], with a measured Q-V curve (R = 300 mm, a = 8 mm and V(peak) = 120 kV).

Since only two time constants are included in the linear-element model in [3], the model is less accurate than the non-linear-element models. This is illustrated in figure 4.12 were the simulated Q-V curves of both model types are compared to a Q-V curve measured in the corona cage geometry proposed in chapter 3. The linear-element model in [3] produces a Q-V curve which is less accurate than the Q-V curve used to extract the elements of the non-linear-element models, in this case obtained from the Q-V curve model in [14]. The linear-element models are however more time and memory efficient for wideband pulse sources. Since only a 50 Hz sinusoidal source is considered in this thesis, the more accurate non-linear-element models will be used.

4.3.2 Comparison of Non-Linear Element Models

It was found in the literature survey that the most accurate non-linear-element model (see figure 4.5) is difficult to implement in certain transmission line programs, in particular the EMTP program. The Siluciu model provided an alternative that is easier to implement but is not as accurate. A method of implementing the more accurate non-linear-element model in a finite-difference time-domain (FDTD) code was presented in the literature survey. Since the only time domain code available is an FDTD code this non-linear-element model will be adopted in this thesis.

4.3.3 Proposed Low-Frequency Corona Cage Model

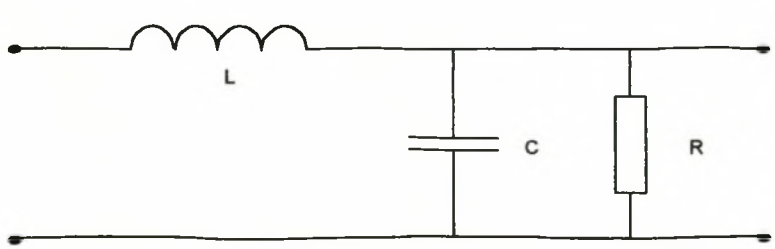

Figure 4.13: Schematic diagram of the proposed low-frequency corona cage model.

Stellenbosch University http://scholar.sun.ac.za/

In the low-frequency regime, the small corona cage is electrically small and the frequency-dependent effects discussed in the literature survey are not significant. The corona cage can therefore be modelled by the lumped-parameter model in figure 4.13. The only longitudinal element is the natural transmission line inductance extracted in section 3.3.2. The DC resistance of the cage metal is insignificant and is therefore excluded as are the frequency-dependent effects. It is not necessary to include the corona branch in the model since the measurement is made between the corona cage and the grounding structure conductors. The electrical parameters of this measurement structure are not affected by the presence of space charge in the inter-electrode gap between the centre conductor and the corona cage. The only transversal element is therefore the natural transmission line capacitance extracted in section 3.3.2. Since the low-frequency transmission line model will be a distributed model due to the length of the line, a per unit RI disturbance voltage element must be extracted. This disturbance voltage source extracted from the model in figure 4.2 is:

$$v_{RI} = \frac{v_{measured}}{l} \qquad [V/m] \tag{4.16}$$

where l is the length of the corona cage.

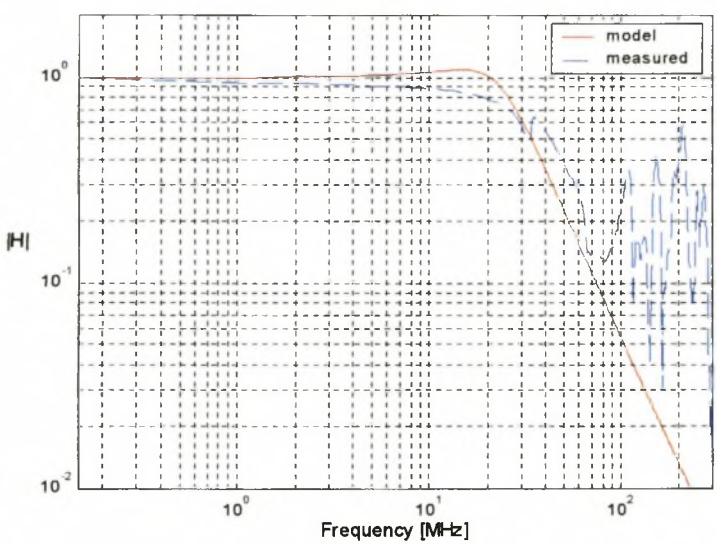

Figure 4.14: The measured frequency response of the measurement system confirming the validity of the low-frequency corona cage model in the frequency range: 150kHz to 30MHz.

The validity of the corona cage model in figure 4.13 is verified by coupling a known sinusoidal voltage onto the corona cage at a point farthest from the measurement point on the cage and measuring the voltage across the measurement resistor. The frequency of the source voltage is varied between 150kHz and 300MHz. The measurement result is plotted in figure 4.14 and indicates that the model in figure 4.13 is valid in the frequency range 150kHz to 30MHz.

The model in figure 4.14 assumes that the capacitive coupling of the electrons, produced during corona discharge, to the corona cage is equal to the natural capacitance. The macroscopic change in capacitance effect that was noted and modelled in the literature survey is therefore assumed to have no effect on this coupling mechanism. This assumption is based on the observation that the generation function (discussed in appendix A1) assumes a constant capacitance equal to the natural capacitance.

Stellenbosch University http://scholar.sun.ac.za/

4.3.4 Proposed Low-frequency Transmission Line Model

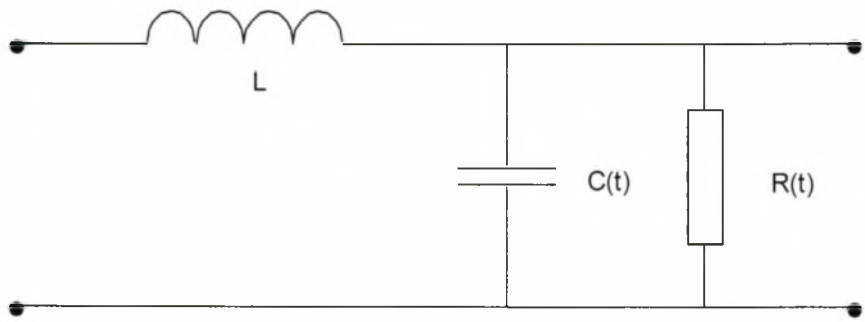

Figure 4.15: Proposed low-frequency distributed-parameter transmission line model.

A proposed model for a two conductor transmission line with corona effects is presented in figure 4.15. The length of the transmission line necessitates the use of distributed elements in the model. Since it is a low-frequency model, the frequency-dependent effects are not included. The corona effects are however frequency-independent and a corona branch, consisting of a shunt capacitance and conductance, is included. This is the more accurate non-linear-element model that is used for either time domain or frequency domain codes. The corona loss resistance, which is included in figure 4.15 as a shunt conductance, was included in the frequency domain models as a series resistance (e.g. [10]). This will not affect the simulation results for a distributed transmission line code and either method is acceptable.

4.4 Model Parameter Extraction

Since the low-frequency models used in this thesis include only the corona branch elements (see figures 4.13 and 4.15), only the extraction of these transmission line elements will be presented in this section.

4.4.1 Q-V Curve Measurement

The two corona branch elements are both extracted from the Q-V relationship of the system. The Q-V relationship must therefore be extracted from the corona cage and the proposed transmission line. Since the proposed transmission line design has not been built, a Q-V model is required so that the Q-V relationship can be predicted. Various Q-V models were discussed in the literature survey in section 4.2. It was found in the survey that the Q-V models best suited to the 50 Hz AC conditions in this thesis were the physics-based models. The validity of these models will be confirmed in this section by comparing the simulated Q-V curves to measured Q-V curves for the corona cage design presented in chapter 3.

Stellenbosch University http://scholar.sun.ac.za/

The Q-V curve measurement setup proposed in [15] was illustrated in figure 4.10. Charge is measured in this setup by integrating the current flow between the corona cage and the grounding structure using a capacitor placed between these two conductors. The charge is then equal to the voltage across the capacitor multiplied by its capacitance. To maintain a low voltage on the corona cage, the capacitance of the shunt capacitor (C_m) should be much larger than the natural capacitance between the corona cage and the centre conductor (C_{12}). A capacitive voltage divider is used to measure the instantaneous applied voltage on the centre conductor. The X-Y mathematical function of an oscilloscope can then be used to plot the applied voltage, at port one, on the X-axis and the charge measurement, at port two, on the Y-axis. The Q-V relationship is therefore displayed in real-time on the oscilloscope. This measurement method will be referred to in this thesis as the real-time Q-V measurement method.

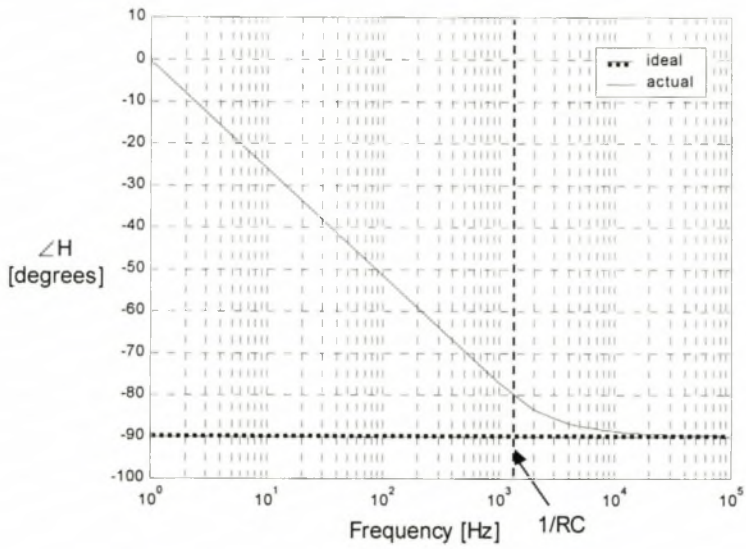

Figure 4.16: The phase of an ideal integrator and that of the non-ideal integrator used in the charge measurement (R = 1kΩ and C = 690nF).

The phase of the integrator used in the real-time Q-V measurement method is plotted in figure 4.16. The phase should be that of an ideal integrator (i.e. -90°) which is also plotted in figure 4.16. To minimize the error caused by the non-ideal integrator, the input impedance of the measurement device (i.e. the oscilloscope) must be resistive and as large as possible so that the value of the 1/RC time constant approaches zero (i.e. as in the case of an ideal integrator). If the coaxial cable connecting the integrator to the oscilloscope is long, a 50 Ω termination is required at the oscilloscope end to prevent reflections at the measurement device input (see figure 4.10). A high impedance buffer is therefore required at the integrator output to ensure that the integration error is negligible. The noise floor of the oscilloscope measurement is about 50 mV (i.e. for an input impedance of 10 MΩ) and the largest measured signal is smaller than 5 V. The dynamic range of the measurement system is therefore smaller than 40 dB. The impedance of the integrator decreases at a rate of 20 dB/decade for $\omega > 1/RC$. With the lowest measured frequency 50 Hz and the maximum dynamic range 40 dB, the highest measured frequency will be smaller than 500 kHz. The 10 metre coaxial cable that connects the integrator to the oscilloscope is therefore electrically small at the highest measured frequency. A 50 Ω termination impedance and a high impedance buffer are therefore not required for the charge measurements in this thesis.

Stellenbosch University http://scholar.sun.ac.za/

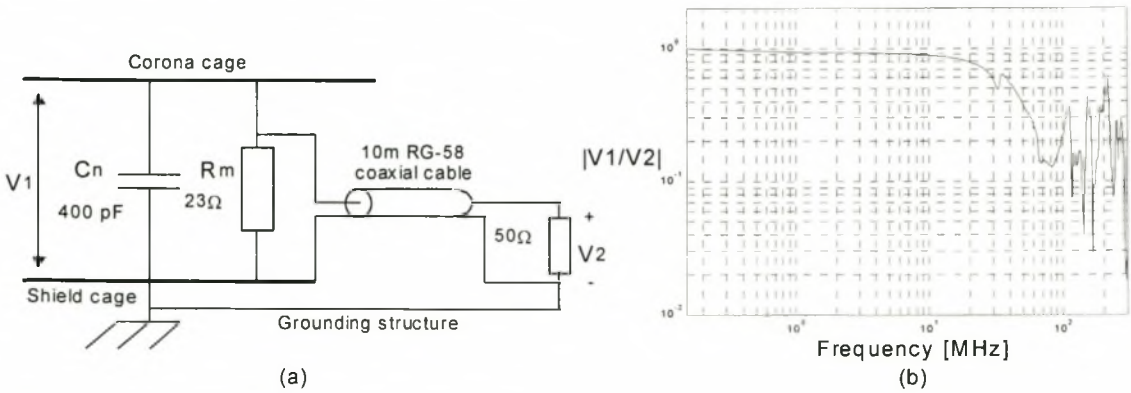

Figure 4.17: Schematic diagram of the experimental setup for an alternative Q-V curve measurement method and (b) the frequency response of this measurement system.

The wideband RI current measurements are made in the measurement setup illustrated in figure 4.17 (a). The highest measured frequency in these measurements is many orders greater than that of the charge measurements (i.e. 500 kHz). The 10 metre coaxial cable connecting the measurement resistor to the measurement device will therefore be electrically large at the highest measured frequency and a 50 Ω termination impedance is required for the coaxial cable. The charge measurements can alternatively be made with the measurement setup in figure 4.17 (a). An integrator is therefore not required and the errors made with the non-ideal integrator are removed from the charge measurements. The frequency response of the alternative charge measurement system is presented in figure 4.17 (b). The plot indicates that the response is flat in the charge measurement bandwidth (i.e. 50 Hz to 500 kHz). The voltage measured off the corona cage can therefore be integrated numerically to calculate the charge on the corona cage. This post-processing is described in appendix C4. Since the numerical integration is ideal, the integration error made in the real-time Q-V measurement method is avoided. The only disadvantage with the post-processing Q-V measurement method is that the Q-V curve cannot be displayed in real-time. This is overcome by using the oscilloscopes GPIB port, with a bit transfer rate of 7 Mb/s, to download the measured voltages onto a PC running Matlab. The calculated Q-V curve can then be displayed in near real-time.

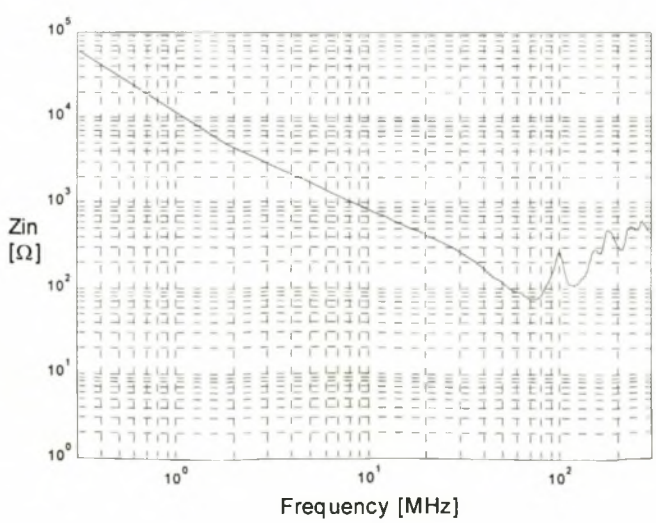

Figure 4.18: The input impedance of the TDS3032 oscilloscope (10 MΩ setting) used in the Q-V measurement system in figure 4.17 (a).

Stellenbosch University http://scholar.sun.ac.za/

The oscilloscope used to make the Q-V measurements in this chapter is the TDS3032 digital phosphor oscilloscope. The measured input impedance of the 10 MΩ setting of this device is plotted in figure 4.18. The low input impedance of the oscilloscope at high frequencies will not affect the charge measurement by loading the 50Ω termination impedance of the measurement cable. This is because the input impedance is above 5 kΩ in the measured frequency band. A high impedance buffer is therefore not required for the alternative charge measurements.

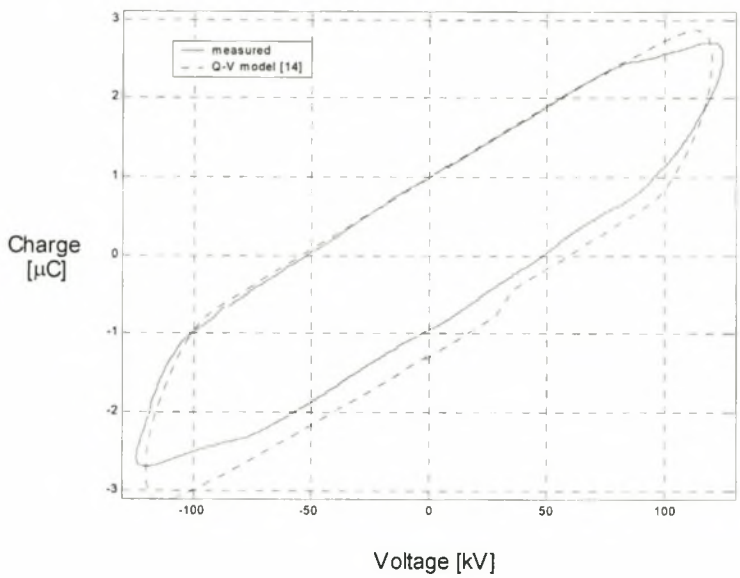

Figure 4.19: Comparison of a simulated Q-V curve for the AC source voltage with an equivalent measured Q-V curve (R = 300 mm, a = 8 mm and V(peak) = 120 kV). The simulated Q-V curve is extracted from the physics-based model in [14].

The static Q-V model used in this section to extract the predicted corona branch element values is the physics-based model in [14]. The simulated Q-V curve obtained from this model for the corona cage design of chapter 3 is compared to an equivalent measured Q-V curve in figure 4.19.

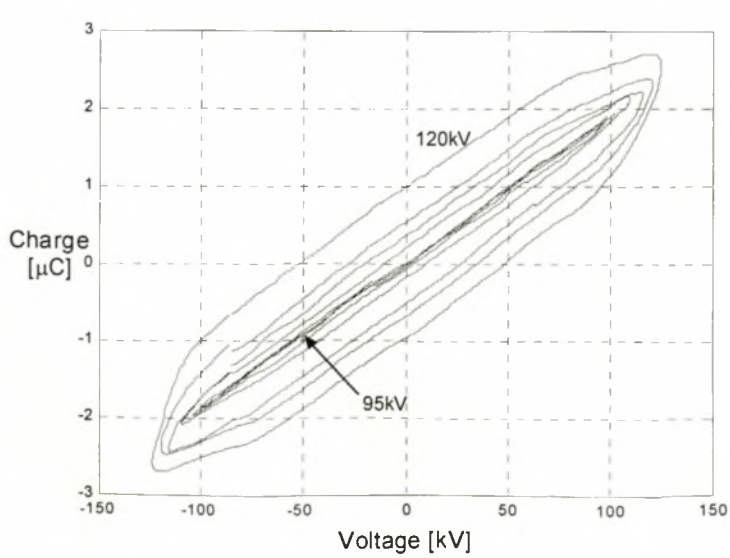

Figure 4.20: A set of Q-V curves measured in the corona cage design in chapter 3 made with 5 kV steps from 95 kV to 120 kV (R = 300 mm, a = 8 mm).

Stellenbosch University http://scholar.sun.ac.za/

The measured Q-V curves for the corona cage design in chapter 3 are presented in figure 4.20. The measurements are made at 5 kV intervals. It is noted in [14] that the Q-V curves only display hysteresis once the inception level has been exceeded. The Q-V curve measurement is therefore an accurate method of determining the inception level of the system. The inception level was experimentally determined to be 100 kV (peak) using this method. The dynamic corona branch capacitance and shunt conductance can now be extracted from the Q-V curves.

In the literature it is mostly assumed that the corona branch model, derived for a cylindrical electric field, can be extended to a non-cylindrical field, such as the field on a transmission line conductor without any modifications. This is based on the assumption that the large dimensions of the single conductor transmission line results in an electric field that is approximately cylindrical in the region where space charge forms. It is then assumed that the applied AC field keeps the space charge in this quasi-cylindrical field region. The proposed transmission line design will consist of compact multi-conductor bundles. The validity of the quasi-cylindrical field assumption should therefore be investigated since it may be necessary in this case to derive a more complex model (i.e. one that does not assume a quasi-cylindrical electric field distribution) to extract the corona branch values from a compact multi-conductor transmission line.

4.4.2 Extraction of the Corona Branch Elements:

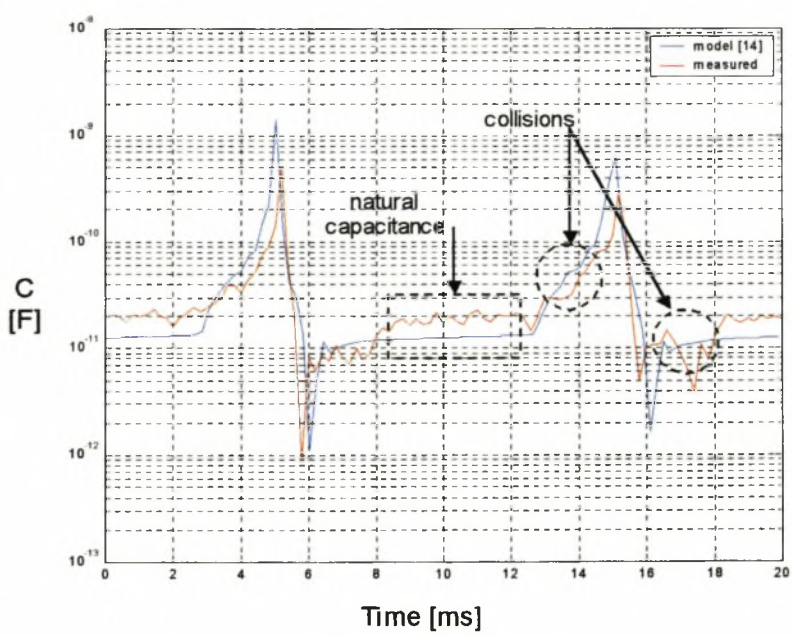

Figure 4.21: The dynamic capacitance between the corona sheath and the corona cage for one period of the AC source voltage waveform, extracted from the measured and simulated Q-V curves (R = 300 mm, a = 8 mm and V(peak) = 120 kV).

The dynamic capacitance is extracted from the Q-V curve by sampling the charge and voltage waveforms at 200 μs intervals. The sampled waveforms are then substituted into equation 4.8 to calculate the capacitance. The results presented in figure 4.21 are extracted from measured and simulated corona cage Q-V curves for a peak applied voltage of 120 kV. They indicate that the capacitance increases significantly when the inception level is exceeded. There is a strong correlation between the simulated and measured curves, verifying the accuracy of the simulation

Stellenbosch University http://scholar.sun.ac.za/

model in [14]. The measurements also verify the natural transmission line capacitance measurement in table 3.1 (i.e. a natural capacitance of 22 pF). The simulated Q-V curve uses the analytical capacitance value in table 3.1 (i.e. 15 pF). It is also noted in figure 4.21 that the Q-V model correctly predicts the collision of space charges into the corona cage conductor (i.e. charge loss in the system) for an applied source voltage of 120 kV (peak).

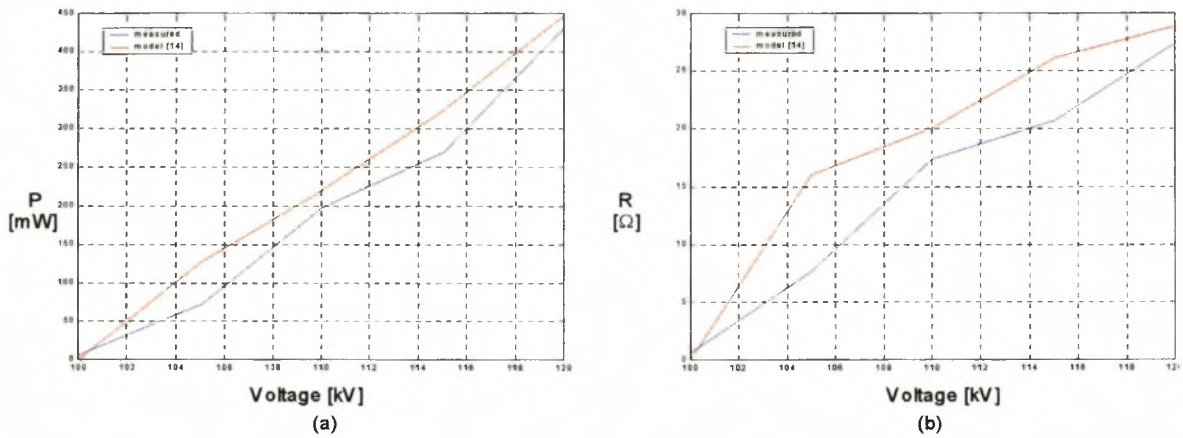

Figure 4.22: The (a) average power loss and (b) series loss resistance in the corona cage extracted from the measured and simulated Q-V curves for a peak applied voltage of between 100 kV and 120 kV. (R = 300 mm, a = 8 mm).

Finally the average power loss in the corona cage is calculated by calculating the area inside the Q-V curve. The series loss resistance is then calculated using equation 4.4. The average power loss and series loss resistance values extracted from the model in [14] and from measured Q-V curves are plotted against the peak applied voltage for the voltage range 100 kV to 120 kV in figure 4.22.

4.5 Conclusions

- A transform method is required to transform corona cage RI current measurements to equivalent RI current flow on the conductors of a proposed transmission line design. The transform most often used in the literature is the generation function method.

- The generation function transform method requires that a geometry-independent corona excitation element be de-embedded from the corona cage and transmission line RI current measurements and predictions. Corona and frequency-dependent effects must therefore be modelled for these systems so that they can be removed.

- Corona and frequency-dependent effects can be modelled either in the frequency domain or in the time domain. The corona effects are non-linear and can be included as non-linear corona branch elements in the model or alternatively they can be approximated by linear elements. The linear-element model simulations are more memory and time efficient but are less accurate. The frequency-dependent effects are significant only at high frequencies. Models that exclude these effects are therefore called low-frequency models in this thesis. Since the only time domain code available is a FDTD code, a non-linear-element model should be used in this case.

Stellenbosch University http://scholar.sun.ac.za/

- The corona excitation elements are included into the corona cage and transmission line models as series voltage sources.

- The corona branch elements which model the non-linear corona effects can be extracted from the Q-V relationship of the system. Since the Q-V relationship cannot be measured in the proposed transmission line design it must be predicted using Q-V models. Mathematical Q-V models require an iterative solution to the non-linear equation derived from the system. Physics-based models derive linear equations that do not require an iterative solution and are therefore more time efficient. The Q-V curve exhibits hysteresis if the applied source voltage exceeds the critical level. The dynamic corona capacitance then equals the gradient of the Q-V curve and the shunt conductance is calculated from the total power loss which is obtained by calculating the area inside the Q-V curve.

- Only low-frequency corona cage transmission line parameters were extracted in chapter 3. The corona cage and transmission line models in this chapter will therefore also be limited to low frequencies (i.e. $f < 30$ MHz). Frequency-dependent effects can be ignored at these frequencies.

- The Q-V relationship of the corona cage can be measured by integrating the current flow between the corona cage and the grounding structure either using a shunt capacitance or by numerical integration using Matlab. Numerical integration avoids the integration error caused by the non-ideal shunt RC integrator. The Q-V curve plot can be displayed in near real-time by downloading the measured charge and voltage waveforms through a GPIB port.

- The Q-V relationship displays hysteresis only when the applied voltage exceeds the inception level. The Q-V curve measurement method can therefore be used to measure the inception level of a corona cage.

- The validity of the quasi-cylindrical field assumption made in the Q-V models should be investigated for compact multi-conductor transmission lines. A more complex model (i.e. one that does not assume a quasi-cylindrical electric field distribution) may have to be extracted.

- The capacitance between the corona sheath and the corona cage and the shunt conductive losses increase significantly when the corona inception level is exceeded.

4.6 References

[1] F.M. Tesche, M.V. Ianoz and T. Karlsson, *EMC Analysis Methods and Computational Models*, John Wiley & Sons, Inc., 1997.

[2] E.W. Boehne, Discussion to paper, "Attenuation and Successive Reflections of Travelling Waves", JC Dowell, Transactions of the American Institute of Electrical Engineers, Vol. 50, June 1931.

[3] H.M. Kudyan and C.H. Shih, "A Nonlinear Circuit Model for Transmission Lines in Corona", IEEE Transactions on Power Apparatus and Systems, Vol. PAS-100, No. 3, March 1981, pp. 1420 - 1430.

Stellenbosch University http://scholar.sun.ac.za/

[4] S. Carneiro, Jr. and J.R. Marti, "Evaluation of Corona and Line Models in Electromagnetic Transients Simulations", IEEE Transactions on Power Delivery, Vol. 6, No. 1, January 1991, pp.334 - 342.

[5] J.R. Marti and J. Lin, "Suppression of numerical oscillations in the EMTP", Paper88 SM 732-0, IEEE Summer Power Meeting, July 1988.

[6] P. Sarma Maruvada, D.H. Nguyen and H. Hamadani-Zadeh, "Studies on Modelling Corona Attenuation of Dynamic Overvoltages", IEEE Transactions on Power Delivery, Vol. 4, No. 2, April 1989, pp.1441 - 1449.

[7] M. Milhailescu-Suliciu and I. Suliciu, "A Rate Type Constitutive Equation for the Description of the Corona Effect", IEEE Transactions on Power Apparatus and Systems, Vol. PAS-100, No. 8, August 1981, pp.3681 - 3685.

[8] X. Li, O.P. Malik and Z. Zhoa, "Computation of Transmission Line Transients Including Corona Effects", IEEE Transactions on Power Delivery, Vol. 4, No. 3, July 1989, pp.1816 - 1822.

[9] A. Inoue, "Propagation Analysis of Overvoltage Surges with Corona Based Upon Charge Versus Voltage Curve", IEEE Transactions on Power Apparatus and Systems, Vol. PAS-104, No. 3, March 1985, pp.655 - 660.

[10] N.L. Ovick and G.L. Kusic, "Including Corona Effects For Travelling Waves on Transmission Lines", IEEE Transaction on Power Apparatus and Systems, Vol. PAS-103, No. 12, December 1984.

[11] L.V. Bewley, *Travelling Waves on Transmission Systems*, Dover Publications , Inc., 1963.

[12] P.C. Magnusson, *Transmission Lines and Wave propagation*, Allyn and Bacon, 1970.

[13] C. Gary, A. Timotin and D. Cristescu, "Prediction of Surge Propagation Influenced by Corona and Skin Effect", IEE proceedings, Vol. 130, Pt. A, No. 5, July 1983.

[14] J.J. Clade, C.H. Gary and C.A. LeFevre, "Calculation of Corona Losses Beyond the Critical Gradient in Alternating Voltage", IEEE Transactions on Power Apparatus and Systems, Vol. PAS-88, No. 5, May 1969.

[15] V. Cooray, "Charge and Voltage Characteristics of Corona Discharges in a Coaxial Geometry", IEEE Transactions on Dielectrics and Electrical Insulation, Vol. 7 No. 6, December 2000, pp. 734 - 743.

[16] C. de Jesus and M.T. Correia de Barros, "Modelling of Corona Dynamics for Surge Propagation Studies", IEEE Transactions on Power Delivery, Vol. 9, No. 3, July 1994, pp.1564 - 1569.

[17] X. Li, O.P. Malik and Z. Zhao, "A Practical Model of Corona for Calculation of transients on Transmission Lines", IEEE Transactions on Power Delivery, Vol. 4, No. 2, April 1989, pp.1145 - 1151.

[18] A. Semlyen and H. Wei-Gang, "Corona Modelling for the Calculation of Transients on Transmission Lines", IEEE Transactions on Power Delivery, Vol. PWRD-1, No. 3, July 1986, pp.228 - 235.

[19] L.M. Wedepohl, *The Theory of Natural Modes in Multi-Conductor Transmission Systems*, Unpublished lecture notes, Westband, British Columbia, Canada, 10 January 1999.

[20] J van der Merwe, "Uniform Multiconductor Transmission Lines Above a Dissipative Earth: Direct FDTD Analysis and Experimental Validation", PhD Dissertation, University of Stellenbosch, October 1999.

Stellenbosch University http://scholar.sun.ac.za/

Chapter 5

Small Corona Cage RI Noise Measurement

5.1 Introduction

The experimental setup needed to measure the required electrical corona phenomena was investigated and a small laboratory corona cage was designed in chapter 3. The electrical environment of the laboratory was also investigated and modified to improve the dynamic range of the measurement system. This system was then modelled in chapter 4 so that the measurements can be correctly interpreted. Accurate corona cage RI noise measurements can now be made and interpreted. These measurements and interpretations are presented in this chapter.

There are various measurement devices that can be used to measure RI noise in the small corona cage. These devices can be classified as time domain and frequency domain devices. The frequency domain devices can further be classified as wideband and narrowband devices. Each device has specific advantages and disadvantages. In this chapter, the measurement method most appropriate to making the required small corona cage RI noise measurements must be identified. This method must also be related to the measurement methods used in the literature so that the results can be compared to reported measurements. If the measurement methods differ from those in the literature, an objective comparison of the methods must be made and a correlation between the methods must be found.

A literature survey of the various measurement techniques that have been used to measure corona cage RI noise is presented in section 5.2. Time domain oscilloscope measurements are then discussed in section 5.4. Sections 5.5 and 5.6 investigate frequency domain EMI receiver and spectrum analyser measurements respectively. It was found in chapters 2 and 4 that it is necessary to extract the statistical properties of the corona discharges since they will greatly influence the measured RI level. The extraction of these statistical properties is considered in section 5.7. Finally, the most important conclusions are summarised in section 5.8.

5.2 Literature Survey

The various corona cage RI noise measurement techniques are classified as time domain and frequency domain techniques. A distinction is also made between narrowband and wideband measurements. Various corona measurements that are not directly related to the research in this thesis will be included in this section since these techniques will be adapted for the specific metrology needs of subsequent sections.

5.2.1 Time Domain Measurements

Time domain measurement of corona discharges using an oscilloscope or fast sampling card has been exclusively used for partial discharge studies in the literature reviewed in this section. In these studies it is important to accurately record the exact pulse shape so that a wideband

Stellenbosch University http://scholar.sun.ac.za/

frequency spectrum can be extracted from the measurement. This ensures that pulses can be classified according to certain characteristic pulse properties. Such time domain measurements are described in [1] and [2]. Most of the partial discharge measurements are made in the frequency range DC to 10 MHz although the measurements in [1] are made up to 1 GHz. It is also noted in both [1] and [2] that the frequency spectrum is significantly affected by the repetition rate of the discharge pulses (i.e. the potential superposition of pulses in a sampled time sequence). Time domain measurements can be used to extract the frequency spectrum of an individual RI pulse. This is however only possible if the individual pulse can be isolated so that the effect of pulse repetition rate is excluded.

5.2.2 Frequency Domain Measurements

Frequency domain RI noise measurement devices are considered in this section. These devices are classified as either narrowband and wideband.

5.2.2.1 Radio Noise Meters

It is noted in [3] that the main research emphasis has historically been focussed on investigating the effect of radiated RI noise on radio and TV reception. The measurement device which best correlates the RI noise level to the human annoyance factor for radio and TV reception was found to be the radio noise meter equipped with a quasi-peak (QP) detector. The QP detector is therefore historically the most popular choice of RI noise measurement device. The average detector is also often used to make radiated RI disturbance measurements for TV and radio interference purposes.

The radio noise meter is a narrowband device and measurements are therefore made at a single frequency (i.e. the meter's centre frequency). A centre frequency of 360 kHz was used in [3]. The reference frequency for these measurements was however 1 MHz and the measurements had to be scaled up to this frequency. The 1 MHz centre frequency is the American RI noise measurement standard. This standard requires further that the bandwidth of the QP detector is in accordance with the ANSI standard. Similarly, the measurements in [4], made at 835 kHz for practical reasons, had to be scaled up to an equivalent 1 MHz measurement. The European RI measurement standard requires that the QP detector has a centre frequency of 500 kHz and a CISPR bandwidth of 9 kHz at this frequency (see [5]). The required frequency response of the radio noise meter and the various detector circuits is presented in [6].

It is noted in [7] that the analytical methods used to predict RI noise generation and propagation consider only the energy and power of the noise signals in order to simplify their mathematical development. The quantities used in and extracted from these methods are therefore RMS values. It is further noted that there is no empirical correlation between measured QP and RMS values. Analytical and numerical conversion techniques are investigated in [8] and [9] respectively. It is noted in [8] that the QP meter has historically been used to provide a single parameter, indicative of the relative degradation that a given noise source would present to a commercial AM receiver. QP detectors use a RC weighting function. The detector output is therefore dependent on the amplitude repetition rate of the pulses. The analytical conversion in [8] therefore requires that the amplitude distribution function is known and the repetition time is assumed to be constant. The conversion is investigated in [9] using digital computer simulations. This conversion does not assume a constant repetition rate as was the case in [8] and therefore should more accurately predict the actual RMS value from a QP measurement.

Stellenbosch University http://scholar.sun.ac.za/

5.2.2.2 The Spectrum Analyser

Wideband RI noise measurements are often required in corona studies. Radio noise meters are only capable of making a RI measurement at a single frequency (i.e. the centre frequency of the meter). A collection of noise meters with various centre frequencies is therefore required to cover a wide frequency band. Such a measurement would only give a rough view of the actual frequency spectrum if a practical number of meters were used and would require that each meter was calibrated within a specified accuracy. Noise meters can therefore not be used to make accurate, meaningful wideband measurements.

Spectrum analysers offer a more practical and accurate alternative to noise meters when making wideband measurements. A comparison between the spectrum analyser and radio noise meter is presented in [10]. In this paper the spectrum analyser was used to make measurements of gap discharges in the frequency range 10 kHz to 1 GHz. Measurement results from the radio noise meters and the spectrum analyser prove that the spectrum analyser can be used to make accurate measurements of the RI noise. The measurement technique and device settings used in this investigation are however not documented. Spectrum analyser RI noise measurements are also made in the bandwidth 15 kHz to 10 GHz in [11].

5.2.2.3 The EMI Receiver

The EMI receiver is a narrowband radio noise meter with various detectors and a centre frequency that can be swept through a wide range of frequency points. The device therefore offers the accuracy of a narrowband radio noise meter with the spectrum analyser's ability to make accurate, meaningful wideband measurements. The detectors typically included in an EMI receiver are the QP, peak, RMS and average detectors. The EMI receiver was used in [12] to measure both conducted and radiated RI disturbances. Peak, QP, average (also known as field intensity) and RMS detectors were used in this paper. Two intermediate frequency (IF) receiver bandwidths of 1 MHz and 100 kHz were chosen for the measurements. It is suggested in this paper that conducted corona can be measured up to 200 MHz in foul weather.

5.2.3 Extraction of Statistical Properties

The correlation between QP measurements and corona pulse characteristics, such as repetition rate and amplitude, is investigated in [13]. This investigation requires that the RI pulse amplitude and repetition rate are known. These pulse properties are measured by sampling the time domain RI current waveform. Since the RI pulses are random in both time and amplitude, the repetition rate and pulse amplitude must be defined statistically. The statistical properties of RI noise are extracted in this paper by analysing a sampled time-domain RI noise waveform that consists of more than 150 pulses in two consecutive periods of the 50 Hz source waveform. The results indicate that the pulse amplitude probability distribution is Gaussian and that the pulse repetition rate probability distribution is Poissonian.

Stellenbosch University http://scholar.sun.ac.za/

5.3 Source Voltage Harmonics

It was concluded in section 2.8 that the AC source voltage has a significant effect on the electrical properties of the corona modes as well as the transition between the various corona modes. The main objective of this thesis, defined in section 1.3, is to study and model specific macroscopic corona phenomena under 50 Hz AC conditions. The source voltage should therefore ideally be a 50 Hz sinusoidal waveform with negligible harmonic components (i.e. a "clean" source voltage). The presence of significant harmonic components in the source voltage will affect the basic corona process and therefore also the associated macroscopic phenomena. Corona measurements made in such a system cannot be compared to equivalent measurements made in a system with a clean source voltage.

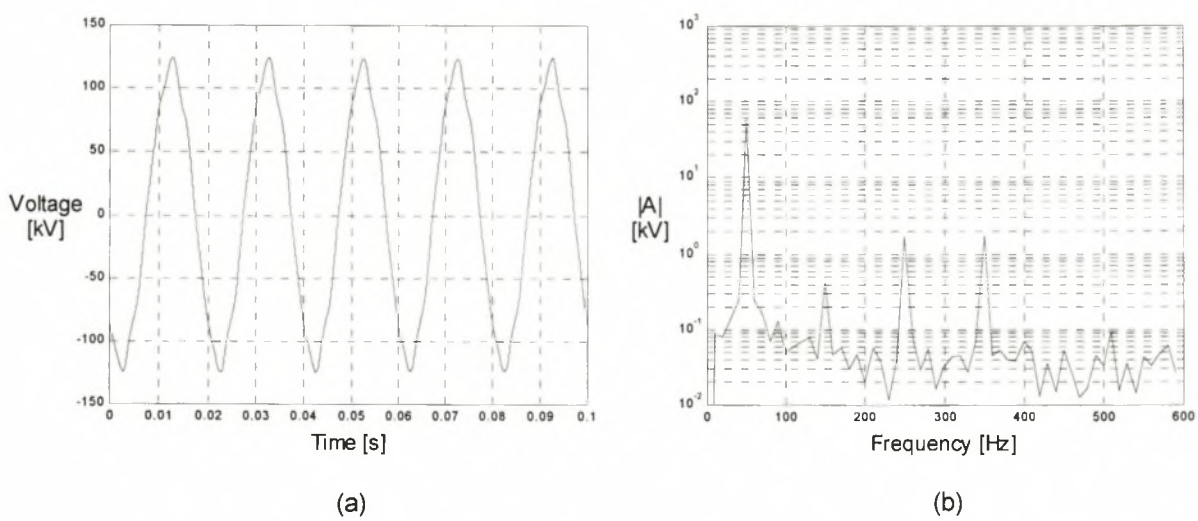

Figure 5.1: The (a) measured time domain and (b) calculated frequency domain plot of the applied source voltage used in the experimental setup described in chapter 3.

The source voltage of the experimental setup described in chapter 3 is measured off the capacitive voltage divider. This shunt capacitive measurement device is placed between the source voltage input to the corona cage and the laboratory grounding structure. It is therefore a low impedance path to ground potential at high frequencies. As a result, the measured voltage has considerable high-frequency noise. This is removed by filtering the measured voltage computationally using Matlab. The filter used was an ideal lowpass filter with a cut-off frequency of 1 kHz. This cut-off frequency is chosen so that all significant harmonic components are unaffected by the filtering process. The filtered source voltage is plotted in the time domain in figure 5.1 (a). The distortion of the 50 Hz waveform by the harmonic components is clearly visible in this plot. The frequency spectrum of the source voltage is calculated using Matlab and is plotted in figure 5.1 (b). This plot indicates that the magnitude of the 3rd, 5th and 7th harmonic components is significant.

Stellenbosch University http://scholar.sun.ac.za/

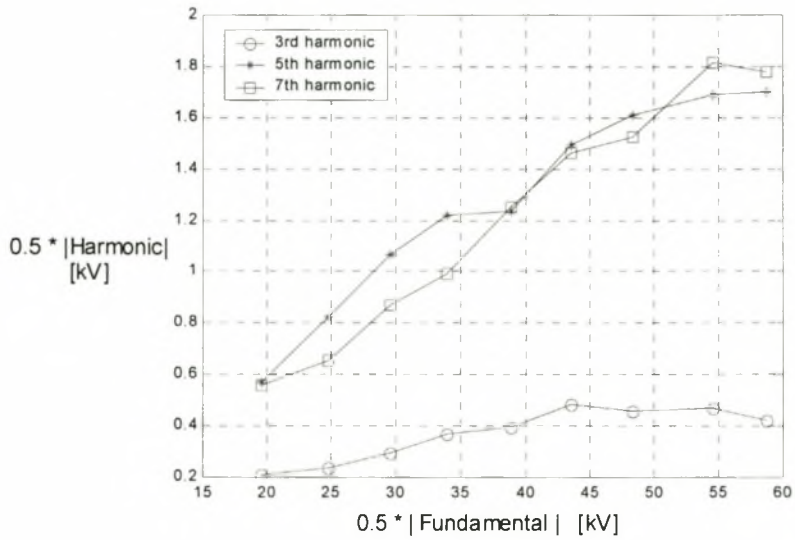

Figure 5.2: The relationship between the fundamental amplitude and the amplitude of the 3rd, 5th and 7th harmonic components.

It is evident in figure 5.2 that the relationship between the fundamental amplitude and the harmonic amplitudes is not linear (see figure 5.2). Corona measurements made at a certain fundamental amplitude cannot therefore be accurately compared to an equivalent measurement made at another fundamental amplitude since the harmonic amplitude will affect the corona properties and is not linearly related to the fundamental amplitude. Equivalent measurements at various fundamental amplitudes must be compared in this chapter. Considerable effort was made to remove the harmonic components but this effort was unsuccessful. It will therefore be assumed that the effect of the non-linear relationship in figure 5.2 is small and will therefore be ignored. The validity of this assumption should then be confirmed or alternatively the harmonics should be removed in future research.

The variation of the harmonic amplitude with time is also investigated by measuring the harmonic amplitudes at the beginning and at the end of each measurement sequence. It was found that the harmonic amplitudes did not vary with respect to time for a constant fundamental amplitude in all the measurements presented in this thesis.

5.4 Time Domain Oscilloscope Measurements

It was found in the literature survey in section 5.2 that the wideband characteristic pulse properties of individual RI pulses can be extracted from time domain oscilloscope measurements. Such measurements require that the exact pulse shape is accurately recorded in a calibrated system. The measurement bandwidth is therefore determined by the calibration bandwidth and the bandwidth of the oscilloscope. The extraction of the frequency spectrum of an individual RI pulse also requires that the individual pulse must be isolated so that the effect of pulse repetition rate is excluded from the calculation of the frequency spectrum. The method used to meet these measurement requirements and extract the individual frequency spectra using an oscilloscope is discussed in this section.

Stellenbosch University http://scholar.sun.ac.za/

5.4.1 Oscilloscope Basics

The oscilloscope used throughout the thesis for time domain RI current measurement is the TDS3032 digital phosphor oscilloscope. It is a two channel, 2.5 Gs/s oscilloscope with a 300MHz bandwidth. The oscilloscope has a record length of 10 kByte.

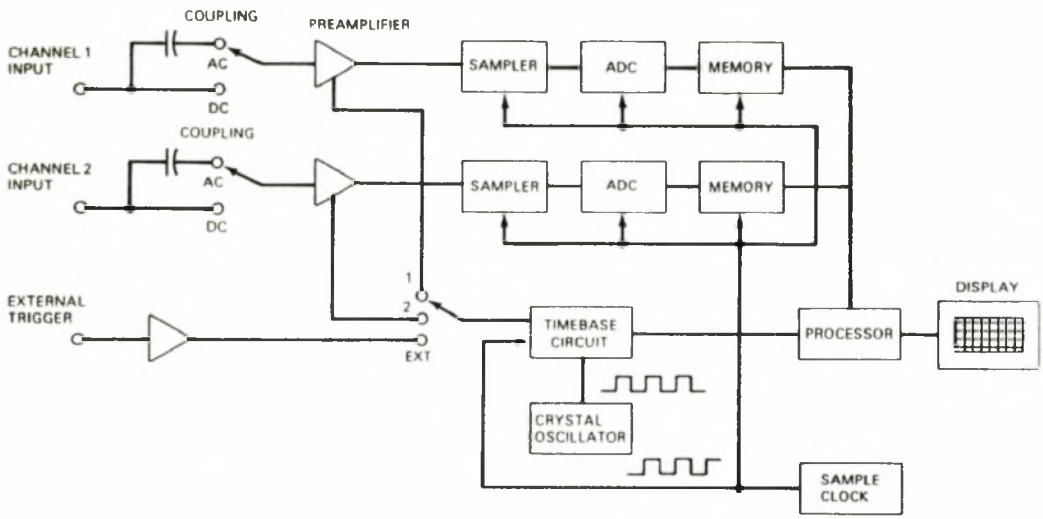

Figure 5.3: Block diagram of a typical digitizing oscilloscope [14].

A block diagram of a typical digitizing oscilloscope is given in figure 5.3. The TDS3032 has a 9-bit ADC providing a vertical sensitivity of 1 mV and a vertical accuracy of 2 %. The oscilloscope will therefore be able to accurately record and display any disturbance at its input that is above the noise floor of the measurement system.

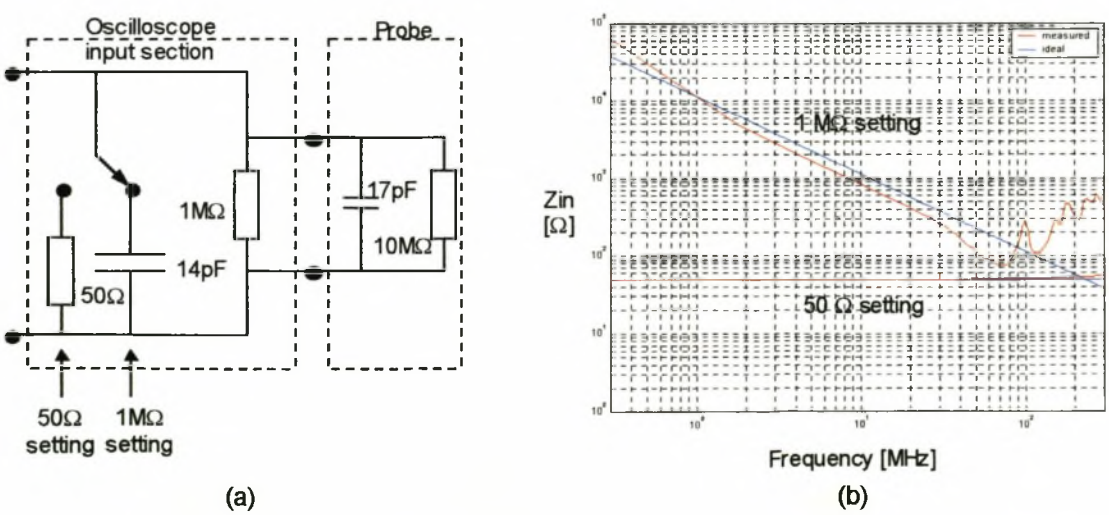

Figure 5.4: (a) Schematic diagram of the input section and (b) the theoretical and measured input impedance of the TDS3032 digital oscilloscope.

The TDS3032 has two input impedance settings. A schematic diagram of the input section of the oscilloscope with a probe attached is illustrated in figure 5.4 (a). The 1 MΩ oscilloscope setting switches a 14 pF capacitance in shunt with the 1 MΩ input impedance while the 50 Ω setting switches a 50 Ω resistance in shunt with the same 1 MΩ impedance. The theoretical and

Stellenbosch University http://scholar.sun.ac.za/

measured input impedance of both oscilloscope settings is plotted in figure 5.4 (b). This plot indicates that the 1 MΩ oscilloscope setting will load the measurement circuit at frequencies above 1 MHz. The experimental setup presented in chapter 3 assumed that the measurement device has a 50Ω input impedance across the measured frequency band. The RI noise measurement is therefore measured directly from the coaxial measurement cable if the 50Ω setting is used. If the 1 MΩ setting is used, the RI noise is measured across a shunt 50Ω terminating impedance placed at the measurement end of the coaxial cable. This measurement setup will however cause reflections at the measurement point at high frequencies due to the loading effect of the oscilloscope input impedance. The measurement calibration derived in chapter 4 for a 50Ω termination impedance will also have to be modified in this case. The 50Ω setting will therefore be used for wideband RI noise measurements. The maximum RMS voltage that can be applied across the 1 MΩ oscilloscope input resistor is 150 V. The maximum RI pulse magnitude is less than 150 V and the pulse duration is short. The RI measurement will therefore not damage the oscilloscope provided flash-over does not occur. To ensure that flash-over does not occur, all corona cage RI noise measurements are made at an applied voltage below 125 kV.

It is evident in figure 5.3 that the sampler, ADC and memory components of the oscilloscope are all controlled by the sample clock. The frequency of this sample clock is determined by the selected time scale. For the TDS3032, the time scale ranges from 1 ns/div to 10 s/div. While the bandwidth of the TDS3032 is rated as 300 MHz, this specification is only valid when the input signal is sampled at the maximum sample rate (i.e. 2.5 Gs/s for the 1 ns/div time scale setting). If a lower sample rate is selected, then the bandwidth will be reduced. Sampling theory states that the highest sampled frequency must be lower than half the sample rate (i.e. the Nyquist frequency). If this Nyquist frequency is exceeded then aliasing will occur. Aliasing will result in an inaccurate account of the RI pulse frequency spectrum and must be avoided. To record and display a fast transient pulse at its input, a digital oscilloscope uses real-time sampling. The sampling system continuously acquires samples uniformly spaced in time. The oscilloscope then displays an equal number of sampled points before and after the trigger event. The disadvantage of real-time sampling is that the waveform must first be reconstructed from the sample points using an interpolation technique. The Nyquist sampling criterion is therefore no longer valid. For the TDS3032, the relationship between the bandwidth (BW) and the sample rate (f_s) is:

$$BW = f_s \Big/ \left(\frac{(f_s)_{rated}}{(BW)_{rated}} \right) \approx \frac{f_s}{8.33} \tag{5.1}$$

To prevent aliasing of the input signal and therefore the corruption of the measured frequency spectrum, the highest frequency component of the RI pulse at the oscilloscope input must be lower than the sample rate divided by 8.33. If higher frequency components are present then the input signal must be filtered so that these components are attenuated below the noise floor.

5.4.2 Triggering on Random Corona Pulses

The oscilloscope timebase circuit (see figure 5.3) determines the horizontal position of the trigger event with respect to the sample time using a crystal oscillator. It therefore determines what is displayed on the screen. The input of the oscilloscope is connected to the input of the trigger circuit via a coupling circuit. Besides the standard AC and DC coupling circuits, the TDS3032 also offers the option of a series high-pass or a low-pass filter. The triggering circuit can be set

Stellenbosch University http://scholar.sun.ac.za/

to trigger on a specified level and either a rising or falling slope of the input voltage. Lastly, the trigger circuit can be triggered on either of the two input ports (i.e. both traces are triggered simultaneously by the trigger setting on one of the channels).

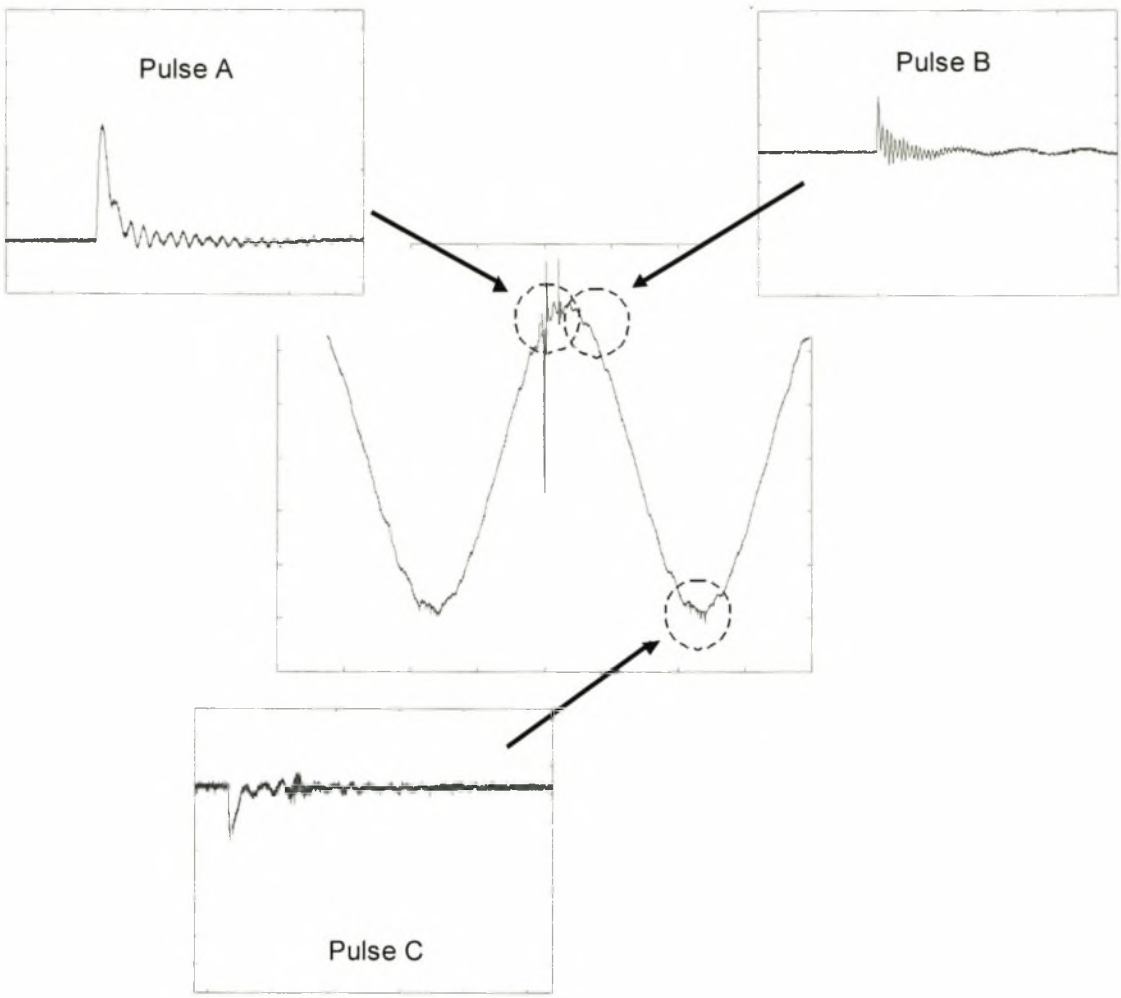

Figure 5.5: The measured RI noise waveform with the source harmonic components removed showing the position and shape of various corona pulses that make up the AC corona modes.

An important requirement for the RI measurements in this thesis is the identification of the various corona modes. The frequency spectrum of each distinctive corona mode can then be calculated and the relationship between the source voltage magnitude and phase and the frequency spectrum of the RI noise can be determined. This is essential if an accurate RI excitation source is to be extracted from the corona cage measurements for the transmission line model with corona effects. A method of triggering the oscilloscope on the random RI noise pulses and specifically on the pulses of a certain AC corona mode must therefore be defined. A measured corona cage RI noise waveform is plotted in figure 5.5. It shows the distribution of the RI pulses on the source waveform. Examples of the various RI pulses that relate to the various AC corona modes are also plotted in this figure. It should be noted that the 50 Hz source voltage component is emphasised in the plot to illustrate the position of the RI noise pulses with respect to the phase of the source voltage.

Ideally, the oscilloscope should be triggered on a specific phase of the source voltage. This triggering method will be referred to in this thesis as phase triggering. The corona cage RI

Stellenbosch University http://scholar.sun.ac.za/

measurement system was modelled in figure 3.10. It was found in this chapter that the source voltage component that is capacitively coupled onto the corona cage is very small. It is therefore not possible to trigger on a specific phase of the source voltage component of the RI waveform measured off the corona cage. This is because the trigger circuit needs a signal that is significantly larger than the noise floor of the measurement system in order to accurately trigger on a specific level of the input voltage. An alternative triggering method is to adjust the trigger level with the high-pass filter trigger-coupling setting active. The low-frequency source voltage components will therefore be removed from the input to the trigger circuit and the oscilloscope will be triggered on the rising edge of a RI noise pulse that exceeds the specified trigger level. This triggering method will be referred to as level triggering in this thesis. Since real-time sampling ensures that pre-trigger data is also displayed, the entire RI pulse will be displayed and not just the section after the trigger event.

Level triggering will be used in this thesis to determine at what source voltage specific corona modes occur. This is done by increasing the source voltage in discrete voltage steps and then setting the trigger level to a value at which only the largest RI pulses cause a trigger event. The disadvantage of level triggering is that only the largest corona mode at a specific source voltage will be observed. For example, both pulse A and pulse B in figure 5.3 will occur at a specific source voltage magnitude but only pulse A will be captured using level triggering. It was noted in chapter 4 that the corona cage RI measurement system was resonant at various frequencies. Fast RI transients induced on the corona cage will therefore have large resonant components. This can be seen on pulse A in figure 5.3. The resonant oscillations of pulse A generate a negative voltage larger than the maximum amplitude of pulse C. Pulse A will therefore exceed the negative trigger level used to capture pulse C. If level triggering were used on the waveform in figure 5.3, only pulse A would be observed. The properties of the corona modes under AC conditions will be affected by the appearance of other corona modes. Level triggering cannot be used to observe these changes. Phase triggering must therefore be used.

Phase triggering is achieved in this thesis by placing the large source voltage measurement made off the capacitive voltage divider (see section 5.3) onto the second, unused oscilloscope channel. The RI waveform on the first channel can then be triggered at a specific phase of the source voltage. The high-frequency noise present on the capacitive voltage divider measurement is removed using the low-pass filter setting of the trigger's coupling circuit. The trigger level and slope-type settings are then used to locate a specific phase point on the source voltage. Unlike the level triggering method, the phase triggering will not capture a RI pulse on each trigger event and it will also not capture the largest pulse for that specific corona mode. Numerous RI pulses should therefore be measured to obtain the average mode properties. Phase triggering will be used in this thesis to determine the RI pulse frequency spectra of the various corona modes.

5.4.3 Measurement Results

The first measurements made in this section will be to determine at what source voltage the various corona modes occur. Level triggering will therefore be used for these measurements. Once the significant voltage levels have been identified, phase triggering will be used to identify the various positive and negative corona modes.

It was found in chapter 2 that the initial positive corona modes are the onset pulse mode and the Hermstein's glow corona mode. It was also noted in this chapter that under AC conditions the onset pulse formation is inhibited and transition to Hermstein's glow is almost immediate. There

Stellenbosch University http://scholar.sun.ac.za/

will therefore be few onset pulses and those that are present will induce small RI currents on the corona cage. The Hermstein's glow corona will induce a DC voltage with a small high-frequency ripple in the Megahertz range on the corona cage. The initial corona mode in the negative half-cycle is the Trichel pulse mode. At low applied voltage the amplitude and repetition rate of these pulses will be low but will not be inhibited by the AC source voltage. The repetition rate of these pulses will then increase as the applied voltage is increased. When the voltage is increased above the inception level, continuous corona will appear. The only continuous corona mode present in the positive half-cycle is the positive streamer mode. Initially the positive streamers will have a low repetition rate and will be more sporadic with respect to time. The RI currents induced on the corona cage will be small in amplitude. The positive streamers will then increase rapidly in both amplitude and repetition rate as the source voltage is increased and the RI current induced on the corona cage will be less sporadic (i.e. it will become stable).

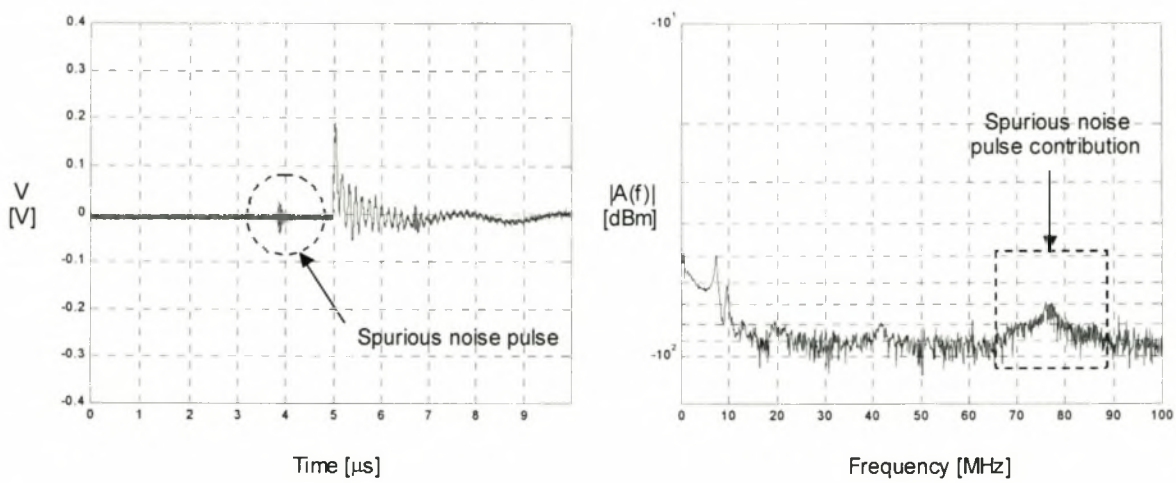

[triggering: level, trigger coupling: low-frequency reject, trigger level: +100mV, sample rate: 1Gs/s]

Figure 5.6 The (a) measured time domain and (b) calculated frequency domain plot of a RI pulse observed at 90 kV (peak) using level triggering.

It was found in chapter 3 that the transfer impedance of the measurement loop was significantly reduced by shielding the coaxial measurement cable and the measurement device. It was however also found that the source loop was susceptible to interference noise and that this susceptibility could only be reduced in a small frequency band with a lumped element LC filter. This was because of the large voltage applied to the high voltage side of the source loop. The result of this high transfer impedance is spurious noise pulses that appear in the time domain oscilloscope measurements made in this section. These pulses have a maximum amplitude of about 50 mV, measured across the 50 Ω input impedance of the oscilloscope. They are also intermittent with a high repetition rate and they significantly reduce the dynamic range of the time domain measurement system.

A few small positive streamers were observed in the voltage range 90 kV to 100 kV. One such RI pulse is plotted in figure 5.6 (a). The trigger level used to trigger on this event was +100 mV. The trigger level cannot be reduced below 50 mV due to the spurious noise pulses. Since the smaller corona modes are expected to be at least an order smaller than the initial positive streamers (see section 2.5), it can be concluded that the smaller corona modes cannot be observed in the experimental setup used in this thesis due to the noise susceptibility of the source loop. The

Stellenbosch University http://scholar.sun.ac.za/

calculated frequency spectrum of the measured RI pulse is plotted in figure 5.6 (b). It is evident in this plot that the bandwidth of the spurious noise pulses is between 70 MHz and 90 MHz. It is also evident that the bandwidth of the RI noise pulse is 40 MHz for the experimental setup described in chapter 3. The spurious noise pulses can therefore be removed by a band-reject filter without affecting the frequency spectrum of the measured RI pulses. This will enable the use of a trigger level below 50 mV in order to observe the smaller corona modes below 100 kV. Since the positive streamers observed below 100 kV (e.g. the RI pulse in figure 5.6) are small in magnitude and are isolated events, they do not constitute a continuous corona event and are therefore pre-inception pulses.

Various resonances are visible in the plots in figure 5.6. A small resonance is present at 40 MHz. The resonant frequency of the corona cage measurement system was measured in chapter 4 at 38MHz (see figure 4.14). The slight difference in frequency could be due to the non-uniform corona cage-shield cage transmission line. A larger resonance appears at 7.35 MHz. This resonance is not predicted by the low-frequency model of the measurement system presented in chapter 4. A more accurate model is therefore required.

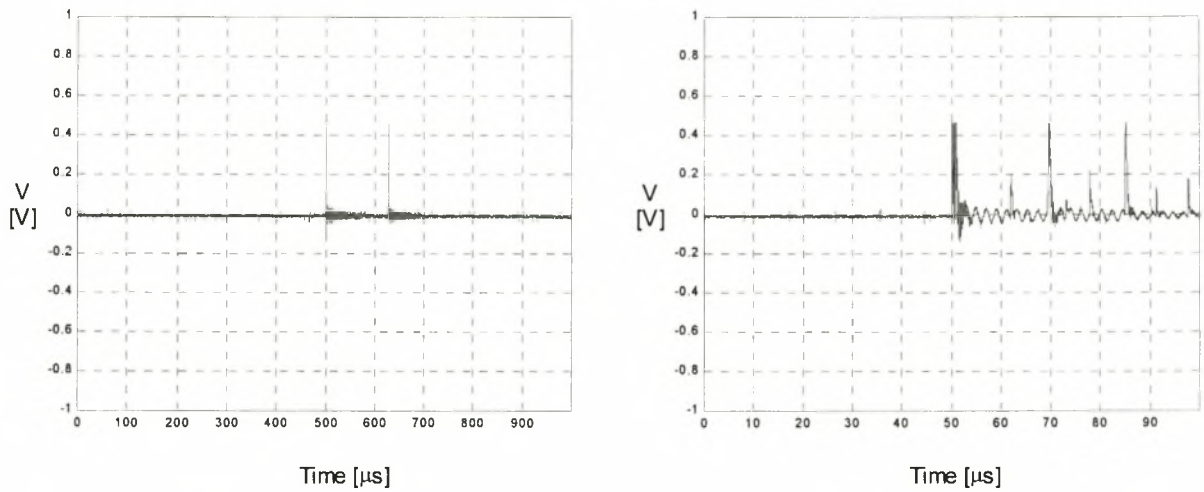

[triggering: level, trigger coupling: low-frequency reject, trigger level: +100mV, sample rate: (a)1.2Ms/s (b)12Ms/s]

Figure 5.7: Time domain RI waveforms measured at (a) 100 kV and (b) 110 kV using level triggering indicating the repetitive pulse sequences at these applied voltages.

The intermittent positive streamer pulses become more numerous and eventually become repetitive as the voltage is increased above the inception level (i.e. 100 kV). Just above the inception level, the pulses occur mainly as single pulses or in groups of two pulses as shown in figure 5.7 (a). As the voltage is increased above the inception level, the pulses become larger in magnitude and the pulse trains contain more pulses, as shown in figure 5.7 (b), but the repetition rate of these pulse trains remains irregular. The repetition rate of the pulses in the pulse trains in figure 5.7 decreases from 160 μs to about 16 μs as the voltage is increased from 100 kV to 110kV.

Stellenbosch University http://scholar.sun.ac.za/

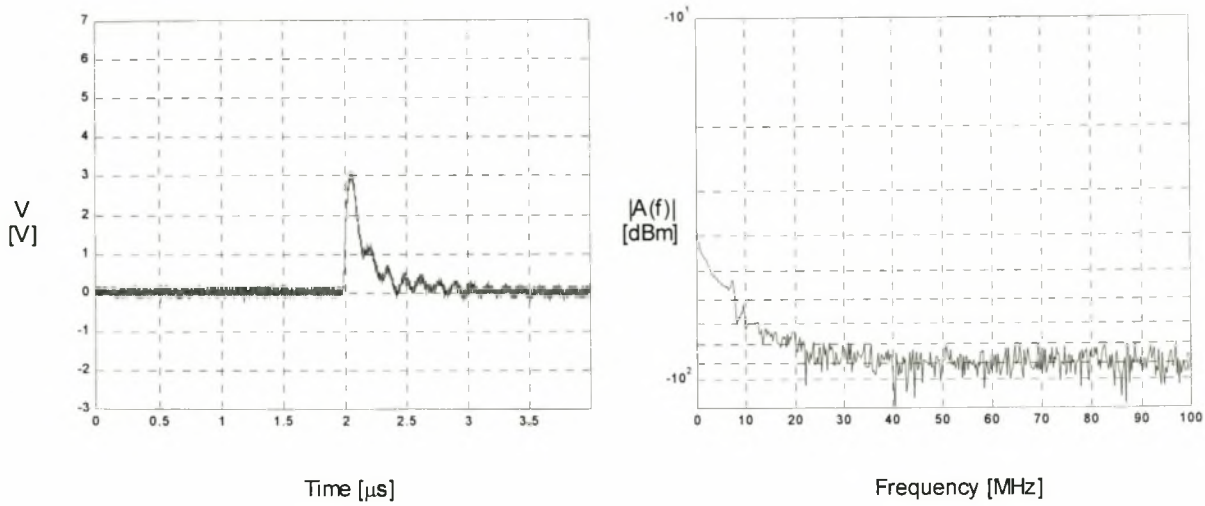

[triggering: level, trigger coupling: low-frequency reject, trigger level: +2V, sample rate: 2.5Gs/s]

Figure 5.8 The (a) measured time domain and (b) calculated frequency domain plot of a RI pulse observed at 110 kV (peak) using level triggering.

The magnitude of the positive streamers increases with increasing applied voltage. The trigger level is therefore increased to + 2 V. An example of a positive streamer pulse capture with this trigger level is plotted in figure 5.8. The 7.35 MHz resonance remains at the same frequency but is less prominent. It does however cause oscillation below the zero volt axis. As a result, a negative trigger level cannot be used to observe Trichel pulses.

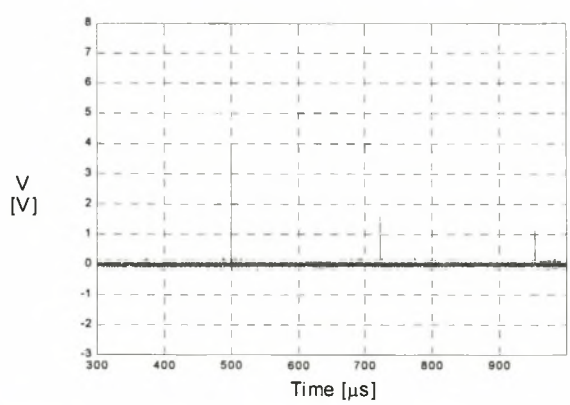

[triggering: level, trigger coupling: low-frequency reject, trigger level: +2V, sample rate: 1.2Ms/s]

Figure 5.9: A time domain RI waveform measured at 120 kV using level triggering.

The pulse trains become more regular with respect to time as the applied voltage is increased above 115 kV. This is illustrated with the RI waveform, measured at 120 kV, which is plotted in figure 5.9.

The pulse magnitude also increases steadily with increasing voltage. The maximum pulse amplitude recorded at 120 kV is 7 V, captured with the trigger level set at + 6 V.

Stellenbosch University http://scholar.sun.ac.za/

Voltage Range	Trigger Level	RI Pulse Characteristics
90 kV - 100 kV	+100 mV	A few isolated, intermittent positive streamers of small magnitude
100 kV - 115 kV	+100 mV to +2 V	Increased number of repetitive, irregularly spaced positive streamers of increasing magnitude
115 kV - 120 kV	+2 V to +6 V	Numerous, repetitive, regularly spaced positive streamers of large magnitude.

Table 5.1: A qualitative summary of the voltage dependence of the RI pulse characteristics extracted from level triggered oscilloscope measurements.

From the measurement results presented thus far in this section it can be concluded that the RI pulse characteristics of the smaller positive corona modes and of the negative Trichel pulse mode cannot be observed using level triggering due to resonances induced by the RI pulses and spurious noise pulses. Phase triggering must therefore be used. The source voltage, measured off the capacitive voltage divider, is applied to the second oscilloscope channel and the trigger-level and trigger-slope settings are selected so that the RI current at the input of the other oscilloscope channel is triggered on a specific phase of the source voltage waveform.

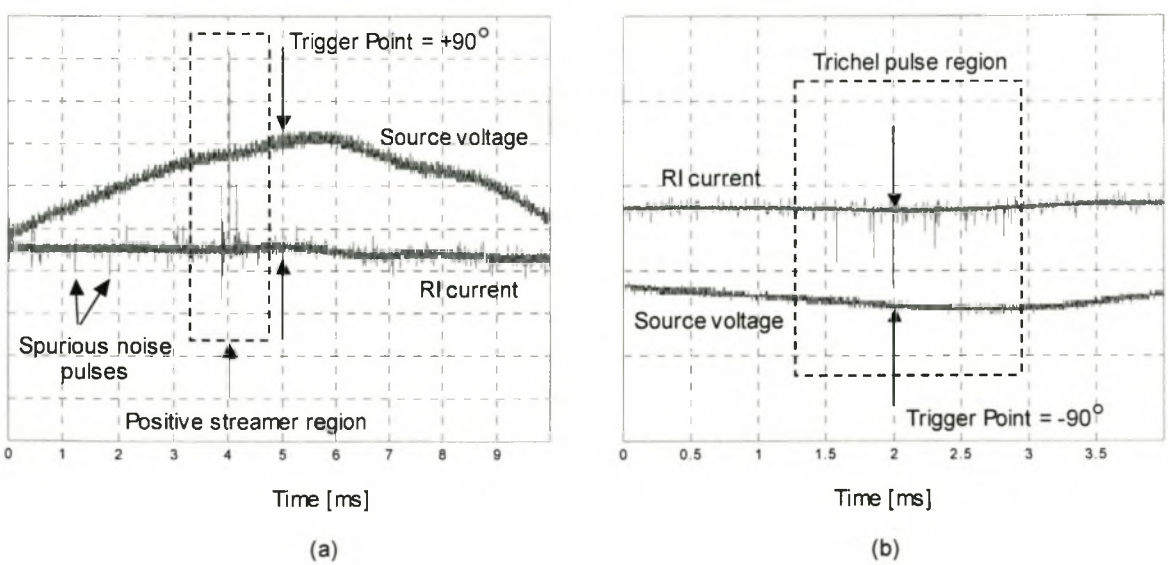

Figure 5.10: Phase triggering applied to a 120 kV source voltage waveform at a phase angle of (a) + 90° and (b) - 90° showing both the applied voltage and RI current waveforms.

Two RI current waveforms, captured using phase triggering in the positive and negative half-cycles of the source voltage, are plotted in figure 5.10. The only corona mode observed in the positive half-cycle, due to the spurious noise pulses, is the positive streamer mode. By triggering at a phase angle of + 90° on the source voltage the captured RI waveform, plotted in figure 5.10 (a), indicates that the positive streamer region is restricted to a 10° region centred at about 72°. Similarly, the RI waveform captured at a phase angle of -90° in figure 5.10 (b) indicates that the

Stellenbosch University http://scholar.sun.ac.za/

Trichel pulse region is restricted to a larger 30° region centred at about -95°. Phase triggering can therefore be used to trigger on the smaller Trichel pulses in the negative half-cycle.

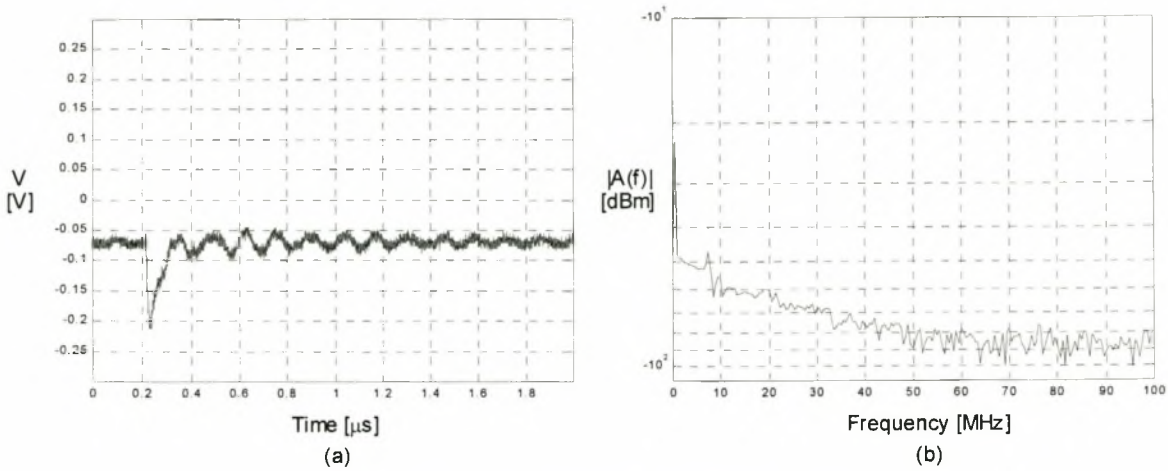

[triggering: phase, trigger phase: -95, sample rate: 2.5Gs/s]

Figure 5.11: The (a) measured time domain and (b) calculated frequency domain plot of a RI pulse observed at 120 kV (peak) using phase triggering and a phase angle of -95°.

A Trichel pulse captured using phase triggering for a trigger phase angle of -95° is plotted in figure 5.11 (a). The calculated frequency spectrum of this pulse is plotted in figure 5.11 (b).

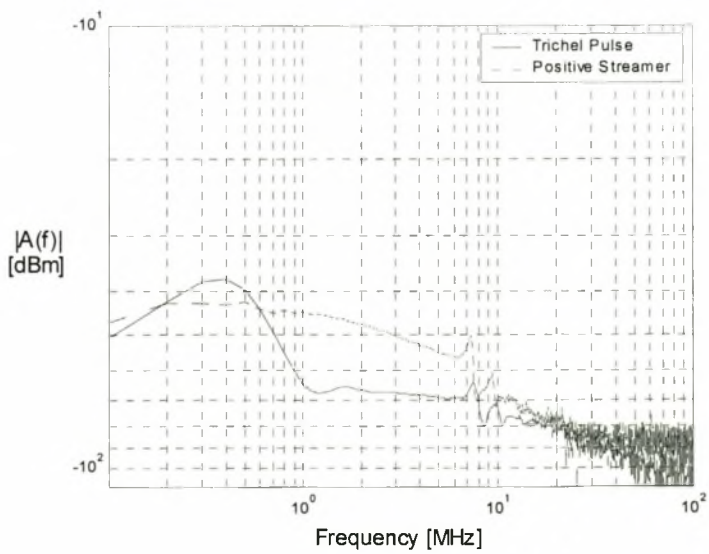

Figure 5.12: Comparison of the frequency spectrum of the Trichel pulse in figure 5.11 (a) and a positive streamer that was also captured at an applied voltage of 120 kV.

The comparison of the frequency spectra of the Trichel pulse and the positive streamer, both obtained at an applied voltage of 120 kV, is plotted in figure 5.12. The comparison indicates that there is a significant difference in the frequency spectra of the two corona modes. A single frequency spectrum cannot be used in the excitation element in the proposed transmission line model in chapter 4 as a result.

Stellenbosch University http://scholar.sun.ac.za/

5.5 Frequency Domain EMI Receiver Measurements

It was found in the literature survey presented in section 5.2 that most RI measurements are narrowband measurements made on a radio noise meter with a standard bandwidth and centre frequency. The EMI receiver allows this centre frequency to be swept through a specified bandwidth at a specified number of points. A wideband account of the RI frequency spectrum can therefore be made while maintaining the accuracy and specifications of the narrowband radio noise meter measurements. The use of the EMI receiver for making wideband RI noise measurements will be discussed in this section.

5.5.1 The Narrowband Radio Noise Meter

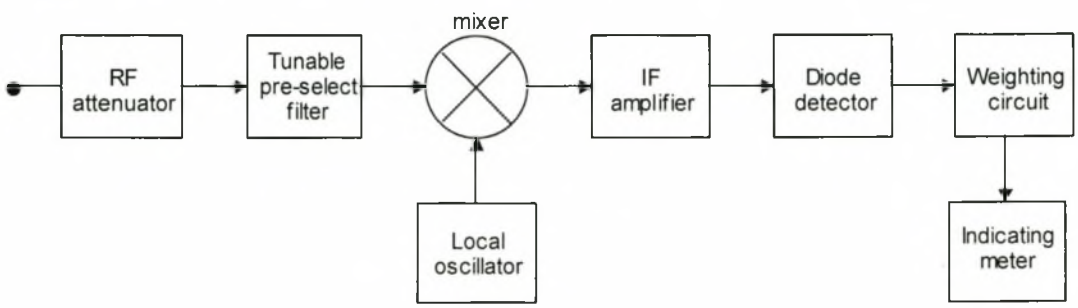

Figure 5.13: A block diagram of a typical radio noise meter (after [9] and [10]).

A block diagram of a typical radio noise meter is presented in figure 5.13. The RI waveform is firstly attenuated by a wideband RF attenuator. This prevents damage to the sensitive proceeding filter and mixer circuits if large frequency components are present in the measurement bandwidth. The next component is the tunable preselect filter. This device is essential for making accurate narrowband measurements. The pre-select filter removes all frequency components outside the measured bandwidth of the meter (i.e. the signal at the mixer input is narrowband). Without the preselect filter, large frequency components outside the measured frequency band (e.g. radio or TV signals) may damage or overload the mixer diode. Overloading of this diode will cause spurious signals that will significantly degrade the noise figure of the measurement device. The RF signal is then mixed to a lower IF frequency and passed through the IF amplifier. The -3dB bandwidth of this narrowband amplifier is called the IF bandwidth and is specified by the appropriate measurement standard.

	Band A	Band B	Band C	Band D
RF frequency [MHz]	0.009 - 0.15	0.15 - 30	30 - 300	300 - 1000
IF bandwidth [kHz]	0.2	9	120	120

Table 5.2: The division of the measured RF frequency spectrum into four frequency bands and their associated IF bandwidth according to the CISPR 16 standard [15].

The specified IF bandwidth for noise measurements according to the CISPR 16 standard is given in table 5.2. Since the RI waveform is broadband, an increase in the IF bandwidth will cause a linear increase in the measured signal level if the circuit is not overloaded. However, since the

Stellenbosch University http://scholar.sun.ac.za/

background noise is also broadband, the noise floor will also be increased linearly and there will be no improvement in the signal-to-noise ratio at the detector input. The increase in the measured noise level with a change in the IF bandwidth from BW_1 to BW_2 is [15]:

$$\Delta dB = 10\log_{10}\left(BW_2 / BW_1\right) \tag{5.2}$$

The maximum sensitivity of the noise meter is obtained with the lowest IF bandwidth setting. The amplified IF signal is then passed through a diode detector and a weighting circuit. This weighting circuit will determine the deflection of the indicating meter which is the output of the radio noise meter. The most common weighting circuits used for noise measurements are the peak, quasi-peak and average detectors.

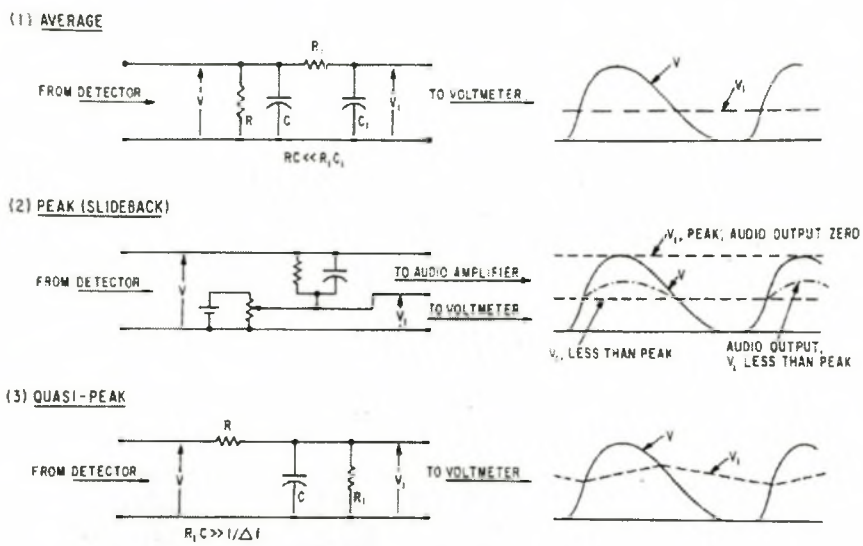

Figure 5.14: Circuit diagrams of (1) an average, (2) a peak and (3) a quasi-peak detector weighting circuit [16].

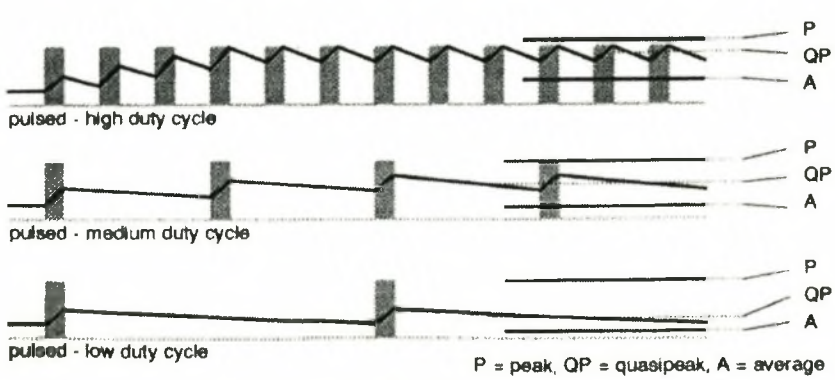

Figure 5.15: The output level of the three weighting circuits for a pulsed RF waveform [15].

The circuit diagrams of the three main weighting circuits are given in figure 5.14. The average circuit outputs the average value of the RF input signal while the peak circuit outputs the peak value of the RF input signal. The peak weighting circuit responds almost instantaneously to the peak value and discharges rapidly once the measurement is made. The quasi-peak detector is

Stellenbosch University http://scholar.sun.ac.za/

effectively a peak detector with weighted charge and discharge times which are chosen so that the output correlates to the human annoyance factor of noise on radio and TV reception. These charge and discharge time constants are specified by the measurement standard used (e.g. the CISPR 16 standard). The response of the weighting circuits to pulsed RF noise is presented in figure 5.15. It is suggested in [15] that the average detector should not be used at low repetition rates due to the poor accuracy of this circuit at these low repetition rates. The quasi-peak value is also affected by repetition rate but this is intended since repetition rate has a direct bearing on the human annoyance factor of pulsed noise.

5.5.2 Making Wideband Measurements with the EMI Receiver

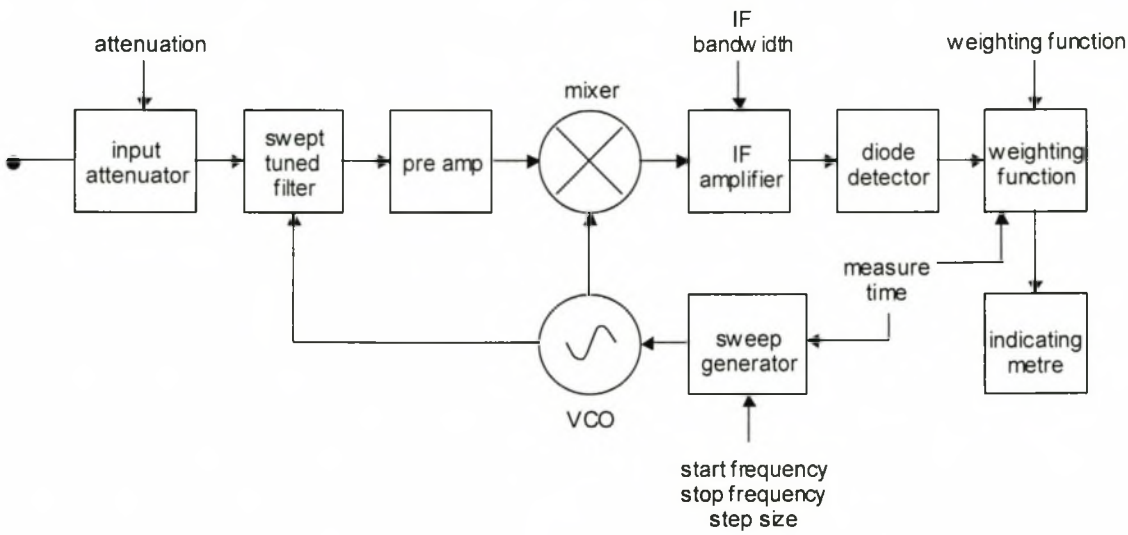

Figure 5.16: A block diagram of a typical EMI receiver (after [10] and [15]).

The EMI receiver is a radio noise meter with various weighting functions and a centre frequency that can be swept through a specified number of frequency points in a specified frequency range. This allows narrowband measurements to be made over a wide frequency band. The EMI receiver used in this thesis is the Rohde and Schwarz ESPC EMI test receiver.

The first component at the RF input port is a wideband attenuator. The input impedance of the device is exactly 50 Ω in the frequency range 150 kHz to 1000 MHz, which is the measurement bandwidth of the device. The attenuation can be manually or automatically set between 0 dB and 100 dB in 10 dB steps. The VSWR at the RF input for any non-zero attenuation is smaller than 1.2. For an attenuation of 0 dB this VSWR increases to some value smaller than 2 thus increasing the reflection co-efficient at the device's input. Autorange operation (i.e. automatic attenuation selection) ensures that the attenuation is always optimally set for the detector circuit used and prevents overloading of the mixer.

Stellenbosch University http://scholar.sun.ac.za/

		ESPC	RI
Input waveform	RF attenuation	(specified limit)	(measured)
DC	all	7 V	<< 7 V (AC corona)
sinusoidal	0 dB	$(V_{RMS})_{max}$ = 3 V	$(V_{RMS})_{max}$ < 50 mV
sinusoidal	> 0 dB	$(V_{RMS})_{max}$ = 7 V	$(V_{RMS})_{max}$ < 50 mV
pulse	0 dB	97 dBμV/MHz	68 dBμV/MHz
pulse	> 0 dB	10 mWs	0.21 mWs

Table 5.3: Input RF power limits of the R&S ESPC and the measured maximum RI power values extracted in section 3.3.4.

To prevent overloading and subsequent damage to the input components, care must be taken to ensure that the power limits specified for the device are never exceeded. These limits are summarized in table 5.3 along with the peak measured powers extracted from the measurements made in section 3.3.4 The comparison confirms that the RI disturbances will not exceed the specified power limits provided that flash-over does not occur. All measurements will therefore be made at an applied voltage below 125 kV (peak).

Three IF bandwidth settings can be used: 200 Hz, 10 kHz and 120 kHz. There are also three types of weighting circuits that can be selected: peak, quasi-peak and average. These weighting circuits monitor the RF input signal for a specified measure time. This measure time can be varied between 1 ms and 100 seconds in the steps 1, 2, 5 and 10. For the peak detector, the weighting circuit is discharged at the beginning of the measurement. At the end of the measure time, the output value is sampled and outputted in the required format. Due to the long charge and discharge times of the quasi-peak detector, the required measure time needed for an accurate measurement is much longer than that of the peak detector which can be as small as 1 ms depending on the nature of the RF input signal. Both analog and digital level indication outputs are available and the measured level can also be downloaded to a PC as data on the devices GPIB port. All device settings can also be controlled via this GPIB communication port and an instruction set. This communication port will be extensively used for PC control of the ESPC in this thesis.

5.5.3 Triggering on Random Corona Pulses

As was the case with the time domain oscilloscope measurements, a measurement technique must be derived for the EMI receiver so that the various corona modes can be observed and an accurate wideband account of their characteristic frequency spectra can be made. The triggering of the measurement (i.e. the starting point of the measurement) and the measure time are of particular importance in this regard. PC control of the ESPC via the devices GPIB port will be used throughout this section to make the EMI receiver measurements. A detailed description of the ESPC instrument control is presented in appendix E1. Only the most important principles will be discussed here.

Stellenbosch University http://scholar.sun.ac.za/

Firstly the start and stop frequencies and the number of frequency points of the frequency scan are entered. The local oscillator frequency is then set to the start frequency and a measurement is started. The measurement is made for the specified measurement time, after which the voltage at the detector output is sampled and transmitted to the PC. The frequency of the local oscillator is then increased by the specified step size and a new measurement is started. This process is repeated until the local oscillator frequency exceeds the required stop frequency, at which time the frequency scan is terminated. To exclude the variation in pulse amplitude and therefore ensure a repeatable measurement, a specified number of measurements are made at each frequency point and the average is calculated and plotted.

The oscilloscope measurements presented in this thesis suggest that the magnitude of the measured frequency spectrum of the positive streamer RI pulses exceeds that of the other corona modes throughout the frequency range 1 MHz to 100 MHz. It can therefore be concluded that if the ESPC measurements is triggered at some random time and the peak detector is used with a measure time that exceeds the period of the 50 Hz source voltage, then an accurate account of the positive streamer RI pulse can be observed. In order to obtain the frequency spectrum of the smaller positive corona modes and the negative Trichel pulse modes, the ESPC measurements must be triggered on a specific phase of the source voltage waveform and the measure time must be restricted so that only a small section of the source waveform is observed. The ESPC provides an external triggering, TTL logic, user port. The external triggering mechanism designed to utilise this option so that the various corona modes can be observed is described in appendix D3. The device samples the source voltage waveform using a fast analog-to-digital converter (ADC) and outputs a logic pulse onto the external trigger port of the ESPC device. This phase triggering method will be used with the peak detector to measure the frequency spectra of the smaller corona modes.

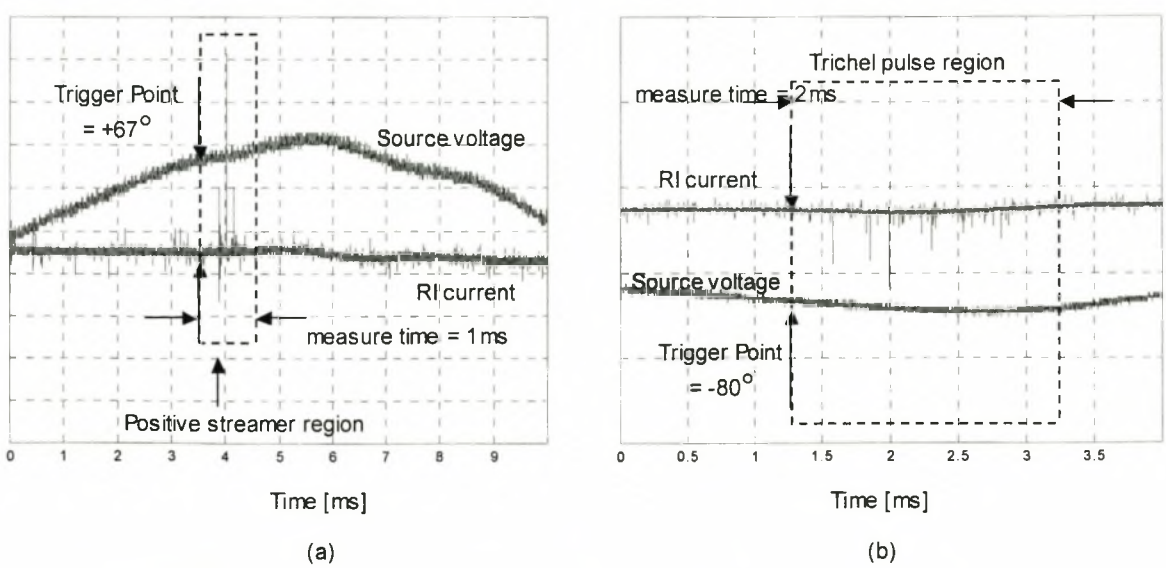

Figure 5.17: Time domain measurements of the source voltage and RI waveforms observed in (a) the positive half-cycle and (b) the negative half-cycle illustrating the phase triggering method of the EMI receiver.

The ESPC phase triggering method for peak detector measurements is illustrated in figure 5.17. The minimum measure time of the ESPC is 1 ms. This corresponds to a phase angle of 18° on the 50 Hz source voltage waveform. As an example, the peak 10 MHz frequency component of

Stellenbosch University http://scholar.sun.ac.za/

a Trichel pulse discharge can be measured by triggering the measurement at a phase of -80° and using a measurement time of 2 ms so that the entire Trichel pulse region can be included while excluding the positive corona discharges region. This example is based on the observations made from the oscilloscope measurements presented in figure 5.10. The quasi-peak detector requires a much longer measure time than the peak detector to make an accurate measurement. The phase triggering method described above is therefore only applicable to the peak detector measurements.

5.5.4 Measurement Results

The optimum measure time and averaging factor must firstly be determined for the peak and quasi-peak detectors.

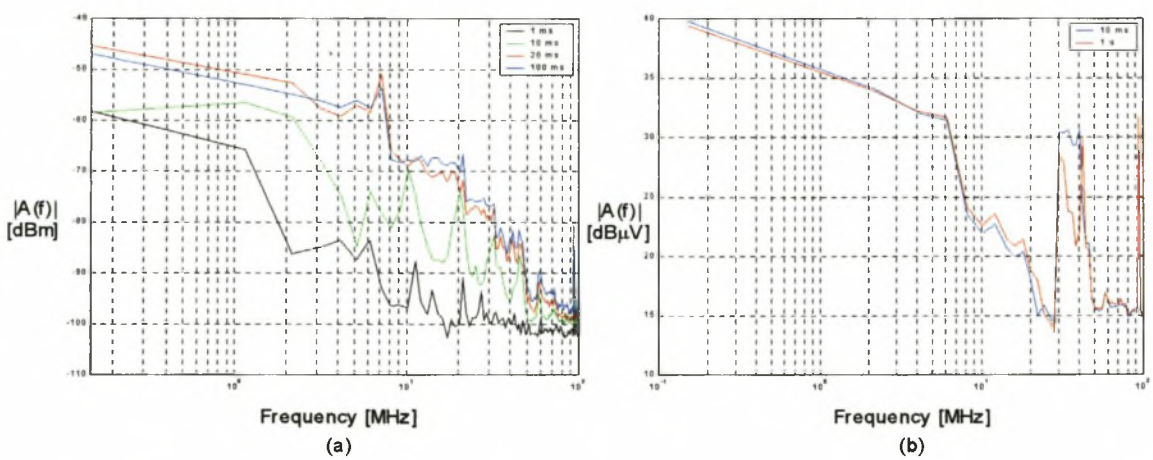

[Detector: (a) peak (b) quasi-peak, IF bandwidth: 10 kHz, Averaging: x4, Vs (peak) = 120 kV, triggering: random]

Figure 5.18: The variation in the measured RI frequency spectrum for (a) the peak and (b) the quasi-peak detectors with various measure times applied.

The RI measurements made with a peak detector with the measure time varied between 1 ms and 100 ms are plotted figure 5.18 (a). The result indicates that a measure time of less than 20 ms will result in an inaccurate , unrepeatable measurement. This is expected since 20 ms corresponds to the period of the 50 Hz source voltage waveform. A randomly triggered measurement with a duration less than the source voltage period is not assured of including the large positive streamer discharges that occur in the narrow 10° window near the positive peak voltage (see figure 5.10 (a)). A further increase in the measure time above 20 ms does not significantly affect the measurement accuracy. The slight increase in the measured frequency spectrum observed in figure 5.18 (a) can be attributed to a slight variation in corona activity between different periods of the source voltage waveform. This variation is small and the measurement can be considered repeatable and accurate for a measure time greater than 20 ms.

The repeatability of the quasi-peak measurement with two different measurement times in figure 5.18 (b) is of particular concern. It has already been mentioned that the long charge and discharge times require a long measure time. The CISPR 16 standard requires that the quasi-peak charge time constant is 1 ms in frequency bands B, C and D (see table 5. 2) and that the discharge time constant is 160 ms in frequency band B and 550 ms in frequency bands C and D. A measure time of 1 second should therefore be necessary for an accurate measurement. A possible explanation

Stellenbosch University http://scholar.sun.ac.za/

is that the small number of RI disturbance sources on the centre conductor of the short corona cage is not sufficient for accurate quasi-peak measurements. Since only the quasi-peak detector and not the peak detector is dependent on the repetition rate of the RI sources, the problem can be resolved by deriving a correlation between peak and quasi-peak measurements.

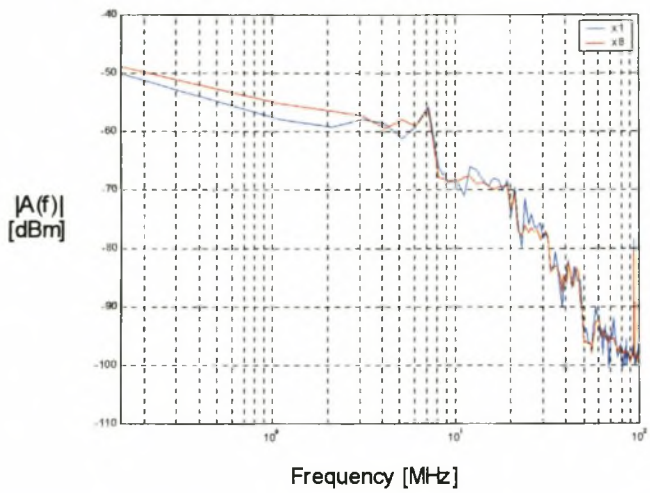

[Detector: peak, IF bandwidth: 10 kHz, Vs (peak) = 120 kV, triggering: random, measure time: 20 ms]

Figure 5.19: The variation in the measured RI frequency spectrum for the peak detector with various averaging factors applied to the measurement.

The averaging factor applied to the peak detector RI measurements was varied between 1 and 8 and the result is plotted in figure 5.19. It indicates that only a small variation in the measured spectrum occurs as is expected. The peak measurements are therefore repeatable if a measure time of 20 ms or more is used.

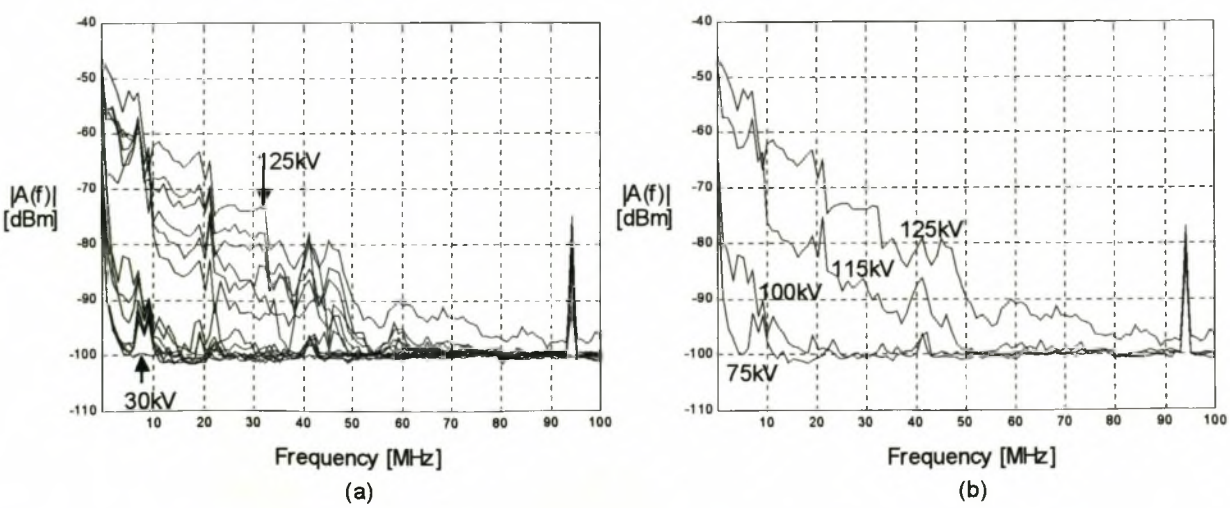

[Detector: peak, IF bandwidth: 10 kHz, Averaging: x4, triggering: random, measure time: 20 ms]

Figure 5.20: (a) A nest of measured peak detector curves for the source voltage range 30 kV to 125 kV in 5 kV steps and (b) the measured curves at four indicated source voltages.

Stellenbosch University http://scholar.sun.ac.za/

The frequency spectrum of the RI current is measured between 150 kHz and 100 MHz for an applied voltage between 30 kV and 125 kV in 5 kV steps. The nest of measured frequency spectrum curves is plotted in figure 5.20 (a). It is important to note that significant frequency components were measured above the noise floor for voltages above 35 kV. It was found in the oscilloscope measurements that the large positive streamers only appeared above 90 kV and were the first detected mode in the positive half-cycle. The measured frequency components must therefore be that of the smaller positive corona modes which could not be observed with the oscilloscope. This is because the spurious noise pulses do not affect the triggering of the EMI receiver and because the EMI receiver has a larger dynamic range. The frequency spectrum then suddenly increases as the voltage is increased above the inception level (i.e. 100 kV). The RI noise frequency spectrum then remains fairly constant until the source voltage exceeds 115 kV, at which point a second sudden increase in the RI noise frequency spectrum occurs. The spectrum then increases in an almost linear relationship with the increase in applied voltage. These observations correlate closely with the oscilloscope findings summarized in table 5.1.

Source voltage range	Bandwidth of the measured RI noise
35 kV - 100 kV	20 MHz
100 kV - 115 kV	45 MHz
> 115 kV	> 100 MHz

Table 5.4: The bandwidth of the measured RI noise in discrete voltage ranges.

Finally the external triggering method, described in the previous section, must be used to observe corona modes other than the positive streamer mode.

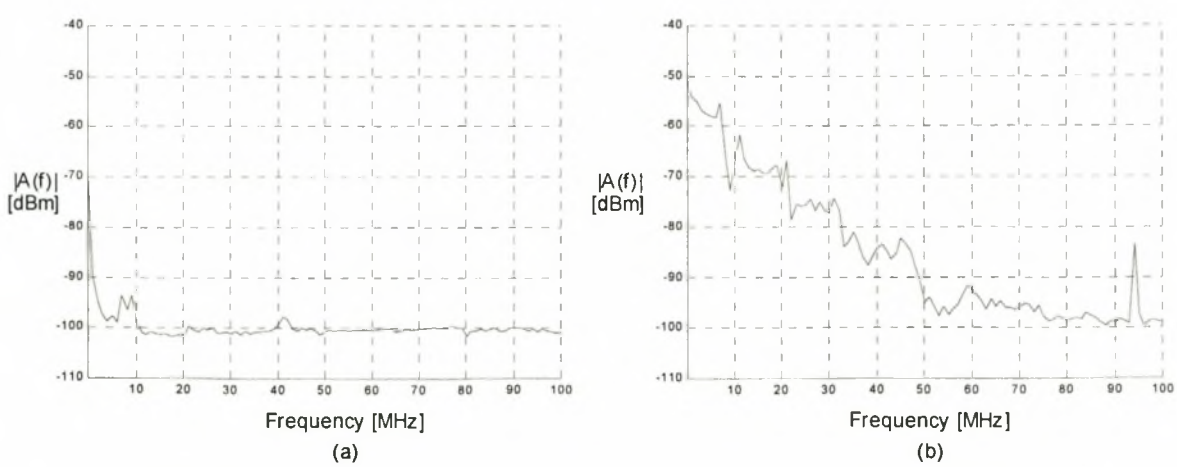

[Detector: peak, IF bandwidth: 10 kHz, Averaging: x4, triggering: phase, measure time: 1 ms]

Figure 5.21: Positive half-cycle corona modes observed with the EMI receiver using a measure time of 1 ms and phase triggering at (a) + 35° and (b) + 65° with a source voltage of 120 kV.

Stellenbosch University http://scholar.sun.ac.za/

The frequency spectrum in figure 5.21 (a) is obtained by triggering each measurement at a phase of 35° and using a measure time of 1 ms. Based on the findings of the oscilloscope measurements presented in figure 5.10 (a), the measurement should not include positive streamer RI pulses. This is confirmed in the EMI receiver measurements and it can be concluded that the frequency spectrum in figure 5.21 (a) is that of the smaller positive corona modes. The frequency spectrum in figure 5.21 (b) is obtained with a trigger phase of 65° in the positive half-cycle and is therefore the frequency spectrum of a positive streamer discharge.

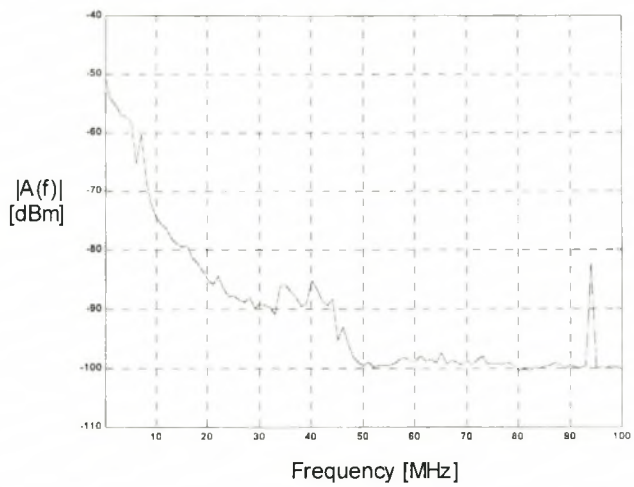

[Detector: peak, IF bandwidth: 10 kHz, Averaging: x4, triggering: phase, measure time: 2 ms]

Figure 5.22: The negative half-cycle Trichel pulse frequency spectrum observed with the EMI receiver using a measure time of 2 ms and phase triggering at - 80° with a source voltage of 120 kV.

The frequency spectrum in figure 5.22 is obtained by triggering each measurement in the negative half-cycle at a phase of -80°. This measurement excludes the positive corona RI disturbances and it can therefore be concluded that the measured frequency spectrum is that of a Trichel pulse.

5.6 Frequency Domain Spectrum Analyser Measurements

It was noted in section 5.2 that spectrum analysers have historically been used to make wideband measurements of RI noise. It was found in the previous section that the EMI receiver can be used to make wideband RI noise measurements while maintaining the accuracy and required measurement standards of the narrowband radio noise meters. The use of the spectrum analyser (SA) for making similar RI noise measurements will be investigated in this section. The EMI receiver and spectrum analyser measurements can then be compared to determine the relative performance of the two devices.

Stellenbosch University http://scholar.sun.ac.za/

5.6.1 Spectrum Analyser Basics

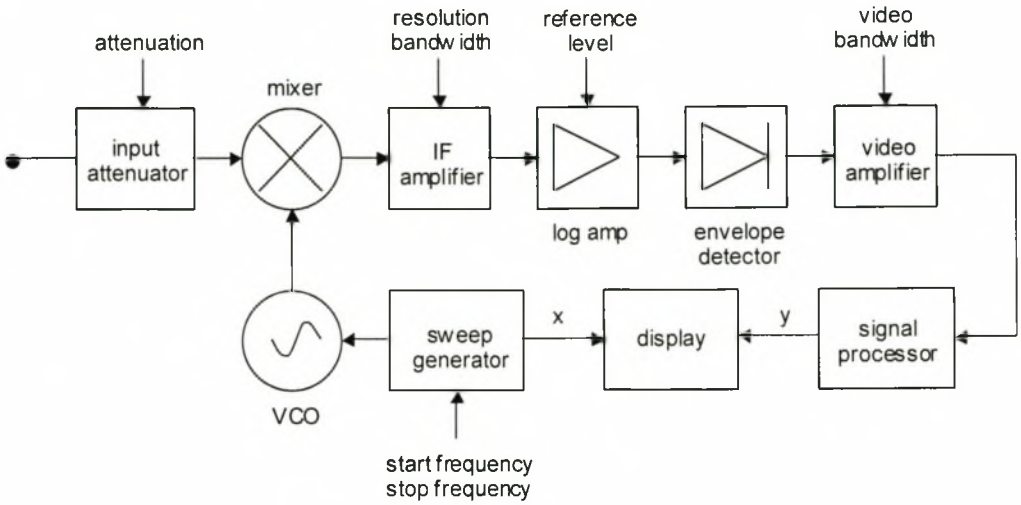

Figure 5.23: A block diagram of a typical spectrum analyser (after [10] and [15]).

A block diagram for a typical spectrum analyser is presented in figure 5.23. The most notable difference between the EMI receiver and the spectrum analyser is the absence of a preselect filter at the input of the spectrum analyser. The input RF signal is therefore fed directly into the mixer. As a result, the spectrum analyser does not have the overload protection that the EMI receiver has and is therefore susceptible to large input signals throughout the entire measurement bandwidth of the device. Besides the IF filter, which the EMI receiver also has, the spectrum analyser has a video amplifier after the detector stage. The IF amplifier serves the same purpose as it did in the EMI receiver. The video amplifier provides post-detection filtering which reduces the variation in the displayed noise. The average noise level is however not affected by this filtering and the signal-to-noise ratio will therefore not be affected. The input impedance of the spectrum analyser is roughly equal to 50 Ω across the measurement bandwidth. Any small variation in input impedance in the measured frequency range will cause negligible reflections of the RI current at the input to the device and can therefore be ignored. The spectrum analyser used in this thesis is the HP 8562A . The specified RF input power limit for this device is 30dBm average power in the IF bandwidth. The maximum DC level is 0 V. A DC block is therefore used to prevent damage to the device.

Another important difference between the spectrum analyser and the EMI receiver is the sweep and detection method. The EMI receiver sets the local oscillator to a specified number of discrete frequency points and remains at these frequencies for a specified measurement time. At the end of the measurement time the output of the selected detector is sampled and outputted. The EMI receiver measurement is therefore a swept narrowband measurement. For the spectrum analyser, a saw-tooth voltage generator causes the voltage controlled oscillator (VCO) to sweep linearly through the specified frequency range. The IF voltage at the output of the detector is then sampled at a discrete number of points, specified by the sweep settings, and outputted. The spectrum analyser measurement is therefore a true wideband measurement.

Stellenbosch University http://scholar.sun.ac.za/

5.6.2 Wideband Measurement of Random Corona Pulses

The minimum sweep time setting is 50 μs. This value is considerably longer than the duration of a single RI noise pulse. It is therefore only possible to observe a few frequency components in a single sweep. It is also not possible to trigger the sweep on a RI pulse as was done in the oscilloscope measurements since the spectrum analyser does not record pre-trigger data. In the case of the EMI receiver, a measurement was made at a single frequency for one or more periods of the source voltage. The spectrum analyser uses a linear sweep method and such a measurement method would require special considerations and will be discussed in the next section. The simplest measurement method will be to make numerous sweeps, all triggered periodically from some random time point. The maximum measured level at each sampled frequency point is then recorded and displayed. This is achieved by using the maximum hold post-processing function of the spectrum analyser.

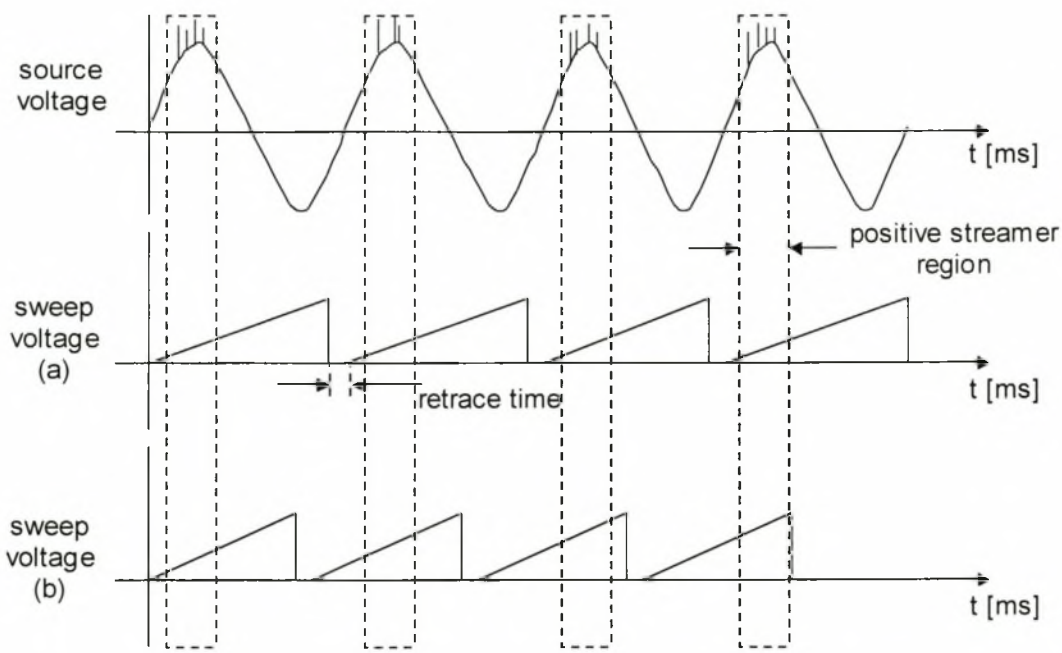

Figure 5.24: A comparison between the source voltage waveform and a spectrum analyser sweep waveform that is (a) periodically related and (b) not periodically related to the source voltage.

As was the case with the EMI receiver measurements, recording the peak frequency component over one or more periods of the source frequency will result in a frequency spectrum of a positive streamer RI pulse. Since the pulses occur randomly in the same section of the source waveform, they can be considered collectively periodic. This is illustrated in figure 5.24 together with the voltage waveform of the sweep generator. If the sweep period has a similar period as the source waveform, as in figure 5.24 (a), the positive streamers will occur at the same sampled frequency points on every sweep. Frequency points outside this band will then not include the effect of the positive streamers. The sweep rate should therefore be carefully chosen as in figure 5.24 (b) so that the frequency range coinciding with the positive streamer region differs between each sweep. The number of sweeps required to obtain an accurate account of the RI noise frequency spectrum will be dependent on the sweep time chosen and should therefore be investigated and noted in the measurements made.

Stellenbosch University http://scholar.sun.ac.za/

5.6.3 Swept Narrowband Measurement of Random Corona Pulses

The wideband spectrum analyser measurement method described in the previous section cannot differentiate between the various corona modes and does not give any information about the variation in amplitude or repetition rate between various periods of the source voltage. Both the oscilloscope and EMI receiver were able to do this. A swept narrowband spectrum analyser measurement method will be proposed in this section that can extract the frequency spectra of the various corona modes as well as information regarding the amplitude and repetition rate of the RI pulses.

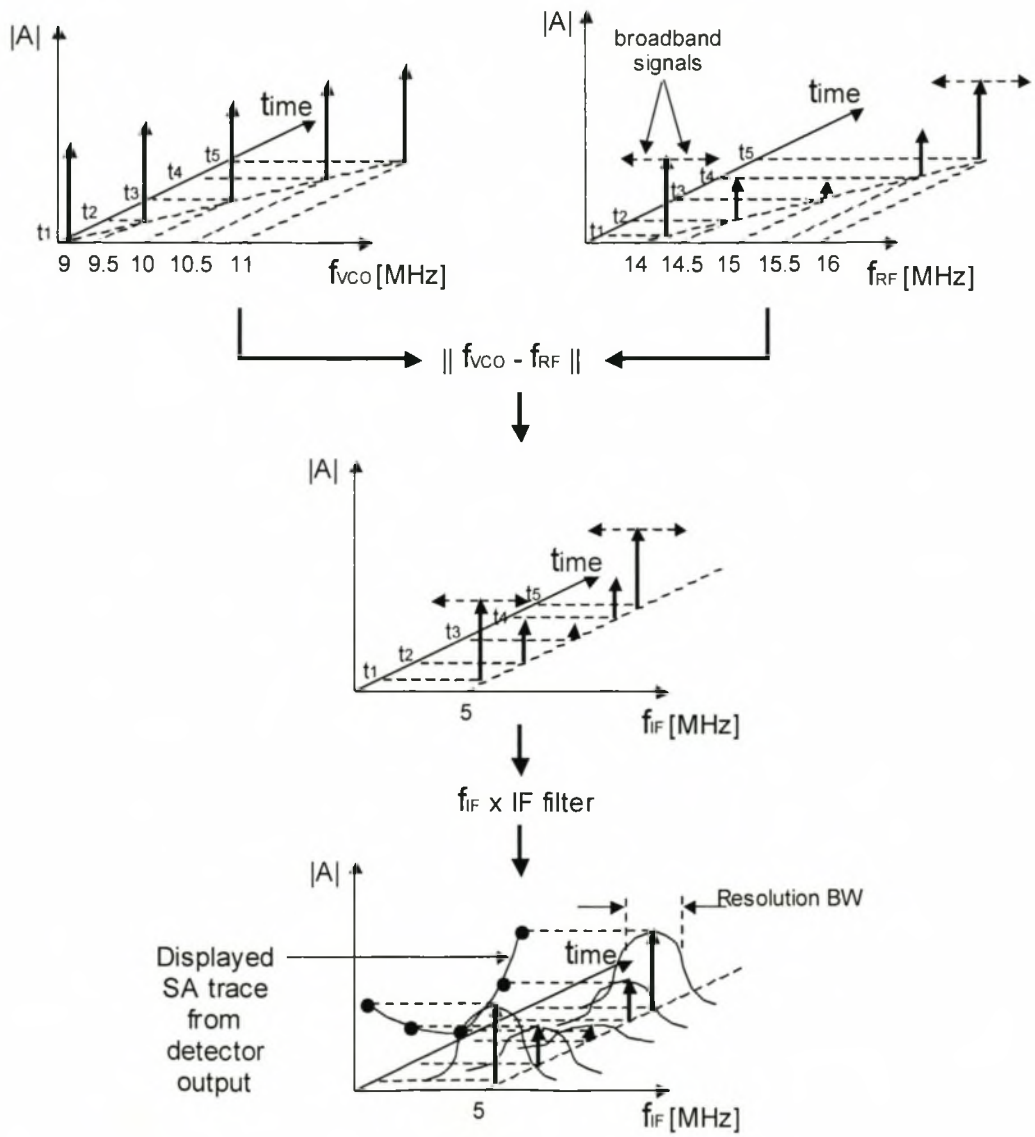

Figure 5.25: Schematic diagram of various signals in the spectrum analyser measurement path described in figure 5.23, illustrating the signal processing for the swept narrowband method.

The simplest method of using the wideband spectrum analyser for narrowband measurement is to set the centre frequency to the measurement frequency, select the zero-span option and reduce the sweep time to less than 30 ms. The spectrum analyser will then detect and display the

Stellenbosch University http://scholar.sun.ac.za/

measured centre frequency component as it appears at the devices RF input. A marker is however not available for such a measurement and the peak value cannot be recorded and sent to a PC via the devices GPIB bus. An alterative method which uses a non-zero frequency span will therefore be used. To understand this method, a more detailed description of the input RF mixer and the IF filter components is required. The frequency of the IF signal at the output of the mixer in figure 5.23 is:

$$f_{IF} = |n.f_{VCO} \pm m.f_{RF}| \tag{5.3}$$

where m and n are non-zero integer values. Since the RI waveform is wideband, the IF signal at the mixer output is a broadband signal but is centred about a lower frequency. This signal is then filtered with the IF amplifier which has a -3dB bandwidth equal to the resolution bandwidth setting.

If the span is set equal to or smaller than the resolution bandwidth, then a wideband RI pulse, occurring at any point in time during the frequency sweep, will have frequency components that pass through the IF filter with negligible attenuation and enter the detection stage causing a deflection of the trace on the CRT display. This is illustrated in figure 5.25 and is only valid if the input RF signal is wideband. The values used in the illustration are hypothetical values and are only used to illustrate the principle. In this diagram it is shown that the displayed trace will be a function of time. The spectrum analyser is therefore effectively a narrowband oscilloscope. If the sweep time is increased to 100 ms, then five complete periods of the source voltage will occur during one spectrum analyser sweep period. The variation of the RI pulse amplitude and repetition rate during these five source voltage periods can then be determined from the frequency sweep. Furthermore, the frequency components centred around the centre frequency from the various corona modes will be displayed separately. The swept narrowband spectrum analyser measurement method therefore has many useful advantages for the research in this thesis since a single frequency sweep will simultaneously provide information about both the frequency content of the various corona modes and the variation of the amplitude and repetition rate between various periods of the source voltage.

5.6.4 Measurement Results

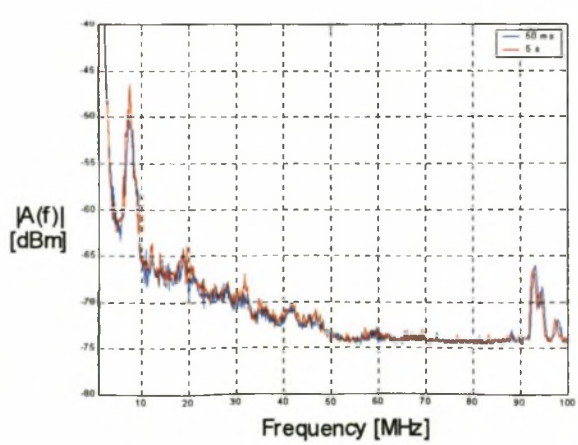

Figure 5.26: Wideband spectrum analyser measurements with various sweep times.

Stellenbosch University http://scholar.sun.ac.za/

The variation of the wideband spectrum analyser measurement (i.e. a maximum hold measurement with multiple sweeps) with a variation in sweep time is investigated in the measurements presented in figure 5.26. The measurements were both made over a time period of five minutes. The result indicates that an increase in the number of sweeps used to make the measurement does not significantly improve the accuracy of the measurement. It was found that the accuracy approached its maximum value if more than 20 sweeps were used in the wideband measurement.

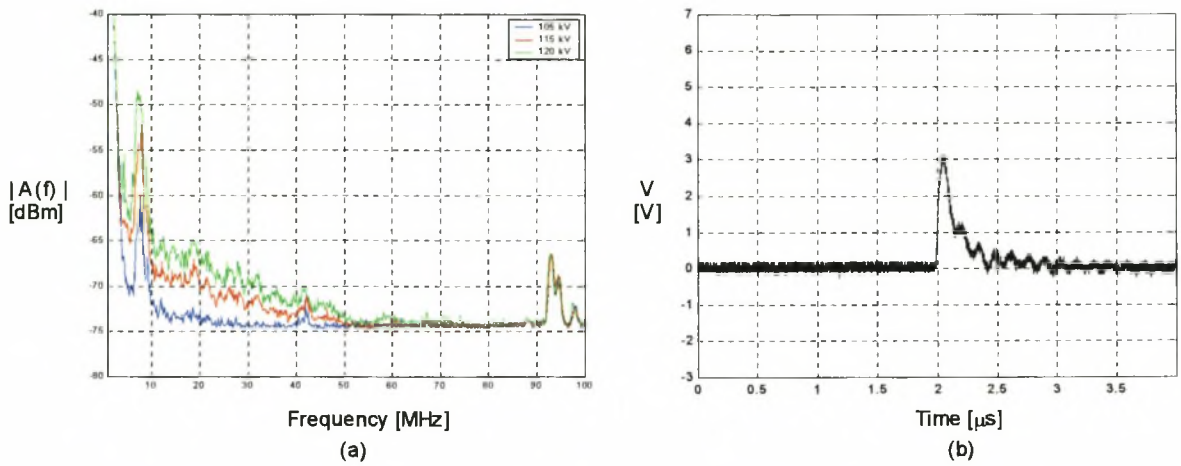

[Wideband SA measurement: RBW = 10 kHz, VBW = 10 kHz, sweep time = 500 ms, # of sweeps = > 100]

Figure 5.27: (a)Wideband measurement results made at various applied voltages with a sweep time of 500 ms and more than 100 sweeps, (b) a time domain positive streamer RI pulse.

The results of the wideband spectrum analyser measurements, made at various applied voltages, is presented in figure 5.27 (a) along with a time domain positive streamer RI pulse measured with an oscilloscope. The wideband measurement results indicate an expected increase in the frequency spectrum magnitude as the applied voltage is increased above the inception level. It is noticeable in the results that the resonant frequency detected in both the oscilloscope and EMI receiver measurements is emphasized in these measurements. The resonance in the oscilloscope measurement of a positive streamer RI pulse in figure 5.27 (b) has a low damping factor. The resonant frequency component therefore persists for a fairly long time period and is therefore easily detected even at low pulse repetition rates. The resonance is narrowband while the RI pulse is wideband and can therefore be de-emphasised by increasing the resolution bandwidth. Since the EMI receiver measurements were made in the same IF bandwidth as the measurements in figure 5.27 (b) and the resonant frequency was not emphasized in those measurements, it can be concluded that the wideband spectrum analyser measurement method does not make as accurate an account of the RI frequency spectrum as was made with the EMI receiver. These comparisons will however be made later in section 5.8 where all the measurement methods are compared.

The final method used in this thesis for measuring RI noise from the corona cage is the swept narrowband spectrum analyser method. The instrument control software needed to make measurements using this method is described in appendix E2.

Stellenbosch University http://scholar.sun.ac.za/

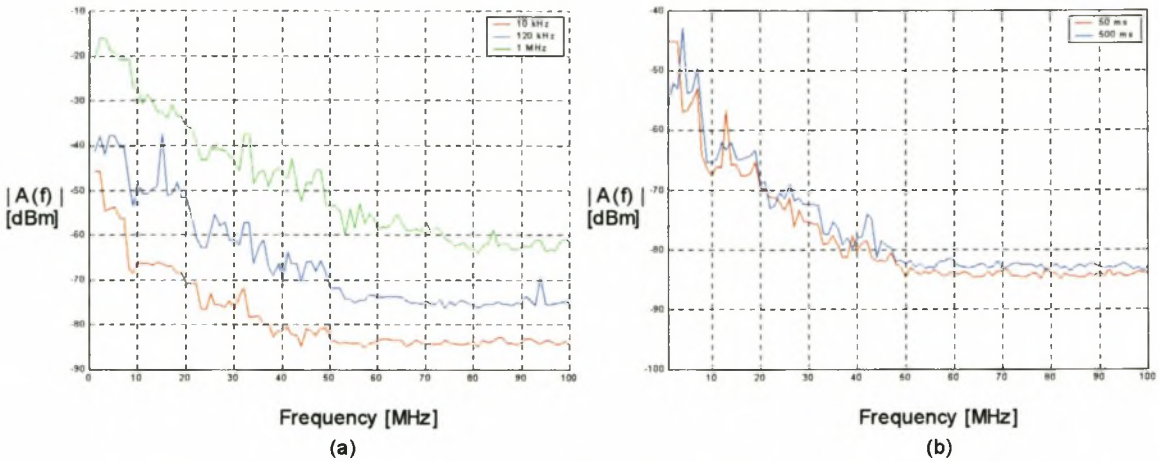

[Swept narrowband SA measurement: VBW = RBW, RBW (b) = 10 kHz, sweep time (a) = 50 ms]

Figure 5.28: The dependence of the swept narrowband spectrum analyser frequency spectrum on (a) the resolution bandwidth and (b) the sweep time.

The dependence of the measured frequency spectrum for the swept narrowband measurements on the resolution bandwidth is plotted in figure 5.28 (a). Since both the input corona cage RI disturbance and the system noise are wideband, an increase in the resolution bandwidth will cause an equivalent increases in both signals and the signal-to-noise ratio will not improve. This is evident in figure 5.28 (a). To make the swept narrowband measurements directly comparable with the EMI receiver measurements, a resolution bandwidth of 10 kHz will be used for the remaining measurements in this section. Figure 5.28 (b) indicates that the sweep time has no significant effect on the measured frequency spectrum. This is because the minimum measure time for the 8562A is 50 ms and therefore is twice the period of the source voltage. The slight increase in the spectrum magnitude in figure 5.28 (b) can be attributed to the small variation in RI pulse amplitudes on the various source voltage periods included with the longer sweep time.

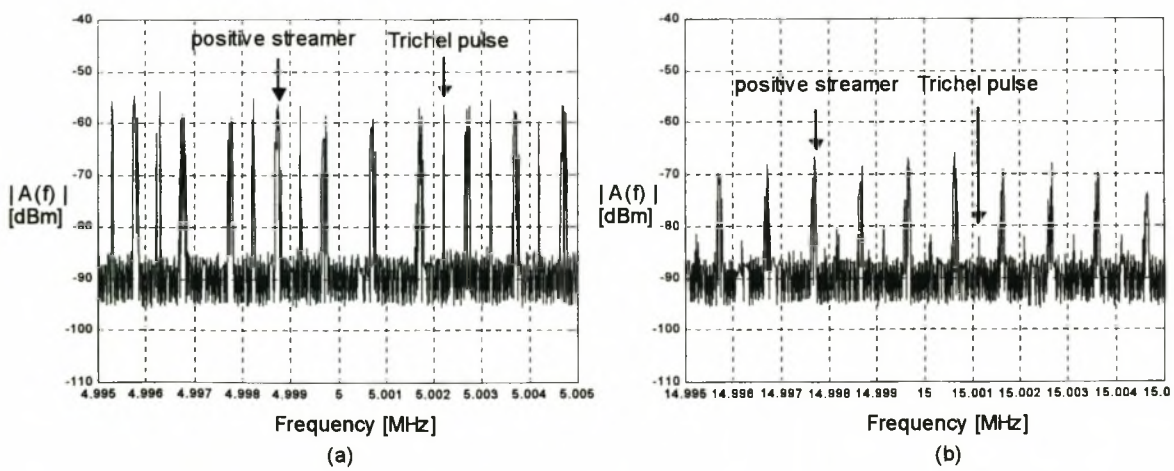

[Swept narrowband SA measurement: RBW = 10 kHz, VBW = 10 kHz, sweep time = 200 ms, Vs = 120 kV]

Figure 5.29: The displayed spectrum analyser trace for an applied voltage of 120 kV at a centre frequency of (a) 5 MHz and (b) 15 MHz.

The displayed spectrum analyser trace is plotted for the swept narrowband measurement method at two frequencies in figure 5.29. The plots illustrate the wealth of information that is contained in the measurement. Both positive streamers and Trichel pulses were observed. It must be noted

Stellenbosch University http://scholar.sun.ac.za/

that the allocation of RI pulse mode to the displayed pulses in figure 5.29 is a guess and must be proven in future research. Based on this guess, it is important to note that at the lower frequency (i.e. figure 5.29 (a)) the Trichel pulse component is larger than the positive streamer component. The assumption made with the randomly triggered EMI receiver measurement method that the largest frequency components, throughout the measured bandwidth, are those of positive streamers is therefore not valid. In this thesis the swept analyser measurement method will only record the maximum peak at each frequency. Phase triggering via the external interrupt input could be used to start the sweep on a particular phase of the source voltage. Unlike the EMI receiver, the peak frequency components in a small time region of the source voltage cannot be isolated since the minimum sweep time for a non-zero span is only 50 ms. A more sophisticated post-processing method can however be developed for the spectrum analyser measurement to extract the same information as the phase triggering method of the EMI receiver if the trigger phase of the sweep is known (i.e. external triggering is also required).

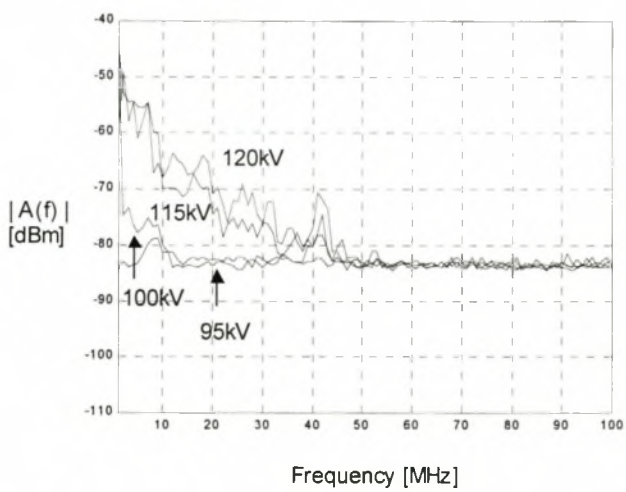

[Swept narrowband SA measurement: RBW = 10 kHz, VBW = 10 kHz, sweep time = 100 ms]

Figure 5.30: The peak frequency spectrum measured at various source voltages using the swept narrowband spectrum analyser method.

The frequency spectra measured with the swept narrowband method display the same voltage dependent characteristics that were observed in the oscilloscope and EMI receiver measurements. These measurements are presented in figure 5.30 for selected source voltages.

5.7 Extraction of Statistical Properties

Two important measurements that are required to derive the relationship between quasi-peak measurements and other measurement detector outputs were found to be the statistical amplitude and repetition rate distributions in the literature survey. This is of particular importance when measuring corona in small corona cages since it was found in this thesis that the quasi-peak EMI receiver measurements are possibly inaccurate due to the low number of corona discharges on the short centre conductor. Quasi-peak or RMS measurements may therefore need to be derived from the peak measurements that were found to be accurate and repeatable. The derivation requires the extraction of the statistical corona properties. The measurement of these properties will be discussed in this section.

Stellenbosch University http://scholar.sun.ac.za/

5.7.1 Sampling Rate and Measurement Bandwidth

The easiest method of extracting the statistical corona properties is from a time domain oscilloscope measurement of the corona cage RI noise waveform. It was suggested in the literature survey of this chapter that the statistical properties should be extracted from two consecutive periods of the source voltage waveform, each of which should contain more than 150 corona pulses. The limited memory of the TDS3032 (i.e. 10 kBytes) results in a maximum sample rate of 250 ks/s if two consecutive periods of the 50 Hz source waveform are to be recorded from a single trigger event. The maximum bandwidth of the measurement is therefore calculated using equation 5.1 as 30 kHz. All RI frequency components above 30 kHz must therefore be attenuated to levels below the noise floor at the oscilloscope input so that aliasing is avoided and an accurate account of the measured RI pulse frequency spectrum can be obtained. The peak RI pulse level was found to be 7 V in the oscilloscope measurements in section 5.4.3 and the noise floor was found to be 50 mV in the same section. The dynamic range of the time domain oscilloscope measurement system is therefore about 40 dB. The required low-pass filter must therefore provide a stop-band attenuation of 40 dB. The ratio of the stop-band frequency to the pass-band frequency must also be as small as possible. The filter used was a sixth order chebyshev filter. The filter is designed for its magnitude response with no consideration given to its phase response. The measured phase spectrum of the RI pulse must therefore be corrected in post-processing to account for the filters' phase response.

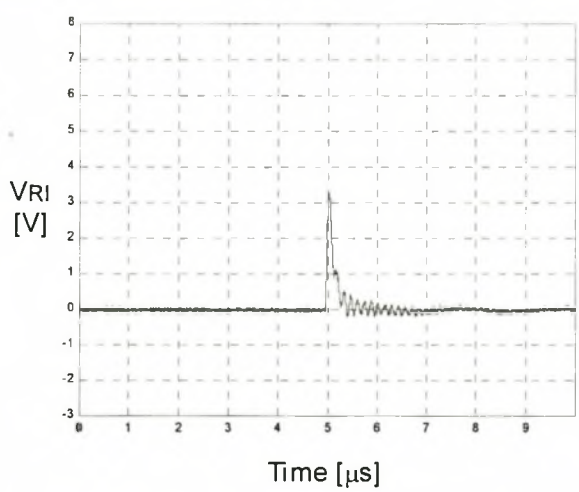

Figure 5.31: The time domain plot of a typical RI pulse (Vs = 120 kV and f_s = 2.5Gs/s)

A typical RI pulse is plotted in figure 5.31. The time axis indicates that the significant part of the RI pulse occurs in the time span of less than 1 μs. By sampling at a rate of 250 ks/s, only one sample every 4 μs is made. The measurement system will therefore not capture all the RI pulses and necessary amplitude information cannot be extracted from those pulses captured since all the information is contained in only one sample point. A faster time domain sampling card is therefore required to extract the statistical properties of corona discharges.

Stellenbosch University http://scholar.sun.ac.za/

5.8 Conclusions

Two repeatable oscilloscope measurement methods were used in section 5.3. These were the level triggering and phase triggering methods. Both methods allowed for the extraction of the frequency spectra of individual corona pulses. The poor dynamic range of the time domain measurement system prohibited the extraction of the smaller corona pulses and therefore the smaller corona modes. The dynamic range can be improved in the measured RI noise bandwidth by using a band-reject filter to remove frequency components in the frequency range 70 MHz to 90 MHz. Level triggering can be used to find the inception levels of the various corona modes but only allows the observation of the largest RI pulses at one fixed voltage (i.e. the positive streamer RI pulses for voltages above the inception level). Phase triggering allows the observation of RI pulses at a particular phase of the source voltage waveform and therefore can be used to extract the frequency spectra of Trichel pulses and positive streamers.

Two repeatable EMI receiver measurement methods were used in section 5.4. These were the random triggering and the phase triggering methods which both used the peak detector. The poor dynamic range of the time domain measurement system in the frequency range 70 MHz to 90MHz did not affect the ability of the frequency domain measurement methods to observe the smaller corona modes since the frequency spectra of these discharges were outside the above mentioned frequency band. Random triggering can be used to observe the largest RI pulse spectrum during a period of the source voltage provided the measure time is greater than 20 ms. Phase triggering permitted the extraction of both large and small positive corona modes and the negative corona mode. A measure time of 1 ms is used for the positive phase triggered measurements and a measure time of 2 ms is used for the negative phase triggered measurements.

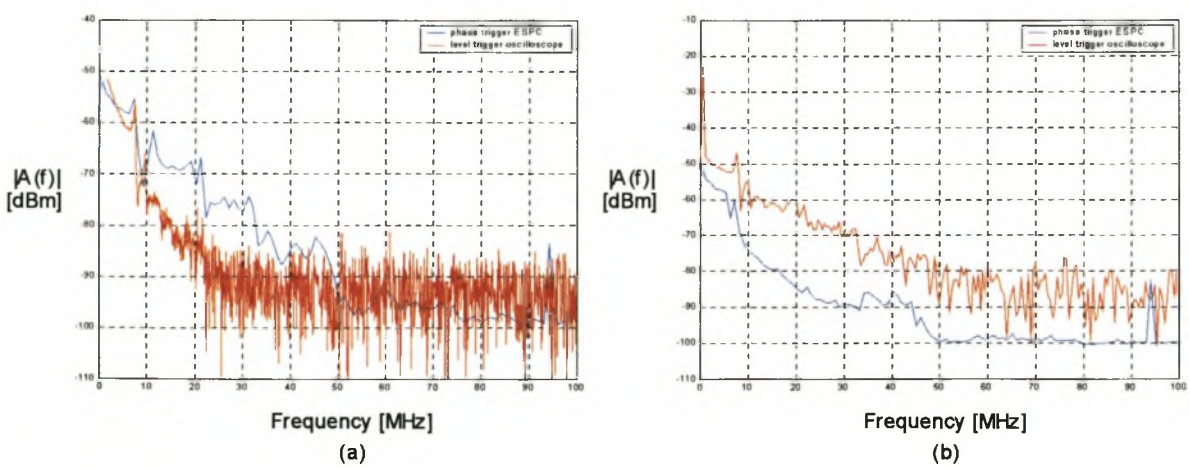

Figure 5.32: A comparison of the measured frequency spectra of (a) positive streamers and (b) Trichel pulses observed with various oscilloscope and EMI receiver measurement methods.

Two repeatable spectrum analyser measurement methods were used in section 5.5. These were the wideband and swept narrowband measurement methods. The wideband measurement method requires numerous spectrum sweeps and the sweep time must be carefully chosen. The narrowband resonant frequency component of the RI pulses is emphasised in these measurements and its magnitude is dependent on the resolution bandwidth. The swept narrowband method can be used to extract the frequency spectra of all the corona modes but sophisticated post-processing

Stellenbosch University http://scholar.sun.ac.za/

is required to do this. A distinct advantage of this spectrum analyser method above that of the phase triggered EMI receiver method, is the CRT display which provides information on the time domain characteristics of the corona discharges during numerous periods of the source voltage.

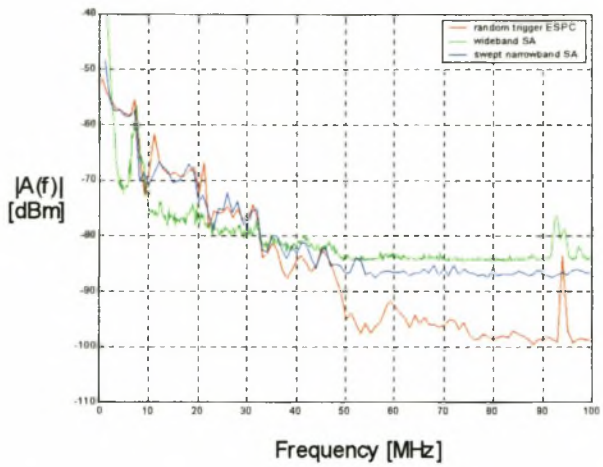

Figure 5.33: A comparison of the measured frequency spectra of positive streamers observed with the random triggering ESPC, wideband and swept narrowband SA measurement methods.

The comparison in figure 5.33 indicates a strong correlation between the random triggered ESPC method and the swept narrowband SA method with the ESPC method having a larger dynamic range. The wideband SA method does not however correlate well with either method.

Quasi-peak EMI receiver measurements displayed no dependence on the measure time. This suggests that these measurements are not accurate or repeatable and no meaningful information can be extracted from them. A possible reason could be the small amount of RI sources on the centre conductor of the short corona cage. Meaningful quasi-peak and RMS measurements are required for comparison with long corona cage measurements and for the RI current models and transform methods. A correlation between peak and quasi-peak or RMS measurements is therefore required.

The statistical properties must be extracted from time domain RI measurements in order to develop a correlation between peak and quasi-peak or RMS measurements. A fast sampling card with a large amount of memory is required for these measurements. The oscilloscope used in this thesis does not meet these specifications and can therefore not be used for the required measurements.

The presence of resonances below 38 MHz suggests that the low-frequency measurement system model proposed in chapter 4 is incomplete and must be revised.

Stellenbosch University http://scholar.sun.ac.za/

5.9 References

[1] T. Brosche, W. Hiller, E. Fauser and W. Pfeiffer, "Novel Characterization of PD Signals by Real-time Measurement of Pulse Parameters", IEEE Transactions on Dielectrics and Electrical Insulation, Vol. 6, No. 1, February 1999.

[2] G. Zingales, "The Requirements of a PD Measuring System Analyzed in the Time Domain", IEEE Transactions on Dielectrics and Electrical Insulation, Vol. 7, No. 1, February 2000, pp. 2 - 5.

[3] V.L. Chartier, D.F. Shankle and N. Kolcio, "The Apple Grove 750-kV Project: Statistical Analysis of Radio Influence and Corona-Loss Performance of Conductors at 775 kV", IEEE Transactions on Power Apparatus and Systems, Vol. PAS-89, No. 5/6, May/June 1970, pp. 867 - 889.

[4] B.M. Bailey, "Long and Short Line Radio Influence Characteristics", IEEE Transactions on Power Apparatus and Systems, Vol. PAS-89, No. 6, July/August 1970, pp. 1151 - 1155.

[5] C. Larsson, B. Hallberg and S. Israelsson, "Long-term Audible Noise and Radio Noise Performance From An Operating 400-kV Transmission Line", IEEE Transactions on Power Delivery, Vol. 3, No. 4, October 1988, pp. 1842 - 1846.

[6] G. Mole, "Basic Characteristics of Corona Detector Calibrators", IEEE Transactions on Power Apparatus and Systems, Vol. PAS-89, No. 2, February 1970, pp. 198 - 204.

[7] O. Nigol, "Analysis of Radio Noise From High-Voltage Lines I - Meter Response to Corona Pulses", IEEE Transactions on Power Apparatus and Systems, Vol. PAS-83, May 1964, pp. 524 - 525.

[8] J. Cook, "Quasi-Peak-to-RMS Voltage Conversion", IEEE Transactions on Electromagnetic Compatability, Vol. EMC-21, No. 1, February 1979.

[9] P. Sarma Maruvada, N. Hylten-Cavallius and N.T. Chinh, "Radio Noise Meter Response to Random Pulses by Computer Simulation", IEEE Transactions on Power Apparatus and Systems, Vol. PAS-93, 1974, pp. 905 - 914.

[10] R.T. Harrold, "The Spectrum Analyzer Applied to the Measurement of EHV Power Line Radio Noise", IEEE Transactions on Power Apparatus and Systems, Vol. PAS-90, 1971, pp. 1837 - 1847.

[11] W.E. Pakala and V.L. Chartier, "Radio Noise Measurements on Overhead Power Lines From 2.4 to 800kV", IEEE Transactions on Power Apparatus and Systems, Vol. PAS-90, No. 3, May/June 1971, pp. 1155 - 1165.

[12] V.L. Chartier, R. Sheridan, J.N. DiPlacido and M.O. Loftness, "Electromagnetic Interference Measurements at 900MHz on 230-kV and 500-kV Transmission Lines", IEEE Transactions on Power Delivery, Vol. PWRD-1, No. 2, April 1986, pp. 141 - 149.

[13] M.M. Khalifa, A.A. Kamal, A.G. Zeitoun, R.M. Radwan and S. El-Bedwaihy, "Correlation of Radio Noise and Quasi-Peak Measurements to Corona Pulse Randomness", IEEE Transactions on Power Apparatus and Systems, Vol. PAS-88, No. 10, October 1969, pp. 1512 - 1518.

[14] R.A. Witte, *Electronic Test Instruments*, Prentice-Hall, Inc., 1993, pp. 90 - 130.

[15] T. Williams, *EMC for product designers*, 2nd edition, Reed Educational and Professional Publishing Ltd., 1996, pp. 60 - 66.

[16] M.G. Comber and R.J. Nigbor, "Radio Noise", Transmission Line Reference Book-345kV and above, Chapter 5, EPRI, Second Edition, Revised 1987, pp. 205-256.

Stellenbosch University http://scholar.sun.ac.za/

Chapter 6

Conclusions

The most important conclusions of each chapter were summarized at the end of the chapter. The most important of these conclusions will be discussed in this chapter in light of the questions raised in section 1.3. These questions formed the basis of the research in this thesis.

(i) The experimental setup used to make measurements must be appropriate to both the facilities available to the research in this thesis and to the measurements that need to be made. It was found in chapter 3 that the most appropriate experimental setup was a small corona cage.

(ii) The small corona cage will be used to extract a wideband radio interference (RI) current source for a transmission line model. Accurate wideband measurements must therefore be made in the corona cage in the frequency range 5 kHz to 1 GHz. The small corona cage will be electrically large in a large portion of this measurement bandwidth. It must therefore be fully characterized electrically so that a high-frequency model can be extracted from it. This model can then be used to derive a calibration for the wideband measurements made in the corona cage. Only a low-frequency model was extracted in this thesis. The measurements presented can therefore only be interpreted at frequencies below 30 MHz.

(iii) Measurements are made in the corona cage by placing a calibrated resistive device between the corona cage and the laboratory grounding structure and observing the current flow through this device. The dynamic range of this measurement is increased by reducing attenuation, reflections and spurious noise in the measurement system. Of particular concern is the noise generated by spurious corona sources. These noise sources must be removed and the susceptibility of the measurement setup must be reduced. In particular, the susceptibility of the source loop greatly reduces the dynamic range of the time domain measurements.

(iv) Small corona cage RI noise measurements can be transformed to equivalent transmission line RI noise currents by duplicating exactly the electric field on the transmission line conductors in the corona cage and then applying a generation function transform to these measurements. The statistical distribution of corona sources on the transmission line is not duplicated in a small corona cage under fair weather conditions at standard temperature and pressure. Existing generation functions cannot therefore be used for the required transformation. A new generation function or an alternative transform must be derived for the small corona cage.

(v) Space charge is formed in the inter-electrode gap by the corona discharge processes. The electric field of this space charge deforms the applied electric field. The presence of significant space charge in the inter-electrode gap will therefore cause attenuation and distortion of high-frequency transients propagating along a transmission line with corona

Stellenbosch University http://scholar.sun.ac.za/

effects. A model for this transmission line with corona effects must therefore include shunt corona branch elements and a series RI voltage source. The corona branch elements for a proposed transmission line design must be extracted from a Q-V model. The most appropriate Q-V model for the 50 Hz AC source voltage conditions is a static physics-based model.

(vi) The extracted corona branch and series RI voltage source elements can be included into either time domain or frequency domain numerical codes. The numerical formulation chosen will determine the format of the extracted corona elements.

(vii) Significant RI noise only appears if the source voltage exceeds the corona inception level.

(viii) A wideband account of the RI noise frequency spectrum can be made up to about 100 MHz in the corona cage design in chapter 3. The low-frequency model extracted from the small corona cage is however only valid up to 30 MHz. Measurements above 30 MHz can therefore not be accurately interpreted.

(ix) The measured RI frequency spectrum is dependent on the magnitude and phase of the source voltage. This relationship can be extracted with various time domain and frequency domain measurement methods and must be included in the series RI voltage source of the transmission line model.

(x) Two repeatable oscilloscope measurement methods, level triggering and phase triggering, can be used to extract the frequency spectra of individual corona pulses. Level triggering can be used to find the inception levels of the various corona modes but only allows the observation of the largest corona mode at a fixed applied voltage. Phase triggering allows the observation of RI pulses at a particular phase of the source voltage waveform and therefore can be used to extract the frequency spectra of smaller corona modes.

(xi) Two repeatable peak detector EMI receiver measurement methods, the random triggering and the phase triggering methods, can be used to observe the peak RI frequency spectrum in either the entire source voltage period or only a specified section of the source voltage period. This measurement device offers the largest dynamic range and is the only measurement method used in this thesis that detects pre-inception corona modes.

(xii) Quasi-peak EMI receiver measurements displayed no dependence on the measurement time. This suggests that these measurements are not accurate or repeatable and no meaningful information can be extracted from them. This is possibly because of the small amount of RI sources on the centre conductor of the short corona cage. Meaningful quasi-peak and RMS measurements are required for comparison with large corona cage measurements and for the RI current models and transform methods. A correlation between peak measurements, which are repeatable, and quasi-peak or RMS measurements is therefore required.

(xiii) Any conversion between peak and quasi-peak or RMS measurements requires the measurement of the statistical properties of the RI noise. A fast sampling card with a large amount of memory is required to extract these statistical properties.

(xiv) Two repeatable spectrum analyser measurement methods, the wideband and swept narrowband measurement methods, can be used to measure the RI frequency spectrum.

Stellenbosch University http://scholar.sun.ac.za/

The wideband measurement method does not correlate with the EMI receiver measurements. It is therefore not an accurate measurement method. There is a strong correlation between the EMI receiver and the swept narrowband spectrum analyser measurements. The swept narrowband method can therefore be used to simultaneously extract an accurate account of the RI frequency spectra of the corona modes and the time domain characteristics of the corona discharges during numerous periods of the source voltage.

Stellenbosch University http://scholar.sun.ac.za/

Chapter 7

Recommendations

(i) A high-frequency model must be extracted from the corona cage so that the RI measurements can be interpreted over the full measurement bandwidth.

(ii) It will be much easier to characterize, shield and extract the required high-frequency model from a smaller corona cage. Such an experimental setup would require a lower source voltage and a smaller transformer could therefore be used. The source voltage harmonics that potentially corrupted the RI noise measurements in this thesis can then be removed. Reducing the inter-electrode gap length will however cause space charges to collide with the corona cage and will therefore affect the steady state of the system. The scaling of the corona cage should be further investigated.

(iii) A transform between peak and quasi-peak or RMS measurements must be derived for the small corona cage measurements since accurate quasi-peak measurements cannot be made in the small corona cage used in this thesis. Such a transform requires the measurement of the statistical properties of the RI noise. A fast sampling card must be used to make these measurements.

Stellenbosch University http://scholar.sun.ac.za/

Appendix A

Theory

A1 Generation Function Theory

A2 Time Domain Non-Linear-Element Siluciu Model Formulation

Stellenbosch University http://scholar.sun.ac.za/

Appendix A1

Generation Function Theory

A1.1 Introduction

The physical corona generation process on a transmission line will be duplicated exactly in a corona cage if the surface gradient and the statistical distribution of RI current sources on the conductors of the transmission line are recreated exactly in the corona cage. The RI current induced on a transmission line will however not be duplicated due to differences in electrical and environmental conditions in the corona cage. In order to determine the RI current that will flow on an actual transmission line from corona cage measurements, an analytical transform must be derived. This transform must be a function of geometry, line voltage and significant environmental factors so that the differences in these properties between the transmission line and corona cage can be accounted for. Such a transform is called a generation function (also known as an excitation function) and was first proposed by G.E. Adams [1]. It is suggested in [2] that the generation function approach adopted in [3] is simpler and more intuitive than that of [1]. The approach in [3] is based on the work of C.H. Gary and will be presented in this appendix.

A1.2 General Theory

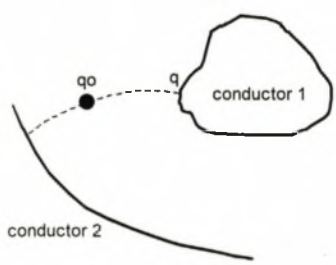

Figure A1.1: Schematic cross-sectional view of a general two conductor transmission line with a corona discharge in the inter-electrode gap (after [3]).

To simplify the development of the derivation of the generation function, the corona discharge is approximated by a plane streamer comprising a line charge per unit length (q_0) which moves along the steepest electric field gradient between the two conductors. This discharge approximation is illustrated in figure A1.1. If P_0 is the Maxwell potential coefficient between the line charge and conductor 1 in figure A1.1, then the charge per unit length (q) induced on that conductor is [2]:

$$q = -q_0 P_0 C \tag{A1.1}$$

where C is the capacitance per unit length between the two conductors. The current flow induced

Stellenbosch University http://scholar.sun.ac.za/

by the corona discharge in conductor 1 is then [2]:

$$i = \frac{dq}{dt} = -q_0 C \frac{dP_0}{dt} \tag{A1.2}$$

The aim of the generation function is to isolate those terms which are independent of the specific transmission line geometry. The remaining excitation terms will then be valid for any conductor geometry and can be used to transform corona current measurements from one geometry (e.g. the corona cage) to another geometry (e.g. a transmission line). These terms are collectively the generation function. If ρ is the distance along the electric flux line which the simplified corona discharge follows, then equation A1.2 can be alternatively expressed as [2]:

$$i = -q_0 C \frac{dP_0}{d\rho} \frac{d\rho}{dt} \tag{A1.3}$$

The $d\rho / dt$ term in equation A1.3 is the velocity of charge q_0 (i.e. the corona discharge) and $dP_0 / d\rho$ is a term that is dependent on the position of q_0 relative to the two conductors.

The current in equation A1.3 presents an impulsive form that can be described by the Fourier spectrum $F(\omega)$. It is also known that the successive impulses all have the same form but fluctuate in amplitude and time intervals around stable average values. The Fourier spectrum is therefore replaced under these conditions by the spectral density $G(\omega)$. If there are n uncorrelated corona sources per unit length along the conductor and $G_i(\omega)$ is the spectral density of the i'th corona source then the resultant RMS current measured in a bandwidth of B Hz and at a centre frequency ω_0, per unit length is [3]:

$$\Gamma = \sqrt{B \sum_{i=1}^{n} G_i^2(\omega_0)} = \frac{q_0}{\rho} \frac{d\rho}{dt} \tag{A1.4}$$

The RMS quantity Γ is called the excitation function.

A1.3 Coaxial Conductors

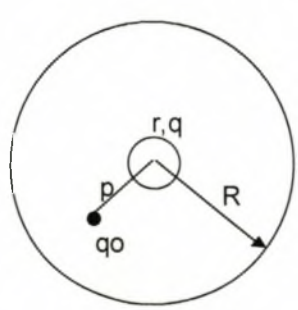

Figure A1.2: Schematic cross-sectional view of a coaxial geometry with a corona discharge in the inter-electrode gap (after [2]).

For the coaxial geometry illustrated in figure A1.2, the simplified corona discharge will move along a radial path between the two concentric cylinders. The Maxwell potential coefficient is

Stellenbosch University http://scholar.sun.ac.za/

then [2]:

$$P_0 = \frac{1}{2\pi\varepsilon}\ln\left[\frac{R^2}{R\rho - r^2}\right] \tag{A1.5}$$

For the corona cage design in chapter 3 it is known that $r/\rho < 1$ and $r/R << 1$. The spatial derivative of equation A1.5 therefore becomes [2]:

$$\frac{dP_0}{d\rho} \approx -\frac{1}{2\pi\varepsilon\rho} \tag{A1.6}$$

Substituting equation A1.6 into equation A1.3 and considering the generation function definition in equation A1.4 [2]:

$$i_{corona_cage} = \frac{C_{cc}}{2\pi\varepsilon}\frac{q_0}{\rho}\frac{d\rho}{dt} = \frac{C_{cc}}{2\pi\varepsilon}\Gamma \tag{A1.7}$$

A1.4 Single Conductor Transmission Line

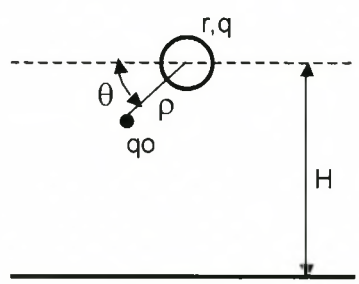

Figure A1.3: Schematic cross-sectional view of a cylinder-to-plane geometry with a corona discharge in the inter-electrode gap (after [2]).

The spatial derivative of the Maxwell potential coefficient for the single conductor transmission line cylinder-to-plane geometry illustrated in figure A1.3 is [2]:

$$\frac{dP_0}{d\rho} = -\frac{1}{[2\pi\varepsilon\rho(1-\sin\theta/2H)]} \tag{A1.8}$$

For a typical transmission line $\sin\theta/2H << 1$. Equation A1.8 therefore simplifies to [2]:

$$\frac{dP_0}{d\rho} \approx -\frac{1}{2\pi\varepsilon\rho} \tag{A1.9}$$

Substituting equation A1.9 into equation A1.3 [2]:

$$i_{Tx_line} = \frac{C_{txl}}{2\pi\varepsilon}\frac{q_0}{\rho}\frac{d\rho}{dt} = \frac{C_{txl}}{2\pi\varepsilon}\Gamma \tag{A1.10}$$

Stellenbosch University http://scholar.sun.ac.za/

A1.5 A Corona Cage to Transmission Line Transform

The RMS RI current flow on a corona cage, measured on a narrowband noise metre with bandwidth B Hz and a centre frequency ω_0, can be transformed to an equivalent RI current flow on a single conductor transmission line (i.e. a RI current that would have been measured with the same noise metre on the transmission line). This is done using the generation function transforms derived for these geometries in the previous sections. The transform is therefore derived by comparing equations A1.7 and A1.10:

$$i_{Tx_line} = i_{corona_cage}\left(\frac{C_{cc}}{C_{txl}}\right) \tag{A1.11}$$

The transform is therefore simply the ratio of the natural transmission line capacities. It should be noted that the transform in equation A1.11 is only valid for the conditions assumed in the derivation of equations A1.7 and A1.10.

A1.6 References

[1] G.E. Adams, "The Calculation of the Radio Interference Level of Transmission Lines Caused by Corona Discharges", AIEE Trans. Part III - June 1956, pp.411 - 419.

[2] M.G. Comber, D.W. Deno and L.E. Zaffanella, "Corona Phenomena on AC Transmission Lines", Transmission Line Reference Book- 345kV and above, Chapter 4, EPRI, Second Edition, Revised 1987, pp. 189-190.

[3] C.H. Gary, "The Theory of the Excitation Function: A Demonstration of its Physical Meaning", IEEE Transactions on Power Apparatus and Systems, Vol. PAS-91, January/February 1972, pp. 305-310.

Stellenbosch University http://scholar.sun.ac.za/

Appendix A2

Time Domain Non-Linear-Element Siluciu Model Formulation

A2.1 Introduction

The most accurate time domain modelling technique for transmission lines with corona and frequency-dependent effects was found to be the non-linear-element modelling methods in the literature survey presented in chapter 4. Of these models the most widely used was the Siluciu model in [1]. This model is also the easiest of the before mentioned models to implement numerically. The model uses a simplified method of characteristics to include the corona effect on a two wire transmission line. It is a phenomenological rate-type model that results in semi-linear system of partial differential equations and corresponds to a model used in one dimensional viscoplasticity [1]. The basic formulation of this model is described in this appendix.

A2.2 Model Formulation

In the general wave propagation problem, the quasi-static partial differential equations that describe the fields are [l]:

$$\frac{\partial \phi}{\partial t} + \frac{\partial v}{\partial z} = 0$$
$$\frac{\partial q}{\partial t} + \frac{\partial i}{\partial z} = 0 \qquad \text{(A2.1)}$$

These equations relate the voltage (v), current (i), charge (q) and magnetic flux (ϕ), which are all functions of time (t) and displacement along the length of the line (z). To be able to solve for the four variables in these equations, two constitutive equations that describe the simulated transmission line, are required. It is these two constitutive equations that will contain the corona branch and frequency-dependent effects. The constitutive equations for a given state $D \in (v, i, \phi, q)$ and given rates $\partial v / \partial t$ and $\partial q / \partial t$ for this state on a fixed section of line at position z are [1]:

$$\frac{\partial \phi}{\partial t} = C_v \frac{\partial v}{\partial t} + L \frac{\partial i}{\partial t} + R$$
$$\frac{\partial q}{\partial t} = C \frac{\partial v}{\partial t} + L_i \frac{\partial i}{\partial t} + G \qquad \text{(A2.2)}$$

The time and spatial dependence of the transmission line parameters C_v, L_i, C, L, R and G in equation A2.2 are known. These parameters are also functions of the charge, voltage, magnetic flux and current, a necessary requirement for including the corona and frequency-dependent

Stellenbosch University http://scholar.sun.ac.za/

effects. A unique solution can then be obtained for the current and voltage from equations A2.1 and A2.2 and a complete set of boundary conditions provided certain physical conditions are met. The first condition is wave symmetry. This requires that a propagating field perturbation propagates with the same speed in both positive and negative directions along the transmission line. This leads to the requirement [1]:

$$C_v + L_i = 0 \tag{A2.3}$$

A further requirement is that the propagating waves are real. This requires that [1]:

$$L_i^2 + LC > 0 \tag{A2.4}$$

In the special case of corona discharge (i.e. a space charge sheath) along the transmission line, the magnetic flux is approximated by [1]:

$$\phi = Li \tag{A2.5}$$

where L is the line inductance and is assumed to be constant. Substituting equation A2.5 into equations A2.2 and A2.3 results in the simplification [1]:

$$C_v = L_i = R = 0 \tag{A2.6}$$

If the propagation speed is assumed to be constant, then C is constant and equals the line capacitance. The Q-V relationship of the line in corona is also assumed to be independent of the current magnitude. The partial differential equations then simplify to [1]:

$$\begin{aligned} L\frac{\partial i}{\partial t} + \frac{\partial v}{\partial z} &= 0 \\ \frac{\partial q}{\partial t} + \frac{\partial i}{\partial z} &= 0 \\ \frac{\partial q}{\partial t} &= C\frac{\partial v}{\partial t} + G(v,q) \end{aligned} \tag{A2.7}$$

The corona effect is therefore included as a shunt conductance that is described by the time dependent Q-V relationship of the transmission line in corona. G is required to be a smooth, piecewise-continuous function of q and v and is extracted from the appropriate Q-V curve.

A2.3 References

[1] M Milhailescu-Suliciu and I Suliciu, "A Rate Type Constitutive Equation for the Description of the Corona Effect", IEEE Transactions on Power Apparatus and Systems, Vol. PAS-100, No. 8, August 1981, pp.3681 - 3685.

Stellenbosch University http://scholar.sun.ac.za/

Appendix B

Simulations

B1 The Coulomb Static/Quasi-static Field Solver

B2 A Repetitive Laplace Electric Field Solver

B3 A Physics-Based Q-V Model

Stellenbosch University http://scholar.sun.ac.za/

Appendix B1

The Coulomb Static/Quasi-static Field Solver

B1.1 Introduction

In order to recreate the exact transmission line conditions in a corona cage, the electric field on the surface of the conductor or sub-conductors of a conductor bundle must be replicated in the corona cage. The applied electric field must therefore be uniform along the length of the centre conductor. The highly energised electric field must also excite corona discharges only on the centre conductor and not on any neighbouring hardware of the experimental setup. To accomplish this, an accurate description of the electric field must be calculated. An electric field solver is therefore required.

The corona cage is electrically small at the 50 Hz power frequency. Furthermore, it is assumed that the electrodes are perfect electrical conductors (PEC) and that the inter-electrode gaps are filled with free space. A static field solver can therefore be used. Since it is the electric field and not the magnetic field that is of interest (i.e. it is an electro-quasi-static system), the PEC assumption is valid. Dielectric materials with permittivities and conductivities other than that of free space will significantly affect the electric field if they are placed in the inter-electrode gaps and must be included in the simulations. A quasi-static electric field solver is therefore required. The Coulomb solver [1] is a static/quasi-static field solver and will be used extensively throughout this thesis to calculate electric fields in the corona cage.

B1.2 Coulomb

Coulomb is a commercial three dimensional, static/quasi-static field solver that uses a boundary element method formulation [1]. It has three different solvers. The first solver calculates three dimensional electric and magnetic field distributions. This solver has a static mode for time-invariant fields and a quasi-static mode for sinusoidally varying fields. The other two solvers calculate the inductance matrix and capacitance matrix for the simulated problem. The boundary element method uses the Green's function of the simulated geometry to solve the fields. The problem does not therefore need to be enclosed in a defined, continuous boundary. This greatly simplifies the problem since the laboratory does not have well defined boundaries and is much larger than the corona cage. Excluding the ground structures in the laboratory will therefore not affect the accuracy of the solution provided that the corona cage is not placed too close to a grounding structure that is omitted in the simulation.

B1.3 Static vs. Quasi-Static Mode

The static and quasi-static solutions will not differ significantly if the simulated geometry is electrically small and if there are no lossy dielectrics present in the simulation model. The corona cage design used in this thesis is electrically small at the applied 50 Hz frequency. The type of solution used is therefore determined by the dielectric properties of the materials used. A

Stellenbosch University http://scholar.sun.ac.za/

guideline for determining wether the static or quasi-static mode should be used is given in [1]: Firstly find the maximum (ε_m) and minimum (ε_e) dielectric constants as well as the maximum (σ_m) and minimum (σ_e) conductivities of the materials included in the simulation model, then:

- If $\omega\varepsilon_e >> \sigma_m$, a static dielectric analysis should be performed.
- If $\omega\varepsilon_m >> \sigma_e$, a static conductivity analysis should be performed.
- If neither of the above two conditions apply then a full quasi-static, lossy dielectric analysis should be performed.

These guidelines will be used throughout the thesis to determine the type of analysis that must be performed.

B1.4 Solution Accuracy

The accuracy of the solution is determined by the gridding (i.e. the division of the surfaces defined in the simulation model into small squares) applied to the boundaries of the problem and by the convergence criteria of the solver. When non-linear models are solved, an iterative procedure is used to find the solution. The accuracy of the iterative procedure is specified by the non-linear exit criteria of the field solver. This is defined as the ratio of the solution in the previous iteration to that of the current iteration. The default ratio is 0.03. Decreasing the ratio will increase both the accuracy and the simulation time. The iterative matrix solver accuracy is determined by the matrix solver exit criteria which is by default set to 10^{-4}. For greater accuracy this value can be decreased to a minimum of 10^{-7}. This was however found to be unnecessary for the simulations in this thesis and significantly increased the simulation time. The default value was therefore used. The accuracy of the solution is also dependent on the size and position of the boundary elements (i.e. the gridding) that are defined in the simulation model. For an accurate solution the following suggestions are made in [1]:

- Boundary elements should be square.
- Each side of a surface or volume should have two or more elements.

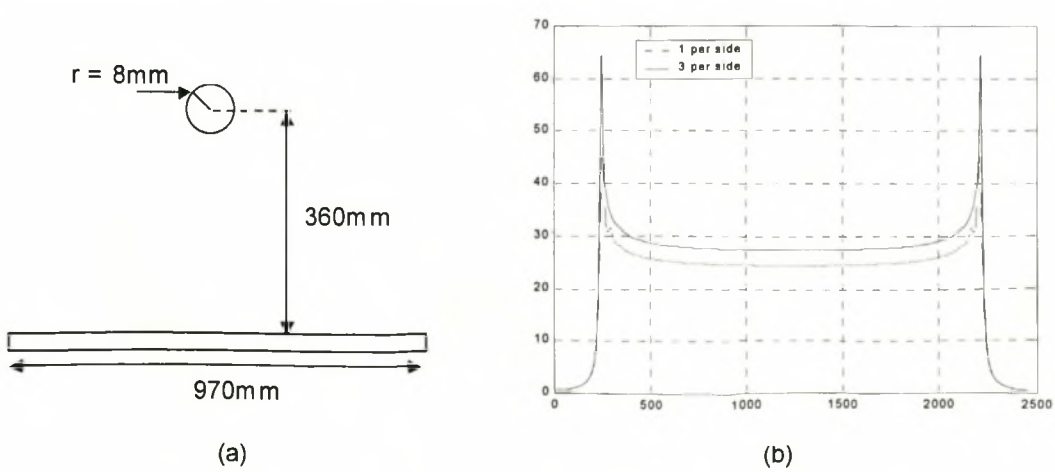

Figure B1.1: (a) Simulated geometry and (b) the simulation results showing the convergence of the solution accuracy as the number of boundary elements per side is increased.

Stellenbosch University http://scholar.sun.ac.za/

A wire-to-plane geometry, with dimensions similar to those of the actual corona cage used in this thesis, is used to investigate the solution accuracy while varying the minimum number of boundary elements on the wires circumference. The result in figure B1.1 (b) shows that a minimum of three boundary elements are required for an accurate solution.

- Boundary element nodes should be aligned across the interface of surfaces.

- The minimum number of elements (n) on each side, with length l, of two surfaces which are separated by a distance d, is [1]:

$$n \geq c\frac{l}{10d} \tag{B1.1}$$

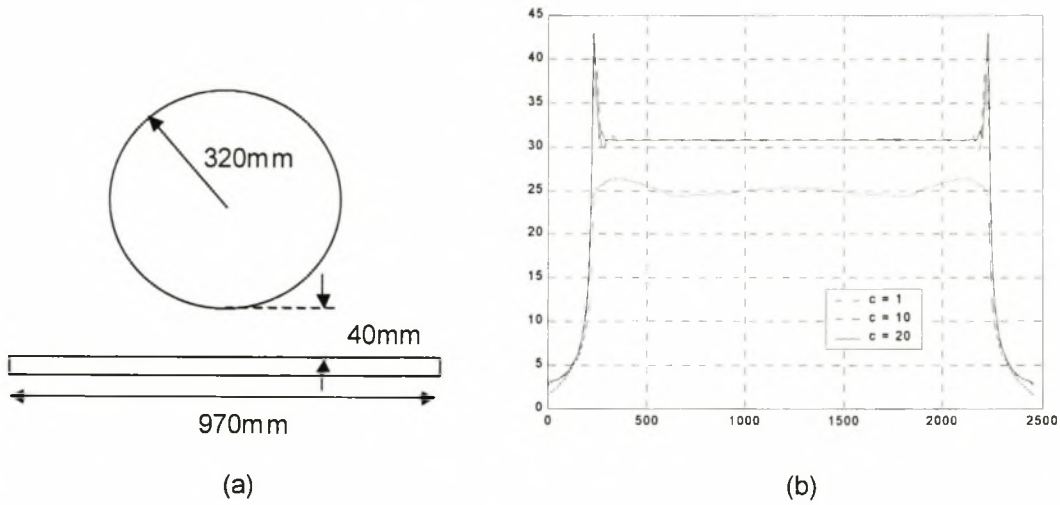

Figure B1.2: (a) The simulated geometry and (b) the simulation results showing the convergence of the solution accuracy as the number of boundary elements on adjacent surfaces is increased.

A cylinder-to-plane geometry with dimensions similar to those of the actual corona cage used in this thesis is used to investigate the solution accuracy while varying the minimum number of boundary elements on adjacent surfaces. The result in figure B1.2 (b) shows that the suggested gridding in equation B1.1, with c = 1, is not sufficient for an accurate solution. The electric field solution on the surface of the conductors is only sufficiently accurate for c > 20. This result was also checked and confirmed for parallel-plate and coaxial geometries.

The above mentioned guidelines were tested and the modifications have been noted. These modified guidelines ensure that the simulation results are accurate. They have therefore been strictly adhered to in the Coulomb simulations throughout this thesis.

B1.5 References

[1] Users and Technical Manual, Coulomb, *Three-dimensional Electric Field Solver*, Integrated Engineering Software, Version 3.0, 1997.

Stellenbosch University http://scholar.sun.ac.za/

Appendix B2

A Repetitive Laplace Electric Field Solver

B2.1 Introduction

An electric field solver is required to accurately solve for the electric field distribution inside the corona cage structure while allowing the dimensions of the corona cage to be changed during the simulation. In this way it will be possible to optimise the dimensions of the guard rings that are used to ensure a uniform electric field distribution along the length of the corona cage. The simplest technique which can accomplish this is the Repetitive Laplace method (also known as the finite difference method). The formulation and implementation of this method is discussed in this appendix.

B2.2 Assumptions

The Repetitive Laplace method requires that the simulation model is bounded by a continuous boundary which has a defined electric potential. The simulation is greatly simplified if the simulated model uses a single orthogonal set of co-ordinate axis. Since the corona cage conductors are all cylindrical, a cylindrical co-ordinate system is used. The grounded boundary conditions are therefore also cylindrical. The corona cage is surrounded by a grounded shield cage. The only important boundary dimension is therefore the distance of the centre conductor from the two end-surfaces of the boundary cylinder .The cylindrical geometries of the simulation model have azimuthal symmetry. The problem is therefore reduced to two spacial dimension (i.e. the radial distance and the distance along the centre conductor).

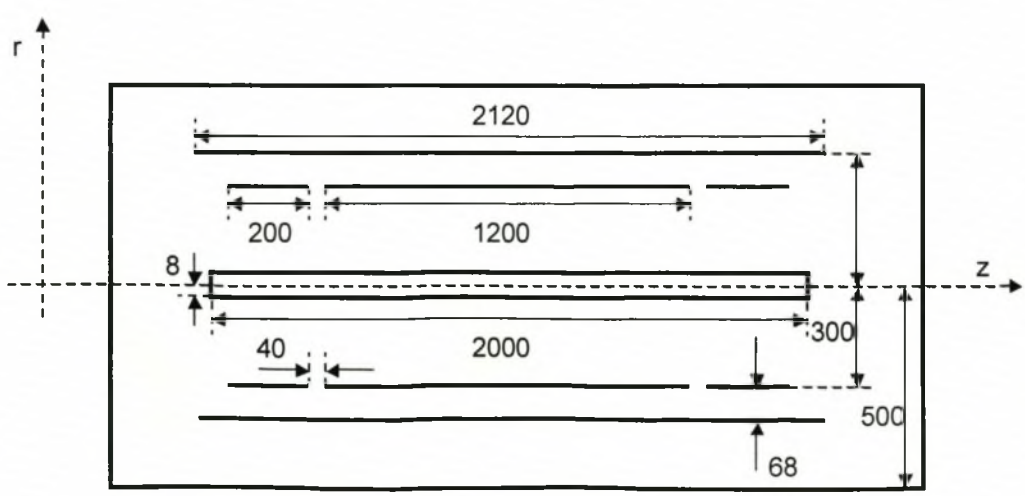

Figure B2.1: Schematic diagram of the simulation model showing the important dimensions (all dimensions are in millimetres).

Stellenbosch University http://scholar.sun.ac.za/

B2.3 Formulation

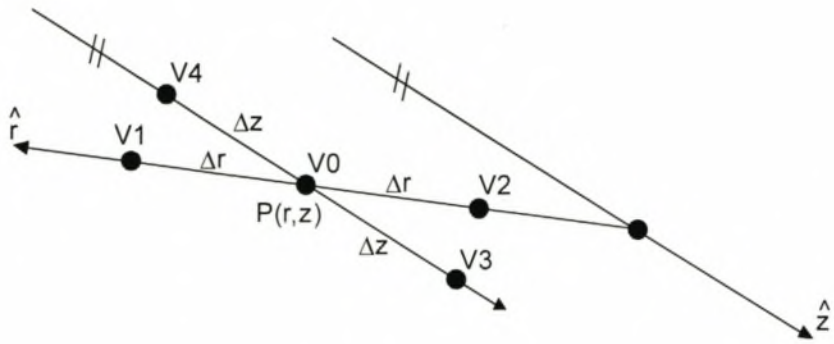

Figure B2.2: Schematic diagram of a few grid points in the simulation space illustrating the finite difference formulation of Laplace's equation in cylindrical co-ordinates.

The two-dimensional Laplace equation in cylindrical co-ordinates is [2]:

$$\nabla^2\Phi = \frac{1}{r}\frac{\partial}{\partial r}\left(r\frac{\partial\Phi}{\partial r}\right) + \frac{\partial^2\Phi}{\partial z^2} \tag{B2.1}$$

The solution of this equation can be approximated by discretising the simulation space as illustrated in figure B2.2 and noting that the potential at any point in the simulation space is the average of the four surrounding points [1]. For the co-ordinates as defined in figure B2.2 and $\Delta r = \Delta z \neq 0$, equation B2.1 is therefore approximated by:

$$V_0 = \frac{1}{4}\left(V_3 + V_4 + \left(\frac{r - 0.5\Delta r}{r}\right)V_2 + \left(\frac{r + 0.5\Delta r}{r}\right)V_1\right) \tag{B2.2}$$

The electric field at point P in figure B2.2 is therefore approximated by:

$$|\overline{E}| = \sqrt{\left(\frac{V_1 - V_2}{2\Delta r}\right)^2 + \left(\frac{V_3 - V_4}{2\Delta z}\right)^2} \tag{B2.3}$$

The formulation must now be implemented in a program.

B2.4 Implementation

The Repetitive Laplace formulation discussed in the previous section is implemented in both Matlab and Visual Basic. The simulated geometry is firstly entered and then discretised with a specified Δr. The Laplace equation in equation B2.1 has a unique solution for a complete set of boundary conditions. The approximation in equation B2.2 will therefore converge to this unique solution after a certain number of iterations. The number of iterations required for a convergence can be greatly reduced by making an accurate initial guess of the unique solution The electric field distribution of the coaxial corona cage geometry is known if the conductors are

Stellenbosch University http://scholar.sun.ac.za/

assumed infinitely long (see section 3.3). This field distribution will therefore be used for the initial guess. The Repetitive Laplace simulation will therefore determine the effect of finite conductor length on the electric field. After the initial guess is made, the electric field is re-calculated at each iteration by calculating the new electric potential at each non-boundary point using the update equation (i.e. equation B2.2) and substituting these values into equation B2.3.

The Matlab simulation time is much longer than that of a Visual Basic code if numerous conditional statements are used in the simulation. A matrix-shift method was therefore implemented in Matlab. The electric potential at all non-boundary points in the simulation space is therefore updated at the same time. In the Visual Basic code, the electric potential at each non-boundary point is updated individually. The convergence of the Visual basic code is considerably faster than that of the Matlab matrix-shift implementation. The Visual Basic implementation will therefore be used in this thesis.

B2.5 Simulation Results

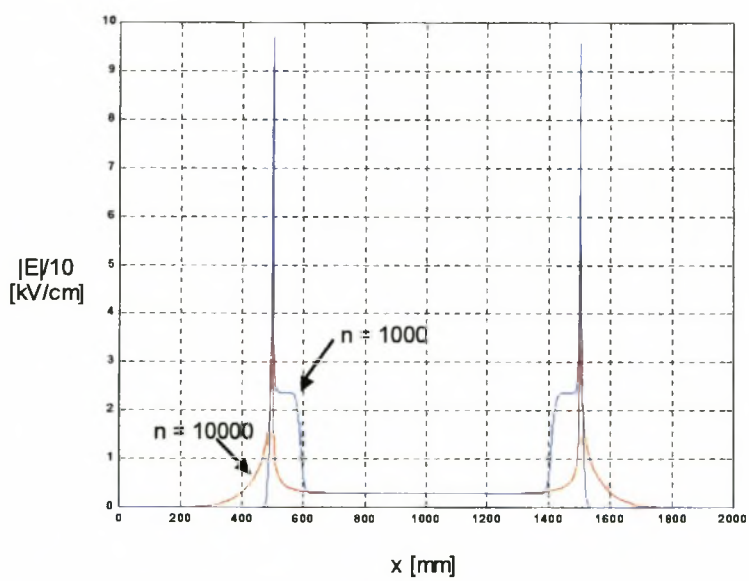

Figure B2.3: The electric field extracted from various Repetitive Laplace simulations with different simulation times indicating the convergence of the solution.

The electric field extracted from various Repetitive Laplace simulations with different simulation times is plotted in figure B2.3 and indicates that the solution converges after about 20000 iterations.

B2.6 References

[1] J.D. Kraus, *Electromagnetics :with applications*, 5th edition, The McGraw-Hill Companies, Inc., 1999, pp. 552 - 556.

[2] S. Ramo, JR Whinnery and T van Duzer, *Fields and Waves in Communication Electronics*, 3rd edition, John Wiley and Sons, 1994.

Stellenbosch University http://scholar.sun.ac.za/

Appendix B3

A Physics-Based Q-V Model

B3.1 Introduction

In order to determine the non-linear corona branch elements of a transmission line with corona effects, the charge-voltage (Q-V) relationship of the modelled system must be extracted. This cannot be measured for a proposed transmission line design. A Q-V model is therefore required so that the relationship can be extracted from simulation results. Mathematical models proposed in the literature do not include recombinations and cannot therefore be used for steady state sinusoidal voltage sources. Physics-based models do include a recombination law and will therefore be used in this thesis. Since the frequency of the source voltage is 50 Hz, a static model can be used. Such a model is proposed in [1]. The formulation, implementation in Matlab code and the extraction of the results will be presented in this appendix.

B3.2 Assumptions

- The corona sheath only forms when the voltage exceeds the inception level.
- The corona sheath is uniform in both cross-section (i.e. it is a right-circular cylinder) and along the length of the conductor.
- The electric field in the corona sheath is constant and equal to the inception field level.
- The critical field level and the inception field level are assumed equal. The positive inception level and the negative inception level are also assumed equal.
- The space charge mobilities are: $\mu^+ = 1.5 \times 10^{-4} \ m^2 / V.s$ and $\mu^- = 1.8 \times 10^{-4} \ m^2 / V.s$.
- The space charge is assumed to have no significant mass and therefore has no potential energy (i.e. it has no inertia). Thermal agitation and diffusion of the space charge is also assumed negligible. The space charge displacement is therefore determined only by the applied electric field.

Stellenbosch University http://scholar.sun.ac.za/

B3.3 Formulation

The model is implemented in Matlab code using a finite difference method (i.e. the source voltage is discretised into finite time intervals). The three dimensional space charge shells used in the model are simplified to one dimensional point charges due to the symmetry of the electric field in the coaxial corona cage. The point charges are therefore fully defined by their radial position and charge.

The simplified finite difference physics laws used in the model for a coaxial geometry with centre conductor radius a, cage radius R and with N charge shells, each with radius r_n and charge q_n where $(n \notin [1,2,3,\ldots N])$ are:

- Emission Law: The instantaneous charge on the centre conductor (q) is the sum of the instantaneous applied charge and the charge induced by the space charge shells in the inter-electrode gap:

$$q(a,t) = Cv(a,t) + \sum_{n=1}^{N} q_n(r_n,t).(1 - \frac{C\ln(r_n / a)}{2\pi\varepsilon_0}) \tag{B3.1}$$

  The charge of the space charge shell emitted during the iteration is then the difference between the instantaneous charge on the centre conductor in equation B3.1 and the inception charge value $Q_0 = Cv_0$:

$$q_n(r_n,t) = \begin{cases} q(a,t) - Cv_0 & ,q > Cv_0 \\ 0 & ,q \leq Cv_0 \end{cases} \tag{B3.2}$$

- Displacement Law: The displacement of charge shell emitted in each iteration is modified since the field is highly divergent near the surface of the centre conductor:

$$dr = \sqrt{1 + 2.dt.\mu.E(a,t)/a} \tag{B3.3}$$

  The displacement of the charge shells emitted in previous iterations (i.e. in a non-divergent field is:

$$dr = \mu.E(r,t).dt \tag{B3.4}$$

- Recombination Law: The charge of a charge shell colliding with another charge shell is:

$$q_n(r_n,t) = \begin{cases} q_n(r_n,t) - q_m(r_m,t) & ,q_n(r_n,t) > q_m(r_m,t) \\ 0 & ,q_n(r_n,t) \leq q_m(r_m,t) \end{cases} \tag{B3.5}$$

  If a charge shell collides with the centre conductor, its charge is removed from the charge shell and added to the centre conductor charge. If a charge shell collides with the corona cage, the charge is removed from the shell and from the system.

Stellenbosch University http://scholar.sun.ac.za/

B3.4 Implementation

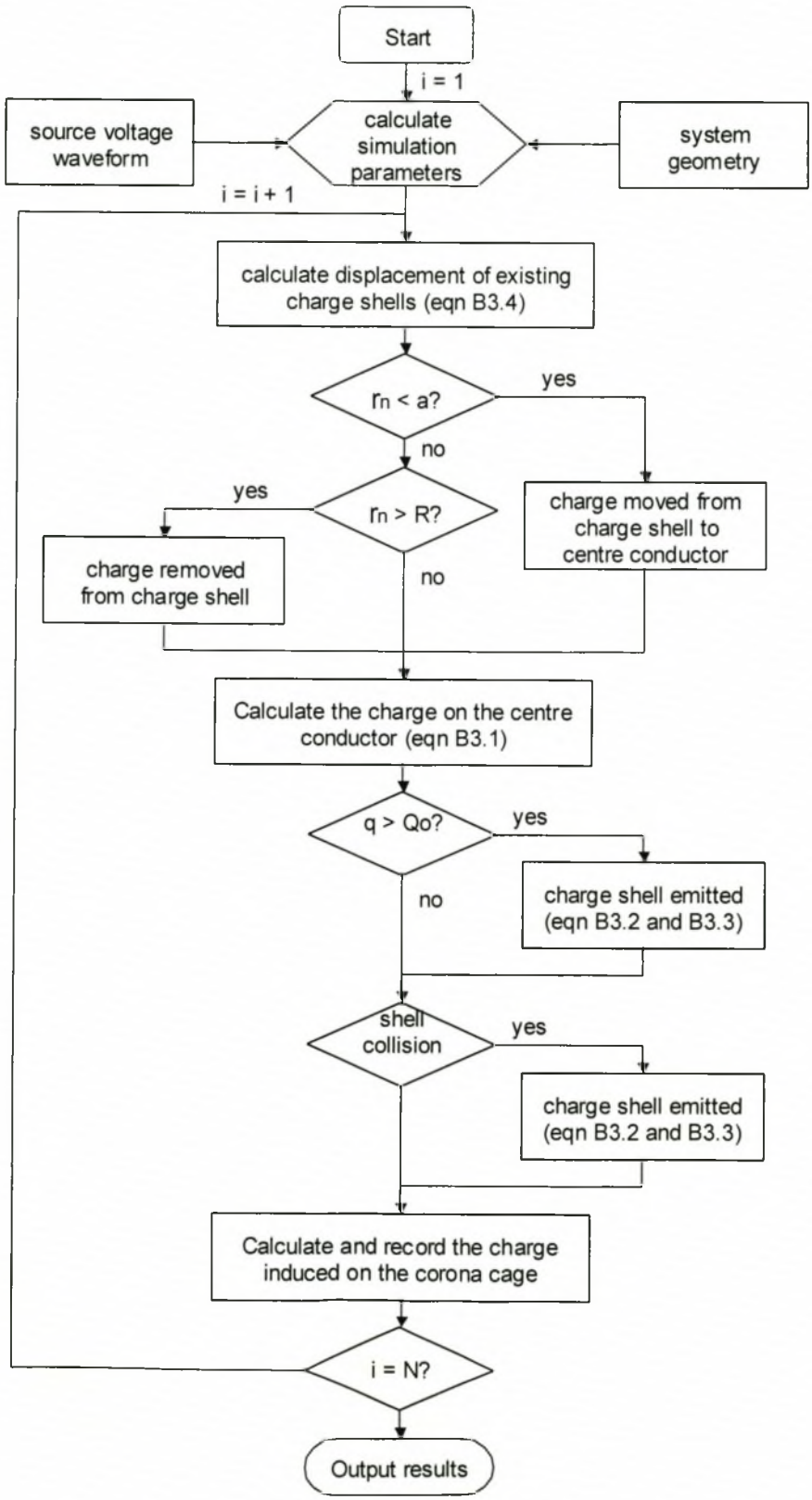

Figure B3.1: Flow diagram of the Matlab implementation of the Q-V model

Stellenbosch University http://scholar.sun.ac.za/

B3.5 Simulation Results

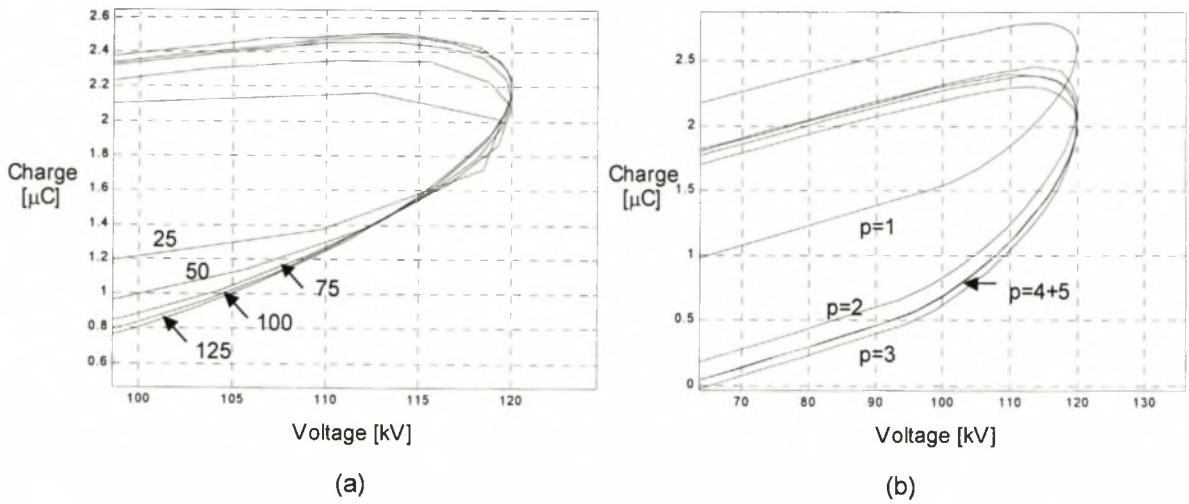

Figure B3.1: Simulation results indicating the convergence of the simulation for (a) various discretisations and (b) the number of source voltage periods.

The code was found to converge to an accurate solution for a discretisation of 125 samples per period and only after 4 periods of the source voltage. The choice of 125 samples per period is a compromise between simulation time and accuracy. The accuracy obtained is sufficient for the purposes of this thesis. Best convergence is obtained for a dicretisation of more than 200 samples per second. The simulation time is however excessive due to the numerous conditional statements which are slowly processed in Matlab. Implementing the model in Visual Basic will significantly reduce the simulation time.

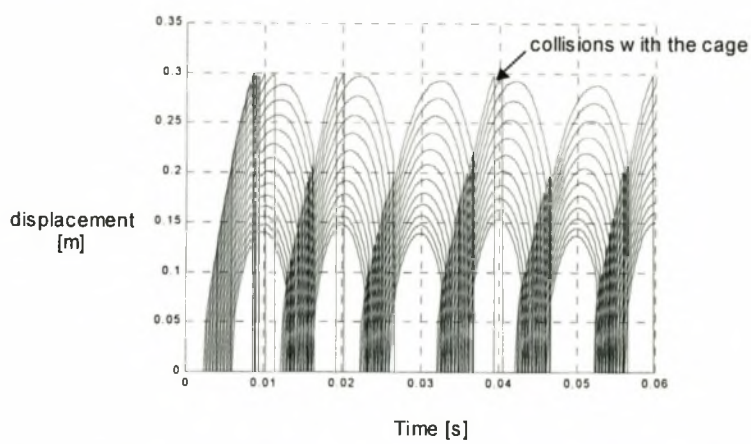

Figure B3.3: Displacement of the charge shells in the simulation.

B3.6 References

[1] JJ Clade, CH Gary and CA LeFevre, "Calculation of Corona Losses Beyond the Critical Gradient in Alternating Voltage", IEEE Transactions on Power Apparatus and Systems, Vol. PAS-88, No. 5, may 1969.

Stellenbosch University http://scholar.sun.ac.za/

Appendix C

Metrology

C1 Extraction of Natural Transmission Line Parameters

C2 Extraction of Low-Frequency Dielectric Properties

C3 Transfer Impedance Measurement

C4 An Alternative Q-V Curve Measurement Method

Stellenbosch University http://scholar.sun.ac.za/

Appendix C1

Extraction of Natural Transmission Line Parameters

C1.1 Introduction

In order to model the corona cage RI noise, the corona cage must be completely characterized. This is done by extracting the natural transmission line parameters of the three conductor transmission line formed by the centre conductor, corona cage and grounding structure, which includes the shield cage and guard rings. The extracted RLC parameters are used throughout sections 3.4 and 3.5 to determine if attenuation or reflections of the noise pulses is potentially a problem and, if so, they are used in the design of devices that can rectify the problem.

C1.2 Approach

The problem stated in section C1.1 must be divided into two problems: extraction of a low-frequency and a high-frequency set of RLC parameters. For the low-frequency parameter extraction problem, the corona cage is electrically small and currents flowing in the conductors are bulk currents. Lumped parameters can therefore be extracted from quasi-static measurements and the resistance and inductance associated with surface current flow can be ignored. This problem will be addressed in this appendix.

The corona cage model presented in this thesis will therefore be restricted to the low-frequency regime defined by the measurements in this appendix. The high-frequency parameter extraction problem involves an electrically large corona cage and surface current flow. Distributed corona cage parameters must therefore be extracted. This will not be attempted in this thesis and will form part of future research where the bandwidth of the extracted corona cage model will be extended.

The extraction of the low-frequency model parameters will be divided into two sections: the extraction of the capacitance matrix and then the extraction of the inductance matrix. To extract the capacitance matrix a high-impedance low-current measurement circuit will be used. The only significant field is therefore the electric field and all inductances in the measurement system can be ignored. To measure the inductance matrix, a low-impedance high-current measurement circuit will be used. The magnetic field is no longer insignificant and the inductances in the measurement circuit must be included. Since the capacitance matrix has already been extracted, the inductance matrix can be calculated.

C1.3 Low-Frequency Parameter Extraction

Sinusoidal signals in the frequency range 150 kHz to 300 MHz will be applied to the centre

Stellenbosch University http://scholar.sun.ac.za/

conductor-to-corona cage transmission line and the corona cage-to-grounding structure transmission line in a calibrated measurement setup.

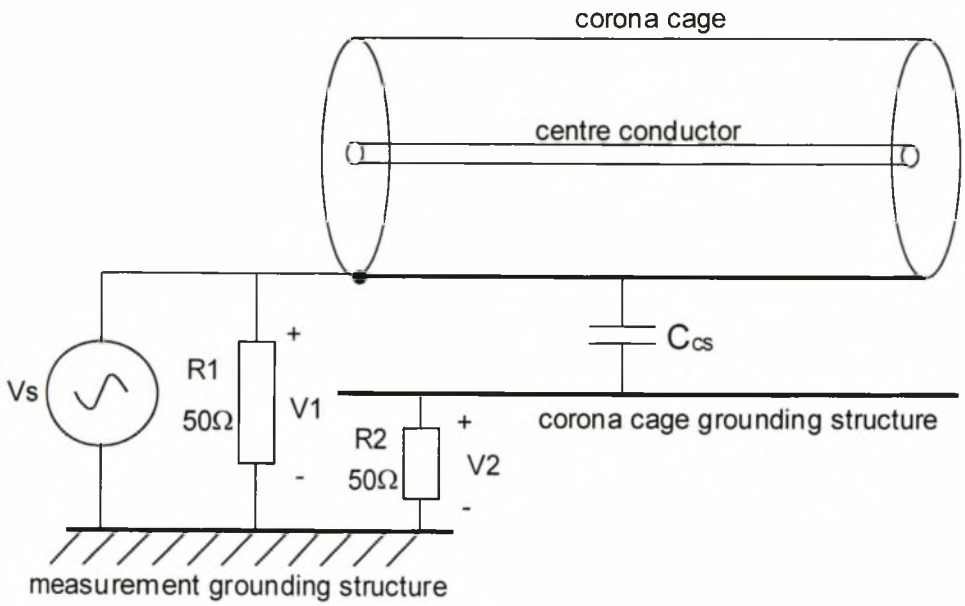

Figure C1.1: Schematic diagram of the quasi-static, high-impedance, low-current measurement circuit used to extract the corona cage-to-grounding structure capacitance.

The impedance of the 50 Ω measurement resistors used in the measurement setup illustrated in figure C1.1 is measured in the frequency range 300 kHz to 300 MHz. The results indicate that they are indeed 50 Ω across the measurement bandwidth. The voltages across these two resistors are measured in the frequency range 150 kHz to 300 MHz. The ratio of the two voltages is:

$$\frac{V_2}{V_1} = \frac{j\omega}{j\omega + (1/R_2 C_{CS})} \tag{C1.1}$$

The corona cage-to-grounding structure capacitance can therefore be calculated from equation C1.1.

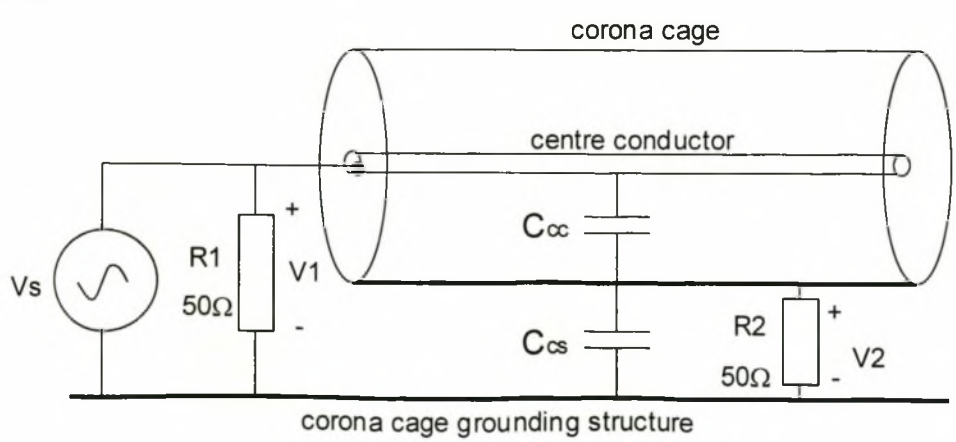

Figure C1.2:Schematic diagram of the quasi-static, high-impedance, low-current measurement circuit used to extract the centre conductor-to-corona cage capacitance.

Stellenbosch University http://scholar.sun.ac.za/

The ratio of the two measured voltages is:

$$\frac{V_2}{V_1} = \left(\frac{C_{cc}}{C_{cc} + C_{cs}}\right) \frac{j\omega}{j\omega + (1 / R_2(C_{CC} + C_{CS}))} \tag{C1.2}$$

The centre conductor-to-corona cage capacitance can therefore be calculated from equation C1.2. It should be noted that the high-impedance low-current assumption is only valid at low frequencies and results should therefore only be extracted from low-frequency measurements.

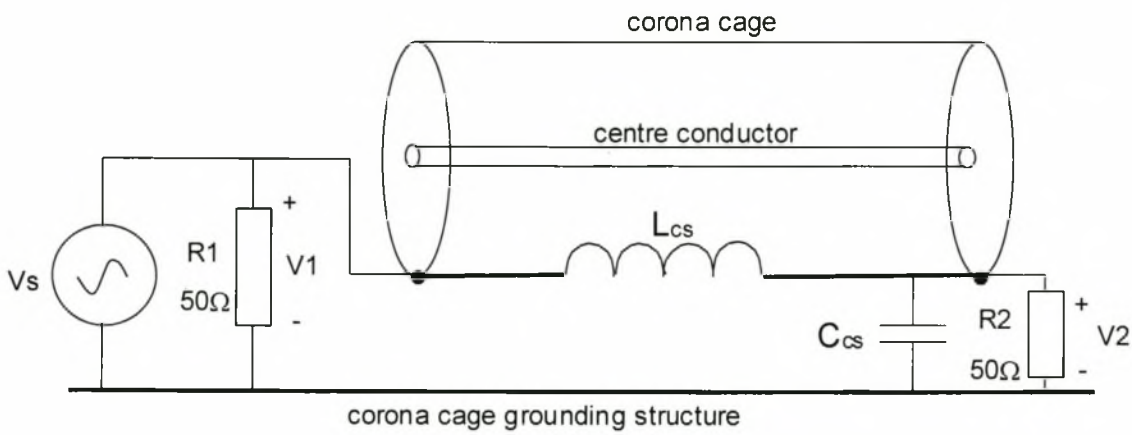

Figure C1.3:Schematic diagram of the quasi-static, low-impedance, high-current measurement circuit used to extract the corona cage-grounding structure inductance.

The ratio of the two measured voltages is:

$$\frac{V_2}{V_1} = \left.\frac{(1 / L_{CS}C_{CS})}{s^2 + s(1 / R_2C_{CS}) + (1 / L_{CS}C_{CS})}\right|_{S=j\omega} \tag{C1.3}$$

Since C_{CS} is known, the corona cage-to-grounding structure inductance can be calculated from equation C1.3.

C1.4 Measurement Results

The extracted LC parameters are tabulated in table 3.1 of chapter 3. The measured results indicate that the parameters extracted from the corona cage-to-grounding structure transmission line is only valid for frequencies below 30 MHz. This will therefore be the frequency limit of the calibrated corona measurements made in the corona cage in this thesis. Measured frequency components above 30 MHz will be affected by the frequency response of the measurement system. The measurement system must therefore be calibrated in this higher frequency regime by extracting a high-frequency model for the corona cage. This will be investigated in future research.

Stellenbosch University http://scholar.sun.ac.za/

Appendix C2

Extraction of Low-Frequency Dielectric Properties

C2.1 Introduction

The cradle structure built to support the corona cage and tension the centre conductor was built out of pressed board since it was available and inexpensive in comparison to high voltage insulation material such as perspex. Material used in high voltage applications such as this corona cage support structure must have a high breakdown strength and a low surface conductivity. These properties must be extracted as well as the permittivity of the material since this will affect the capacitance matrix of the corona cage. Tests show that pressed board has a sufficiently high breakdown strength to withstand the electric field in the corona cage. In this appendix, the measurement technique used to extract the permittivity is described.

C2.2 Approach

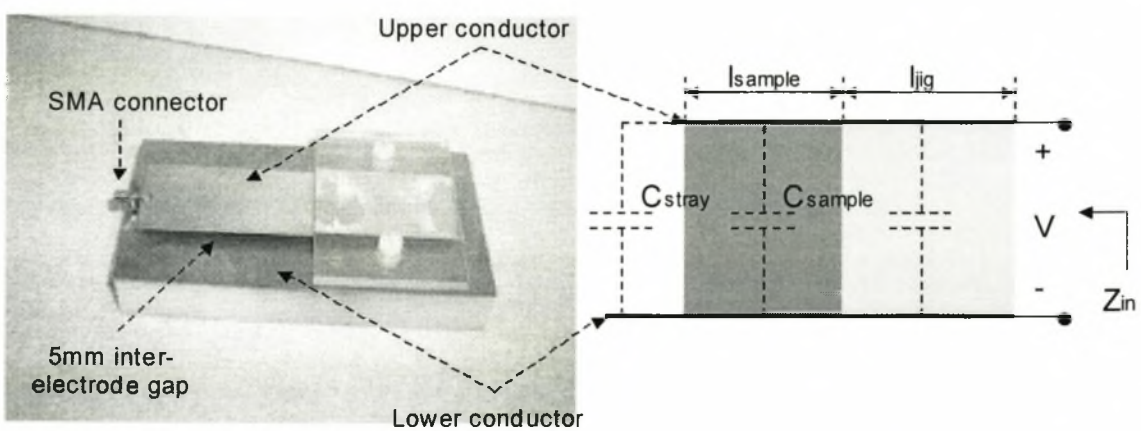

(a) (b)

Figure C2.1: (a) A photograph of the jig used to extract the dielectric properties of pressed board and (b) its quasi-static equivalent lumped parameter circuit.

The jig used to extract the dielectric properties is shown in figure C2.1 (a). It consists of a parallel plate transmission line held in place by a tightening device made out of non-conductive material, perspex. A dielectric sample with thickness equal to the distance between the parallel plates is placed between a section of the plates. The tightening device is used to hold the sample firmly in place. The S_{11} parameter is then measured on the HP 8753 ANA and is used to calculated the input impedance [1]:

$$Z_{input} = Z_0 \frac{1+S_{11}}{1-S_{11}} \tag{C2.1}$$

Stellenbosch University http://scholar.sun.ac.za/

The highest measurement frequency is chosen low enough to ensure that the measurement jig is electrically small. A frequency range between 300 kHz and 100 MHz is therefore chosen. The quasi-static equivalent circuit in figure C2.1 (b) can therefore be used to find the low-frequency permittivity of the pressed board sample.

The capacitance (C) of the parallel plates with length l, width w and separation d is [1]:

$$C = \frac{\varepsilon_r \varepsilon_0 wl}{d} \qquad [F] \qquad \text{(C2.2)}$$

The relative permittivity of the sample, with known length, area and thickness, can be calculated using equation C2.2 if C_{sample} in figure C2.1 is known. To find C_{sample}, both C_{jig} and C_{stray} must be known. These are obtained by measuring the input impedance of the jig with no dielectric sample in place. In this case $C_{sample} + C_{jig}$ is the ideal free-space capacitance of the parallel plate capacitor. C_{stray} is the stray capacitance due to the edge effects of the finite length plates. The value of C_{jig} and C_{stray} is:

$$C_{jig} = \frac{\varepsilon_0 . w}{d} l_{jig} \qquad [F] \qquad \text{(C2.3)}$$

$$C_{stray} = \frac{-\operatorname{Im}(Z_{input})}{\omega} - \frac{\varepsilon_0 w(l_{jig} + l_{sample})}{d} \qquad [F] \qquad \text{(C2.4)}$$

The sample is then inserted into the jig and the input impedance is again measured. C_{sample} Can now be calculated as:

$$C_{sample} = \frac{-\operatorname{Im}(Z_{input})}{\omega} - (C_{jig} + C_{stray}) \qquad [F] \qquad \text{(C2.5)}$$

The relative permittivity is then determined by substituting C_{sample} and the dimensions of the sample into equation C2.2.

C2.3 Measurement Results

The choice of sample was discussed in section 3.3 where it was decided to investigate the permittivity of both a section from the board edge (i.e. a sample that has the surface treatment) and also a sample from the centre of the board (i.e. a sample that has no surface treatment).

Stellenbosch University http://scholar.sun.ac.za/

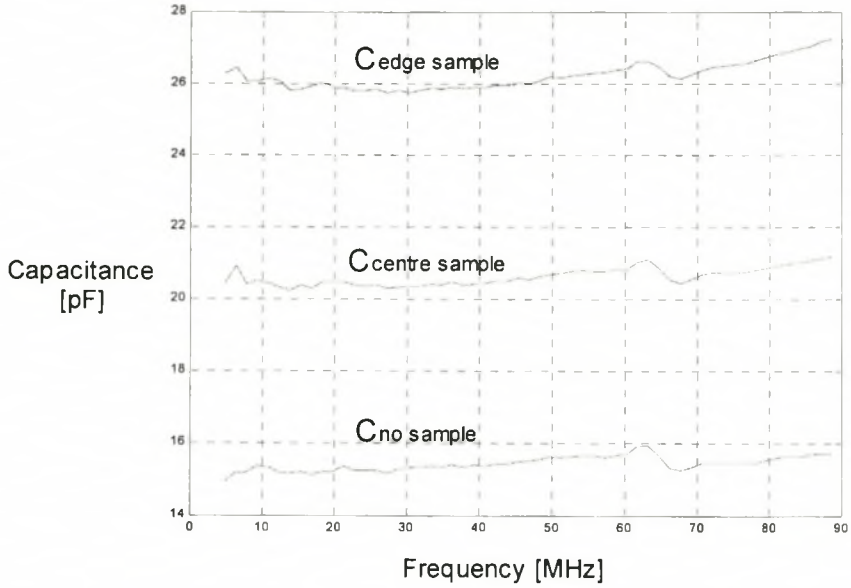

Figure C2.2: The measured capacitances of the jig in figure C2.1.

It was found that a quasi-static region between 300 kHz and 90 MHz could be used to extract the permittivity. The average measured values over this frequency band were: $C_{stray} = 3.49$ pF, $C_{jig} =$ 12.08 pF, $(C_{sample})_{edge} =$ 12.37 pF and $(C_{sample})_{centre} =$ 6.76 pF. From these values the relative permittivity of the surface treated board is 2.94 and that of the untreated board is 1.93.

C2.4 References

[1] S. Ramo, J.R. Whinnery and T. van Duzer, *Fields and Waves in Communication Electronics*, 3rd edition, John Wiley and Sons, 1994.

Stellenbosch University http://scholar.sun.ac.za/

Appendix C3

Transfer Impedance Measurements

C3.1 Introduction

The transfer impedance of various ground loops in the experimental setup must be measured in order to quantify the susceptibility of the experimental setup to interference fields and objectively compare various shielding methods used to improve this susceptibility. The two most important ground loops in the experimental setup were identified in section 3.4. These are the source loop and the measurement loop. The measurement technique used to measure the transfer impedance of these two ground loops is presented in this appendix.

C3.2 Approach

The transfer impedance per unit length is defined in [1] as:

$$Z_T^{'}(\omega) = \frac{V_{DM}(\omega)}{I_{CM}(\omega)l} \qquad [\Omega / m] \qquad \text{(C3.1)}$$

The approach adopted in this appendix will therefore be to inject a known sinusoidal current in the frequency range 150 kHz to 1 GHz onto the relevant ground loop and then measure the differential mode voltage across the relevant measurement resistor.

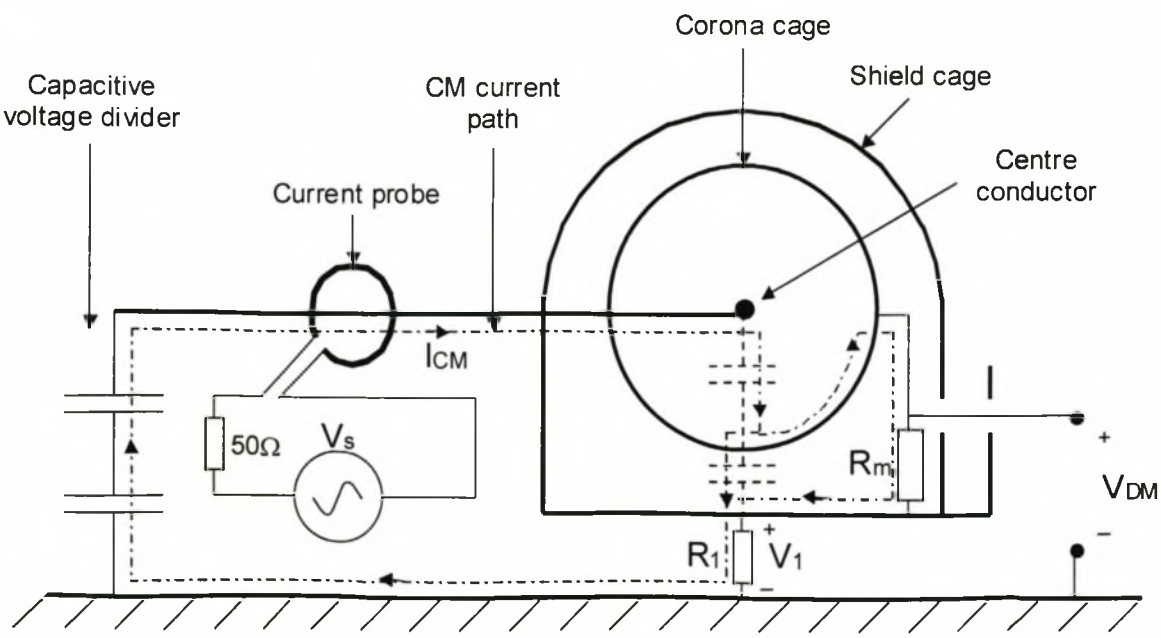

Figure C3.1: Schematic diagram of the source loop transfer impedance measurement setup

Stellenbosch University http://scholar.sun.ac.za/

The setup used to measure the transfer impedance of the source loop is presented in figure C3.1. The common mode current is injected into the source loop by applying a voltage across the terminals of a current probe. Since the impedance of the source loop is not known, the current cannot be calculated from the applied voltage magnitude and current probe transfer impedance. A low-impedance resistor (R_1 in figure C3.1) is therefore placed in series with the connection between the laboratory and corona cage grounding structures. The resistance value chosen is small (a value of $0.5\,\Omega$ is chosen for measurements in this thesis) so that the source loop impedance remains low at all measured frequencies. The CM current is therefore:

$$I_{CM} = \frac{V_1}{R_1} = 2V_1 \qquad [\mathrm{A}] \qquad \text{(C3.2)}$$

The possible significant common mode current paths are indicated in figure C3.1. One such path flows through the corona cage measurement resistor (R_m). The DM voltage is therefore measured across this resistor since it excludes the current flowing in the measurement loop (now disconnected). The transfer impedance of the source loop can therefore be isolated:

$$Z_T = \frac{V_{DM}}{2V_1} \qquad [\Omega] \qquad \text{(C3.3)}$$

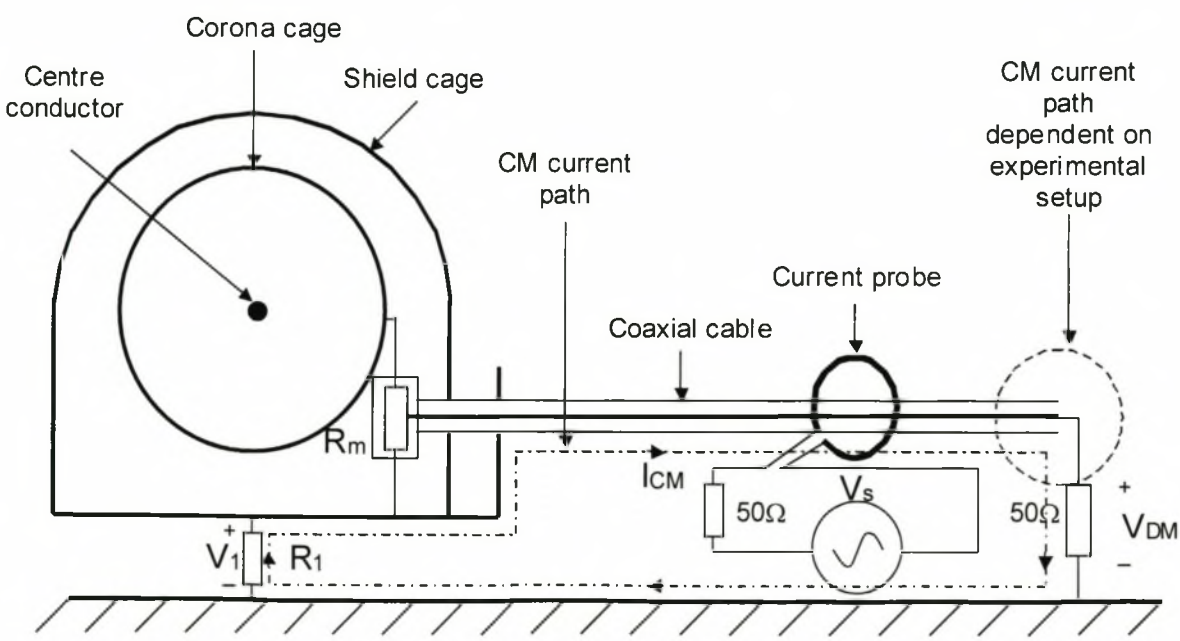

Figure C3.2: Schematic diagram of the measurement loop transfer impedance measurement setup

The setup used to measure the transfer impedance of the measurement loop is presented in figure C3.2. The common mode current is injected onto the outer conductor of the coaxial measurement cable with a current probe. The same low-impedance resistor is used to measure the injected CM current in the measurement loop and is again placed in series with the connection between the laboratory and corona cage grounding structures. Equation C3.2 is therefore used to calculate the

Stellenbosch University http://scholar.sun.ac.za/

CM current flow in the ground loop. A 50 Ω shunt resistor is used to model the input impedance of the measurement device at the coaxial cable termination. The DM voltage is therefore measured across this resistor. The source loop is disconnected during the measurements so that no other CM current loops are formed. The transfer impedance of the measurement loop is therefore isolated and is calculated using equation C3.3.

C3.3 References

[1] M.A. van Houten, Ph.D. Thesis, "Electromagnetic Compatibility in High-Voltage Engineering", October 1990.

Stellenbosch University http://scholar.sun.ac.za/

Appendix C4

An Alternative Q-V Curve Measurement

C4 .1 Introduction

In order to extract the shunt corona branch elements from the transmission line model proposed in chapter 4, the charge-voltage (Q-V) relationship of the system must be derived. Various numerical Q-V models were investigated in section 4.2 which will enable the prediction of the Q-V relationship from simulations. The accuracy of these models must however be confirmed by comparison with the actual corona cage Q-V curves extracted from measurements. The measurement technique used in the literature involves the real-time integration of the current flow between the corona cage and the grounding structure. This method requires additional hardware (i.e. an integrator) and a change in experimental setup from the one used to measure the RI current. An error is also inherent to the non-ideal real-time integrator used to make the measurement. An alternative Q-V curve measurement technique is proposed in this appendix which uses the same experimental setup as the RI current measurements and does not make an integration error.

C4 .2 Approach

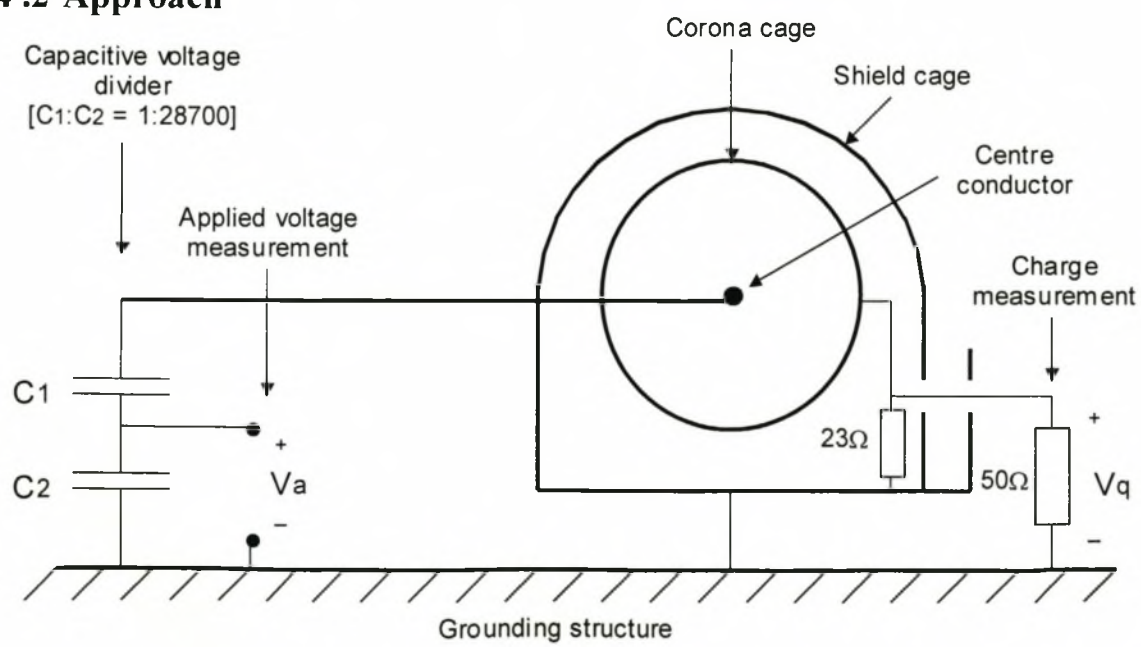

Figure C4.1: The experimental setup used to make the Q-V curve measurements in this thesis.

The experimental setup used to measure the Q-V curves in this thesis is illustrated in figure C4.1. The applied voltage is measured off the capacitive voltage divider. This measurement device offers a low impedance path to the laboratory grounding structure for high frequency signals. The measured waveform is therefore filtered with an ideal low-pass filter (cutt-off frequency =

Stellenbosch University http://scholar.sun.ac.za/

1MHz) in Matlab post-processing. The current flow between the corona cage and grounding structure is measured from the corona cage measurement resistor. This current is integrated numerically with an ideal integrator in Matlab post-processing. It was discussed in section 4.5 that the frequency response of the RI current measurement system used for these Q-V measurements does not have a significant effect below 500 kHz (i.e. the bandwidth of the Q-V curve measurements). No calibration of the measurement system is therefore required.

C4 .3 Matlab Post-Processing

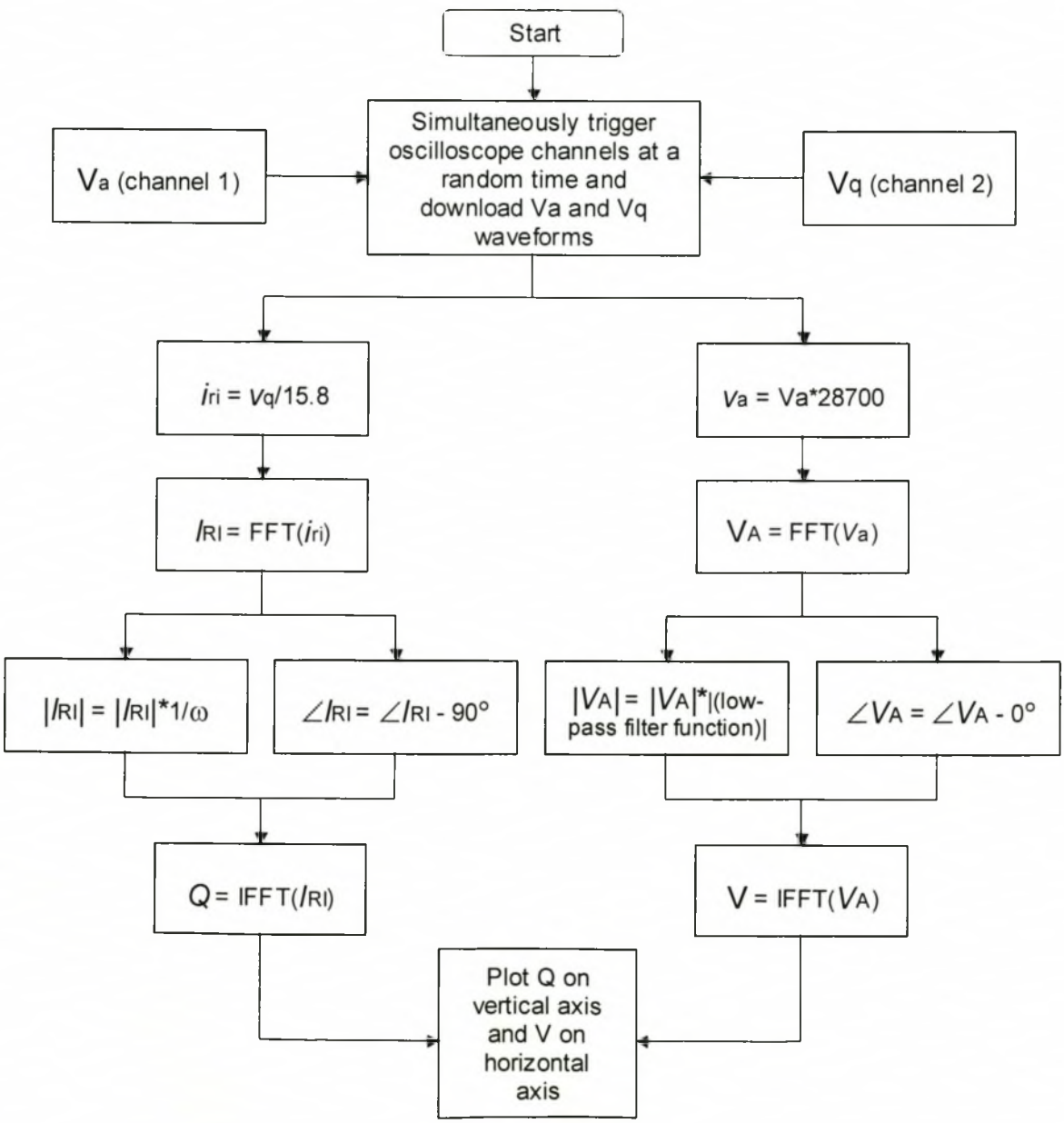

Figure C4.2: Flow diagram of the Matlab post-processing required for the alternative Q-V curve measurement method presented in this appendix

Stellenbosch University http://scholar.sun.ac.za/

Appendix D

Hardware

D1 Coaxial Shunt Design

D2 High Voltage Coupling/Decoupling Capacitor Design

D3 External-Trigger Hardware Design

Stellenbosch University http://scholar.sun.ac.za/

Appendix D1

Coaxial Shunt Design

D1.1 Introduction

The measurement of the corona cage RI noise, presented in chapter 5, requires a series resistive element. The element must have a resistance matched to that of the cage-to-shield surge impedance and a negligible reactive component. The power rating of the element must be sufficient to meet the instantaneous and average power content of the pre-breakdown RI current. The use of series carbon resistors to meet these requirements is not possible due to the large inductance of such a series combination. The coaxial shunt is a concentric ring of equal value resistors surrounding a central measurement resistor. The power and ohmic requirements can therefore be met while maintaining small size and low inductance. Th design of such a coaxial shunt is discussed in this appendix.

D1.2 Design Equations

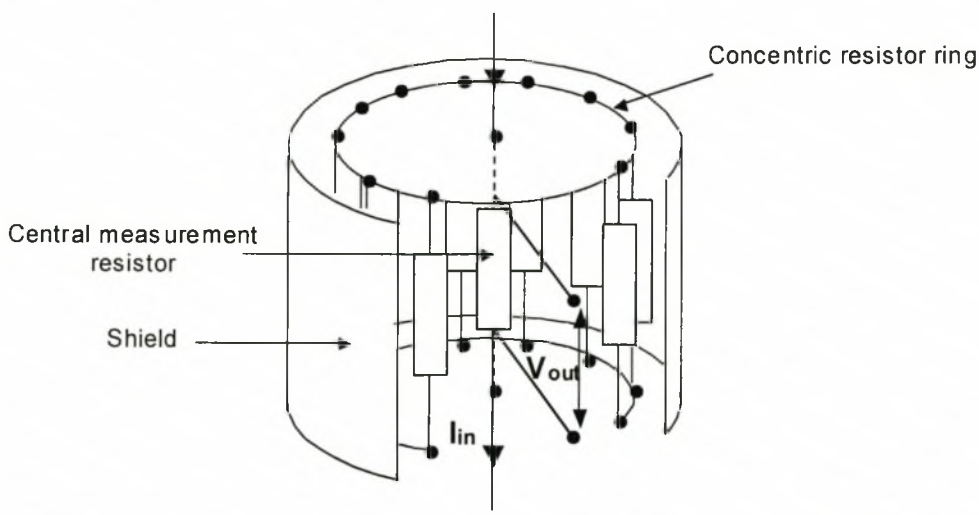

Figure D1.1: A cut-away schematic view of the coaxial shunt design used in this thesis.

For a coaxial shunt of resistance R_{cs} and power rating P_{cs}, the voltage across the N shunt resistors of resistance R and power rating P is:

$$V = \sqrt{P_{cs} R_{cs}} = \sqrt{PR} \tag{B3.1}$$

The resistance of the coaxial shunt is:

$$R_{cs} = \frac{R}{N} \tag{B3.2}$$

Stellenbosch University http://scholar.sun.ac.za/

From equations B3.1 and B3.2:

$$N \geq \frac{P_{cs}}{P} \tag{B3.3}$$

D1.3 Measured specifications

The coaxial shunt required in this thesis has a 43 Ω resistance, a power rating of 2 W and is made up of 0.25 W carbon resistors. It is therefore realized with 24 × 1 kΩ resistors.

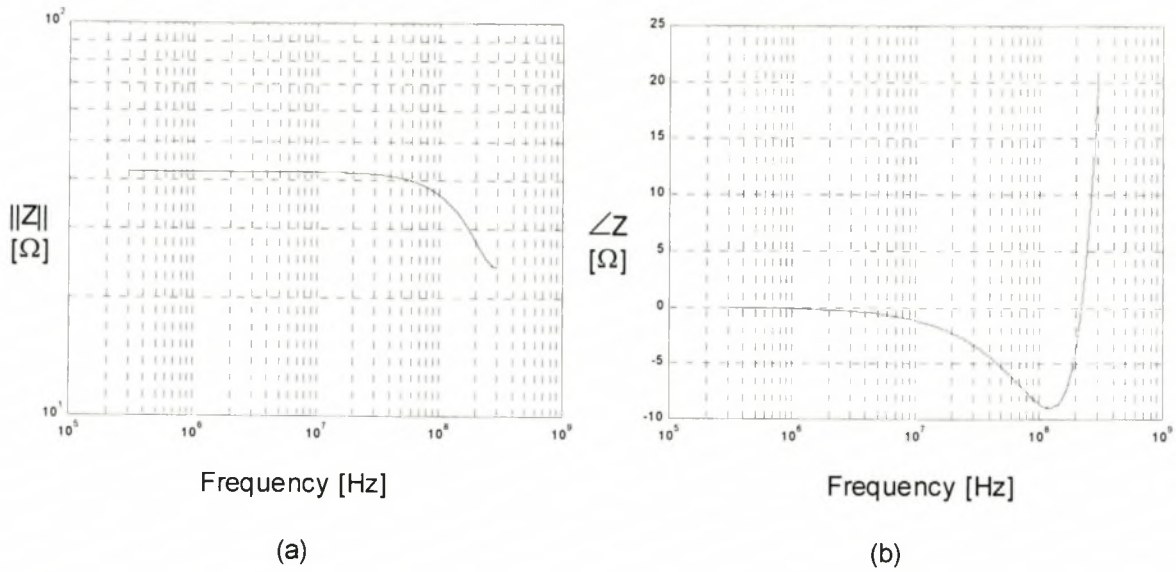

Figure B1.2: The measured (a) magnitude and (b) phase of the impedance of the coaxial shunt design used in this thesis.

The measured impedance of the coaxial shunt design used in this thesis is presented in figure B3.2. It indicates that the inductance is negligible in the frequency range DC to 200 MHz.

Stellenbosch University http://scholar.sun.ac.za/

Appendix D2

High Voltage Capacitor Design

D 2.1 Introduction

The susceptibility of the source loop, defined in section 3.4, to spurious noise is of particular concern since it causes significant interference with serious consequences for the time domain measurements. The use of a LC filter to reduce this susceptibility in a specific frequency band requires that a high voltage capacitor must be designed. Extraction of a high-frequency model also requires that high-frequency signals are coupled onto and decoupled from the highly energized centre conductor of the experimental setup discussed in chapter 3. A high voltage capacitor is therefore also required. The design of such a capacitor is discussed in this appendix.

D 2.2 Design Specifications

The high voltage capacitor must offer a high impedance path to the grounding structure at the source voltage frequencies and a low impedance path at the spurious noise frequencies. It must also offer a low impedance path in the coupling/decoupling frequency band. The capacitor must also have negligible internal partial discharges at a maximum applied voltage of 120 kV (peak). Finally the coupling/decoupling point must be connected to the centre conductor at the edge of the guard rings so that the transmission line along which the signals propagate has uniform electrical properties. The capacitor must therefore be able to fit easily into the experimental setup at this point.

D 2.3 Capacitor Design

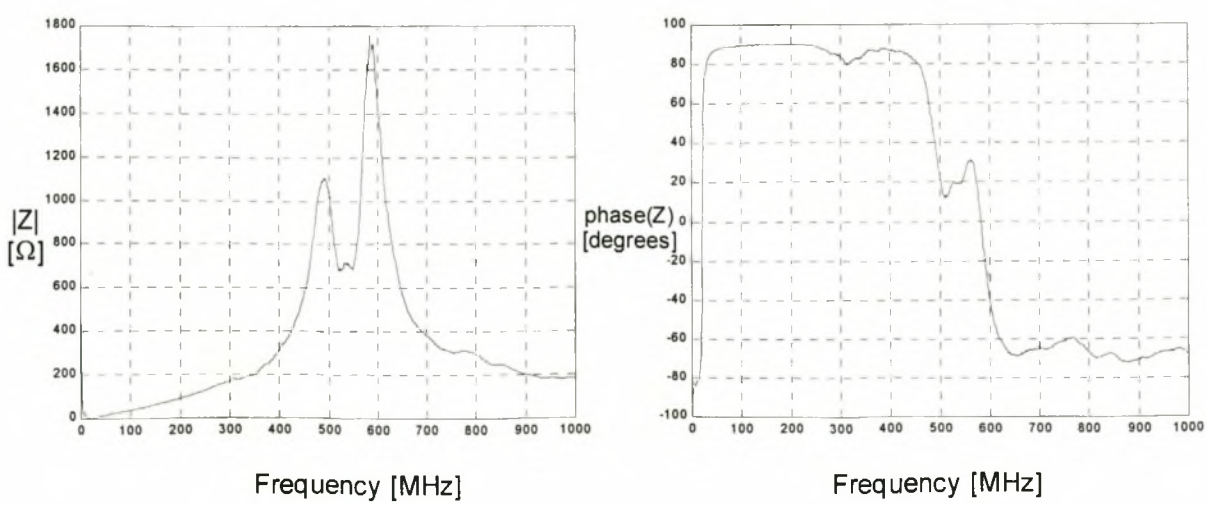

Figure D2.1: The measured impedance of the HV capacitor used.

Stellenbosch University http://scholar.sun.ac.za/

The impedance of the high voltage ceramic disk capacitor used (i.e. a Panasonic ECKD series capacitor) is presented in figure D2.1. The plots indicate that the capacitor becomes inductive at 20 MHz. The capacitor can therefore not be used to remove the spurious noise in the source ground loop in chapter 3 above this frequency. The capacitor can however be used to couple a high-frequency signal onto the centre conductor in the frequency range 700 MHz to 1000 MHz since the impedance of the capacitor is almost equal to the surge impedance of the centre conductor-to-corona cage transmission line in this frequency band. The maximum rated RMS withstand voltage of the capacitor is 15 kV and its capacitance is 1000 pF. The capacitor was tested under high voltage 50 Hz AC conditions and it was found that the maximum peak withstand voltage was 18 kV. A series connection of at least 7 of these capacitors is therefore required to withstand the maximum applied voltage of 120 kV (peak). The total capacitance of the series capacitance branch is therefore 143 pF. A shunt connection of 4 of these series capacitance branches will be used for a total shunt capacitance of 570 pF.

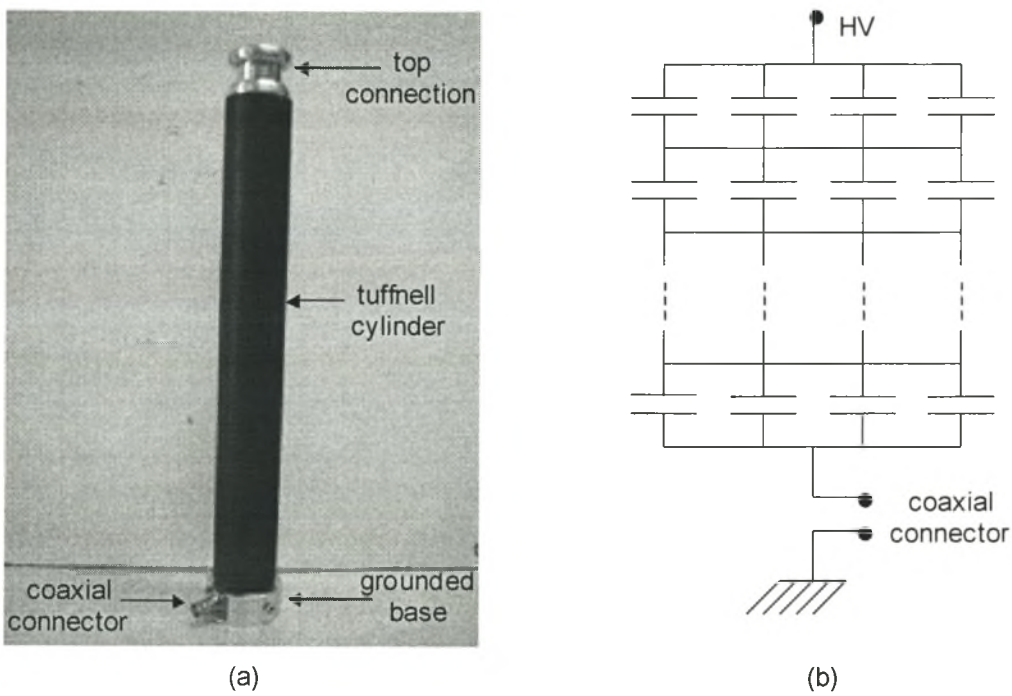

Figure D2.2: (a) A photograph and (b) a circuit diagram of the high voltage capacitor design.

The capacitors are mounted as in the circuit diagram in figure D2.2 (b) on a printed circuit board (PCB). To prevent partial discharges on the PCB and capacitor connectors, the PCB is submersed in transformer oil which is contained in a sealed cylinder. To prevent surface current flow on the outer surface of the cylinder, the cylinder is made out of tuffnell.

Stellenbosch University http://scholar.sun.ac.za/

Appendix D3

External-Trigger Hardware Design

D 3.1 Introduction

In order to observe the frequency spectra of various corona modes under AC voltage conditions, it is necessary to trigger the EMI receiver peak measurements on a specific phase of the 50 Hz source voltage at each frequency in the measured frequency band. The duration of measurement is then restricted to a specified phase width so that only one region of the source voltage waveform is observed. The design of an external-triggering mechanism that can perform this task is the subject of this appendix.

D 3.2 Approach

The ESPC EMI receiver used in this thesis allows external-trigger control of the measurements through an external TTL logic pin and a software special function (special function 52 for a negative TTL edge). The approach adopted in this design is therefore to sample the 50 Hz source waveform in order to determine the exact phase of the source voltage applied to the corona cage. A TTL-level pulse is then outputted on the ESPC external-trigger pin at a specified phase. Care must be taken that no significant phase delay occurs in the triggering hardware so that the phase triggered on is equal to the phase applied to the corona cage. The external-trigger pin must be only pulsed once on request of the PC control program that also controls the GPIB port (see appendix E1 for a discussion on the GPIB control program).

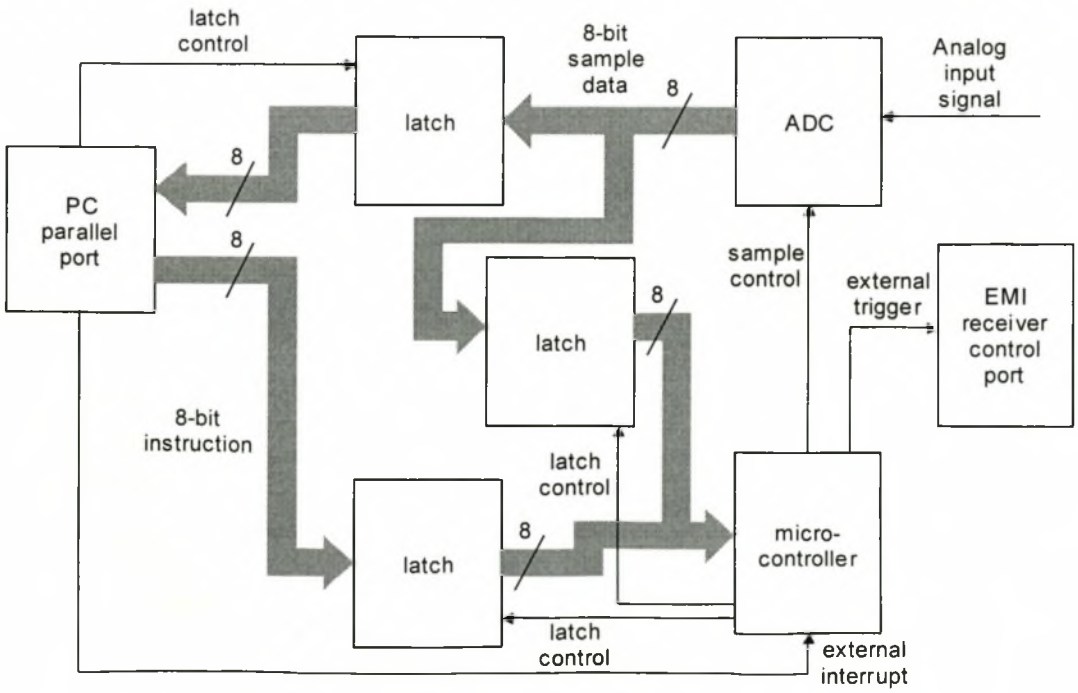

Figure D3.1: Block diagram of the proposed external-trigger hardware.

Stellenbosch University http://scholar.sun.ac.za/

The analog-to-digital converter (ADC) and the external-trigger pin of the ESPC are both controlled by a micro-controller, the ATMEL 90S1200, and not directly by the PC. This control ensures accurate timing that is independent of the PC processor speed and minimal time delay between the phase calculation and a trigger pulse. The ADC chosen is the National Semiconductor ADC1061. This device accommodates sample/hold micro-controller control. It is a fast-sampling device and a sample rate of 50 ks/s is used to sample the 50 Hz source waveform. This corresponds to a sample point every 0.36° of the input waveform. Due to the choice of micro-controller, only 8-bit precision is used. The analog input signal is biased around 2.5 V DC and the maximum signal level measured is 5 V (AC peak). The minimum change in voltage level that can be detected by the device is therefore 20 mV. The analog input voltage level is used to determine the phase of the input waveform. The accuracy of the device is therefore dependent on the rate of change of the source voltage.

D 3.3 Software Control

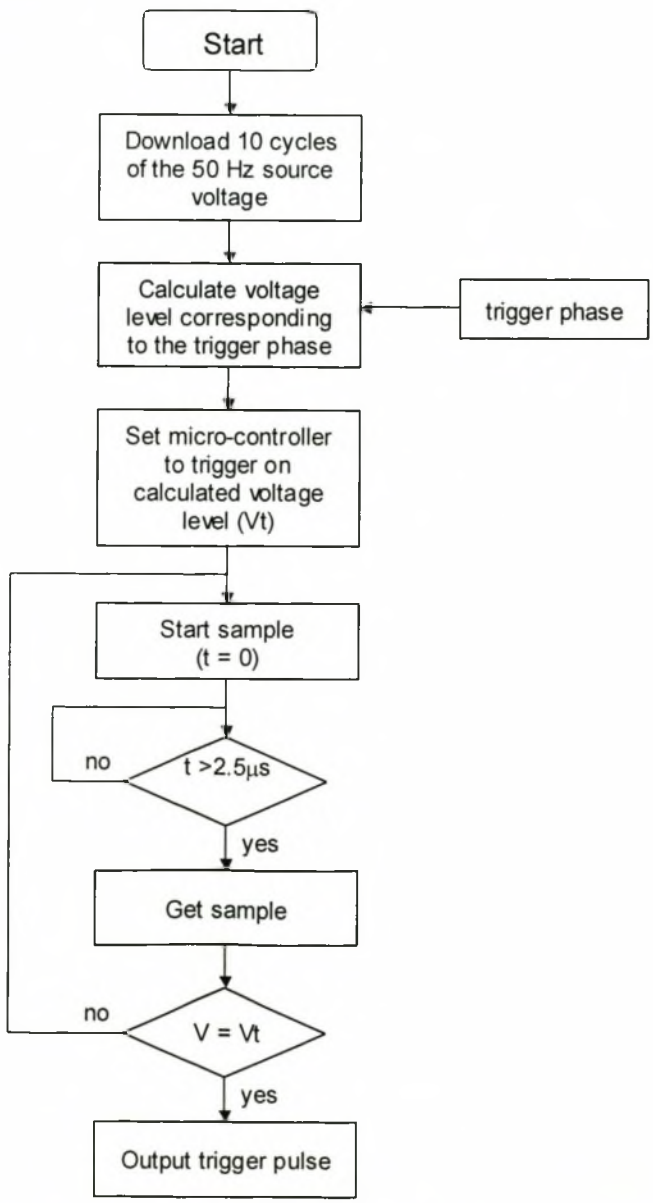

Figure D3.2: Flow diagram of the external-trigger hardware PC control.

Stellenbosch University http://scholar.sun.ac.za/

Appendix E

GPIB Instrument Control

E1 ESPC EMI Receiver Control

E2 HP 8562A Spectrum Analyser Control

Stellenbosch University http://scholar.sun.ac.za/

Appendix E1

ESPC EMI Receiver Control

E 1.1 Introduction

Two EMI receiver measurement methods were used in chapter 5 to make an accurate account of the corona cage RI noise frequency spectrum. Both methods require PC control of the ESPC EMI receiver via the GPIB port of the device. The GPIB port installed in the PC is the National Instruments PCI-GPIB IEEE 488.2. This PC control is described in this appendix.

E 1.2 Useful Commands from the Instruction Set

• GPIB control:	*IDN?	- Query device identification
	* SRE 16	- Set Service Request Enable mask register so that device indicates when the output message is available
• Initializing ESPC:	SPECIALFUNC 20 ON	- Measurement units = dBm
	DETECTOR PEAK	- Select the peak detector
	MEASUREMENT:TIME 10 ms	- Set measurement time to 10 ms
	BANDWIDTH:IF 10 kHz	- Set the IF bandwidth to 10 kHz
• Setting Frequency:	FREQUENCY 150 kHz	- centre frequency = 150 kHz
	FREQUENCY:STEPSIZE 1 MHz	- Set the step size to 1 MHz
	FREQUENCY INCREMENT	- Increment the centre frequency by the set step size
• Triggering:	LEVEL?	- Start measurement and output measured level on GPIB port
	SPECIALFUNC 52 ON	- Switch to external- triggering
	LEVEL:LASTVALUE?	- Output measured level from external-trigger measurement

Stellenbosch University http://scholar.sun.ac.za/

E 1.3 Visual Basic Implementation

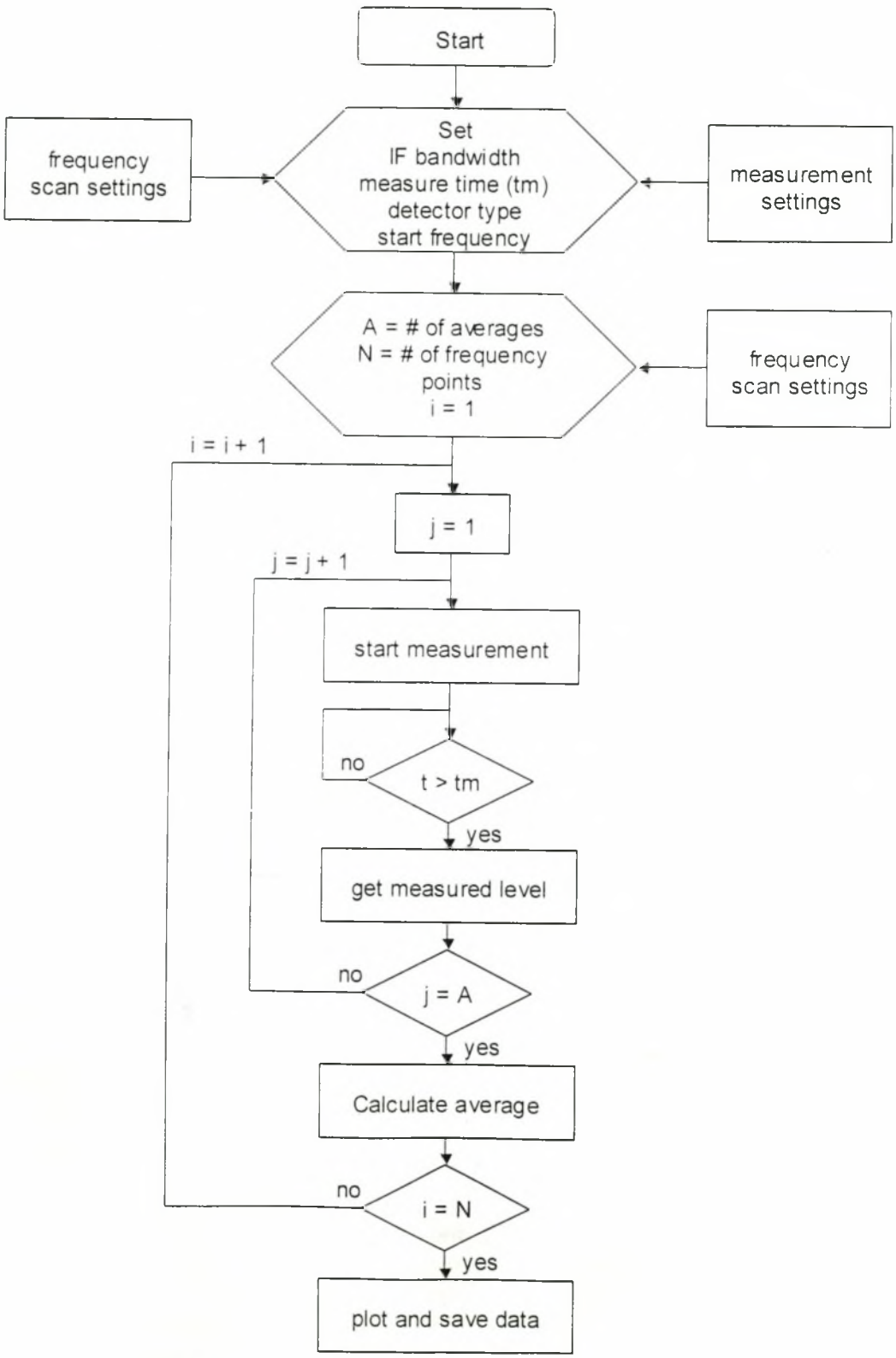

Stellenbosch University http://scholar.sun.ac.za/

Appendix E2

HP 8562A Spectrum Analyser Control

E 2.1 Introduction

Two spectrum analyser measurement methods were used in chapter 5 to make an accurate account of the corona cage RI noise frequency spectrum. The swept narrowband method requires PC control of the HP 8562A SA via the HPIB port of the device. It was found that more sophisticated post-processing is required to extract all the necessary information. A Matlab program should be used for this. Only the Visual Basic PC control is used in this thesis and is described in this appendix.

E 2.2 Useful Commands from the Instruction Set

• GPIB control:	DEV?	- Query device identification
• Initializing SA:	AT 10 DB	- Set the input attenuation to 10 dB
	AUNITS DB	- Measurement units set to dBm
	RB 10 kHz	- Set the resolution bandwidth to 10kHz
	VB 10 kHz	- Set the video bandwidth to 10kHz
	ST 50 ms	- Set the sweep time to 10 ms
• Setting Frequency:	CF 1 MHz	- Set the centre frequency to 1MHz
	SP 10 kHz	- Set the span to 10 kHz
• Triggering:	SNGLS	- Start a single sweep
• Measurement:	MKPK HI	- Set the marker to the highest measured peak level in the span
	MKA?	- Output the value of marker A

Stellenbosch University http://scholar.sun.ac.za/
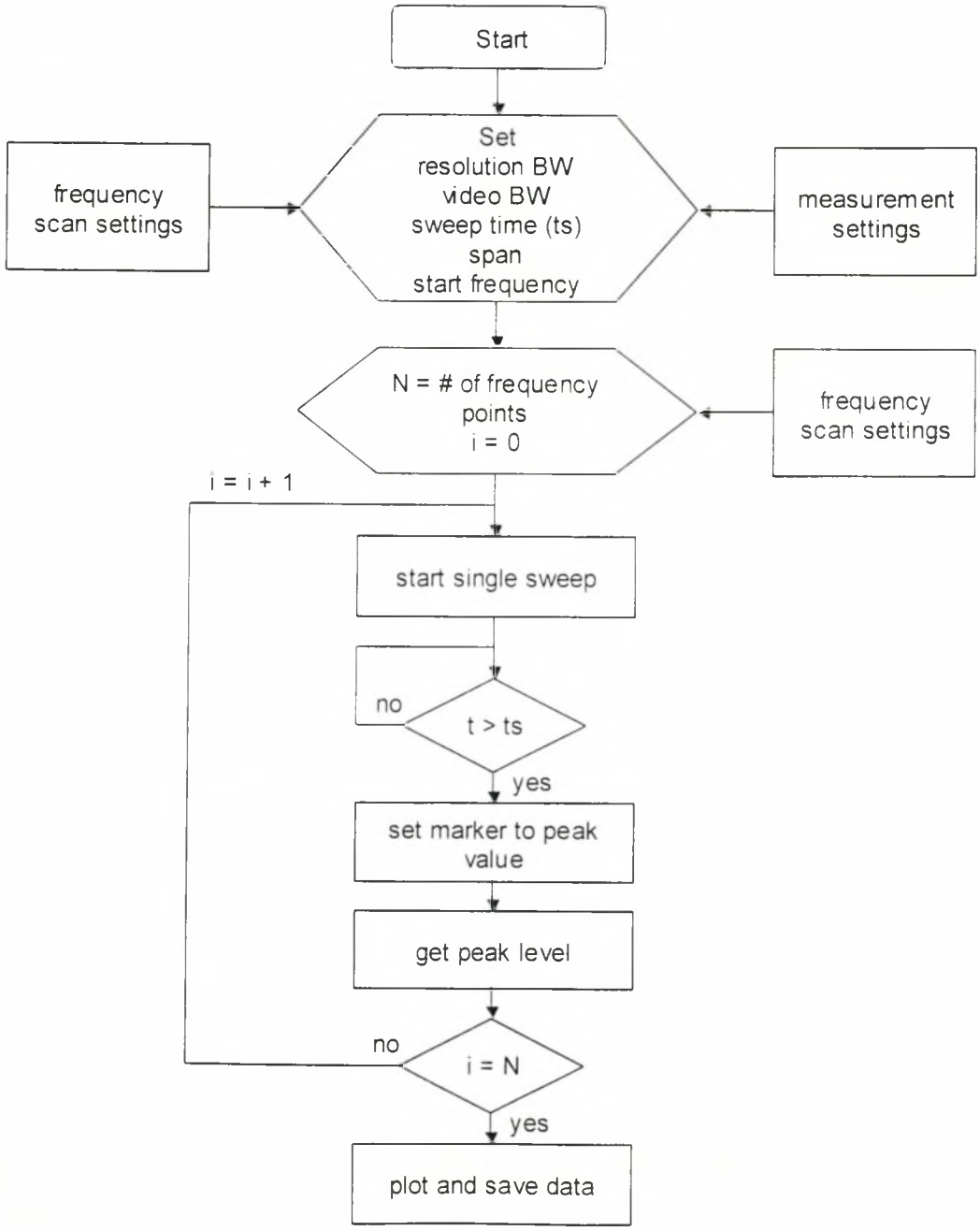
E 2.3 Visual Basic Implementation